Searching for Supersymmetry with the ATLAS Detector at the Large Hadron Collider

Sky Trillium French

of
Peterhouse

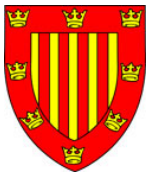

A dissertation submitted to the University of Cambridge
for the degree of Doctor of Philosophy
May 2011

Searching for Supersymmetry with the ATLAS Detector at the Large Hadron Collider

Sky Trillium French

Abstract

On Monday 23rd November 2009, the ATLAS experiment at the Large Hadron Collider began taking data at $\sqrt{s} = 900$ GeV. On the penultimate day of March the following year, after a brief shutdown, ATLAS resumed data taking but at $\sqrt{s} = 7$ TeV. These $\sqrt{s} = 7$ TeV collisions continued until the end of October 2010. This thesis presents the very first low-p_T electron candidates from the complete 9 μb^{-1} $\sqrt{s} = 900$ GeV dataset, and higher-p_T candidates from the first 1 nb^{-1} of the $\sqrt{s} = 7$ TeV dataset. These candidates are presented in the context of electron reconstruction and identification and illustrate how various properties of these electrons compare with expectations based on Monte Carlo simulations. An observation is made of the Z candidates present in the first $\sim$220 nb^{-1} of $\sqrt{s} = 7$ TeV collision data, these being amongst the first Z bosons ever produced by a proton-proton collider. A detailed study is then presented of the full $\sim$35 pb^{-1} 2010 $\sqrt{s} = 7$ TeV dataset in the context of a search for supersymmetry in final states with two leptons (electrons or muons) and high missing transverse energy. No significant deviations from standard model expectations are observed. A "flavour subtraction" analysis is then performed on this data to search for supersymmetry with reduced dependence on experimental and theoretical uncertainties, and increased sensitivity towards particular event topologies. Limits are set at 95% confidence on the number of excess identical-flavour lepton-pairs, over those of different-flavour, multiplied by detector acceptances and efficiencies, from supersymmetry.

Two distinct Monte Carlo studies are also documented, studies carried out in the year preceding the successful running of the Large Hadron Collider. Supersymmetric models which violate R-parity through non-zero λ''_{112} are investigated. In this study, which uses the full ATLAS detector simulation, it is shown that given a well understood detector, R-parity violating supersymmetric $\tilde{\chi}^0_1 \to qqq$ decays may be detectable using jet substructure. This thesis also investigates how a Large Hadron Collider experiment could be used to measure the mixings and masses of the six sleptons in models in which lepton flavour is violated, given significant integrated luminosity. This analysis uses a generic detector simulation package to reasonably model the effects of a detector on the observable particles.

Declaration

This dissertation is the result of my own work and includes nothing which is the outcome of work done in collaboration except where specifically indicated in the text. This dissertation has not been submitted for another qualification to this or any other university and does not exceed the word limit for the respective Degree Committee.

Sky Trillium French

Acknowledgements

In providing the financial support that has enabled me to undertake this degree, I would like to thank both the University of Cambridge and the United Kingdom's Science and Technology Facilities Council (STFC) for the award of an STFC Studentship. I would also like to thank Peterhouse, the college at which I have spent my time since leaving school, for accommodating me and making my time there an enjoyable one.

I would like to thank my supervisors: Andy Parker and Christopher Lester for all their guidance and support, not just over the course of my PhD but over the entire length of my time at Peterhouse. I remain incredibly indebted to Andy Parker for his support and encouragement throughout my undergraduate degrees, and the opportunities for project work which he so kindly gave me on more than one occasion.

In addition I would like to thank James Frost and Christopher Cowden for their never ending technical support during my first year. I am also grateful to Are Raklev for inspiration, but also the entire Cambridge Supersymmetry Working Group and Cambridge ATLAS groups. For much of the analysis presented here I have made use of software tools, simulated and real data samples that are the result of collaboration-wide efforts within ATLAS. I thank Are Raklev for his assistance with non-ATLAS software.

I have greatly enjoyed the time I have so far spent working as part of the Cambridge High Energy Physics group. The members of the group make the lab a fun place to work, and the group a rewarding one of which to be a part.

This thesis would not exist without all the advice and encouragement given to me over the years by my family, nor would it exist without James' love, friendship and support throughout all the challenging moments of the last few years.

Preface

This thesis collects together all the work carried out by the author in the field of experimental high energy physics between October 2008 and April 2011. This work was completed in preparation for the Large Hadron Collider start-up, during ATLAS' brief spell of $\sqrt{s} = 900$ GeV data taking and throughout its first year of $\sqrt{s} = 7$ TeV running. The content of this thesis is roughly divided into three distinct sections. The first section provides an overview of the standard model of particle physics and supersymmetry, the beyond the standard model theory investigated in the bulk of this thesis. An overview of the ATLAS experiment is also provided. The second section brings together all the ATLAS data studies undertaken by the author, including detector performance work at $\sqrt{s} = 900$ GeV and $\sqrt{s} = 7$ TeV, and early physics studies performed with $\sqrt{s} = 7$ TeV data. With the operation of the Large Hadron Collider comes an exciting new era for exploration. The ATLAS experiment has the potential to discover and explore a wide range of new physics processes and in this spirit the section which falls last details a collection of Monte Carlo studies undertaken by the author to investigate this. The closing section brings together the conclusions from the entire body of this thesis.

The figures and tables in this thesis are those of the author, except where explicitly stated in the caption. This includes the author's figures labelled ATLAS Preliminary or ATLAS showing data results in Chapters 4, 5 and 6, and those showing only Monte Carlo in Chapter 7. The author was privileged to be granted the opportunity to produce some of the first $\sqrt{s} = 900$ GeV and first $\sqrt{s} = 7$ TeV physics and performance figures for public release, and very grateful to the collaboration for giving approval for the results in Chapter 6 to proceed to a journal for publication, and for approving the R-parity violating analysis of Chapter 7 for public viewing. All figures illustrating data and Monte Carlo distributions were produced using `ROOT`[1]. The fully simulated Monte Carlo samples and data samples used in this thesis were all produced by the ATLAS central production teams. All cross-sections for these datasets were determined by members of the ATLAS collaboration as described in the body of this thesis.

The $\sqrt{s} = 900$ GeV electron studies briefly presented in Chapter 4 are all the work of the author, but results which all the people who combined their efforts to validate, cross-check and understand the reconstruction and identification of electron candidates in ATLAS at $\sqrt{s} = 900$ GeV also have. Full details of the whole collaborative effort, without the present focus on the results the author obtained can be found in Ref. [2]. This reference is one of the very first ATLAS "Conference Notes", a note which was edited by the author and Marc A. Escalier. The $\sqrt{s} = 7$ TeV early electron results are entirely the work of the author, but results which were also obtained by others working on electron performance with the early $\sqrt{s} = 7$ TeV data.

The Z observation presented in Chapter 5 is once again solely the work of the author, but again presents results which were also obtained by others in the ATLAS collaboration working to observe Z candidates in the first $\sqrt{s} = 7$ TeV data. Whilst undertaking this work the author contributed to the first ATLAS standard model conference notes, Ref. [3–5].

The search for supersymmetry in 2010 $\sqrt{s} = 7$ TeV events with two-leptons is an ATLAS collaboration wide endeavour, and so the author has used in the study presented in Chapter 6 and Appendix B "data-driven" background estimates obtained by other members of the ATLAS "two-lepton" analysis team also looking at and analysing this data. Where these estimates are presented and used, this is explicitly stated in the text and table captions. Otherwise, the analysis presented in this chapter is entirely the author's own work. The author developed the "flavour subtraction" analysis as it appears in this chapter, whilst the rest of the analysis team focused their efforts on an "inclusive" analysis of the two-lepton events, Ref. [6]. The author was co-editor of the two-lepton analysis effort, Ref. [7], with Tapas Sarangi, and co-editor of the papers which resulted from these studies, Refs. [6] and [8], with Dan R. Tovey, Giacomo Polesello and Tapas Sarangi. Although the tables and figures in this chapter are only those, except as just detailed, belonging to the author, others also working on these two-lepton analyses have of course reproduced the same observations in data and Monte Carlo, but no-one else in this group has analysed them in the context of flavour subtraction. The final exclusion plots which appear in Ref. [8] (and the last figure of this chapter) were very kindly produced from the author's p-values for each point by Ximo Poveda.

The Full Simulation Monte Carlo samples used in the R-parity violating supersymmetry analysis presented in Chapter 7 were created from ATLAS centrally produced events by Christopher S. Cowden and James A. Frost. The analysis in this chapter is entirely the author's own work.

The Lepton Flavour Violation analysis detailed in Chapter 8 is the result of collaborative work with Jonathan L. Feng, Iftah Galon, Christopher G. Lester, Yosef Nir, Yael Shadmi, David Sanford and Felix Yu. The realised model, and its corresponding input file, were devised by members of this group. The author's only contribution to this process was to input thoughts on the ideal properties of the model particles. The author was solely responsible for generating from the `HERWIG` input file produced of this model the Monte Carlo events, passing these through `AcerDET` detector simulation and then carrying out the analysis to produce all the displayed figures and numerical measurements in this chapter. The members of this collaboration helped shape the direction of this analysis, and then joined with the author to draw conclusions from the results. The class of supersymmetric model considered in Chapter 8 are the work of Jonathan L. Feng, Yael Shadmi and Yosef Nir and described and motivated in significant detail in Ref. [9]. The author was not involved in the formulation of these models and so the reader is referred to Refs. [9] and [10] for further details.

The "Shifted Peak" method presented in Appendix C is the result of collaborative work with Jonathan L Feng, Christopher G. Lester, Yosef Nir and Yael Shadmi. The author played a leading role in the "discovery" of this method with this group, and was solely responsible for testing the method on the toy decay chains as described. J. Feng, Y. Nir and Y. Shadmi were together responsible for developing the rigorous mathematical derivation of the shift, the details of which are presented here for completeness as they are used in Chapter 8. The author played no significant role in developing the mathematical results.

Most of this work has already been published. The $\sqrt{s} = 900$ GeV electron studies in Chapter 4 are available as already mentioned in an ATLAS first data conference note, Ref. [2], and form part of the first ATLAS data paper, Ref. [11]. The work in Chapter 5 appears in Ref. [5]. The flavour subtraction analysis in Chapter 6 is presented in Ref. [8] (a paper submitted to EPJC Letters for publication on April 1st 2011). The results in this chapter also contribute to the inclusive analysis of lepton-pair events presented

in Ref. [6] (also submitted to EPJC Letters on the same date). The analysis detailed in Chapter 7 has been written up in various ATLAS notes, given by Refs [12–14]. The results of the analysis presented in Chapter 8 are also available in Ref. [10]. The contents of Appendix C are also available in Ref. [15].

The author spent from early December 2009 until late July 2010 based at CERN. Whilst at CERN, in addition to the subset of the work above carried out during this time, the author took the opportunity to become involved in different aspects of the experiment. Joining the Level 1 Calorimeter Trigger collaboration, the author worked with Pete Faulkner from the University of Birmingham and others to write and maintain code to monitor both offline and online the Level 1 Calorimeter Trigger. This work is detailed briefly in Appendix A. Additionally, the author took numerous "Offline Trigger Shifts" - monitoring the HLT "Tier0 histograms" and checking the debug streams for each run pre- and post-reprocessing.

During the first few months of $\sqrt{s} = 7$ TeV data taking the author participated in a couple of early ATLAS data studies which are not described in this thesis. For details of these the interested reader is referred to Refs. [16] and [17].

Contents

"Nothing is too wonderful to be true, if it be consistent with the laws of nature, and in such things as these, experiment is the best test of such consistency."

— Michael Faraday, diary, 19th March 1849

Part I

Foundation

Chapter 1

Introduction

One of the greatest triumphs of twentieth century physics was the development of the standard model of particle physics, a unified description of the fundamental particles which make up our universe, their properties and interactions via three of the four fundamental forces. Despite its great successes, and the ever increasing accuracy to which it has been verified experimentally, it has flaws. The mechanisms it describes are incomplete and it makes predictions only after the insertion of key parameters measured by particle and astrophysical experiments. Most seriously, this theory must break down at higher energies as yet unexplored.

The quest for a theory describing physics beyond the standard model ("new physics") has engaged physicists for the last quarter of a century - with theorists postulating an assortment of models and conjectures, attempting to address the big unanswered questions. Supersymmetry is one such theory. For each known particle, it postulates an almost identical partner differing only in spin and mass. Their introduction solves several problems of the standard model, offering an explanation for the origin of mass and dark matter. Only as experiments probe the high energy frontier can we test these theories, to which we must look to interpret our findings.

The Large Hadron Collider (LHC), built at CERN in Geneva, Switzerland, will explore new energies to take us from current conjecture to concrete discovery. Taking over 20 years to complete, this testament to years of hard work is now for the first time successfully colliding together bunches containing billions of protons, millions of times each second. After a brief commissioning run during Winter 2009, now it has

reached energies never examined before, offering physicists unparalleled opportunities for fundamental physics. The ATLAS experiment, a collaboration of 3000 physicists and engineers from 38 countries, is the largest detector ever built and records these collisions. Interactions between proton constituents probe and test our standard model for deviations or new phenomena. Particle physicists strive to piece together what happens during collisions, refining our knowledge of these interactions, and looking to discover evidence of new ones.

In the chapters of this thesis the very first datasets collected by the ATLAS experiment are studied. Firstly the very first electron candidates are presented. Then observation is made of ATLAS' first Z bosons - key particles in the standard model, first discovered in 1983. Finally, a detailed search for supersymmetry in events with exactly two leptons in the full 2010 $\sqrt{s} = 7$ TeV dataset is given. In the years to come the data will be sufficient to allow subtle searches for yet rarer processes, and it is towards this goal that the concluding chapters consider the future potential of the LHC through a series of studies on simulated data.

Chapter 2

Theory and Motivation

"In her [Nature's] inventions nothing is lacking, and nothing is superfluous."
— Leonardo da Vinci

2.1 Introduction

The standard model of particle physics is a remarkable theory. It explains the huge wealth of observational and experimental data on the properties and behaviour of particles collected so far, by particle and astrophysical experiments located around the globe. Developed during the twentieth century, it is a theory which describes the particles from which our universe is composed, and their interactions with each other, in a way which matches well to observation (when the model is extended to include massive neutrinos). It is therefore reasonable to ask, why is it that entire new theories and extensions to the standard model have been and continue to be proposed despite the existence of such a successful and established theory? Put quite simply - despite its successes the standard model is, unfortunately, almost certainly incomplete.

The standard model explains matter and its interactions in terms of three forces (the weak, strong and electromagnetic). The existence of the fourth, gravity, is not accounted for. Experiments have collected a treasure trove of evidence for the existence of "dark matter", but the standard model does not describe it. Even if this and other

problems were ignored, the standard model itself hints at its own incompleteness. It contains nineteen free parameters which must be fixed by measurement and it supposes the universe possesses an $\mathrm{SU}(3) \times \mathrm{SU}(2)_L \times \mathrm{U}(1)_Y$ local gauge invariance but makes no attempt to suggest why this might be. In this chapter the standard model of particle physics is introduced (first in its unbroken form and then after its symmetries are broken) and its limitations discussed. One of the most popular extensions to the standard model and the main topic of this thesis, supersymmetry, is then introduced and the ways in which it fixes some of the problems with the standard model highlighted.

2.2 The Standard Model

2.2.1 Overview

The standard model of particle physics is a gauge field theory, developed in the early 1970s, to explain matter and its interactions. It describes two different types of particle, so called "fermions" (Table 2.1) and "bosons" (Table 2.2). Fermions fall into two categories, quarks and leptons. Leptons interact only via the weak and electromagnetic forces (unified as the electroweak force) whilst quarks are also able to interact via the strong force. Fermionic particles interact by exchanging vector bosons. These particles are all point-like and all carry internal angular momentum (called "spin" and characterised by a quantum number, s). The gravitational interaction between elementary particles is so small that it is safely neglected, and the standard model, which considers only three fundamental forces is still a powerful description of particles and interactions. Quarks are always found paired in either doublets (mesons) or combined in triplets (baryons) whilst leptons are always found alone. Unlike leptons, quarks are not eigenstates of the weak force. They couple preferentially, but not uniquely, via the weak force to quarks of the same family. The Cabibbo-Kobayashi-Maskawa (CKM) matrix [18] describes this weak-force quark-family mixing.

In the language of field theories, the standard model is a renormalisable quantum field theory which results from a spontaneously broken $\mathrm{SU}(3) \times \mathrm{SU}(2)_L \times \mathrm{U}(1)_Y$ local gauge invariance. That is, each of the three forces is associated with a local symmetry transformation. The strong force is characterised by local SU(3) transformations and the weak and electromagnetic forces combined in the electroweak force characterised by an

	1st Generation	2nd Generation	3rd Generation
Quarks	up (u)	charm (c)	top (t)
	down (d)	strange (s)	bottom (b)
Leptons	electron neutrino (ν_e)	muon neutrino (ν_μ)	tau neutrino (ν_τ)
	electron (e)	muon (μ)	tau (τ)

Table 2.1: *The three successive generations of standard model fermions. Each generation is successively heavier. The top row of quarks carry charge $+\frac{2}{3}$, the bottom row charge $-\frac{1}{3}$, the neutrinos zero charge and the three remaining leptons a charge of -1 (all in units of electron charge, e). All twelve particles have been observed experimentally, and all twelve are believed to be fundamental. Note also that each lepton has an antiparticle, differing only in charge from the particle.*

$\mathrm{SU}(2)_L \times \mathrm{U}(1)_Y$ symmetry. The strong force is often called quantum chromodynamics (QCD). The quarks are "colour" triplets of the QCD gauge group. Gluons (which themselves also carry "colour charge") are the bosons which mediate the strong force. The charges of the fermions are weak "isospin" and weak "hypercharge". In the standard model there are three generations of quarks and leptons which differ only by mass, each family successively heavier. The forces accounted for by the standard model (the weak, the strong and the electromagnetic) are all mediated by the exchange of particles. The bosons of the electroweak force are the W and Z, and the photon. Interacting fermions carry spin-$\frac{1}{2}$, whereas the force-mediating bosons carry integer spin.

Force	Mediating Boson
electromagnetic	photons (γ)
weak	W^+, W^-, Z
strong	gluons (g)

Table 2.2: *The three fundamental forces accounted for by the standard model, and the appropriate force mediating standard model bosons. The photons and gluons are massless, the carriers of the weak force (the W and Z vector bosons) massive. All five mediating bosons have been observed experimentally.*

The particles just described have all been discovered, and are all believed to be fundamental. The electron, with a mass $\sim \frac{1}{2000}$ the mass of the proton was first discovered in 1897 by J.J. Thomson whilst he experimented with cathode rays [19]. The muon, 207

times more massive than the electron and unstable, was discovered in 1936 by Carl D. Anderson (who incidentally discovered the electron's antiparticle, the positron [20]) whilst looking at cosmic rays in a cloud chamber [21]. The τ was not discovered until the e^+e^- collider SPEAR observed a strange excess of e^+e^- decays to $e^\pm\mu^\pm$ associated with at least two undetectable particles. This excess was accounted for by the presence of the decays $\tau \to e\nu$ and $\tau \to \mu\nu$ between 1974 and 1977 by Martin Lewis Perl and his colleagues [22–24].

The elusive electron neutrino's existence was strongly hinted at by β decays. Observations of these decays suggested the presence of a particle with nearly zero mass and neutral charge (existing but not observed). In 1956 Clyde Cowan and Frederick Reines designed an experiment sensitive to neutrinos, eventually observing the electron neutrino for the first time [25–29]. The muon neutrino was discovered just six years later by Leon Lederman, Melvin Schwartz and Jack Steinberger and colleagues through observations of neutrinos involved in the production of muons, but not electrons, very likely neutrinos different from the neutrinos associated with β decay [30]. Thus by the early 1960s experiments had observed the electron, the muon and then the electron and muon neutrinos. The observation of the τ which followed predicted the existence of the third neutrino. The DONUT experiment was designed to discover the tau neutrino, doing so in 2000 [31].

The existence of only bound quark states ensures that no direct observation of any of the six quarks is possible. In 1968, indirect evidence for the existence of the up and down quarks was discovered at SLAC in deep inelastic scattering experiments [32, 33]. Discovery of the strange quark came with the observation of kaons (states containing at least one bound strange quark) in 1947. The charm quark was discovered in 1974 [34, 35] with the discovery of the J/Ψ, a charmed meson. The bottom quark was discovered in 1977 by the Fermilab E288 experiment team led by Leon Lederman, when collisions produced bottomonium [36]. The top quark was not discovered until 1994, when it was detected by the DØ and CDF experiments at Fermilab [37, 38]. Gluons were discovered in 1979 by the TASSO collaboration, an experiment at DESY [39]. The W and Z bosons, propagators of the electroweak force, were first observed and measured in 1983 [40–43] by the UA1 and UA2 collaborations (experiments at the CERN anti-proton proton collider).

An Unbroken $\mathbf{SU(3) \times SU(2)_L \times U(1)_Y}$ Symmetry

The gauge field theory in its unbroken form gives a spectrum of entirely massless particles. Given that particles in the universe have mass, the symmetries cannot be left unbroken and a means through which particles can acquire mass is required. For now, however, the consequences of imposing an $\mathrm{SU}(3) \times \mathrm{SU}(2)_L \times \mathrm{U}(1)_Y$ symmetry on the universe, in its unbroken form, are explored. The standard model Lagrangian is initially built from terms which lead to the correct equations of motion for all the different fermionic particles. Forcing the standard model Lagrangian to be invariant under $\mathrm{U}(1)_Y$ and $\mathrm{SU}(2)_L$, introduces gauge bosons (the mediators of two of the three forces, the weak and the electromagnetic). Forcing invariance under SU(3) introduces the gauge bosons of the strong force. In what follows, for clarity, the consequences of imposing local gauge invariance are illustrated only for the $\mathrm{U}(1)_Y$ and $\mathrm{SU}(2)_L$ symmetries. The gauge quantum numbers of the three forces are referred to as hypercharge (Y), weak isospin (I_W) and colour so that the $\mathrm{U}(1)_Y$ part of the theory gives a weak hypercharge gauge boson, the $\mathrm{SU}(2)_L$ part three isospin bosons and the final SU(3) part the eight coloured gluons.

Quantum field theory states that a free fermionic particle, for example an electron, can be described by the Lagrangian $\mathcal{L}_0$ (Equation 2.1), a Lagrangian correctly predicting the Dirac equation to describe the fermion's motion (m is the mass of the fermion).

$$\mathcal{L}_0 = \bar{\psi} i \gamma^\mu \partial_\mu \psi - m \bar{\psi} \psi \tag{2.1}$$

A vector field A_μ, the electromagnetic photon, can be introduced using the minimal substitution $\partial_\mu \rightarrow \partial_\mu + ieA_\mu$ (e is a constant, the electric charge of an electron). This transforms the Lagrangian $\mathcal{L}_0$ into a new Lagrangian, $\mathcal{L}_D$ (Equation 2.2).

$$\mathcal{L}_D = \mathcal{L}_0 - eA_\mu \bar{\psi} \gamma^\mu \psi \tag{2.2}$$

The field A_μ itself should contribute the term $-\frac{1}{4} F_{\mu\nu} F^{\mu\nu}$ where $F^{\mu\nu} = \partial^\mu A^\nu - \partial^\nu A^\mu$, this term being the Lagrangian for a free electromagnetic field, one which predicts the correct behaviour of A_μ (Maxwell's equations). Inclusion of this free electromagnetic field term completes the full Lagrangian for a charged fermion interacting with an electromagnetic field, $\mathcal{L}_{EM}$ (Equation 2.3). It contains the free fermion and free electromagnetic field Lagrangians, and a term describing their interaction (the $-eA_\mu \bar{\psi} \gamma^\mu \psi$ term, giving $\gamma \rightarrow ee$

vertices).

$$\mathcal{L}_{EM} = \bar{\psi} i\gamma^{\mu}\partial_{\mu}\psi - m\bar{\psi}\psi - eA_{\mu}\bar{\psi}\gamma^{\mu}\psi - \frac{1}{4}F_{\mu\nu}F^{\mu\nu} \tag{2.3}$$

The resulting Lagrangian must be made invariant under an $\mathrm{SU}(3) \times \mathrm{SU}(2)_L \times \mathrm{U}(1)_Y$ symmetry.

U(1) *Symmetry* - The Lagrangian, $\mathcal{L}_{EM}$, is not, as it stands, gauge invariant under the gauge transformation in Equation 2.4 but can be made invariant if both the gauge transformation and the phase transformation in Equation 2.5 are applied simultaneously (with $\phi(x) = -e\chi(x)$). In this $\phi(x)$ is the phase, a function of x and the transformation a local one.

$$A^{\mu} \rightarrow A^{'\mu} = A^{\mu} + \partial^{\mu}\chi \tag{2.4}$$

$$\psi \rightarrow \psi^{'} = e^{i\phi(x)}\psi \tag{2.5}$$

Conversely this is identical to taking the Dirac Lagrangian (Equation 2.1) and forcing invariance under a local U(1) phase transformation (Equation 2.5) by introducing a vector field, A^{μ}, which transforms according to Equation 2.4. This Lagrangian is the theory of electromagnetism, the U(1) symmetry under which it is invariant requiring simultaneous phase and gauge transformations to be applied.

SU(2) *Symmetry* - A Lagrangian could involve two fermion fields, ψ_1 and ψ_2, and symmetry can be demanded under transformations that mix them together. Let Ψ be a doublet of the fields $\psi_{1,2}$, (ψ_1, ψ_2). SU(2) is a local phase transformation which takes the form of Equation 2.6 (compared to U(1), Equation 2.5). $T_j = \frac{1}{2}\tau_j$, where τ_j are the Pauli matrices. $U(x)$ in this case is a 2D-matrix, mixing the ψ_1 and ψ_2 states.

$$\Psi \rightarrow \Psi^{'} = e^{[ig\omega_j(x)T_j]}\Psi = U(x)\Psi \tag{2.6}$$

Using the same procedure as illustrated for a U(1) symmetry, the Lagrangian for a free fermion (Equation 2.1) can only be made invariant under SU(2) if ∂_{μ} is replaced by a

covariant derivative D_μ (Equation 2.7).

$$D^\mu = \partial^\mu + igA^\mu_j(x)T_j \tag{2.7}$$

This introduces three new vector fields, A^μ_j, each transforming as in Equation 2.8 (g is a constant which will appear in the terms of the resulting interactions), here $A^\mu(x) = A^\mu_j(x)T_j$.

$$A^\mu \rightarrow A'^\mu = UA^\mu U^\dagger + \frac{i}{g}(\partial^\mu U)U^\dagger \tag{2.8}$$

As a consequence of introducing the three new gauge fields, $A^\mu_j(x)$, three terms must be added to the Lagrangian to allow for their propagation. Unlike in the electromagnetic case these terms do not take the form $-\frac{1}{4}F_{\mu\nu}F^{\mu\nu}$ as this is not gauge invariant under SU(2) (only U(1)). Instead the relevant gauge invariant term is given by an $F^j_{\mu\nu}$ as defined in Equation 2.9.

$$F^j_{\mu\nu} = \partial_\mu A^j_\nu - \partial_\nu A^j_\mu - g\epsilon_{jkl}A^k_\mu A^l_\nu \tag{2.9}$$

The SU(2) gauge invariant Lagrangian is thus given in full by Equation 2.10.

$$\mathcal{L} = -\frac{1}{4}F^{\mu\nu}_j F_{j\mu\nu} + i\bar{\Psi}\gamma^\mu D_\mu \Psi - m\bar{\Psi}\Psi \tag{2.10}$$

$\mathbf{SU(2)_L \times U(1)_Y}$ *Symmetry* - The U(1) gauge invariant Lagrangian, $\mathcal{L}_{EM}$ (Equation 2.3), accounts for electromagnetism. The SU(2) gauge invariant Lagrangian (Equation 2.10), is a good candidate for the Lagrangian of the weak force. When it is expanded in terms of the three vector boson fields, A^μ_j, it gives fermion-boson interactions (similar to those of quantum electrodynamics) and boson self-interactions. The fermion-boson interaction terms include the term $\frac{g}{2}\bar{\psi}_1\gamma^\mu\psi_1 W_{3\mu}$ (A^μ_j substituted with W^μ_j to bring familiarity with the weak force), interaction of a fermion (ψ_1) with a boson (W_3) which must be neutral to conserve charge at the interaction vertex. Boson self-interaction terms include the term $\frac{g^2}{4}\epsilon_{jkl}\epsilon_{jmn}W^\mu_k W^\nu_l W_{m\mu}W_{n\nu}$, interactions involving pairs of Ws (W_1s and W_2s).

If the two charge states of quarks and leptons within each generation are represented as two component fields (Equations 2.11 and 2.12) then it seems natural to try and

describe weak interactions with an SU(2) gauge theory.

$$\Psi_l = \begin{pmatrix} \psi_{\nu_e} \\ \psi_e \end{pmatrix}, \begin{pmatrix} \psi_{\nu_\mu} \\ \psi_\mu \end{pmatrix}, \begin{pmatrix} \psi_{\nu_\tau} \\ \psi_\tau \end{pmatrix} \tag{2.11}$$

$$\Psi_q = \begin{pmatrix} \psi_u \\ \psi_d \end{pmatrix}, \begin{pmatrix} \psi_c \\ \psi_s \end{pmatrix}, \begin{pmatrix} \psi_t \\ \psi_b \end{pmatrix} \tag{2.12}$$

Interaction terms then take a familiar form, with the ψ_2 an electron, which interacts with the neutral W_3, and the ψ_1 the ν_e (these neutral current interactions familiar interactions between standard model particles). These observations tempt the statement that W_3 is the Z boson, and the W_1 and W_2 the $W^\pm$. The Lagrangian must, however, be adapted. Experiment shows that weak charged vector bosons (W^+ and W^-) only interact with left-handed chiral states. This suggests that the Ψ of Equation 2.10 should be $\Psi_L = \frac{1}{2}(1-\gamma^5)\Psi$, the left-handed chiral components of the fermions, to ensure $W^\pm$ interactions with left-handed fermions only, if W_1 and W_2 are to be labelled $W^\pm$.

The transformation $\Psi \rightarrow U(x)\Psi$ (Equation 2.6) is termed a weak isospin gauge transformation, the top and bottom doublets are assigned weak isospin $I_W = \pm\frac{1}{2}$ and the right-handed fermions are made invariant under weak isospin transformation ($I_W = 0$). The resulting replacement of Ψ with Ψ_L in Equation 2.10 and its expansion then reveals the interaction terms of the fermions with the three bosons, but appropriately only interactions between $W^\pm$ with left-handed fermions.

This expansion also gives terms involving the W_3^μ and the left-handed fermions (terms of the form $\frac{g}{4}\bar{\psi}_1\gamma^\mu(1-\gamma^5)\psi_1 W_{3\mu}$), but no terms involving interactions between it and the right-handed fermions. Experiment demonstrates that the neutral Z boson interacts with both right-handed and left-handed fermions. The W_3^μ is therefore not trivially the Z boson. The Z also has a different mass to the $W^\pm$, and so W_3 cannot be the Z.

Remembering that imposing $\mathrm{U}(1)_Y$ already gave a neutral gauge boson, the photon A_μ, suggests W_3 could be a mixture of the photon and the Z (Equation 2.13).

$$W_3^\mu = \cos\theta_W Z^\mu + \sin\theta_W A^\mu \tag{2.13}$$

This is electroweak unification. It unites the electromagnetic force with the weak force to give the electroweak force, summarised as $\mathrm{SU}(2)_L \times \mathrm{U}(1)_Y$ and allows predictions of the mass of the Z given the mass of the W.

The fermion mass term $m\bar{\psi}\psi$ (Equation 2.14) is no longer gauge invariant because the left and right-handed chiral components transform differently.

$$\mathcal{L} = -m\bar{\psi}\psi = -m\bar{\psi}_R\psi_L - m\bar{\psi}_L\psi_R \tag{2.14}$$

Mathematically, the above is to say that, imposing independent $\mathrm{SU}(2)_L$ and $\mathrm{U}(1)_Y$ gauge symmetries (Equations 2.15 and 2.16) on the free fermion Lagrangian (Equation 2.1) leads to the electroweak Lagrangian. Y_L, Y_{1R} and Y_{2R} are the weak hypercharges, $g^{'}$ a constant.

$$\Psi_L \rightarrow e^{\left[i\frac{g}{2}\omega_j\tau_j\right]}\Psi_L, \psi_{1R} \rightarrow \psi_{1R}, \psi_{2R} \rightarrow \psi_{2R} \tag{2.15}$$

$$\Psi_L \rightarrow \exp\left[ig^{'}Y_L\omega_0\right]\Psi_L, \psi_{1R} \rightarrow \exp\left[ig^{'}Y_{1R}\omega_0\right]\psi_{1R}, \psi_{2R} \rightarrow \exp\left[ig^{'}Y_{2R}\omega_0\right]\psi_{2R} \tag{2.16}$$

The electroweak Lagrangian, $\mathcal{L}_{EW}$ (Equation 2.17, terms given by Equations 2.18 to 2.23) involves fermions (leptons, l, and quarks, q), three new gauge fields $W^{\mu}_{1,2,3}$ for SU(2) and one gauge field B^{μ} for U(1).

$$\mathcal{L}_{EW} = -\frac{1}{4}F^{\mu\nu}_j F_{j\mu\nu} - \frac{1}{4}B^{\mu\nu}B_{\mu\nu} + \sum_{l,q}\mathcal{L}_{q,l} \tag{2.17}$$

$$\mathcal{L}_{q,l} = i\bar{\Psi}_L\gamma^{\mu}D_{\mu}\Psi_L + i\bar{\psi}_{1R}\gamma^{\mu}D_{\mu}\psi_{1R} + i\bar{\psi}_{2R}\gamma^{\mu}D_{\mu}\psi_{2R} \tag{2.18}$$

$$F^{\mu\nu}_j = \partial^{\mu}W^{\nu}_j - \partial^{\nu}W^{\mu}_j - g\epsilon_{jkl}W^{\mu}_k W^{\nu}_l \tag{2.19}$$

$$B^{\mu\nu} = \partial^{\mu}B^{\nu} - \partial^{\nu}B^{\mu} \tag{2.20}$$

$$D^{\mu}\Psi_L = (\partial^{\mu} + ig\frac{1}{2}\tau_j W^{\mu}_j + ig^{'}Y_L B^{\mu})\Psi_L \tag{2.21}$$

$$D^{\mu}\psi_{1R} = (\partial^{\mu} + ig^{'}Y_{1R}B^{\mu})\psi_{1R} \tag{2.22}$$

$$D^{\mu}\psi_{2R} = (\partial^{\mu} + ig^{'}Y_{2R}B^{\mu})\psi_{2R} \tag{2.23}$$

The three vector fields, W^{μ}, are the three $\mathrm{SU}(2)_L$ isospin bosons and B^{μ} the weak hypercharge boson. To relate B^{μ} and W_3^{μ} to the observed neutral bosons, the Z (Z^{μ}) and the photon (A^{μ}), W_3^{μ} and B^{μ} are considered as mixtures of these two fields (Equations 2.13 and 2.24).

$$B^{\mu} = -\sin\theta_W Z^{\mu} + \cos\theta_W A^{\mu} \tag{2.24}$$

This can be made consistent with observed electromagnetic currents (from the pure interaction of a particle of charge e with the electromagnetic field) by relating the weak hypercharges ($Y_{L,1R,2R}$) to electric charge and weak isospin (I_3^W). In doing this it must be true that $g\sin\theta_W = g^{'}\cos\theta_W = e$ and weak hypercharge, Y has the assignment $Y = Q - I_3^W$, where Q is the charge of the fermion (in units of electron charge, e).

The resulting particles and their electroweak quantum numbers are given in Table 2.3. The right-handed quarks and leptons are listed with zero isospin, and so do not couple to isospin bosons. The electroweak Lagrangian, Equation 2.17, written in terms of the observed fields, shows clearly that both gauge boson and fermion mass terms are forbidden by $\mathrm{SU}(2)_L \times \mathrm{U}(1)_Y$ gauge symmetry.

An equivalent demonstration of imposing SU(3) local gauge invariance would generate the eight force carriers of the strong force, the gluons.

Spontaneous Symmetry Breaking and the Standard Model

The fundamental particles described by the standard model have all been experimentally observed (Section 2.2.1) and many are known to be massive. The approximate masses of the standard model fermions are given in Table 2.4, and those of the gauge bosons are given in Table 2.5. The three generations of quarks and leptons are successively heavier, a feature not predicted by the standard model and unaccounted for.

	Q	I_3^W	Y
$\begin{pmatrix} \nu_e \\ e \end{pmatrix}_L$	0	$+\frac{1}{2}$	$-\frac{1}{2}$
	-1	$-\frac{1}{2}$	$-\frac{1}{2}$
ν_{eR}	0	0	0
e_R	-1	0	-1
$\begin{pmatrix} u \\ d \end{pmatrix}_L$	$+\frac{2}{3}$	$+\frac{1}{2}$	$+\frac{1}{6}$
	$-\frac{1}{3}$	$-\frac{1}{2}$	$+\frac{1}{6}$
u_R	$+\frac{2}{3}$	0	$+\frac{2}{3}$
d_R	$-\frac{1}{3}$	0	$-\frac{1}{3}$

Table 2.3: *Electroweak (non-mass) quantum mumbers for the 1st generation of quarks and leptons (the quantum numbers of the 2nd and 3rd generations are analogous). $Q = I_3 + Y$. Y (weak hypercharge) is the gauge quantum number of the $\mathrm{U}(1)_Y$ symmetry and I_3^W (weak isospin) the gauge quantum number of the $\mathrm{SU}(2)_L$ symmetry. Q is here the fermion charge, in units of electron charge e.*

	Leptons (Mass / GeV)	Quarks (Mass / GeV)
1st Generation	e (0.0005)	d (0.004-0.006)
	ν_e (≈ 0)	u (0.002-0.003)
2nd Generation	μ (0.106)	s (0.10)
	ν_μ (≈ 0)	c (1.3)
3rd Generation	τ (1.78)	b (4.7)
	ν_τ (≤ 0.016)	t (172)

Table 2.4: *Approximate masses of the standard model fermions (from [44]). Each generation of quarks and leptons has very different masses to the generation before. The particles in each generation are copies of each other, differing only in mass. The standard model does not predict these masses.*

Force	Boson	Mass (GeV)
Electromagnetic	photon (γ)	0
Weak	$W^{\pm}$	80
Weak	Z	91
Strong	gluons (g)	0

Table 2.5: *Approximate masses of the standard model bosons (from [44]). Only the $W^{\pm}$ and Z vector bosons are massive, the bosons of the electromagnetic and strong forces are massless. The W and Z masses are not independently predicted by the standard model.*

The electromagnetic and weak forces can be unified, but the imposed gauge invariance prevents gauge boson and fermion mass terms. Masses may be introduced through a process called "Spontaneous Symmetry Breaking". In gauge theories this symmetry breaking is introduced by the addition of scalar fields to the Lagrangian. The scalar degrees of freedom from these new scalar particles transfer to the gauge boson fields to give them mass. Spontaneous Symmetry Breaking can be introduced into a global U(1) symmetry as follows. The Lagrangian given by Equation 2.25, where $\phi(x)$ is a single complex (non-Hermitian) scalar field, possesses a global symmetry if $\phi(x)$ is transformed as $\phi(x) \rightarrow e^{i\alpha}\phi(x)$ where α is a real number.

$$\mathcal{L} = (\partial^{\mu}\phi^{\dagger})(\partial_{\mu}\phi) - \mu^2\phi^{\dagger}\phi - \lambda(\phi^{\dagger}\phi)^2 \tag{2.25}$$

The minimum of the potential term in this Lagrangian (Equation 2.26) is of particular importance.

$$V(\phi) = \mu^2\phi^{\dagger}\phi + \lambda(\phi^{\dagger}\phi)^2 \tag{2.26}$$

For the minimum (vacuum) energy to be bounded from below, $\lambda > 0$. For the simple case where $\mu^2 > 0$, the potential has a single minimum value $V_{min} = 0$ at $\phi = \phi_0 = 0$. The case $\mu^2 < 0$ is more instructive. In this case the minimum of the potential lies on a circle of radius $-\mu^4/4\lambda$. This minimum occurs when ϕ_0 is given by Equation 2.27.

$$\phi_0 = \langle 0|\phi|0\rangle = \sqrt{\frac{-\mu^2}{2\lambda}}e^{i\theta} \tag{2.27}$$

Only the magnitude of the potential is determined at this minimum, the phase is arbitrary and there are an infinite number of minima, degenerate in all possible values of θ. The physical vacuum state realised could be any one of these degenerate states. By realising a particular vacuum the U(1) symmetry is broken. There results a symmetry of the Lagrangian which is not shared by the true, realised vacuum. To progress, $\phi(x)$ is expanded about the chosen vacuum (Equation 2.28), defining $\phi_0 = \frac{v}{\sqrt{2}}$ where $v = \sqrt{\frac{-\mu^2}{\lambda}}$.

$$\phi(x) = \frac{1}{\sqrt{2}}[v + \sigma(x) + i\eta(x)] \tag{2.28}$$

The Hermitian fields introduced, σ and η, must have zero vacuum expectation values. Expanding the Lagrangian in terms of these fields gives the Lagrangian in Equation 2.29 where $\mathcal{L}_I$ contains the interaction terms.

$$\mathcal{L} = \frac{1}{2}(\partial^\mu\sigma)(\partial_\mu\sigma) - \frac{1}{2}m_\sigma^2 + \frac{1}{2}(\partial^\mu\eta)(\partial_\mu\eta) + \mathcal{L}_I + \text{const.} \tag{2.29}$$

This Lagrangian states that the σ field has mass ($m_\sigma^2 = 2\lambda v^2$) but that the η field remains massless. One massive and one massless scalar boson have been obtained by introducing the complex scalar field (which had two degrees of freedom).

If a weak isospin doublet of complex scalar fields (four degrees of freedom) is introduced to the electroweak Lagrangian and $\mathrm{SU}(2)_L \times \mathrm{U}(1)_Y$ group, masses can be given to the gauge bosons. Three of the four introduced degrees of freedom are given to the $W^\pm$ and Z masses, leaving one real scalar field (the Higgs boson) and the photon massless. The introduced scalar doublet $\Phi(x)$ (Equation 2.30) transforms under $\mathrm{SU}(2)_L \times \mathrm{U}(1)_Y$ in the familiar way.

$$\Phi = \begin{pmatrix} \phi^+ \\ \phi^0 \end{pmatrix}, \bar{\Phi} = \begin{pmatrix} \bar{\phi}^0 \\ \phi^- \end{pmatrix} \tag{2.30}$$

The doublet transforms under $\mathrm{SU}(2)_L$ according to Equation 2.31.

$$\Phi \rightarrow \exp\left(i\frac{g}{2}\tau_j w_j(x)\right)\Phi \tag{2.31}$$

Transformation under $U(1)_Y$ is according to Equation 2.32, Y_H is the weak hypercharge of the Higgs.

$$\Phi \rightarrow \exp\left(ig^{'}Y_H w_0(x)\right)\Phi \tag{2.32}$$

The introduction of the complex scalar field doublet requires the gauge invariant scalar component given by Equation 2.33 to be added to the electroweak Lagrangian,

$$\mathcal{L}_D = (D_\mu\Phi)^\dagger(D^\mu\Phi) - \mu^2\Phi^\dagger\Phi - \lambda(\Phi^\dagger\Phi)^2 \tag{2.33}$$

with the covariant derivative in Equation 2.34.

$$D^\mu\Phi(x) = [\partial^\mu + i\frac{g}{2}\tau_j W_j^\mu(x) + ig^{'}Y_H B^\mu(x)]\Phi(x) \tag{2.34}$$

Realising, for $\mu^2 < 0$, one unique ground state for the Higgs field as before, gives an electroweak Lagrangian scalar component which includes a term of the form $\frac{1}{4}g^2v^2W_\mu^\dagger W^\mu$, corresponding to a mass m_W for the $W^\pm$ gauge boson $\frac{1}{2}vg$. The fields $W_{3\mu}$ and B_μ only appear in the linear combination $\frac{1}{2}gW_{3\mu} - g^{'}Y_H B_\mu$, and so this combination alone gains a mass. Fixing $Y_H = \frac{1}{2}$ ensures that only the Z gains mass, $m_W/\cos\theta_W$. This method of introducing a complex scalar doublet is called the Higgs mechanism and it is used in the standard model to obtain massive gauge bosons [45, 46].

The same Higgs doublet can be used to obtain massive quarks and leptons. This is done by adding so-called Yukawa interaction terms (e.g. Equation 2.35, where g_d is a constant, Ψ_L and ψ_{dR} the down quark fields) to the Lagrangian which are invariant under both $SU(2)_L$ and $U(1)_Y$ gauge transformations.

$$\mathcal{L} = -g_d\bar{\Psi}_L\psi_{dR}\Phi \tag{2.35}$$

These terms give leptons masses which are proportional to the vacuum expectation value of the scalar field and interactions between leptons and the Higgs field which are proportional to lepton mass (neutrinos being left massless). The quark mass eigenstates are not equal to the weak eigenstates which allows charged weak interactions to involve transitions between the three generations. This mixing matrix (the CKM matrix) allows charge parity ($\mathcal{CP}$) violation (a symmetry in which particles are exchanged for their antiparticles, and spatial coordinates switched).

Concluding Remarks

This has not been a full treatise on the standard model. A discussion of QCD (the strong force) has been neglected. It has been demonstrated that by imposing gauge invariance and spontaneous symmetry breaking, it is possible to predict the interactions of all the standard model particles, and their masses. The resulting masses are however, only defined in terms of the introduced model parameters, no absolute predictions for the masses of the leptons, quarks and bosons are obtained similarly. No absolute predictions for the interaction strengths are made.

The first experimental results to show deviations from standard model predictions were measurements of neutrino oscillations [47, 48]. Neutrinos were observed to "oscillate", to be pure-mass, but not pure-flavour states. These observations, of both solar and atmospheric neutrinos, were at odds with a theory predicting pure, massless neutrinos. Neutrino mixing and masses can be incorporated into the standard model. The next section details problems with the standard model which cannot be fixed within its framework. Note that whilst there are many ways of introducing neutrino masses, and mixings, into the standard model, these could just as well emerge as a side effect of a more fundamental theory. For example, in supersymmetry, non-zero R-parity or lepton number violating terms lead to neutrino mixing [49].

2.2.2 Problems with the Standard Model

There are nineteen free parameters in the standard model. These include parameters which describe electroweak mixing and $\mathcal{CP}$ violation. These can all be measured using experiments, and much work has gone into doing so. Despite this, it is somewhat unsatisfactory to believe that these parameters can only be determined by measurement. A more elegant theory of nature would predict these parameters.

Imposing $\mathrm{SU}(3) \times \mathrm{SU}(2)_L \times \mathrm{U}(1)_Y$ local gauge invariance gives a very good match between theory and experiment, but there is no explanation within the standard model for this choice (many have suggested this may only be a subset of a greater gauge invariance). By construction, rather than consequence, it describes three generations of quarks and leptons. The Higgs boson is a particle as yet unobserved and gravity is entirely absent. Perhaps of greatest relevance for motivating supersymmetry, and

therefore the discussions here, the standard model contains a hierarchy problem.

A Hierarchy Problem

A calculation of the mass of the Higgs boson from the standard model Lagrangian, gives to first order, a Higgs mass, $m_H = \sqrt{2}\mu h/2\pi c$ (this is the bare Higgs mass, m_h^{bare}). To compute the mass of the Higgs to higher orders (by considering radiative corrections through loop diagrams), every particle which couples to the Higgs must be included. The Higgs-fermion coupling takes the form $-\lambda_f H\bar{f}f$. It is not sufficient to calculate the contribution from just one loop, instead every loop correction for all particles coupling to the Higgs boson is needed. Attempting to calculate the fermionic contributions gives an integral over all possible momentum states, which diverges quadratically. This is the consequence of placing no upper limit on the momentum allowed to circulate in the loop. To fix this, it is reasonable to note that since the standard model is incomplete, the integral should be cut-off at an energy Λ_{UV}, the scale where new physics is expected. Doing so gives the result for the Higgs mass in Equation 2.36, where m_f is the mass of the fermion in the loop, λ_f the Higgs to fermion coupling and Λ_{UV} the cut-off energy. Suggesting the scale of new physics to be the Planck mass gives a massive value for m_H.

$$\Delta m_H^2 = \frac{|\lambda_f|^2}{16\pi^2}\left[-2\Lambda_{UV}^2 + 6m_f^2 \ln(\Lambda_{UV}/m_f) + ...\right] \tag{2.36}$$

Since there are contributions from loops including scalars and other particles coupling to the Higgs, these various terms can cancel out the divergent terms. In order to do so, the bare mass must be fixed very precisely in order to achieve sufficient cancellation of the divergent terms. This is termed a hierarchy problem. The parameters must be precisely fine tuned to get a suitable level of cancellation. The bare Higgs mass must be fixed to twelve decimal places in order to reproduce the observed W and Z masses. A favoured Higgs expectation value of around 174 GeV would require a value calculated for m_H^2 of the order of $(100\text{ GeV})^2$. Though the Higgs is the only standard model particle yet to have been observed there are constraints on the Higgs mass from indirect experimental results. The elastic scattering process $W^+W^- \to W^+W^-$, for example, constrains the renormalised Higgs mass to be less than 1 TeV to give a unitary scattering matrix for the process. The precise upper limit on m_H from imposing unitarity on the W-W scattering amplitude is $m_H \leq (8\pi\sqrt{2}/3G_F)^{1/2} \approx 1$ TeV [50] (here G_F is the Fermi coupling constant). Fitting electroweak observational data to the standard model also

favours a light Higgs [51].

2.3 Supersymmetry

2.3.1 Introduction

Supersymmetry is an extension to the standard model predicting a symmetry between fermions and bosons (in other words, a symmetry between particles whose spins differ by $\frac{1}{2}$). In supersymmetry each fermion has a scalar boson superpartner and each boson a fermionic superpartner. Supersymmetry solves the described hierarchy problem (Section 2.2.2). In supersymmetry the fermionic and scalar Higgs interactions cancel to stabilise the Higgs mass. Since the new particles introduced, called "sparticles", must have masses ≤ 1 TeV, they should be abundantly produced at the LHC. Supersymmetry does not just remove the need for fine-tuning of the Higgs mass. It also provides a candidate for dark matter and a means of unifying the fundamental forces at high energies. The discussion here is limited to two of the major accomplishments of the theory: (i) solving this hierarchy problem and (ii) unification of the couplings at high energies. For further information the reader is referred to Refs. [52–54]. In particular, Ref. [54] explains that supersymmetry is actually one of very few symmetries which could have been introduced to address the flaws of the standard model. Supersymmetry is one of many theories attempting to explain physics beyond the standard model, but it is also perhaps the most discussed solution.

2.3.2 Solving a Hierarchy Problem

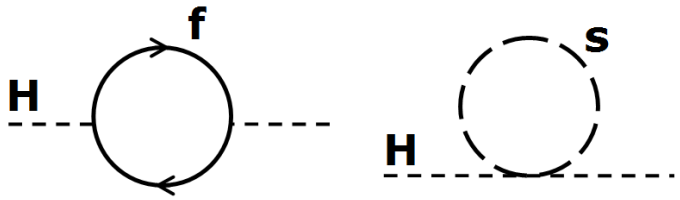

Figure 2.1: *Loop corrections to the standard model Higgs mass in supersymmetry. The left-hand loop illustrates Higgs coupling to fermions, the right Higgs coupling to scalars. Additional scalar contributions can be used to cancel the divergent terms from the fermionic contributions in the standard model.*

The right-hand loop diagram in Figure 2.1 is the loop diagram for Higgs coupling to scalar particles. This loop contributes the term in Equation 2.37 to the Higgs mass (where m_s is the mass of the relevant scalar and λ_s the Higgs to scalar coupling).

$$\Delta m_H^2 = \frac{\lambda_s}{16\pi^2}\left[\Lambda_{UV}^2 - 2m_s^2 \ln(\Lambda_{UV}/m_s) + ...\right] \tag{2.37}$$

The form of scalar contributions to the Higgs mass suggests that if two scalars also exist for every existing fermion, the divergent fermionic terms (those proportional to Λ_{UV}^2 in Equation 2.36) could cancel with the scalar terms. If $|\lambda_f^2|$ is set to equal λ_s, the cancellation would be complete and inserting the Planck mass into the resulting expression would give a Higgs mass of the order of a few hundred GeV. The leading terms in the cut-off for the two diagrams have an important relative minus sign, resulting from the fermion-boson interchange. The leading order corrections to the Higgs mass cancel exactly. Supersymmmetry is a symmetry which naturally introduces two scalars for every fermion. It gives cancellation without the need to delicately and artificially fine tune parameters. This cancellation must always be preserved. The correction to m_H^2 becomes $\sim |g_f|^2 m_f^2 \ln(\Lambda_{UV}/m_f)$, where g_f is a coupling. To keep the correction in the electroweak scale (100 GeV or below), the masses of the new supersymmetric particles must be less than ~ 1 TeV.

Were supersymmetry an exact symmetry sparticles would have the same masses as their standard model partners. Since no supersymmetric particle has yet been discovered this is unlikely. Supersymmetry must therefore be a broken symmetry. The minimal supersymmetric standard model (MSSM) is the supersymmetric theory which adds the minimum extra particle content to the standard model.

2.3.3 Supersymmetric Transformations and the MSSM

A supersymmetric transformation is one which turns a bosonic state into a fermionic state and a fermionic state into a bosonic state. The transformation operator, Q, satisfies Equations 2.38 and 2.39.

$$Q\,|\text{Boson}\rangle = |\text{Fermion}\rangle \tag{2.38}$$

$$Q\,|\text{Fermion}\rangle = |\text{Boson}\rangle \tag{2.39}$$

Q is an anti-commuting spinor, with hermitian conjugate $Q^\dagger$ (also a generator of the symmetry), and a fermionic operator which carries spin-$\frac{1}{2}$. Further discussion of these generators and the algebra they satisfy is neglected, but it should be noted that the single-particle states of the supersymmetric theory fall into irreducible representations of the supersymmetry algebra. These are called supermultiplets, each containing fermion and boson states which are the superpartners of each other. Members of the same supermultiplet must have equal masses and the same electric charge, weak isospin and colour degrees of freedom. Further to this, the supermultiplets must have equal numbers of fermionic and bosonic degrees of freedom. There are two types of supermultiplet. A multiplet containing a Weyl fermion (which has two spin helicity states) and a complex scalar field is called a chiral multiplet. A gauge supermultiplet contains a vector boson and two spin-$\frac{1}{2}$ fermions.

All the particles in the standard model can be assigned to supermultiplets. The introduction of new superpartners completes the supermultiplets. The spin-0 partners of the standard model quarks and leptons are called squarks and sleptons. Both the left-handed and right-handed quarks and leptons must have a superpartner (which are labelled by the handedness of their standard model counterpart, but are themselves spinless). The squarks and sleptons are notated by drawing a $\sim$ over the top of the symbol for their standard model counterpart. For example, the partner of the left-handed up quark is the squark, $\tilde{u}_L$. The spin-$\frac{1}{2}$ partner of the spin-1 standard model gluon is called a gluino, notated $\tilde{g}$, the spin-$\frac{1}{2}$ partners of the $W^\pm$ and W^0 gauge bosons, "winos" ($\tilde{W}^\pm$, $\tilde{W}^0$) and the spin-$\frac{1}{2}$ counterpart of the B boson, "bino" ($\tilde{B}$).

Tables 2.6 and 2.7 give the chiral and gauge supermultiplets of a minimum extension to the standard model. The superpartners of the standard model scalars have spin greater than their scalar partners, but the superpartners of the standard model fermions and bosons spin less than their fermionic and bosonic partners. The Higgs particles (which have spin-0) must be put into chiral supermultiplets and the spin-1 vector bosons into gauge supermultiplets. Quarks and leptons must be placed in chiral supermultiplets so that the left and right-handed spin-$\frac{1}{2}$ particles transform differently under Lorentz transformation. Two Higgs doublets are needed to give mass to both the up and down type quarks in the standard model. Were a chiral supermultiplet containing (ν_L, e_L) and a Higgs doublet formed, the sneutrino would be equivalent to the Higgs boson, and only one new particle would need introducing. This would give a supersymmetric model

Names		spin-0	spin-$\frac{1}{2}$	$SU(3)_c, SU(2)_L, U(1)_Y$
squarks, quarks	Q	$(\tilde{u}_L, \tilde{d}_L)$	(u_L, d_L)	$(3, 2, \frac{1}{6})$
($\times 3$ families)	$\bar{u}$	$\tilde{u}^*_R$	$\bar{u}^\dagger_R$	$(\bar{3}, 1, -\frac{2}{3})$
	$\bar{d}$	$\tilde{d}^*_R$	$\bar{d}^\dagger_R$	$(\bar{3}, 1, \frac{1}{3})$
sleptons, leptons	L	$(\tilde{\nu}, \tilde{e}_L)$	(ν, e_L)	$(1, 2, -\frac{1}{2})$
($\times 3$ families)	$\bar{e}$	$\tilde{e}^*_R$	$e^\dagger_R$	$(1, 1, 1)$
Higgs, Higgsinos	H_u	(H^+_u, H^0_u)	$(\tilde{H}^+_u, \tilde{H}^0_u)$	$(1, 2, \frac{1}{2})$
	H_d	(H^0_d, H^-_d)	$(\tilde{H}^0_d, \tilde{H}^-_d)$	$(1, 2, -\frac{1}{2})$

Table 2.6: *Chiral supermultiplet fields in the MSSM. Chiral supermultiplets consist of a single Weyl fermion and two real spin-0 scalar superpartners. Fermions and bosons in the same supermultiplet are superpartners of each other. The members of a supermultiplet must have equal mass, charge, weak isospin and colour degrees of freedom.*

Names	spin-$\frac{1}{2}$	spin-1	$SU(3)_c, SU(2)_L, U(1)_Y$
gluinos, gluons	$\tilde{g}$	g	(8,1,0)
winos, W bosons	$\tilde{W}^\pm, \tilde{W}^0$	$W^\pm, W^0$	(1,3,0)
bino, B boson	$\tilde{B}$	B	(1,1,0)

Table 2.7: *Gauge supermultiplet fields in the MSSM. Gauge supermultiplets contain a vector boson and two spin-$\frac{1}{2}$ fermions. Fermions and bosons in the same supermultiplet are superpartners of each other. The members of a supermultiplet must have equal mass, charge, weak isospin and colour degrees of freedom.*

$$\widetilde{\mathrm{B}}^0, \widetilde{\mathrm{W}}^0, \widetilde{\mathrm{H}}^0_{\mathrm{u}}, \widetilde{\mathrm{H}}^0_{\mathrm{d}} \rightarrow \widetilde{\chi}^0_1, \widetilde{\chi}^0_2, \widetilde{\chi}^0_3, \widetilde{\chi}^0_4 \quad \text{neutralinos}$$

$$\widetilde{\mathrm{W}}^{\pm}, \widetilde{\mathrm{H}}^+_{\mathrm{u}}, \widetilde{\mathrm{H}}^-_{\mathrm{d}} \rightarrow \widetilde{\chi}^{\pm}_1, \widetilde{\chi}^{\pm}_2 \quad \text{charginos}$$

$$\widetilde{\tau}_{\mathrm{L}}, \widetilde{\tau}_{\mathrm{R}} \rightarrow \widetilde{\tau}_1, \widetilde{\tau}_2 \quad \text{stau}$$

$$(\widetilde{\mathrm{t}}_{\mathrm{L}}, \widetilde{\mathrm{t}}_{\mathrm{R}}), (\widetilde{\mathrm{b}}_{\mathrm{L}}, \widetilde{\mathrm{b}}_{\mathrm{R}}) \rightarrow (\widetilde{\mathrm{t}}_1, \widetilde{\mathrm{t}}_2), (\widetilde{\mathrm{b}}_1, \widetilde{\mathrm{b}}_2) \quad \text{stop and sbottom}$$

Figure 2.2: *Mixing in the MSSM. Neutral winos, binos and higgsinos mix to form neutral neutralinos. The charged winos and higgsinos mix to form charginos. Stop, sbottoms and staus mix significantly, the resulting stop, sbottom and stau states are thus denoted by subscripts* 1 *and* 2 *rather than* L *and* R*.*

with fewer extra particles. It has been shown, however, that phenomenologically this is impossible [52] and so the particle content of the standard model must be doubled in any minimal supersymmetric standard model.

After three degrees of freedom give masses to the $W^{\pm}$ and Z bosons, five physical Higgs states (H^+, H^-, A^0, h^0 and H^0) remain. The states in the MSSM (Tables 2.6 and 2.7) mix to form the physical mass states. The neutral bino ($\tilde{B}$), wino ($\tilde{W}^0$) and higgsino ($\tilde{H}^0_u$, $\tilde{H}^0_d$) states mix to form four neutral particles called neutralinos ($\tilde{\chi}^0_{1,2,3,4}$). The charged wino ($\tilde{W}^{\pm}$) and higgsino ($\tilde{H}^+_u$, $\tilde{H}^-_d$) states mix to form two charged charginos ($\tilde{\chi}^{\pm}_{1,2}$). Neutralinos and charginos are both gauginos. Of the quarks, only the top bottom family mixes significantly, $\tilde{t}_L$ and $\tilde{t}_R$ mixing to form the mass states $\tilde{t}_1$ and $\tilde{t}_2$, and equivalently $\tilde{b}_L$ and $\tilde{b}_R$ mixing to form $\tilde{b}_1$ and $\tilde{b}_2$. Up-down family and charm-strange family mixing is often neglected. Mixing of the leptons in the first two generations is also often neglected, but the left-handed and right-handed staus are commonly taken to mix significantly ($\tilde{\tau}_L$ and $\tilde{\tau}_R$ mixing to form $\tilde{\tau}_1$ and $\tilde{\tau}_2$). The large left-right mixing between the stops, sbottoms and staus means that they are usually denoted by subscripts 1 and 2 rather than L and R. This mixing is summarised in Figure 2.2.

Supersymmetry provides a candidate for dark matter. This candidate is the lightest supersymmetric particle (LSP) which is both stable and weakly interacting (often the $\tilde{\chi}^0_1$). Introducing supersymmetry also improves the degree to which the three standard model forces unify at the right energy scales. In a Grand Unified Theory (GUT) the standard model $\mathrm{SU}(3) \times \mathrm{SU}(2)_L \times \mathrm{U}(1)_Y$ gauge groups are embedded in a simpler gauge group which is broken at a high scale. That is, a simple gauge group is found which, at

some high scale, is spontaneously broken to produce the $\mathrm{SU}(3) \times \mathrm{SU}(2)_L \times \mathrm{U}(1)_Y$ symmetry group. Above the high scale, Λ_{GUT}, the couplings are equal. If supersymmetric particles are added near the electroweak scale then the gauge couplings can unify. It is possible to extract, by considering the renormalisation group equations (RGEs), how the coupling strengths vary with increasing energy. New physics alters this running, because running is dependent on the particle states accessible at any given energy scale. If supersymmetric particles with masses near the TeV scale are introduced, grand unification is possible at a scale of $\sim 10^{16}$ GeV [52].

2.3.4 R-parity in the MSSM

The superpotential of the MSSM is given by Equation 2.40.

$$W_{MSSM} = \bar{u} y_u Q H_u - \bar{d} y_d Q H_d - \bar{e} y_e L H_d + \mu H_u H_d \tag{2.40}$$

H_u, H_d, Q, L, $\bar{u}$, $\bar{d}$ and $\bar{e}$ are chiral superfields corresponding to the chiral supermultiplets (Table 2.6). The dimensionless Yukawa coupling parameters are 3×3 matrices in family space, identical to those of the standard model and μ a constant. Additional gauge invariant terms could be added to this potential, but these are terms which violate either baryon or lepton number. Introducing a symmetry called "R-parity", $R_p = (-1)^{2s+3B+L}$, where B and L are baryon and lepton numbers respectively, s spin, prevents these terms from being added to the superpotential. R-parity is a multiplicative quantum number. All standard model particles, and the Higgs boson, have an R-parity of $+1$, whereas all squarks, sleptons, gauginos and higgsinos have an R-parity of -1. R-parity conservation suppresses proton decay to fit with observed long proton lifetimes.

If the violation of R-parity is permitted (through couplings which evade current experimental bounds, as discussed further in Chapter 7), the additional baryon and lepton number violating terms (as given in Equation 2.41) can be added to the superpotential. These terms obey the gauge symmetries of the standard model. In this superpotential Q, L, H, $\bar{e}$, $\bar{d}$ and $\bar{u}$ are the familiar supermultiplets, the $\mu^{'}$, λ, $\lambda^{'}$ and $\lambda^{''}$ couplings.

$$W = \frac{1}{2}\lambda^{ijk} L_i L_j \bar{e}_k + \lambda^{'ijk} L_i Q_j \bar{d}_k + \mu^{'i} L_i H_u + \frac{1}{2}\lambda^{''ijk} \bar{u}_i \bar{d}_j \bar{d}_k \tag{2.41}$$

The conservation, or non-conservation of, R-parity has important experimental consequences for LHC physics. If R-parity conservation (RPC) is assumed, any initial state produced at the LHC must have an R–parity of +1. Sparticles (which each have R-parity of −1) must therefore be pair produced, and the energy of the decaying particle must also be twice the mass of the produced supersymmetric particles. If a supersymmetric particle decays, it must decay to a particle with R-parity of −1 so that each final state contains another supersymmetric particle. The LSP must be stable, and any stable LSP electrically neutral and weakly interacting (as no such stable particle has been observed to date).

In R-parity violating (RPV) models, the expected event phenomenology may be rather different and dependent on which additional terms are non-zero. In RPV supersymmetry, the LSP, and any other heavier sparticles, may decay into standard model particles. If the dominant terms in the superpotential are the λ or $\lambda^{'}$ couplings then the next-to-lightest supersymmetric particle (NLSP) will decay to leptons and neutrinos. If $\lambda^{'}$ is really dominant then the NLSP will be a slepton or sneutrino, which will decay into quarks. Dominant $\lambda^{''}$ couplings allow decays of the lightest neutralino into three quarks (see Chapter 7).

2.3.5 Supersymmetry Breaking

If supersymmetry were an exact symmetry, a particle and its superpartner would have equal mass. Since supersymmetric particles haven't yet been observed, the symmetry must be a broken one. Supersymmetry must be broken in the current vacuum state of the universe, but relationships between couplings cannot change when it is broken in order to ensure supersymmetry continues to provide a solution to the described hierarchy problem. This type of breaking is called "soft" supersymmetry breaking. The scale, m_{soft}, sets the supersymmetric particle masses. The scale must be less than 1 TeV in order to keep splittings between the superpartner masses natural and generate a correct standard model Higgs vacuum expectation value.

The standard model particles acquire their masses from electroweak symmetry breaking at the scale of the Higgs vacuum expectation value (174 GeV) and supersymmetric particles theirs from m_{soft}. Supersymmetry breaking introduces terms into the Lagrangian involving only supersymmetric particles.

There is no single mechanism for breaking supersymmetry. A Higgs mechanism, giving masses to the MSSM particles via Yukawa interactions, would predict MSSM particles with masses equal to their standard model counterparts. The approach taken instead is to introduce an effective Lagrangian, to which all possible supersymmetric mass breaking terms are added. These terms do not spoil the solution to the hierarchy problem discussed, nor do they break gauge invariance. This effective Lagrangian introduces 105 new parameters, though many of these can be set to zero. Supergravity and gauge mediated supersymmetry breaking are two different symmetry breaking mechanisms. Both mechanisms introduce a new set of fields, at a high energy scale, which interact weakly with the fields of the MSSM.

Supergravity

Gravity mediated supersymmetry breaking, or supergravity (SUGRA), is a well studied model of supersymmetry breaking. The simplest models are referred to as minimal supergravity (mSUGRA) models. The new Lagrangian, $\mathcal{L}_{soft}$, which contains all possible mass breaking terms is simplified to depend upon only five parameters. The first parameter, m_0, gives a common mass for all scalar sparticles at the GUT scale whilst $m_{1/2}$ gives a common gaugino mass at this scale. The supersymmetry breaking trilinear $Hf\bar{f}$ coupling terms and the supersymmetry conserving Yukawa couplings are proportional, with constant A_0 and $\tan\beta$ is used to define the ratio of the vacuum expectation values of the two Higgs doublets. The set of parameters is completed by the sign of μ, where μ is the higgsino mass parameter.

These mSUGRA models are used extensively in the production of benchmark points for study. The MSSM particle spectrum and their interactions can be determined from a given set of mSUGRA parameters. It is likely the case that these models are too minimal to describe supersymmetry in nature well. Different benchmark points in mSUGRA, despite the elegance of the mechanism and the small parameter set, still give very different phenomenologies to each other.

Gauge Mediated Supersymmetry Breaking

In Gauge Mediated Supersymmetry Breaking (GMSB), messenger particles communicate with the MSSM via ordinary gauge interactions. These messenger particles could

be states from a larger gauge group, such as SU(5). There are commonly six parameters in GMSB models. The scale of supersymmetry breaking is set by a parameter F_m, M_m defines the messenger scale and N_5 the number of messenger supermultiplets. The two parameters $\tan\beta$ and $\mathrm{sgn}\,\mu$ are the same as in the mSUGRA framework, but a sixth parameter C_{grav} gives the couplings for decays into gravitinos. The gravitino is not related to m_{soft} and is therefore expected to be very light. Every final state will contain a gravitino, but the weak coupling between the gravitino and other sparticles will give the NLSP a long lifetime. This gives GMSB a rather interesting and different phenomenology.

2.3.6 Observing Supersymmetry

Section 2.3.4 concluded with a hint at the sorts of decays supersymmetric particles undergo, in both the R-parity violating and R-parity conserving cases. The following discussion assumes an MSSM model for which R-parity is conserved, and that the $\tilde{\chi}_1^0$ is the LSP.

Squarks and gluinos are easily pair produced at hadron colliders (Figure 2.3). If kinematically allowed, $\tilde{q} \to q\tilde{g}$ decay will dominate. Otherwise the $\tilde{q}$ will decay into a quark plus a neutralino or a quark plus a chargino (Figure 2.4). Left-handed squarks, $\tilde{q}_L$, may prefer to decay into heavier neutralinos or charginos ($\tilde{q} \to q\tilde{\chi}_2^0$ or $\tilde{q} \to q'\tilde{\chi}_1^+$), because the relevant squark-quark-wino couplings are much bigger than the squark-quark-bino couplings.

Any neutralinos (except, of course, the LSP) or charginos produced will themselves decay. Each neutralino and chargino will be at least a small admixture of $\tilde{B}$, $\tilde{W}^0$ and $\tilde{W}^\pm$. Neutralinos and charginos may decay to any lighter neutralino or chargino, and a Higgs scalar or electroweak gauge boson (Figure 2.5). Gauginos may also decay into lepton-slepton, neutrino-sneutrino, lepton-slepton or neutrino-slepton pairs (Figure 2.5). Neutralino decays to quark-squark pairs are less favoured, to the extent that the lepton-slepton pairs are probably lighter.

Sleptons will decay into a lepton and a neutralino, or a neutrino and a chargino, because of their gaugino admixture. These two body decays ($\tilde{\ell} \to \ell\tilde{\chi}_1^0$, $\tilde{\ell} \to \nu\tilde{\chi}_1^+$) can

$$(\tilde{q})(\bar{\tilde{q}}) \to (q\tilde{\chi}_1^0)(\bar{q}\tilde{\chi}_1^0) \qquad (\tilde{q})(\bar{\tilde{q}}) \to (q\tilde{\chi}_2^0)(\bar{q}\tilde{\chi}_1^0) \quad \text{squark pair production}$$
$$(\tilde{g})(\tilde{g}) \to (q\bar{\tilde{q}})(\bar{q}\tilde{q}) \qquad (\tilde{g})(\tilde{g}) \to (\bar{q}\tilde{q})(\bar{q}\tilde{q}) \quad \text{gluino pair production}$$

Figure 2.3: *Squark and gluino pair production. Squark and gluino pairs should be easily produced at hadron colliders. Pair produced gluinos (which are their own antiparticle) decay to quark-squark combinations.*

$$\tilde{q} \to q\tilde{\chi}_1^0 \qquad \bar{\tilde{q}} \to \bar{q}\tilde{\chi}_1^0 \qquad \text{squark decay}$$
$$\tilde{q} \to q\tilde{\chi}_2^0 \qquad \bar{\tilde{q}} \to \bar{q}\tilde{\chi}_2^0 \qquad \text{to neutralinos}$$

$$\tilde{q} \to q\tilde{\chi}_1^+ \qquad \bar{\tilde{q}} \to q\tilde{\chi}_1^- \qquad \text{squark decay}$$
$$\tilde{q} \to q\tilde{\chi}_2^+ \qquad \bar{\tilde{q}} \to q\tilde{\chi}_2^- \qquad \text{to charginos}$$

Figure 2.4: *Squark decays to neutralinos and charginos. The decay $\tilde{q} \to q\tilde{g}$ (not illustrated above) will dominate if kinematically allowed.*

be of weak interaction strength. If the sleptons are heavy enough, in principle the two body decay $\tilde{\ell} \to \ell\tilde{\chi}_2^0$ is also possible. The right-handed slepton, $\tilde{\ell}_R$, may favour the decay $\tilde{\ell}_R \to \ell\tilde{\chi}_1^0$, if $\tilde{\chi}_1^0$ is bino-like. The $\tilde{\ell}_R$ is unable to couple to $\mathrm{SU}(2)_L$ gauginos.

The initial pair production of either squarks or gluinos gives rise to two independent cascade decays. These decays produce many particles, through a cascade of the described two-body decays. The resulting final states are characterised by leptons, jets and "missing energy" (a measure of the unbalance in the total event momentum, resulting from the production of invisible undetected particles like neutrinos and the LSP, see Chapter 5). For example, squark pair production $(\tilde{q})(\bar{\tilde{q}})$ can produce the final state $(q\tilde{\chi}_1^0)(\bar{q}\tilde{\chi}_1^0)$. This state contains two jets and has high missing energy. Cascades can give unusual signatures, very different to anything predicted by the standard model. Gluino pair production, $(\tilde{g})(\tilde{g})$, could lead to two independent very long cascades $(\bar{q}\tilde{q})(\bar{q}\tilde{q}) \to (q\bar{q}\tilde{\chi}_1^+)(q\bar{q}\tilde{\chi}_1^+) \to (q\bar{q}W^+\tilde{\chi}_1^0)(q\bar{q}W^+\tilde{\chi}_1^0) \to (q\bar{q}\tilde{\chi}_1^0\ell^+\nu)(q\bar{q}\tilde{\chi}_1^0\ell^+\nu)$. These two cascades give final states with four jets, two same-sign leptons and high missing energy. The standard model does not predict significant same-sign lepton-pair production (see Chapter 6).

$\tilde{\chi}_2^0 \to Z\tilde{\chi}_1^0,\ W^{\mp}\tilde{\chi}_1^{\pm},\ h^0\tilde{\chi}_1^0$	neutralino decays to gaugino and electroweak boson
$\tilde{\chi}_2^0 \to \ell\tilde{\ell},\ \nu\tilde{\nu}$	neutralino decays to lepton-slepton, neutrino-sneutrino
$\tilde{\chi}_2^+ \to W^+\tilde{\chi}_1^0,\ Z\tilde{\chi}_1^+,\ h^0\tilde{\chi}_1^+$	chargino decays to gaugino and electroweak boson
$\tilde{\chi}_2^+ \to \ell\tilde{\nu},\ \tilde{\ell}\nu$	chargino decays to lepton-sneutrino, slepton-neutrino

Figure 2.5: *Common chargino and neutralino decays. Chargino and neutralinos can decay into any lighter neutralino or chargino, and a Higgs scalar or electroweak gauge boson. Gaugino decays to lepton-slepton, lepton-sneutrino, slepton-neutrino and neutrino-sneutrino states. This list of decays is not exhaustive, the lighter Higgs scalar and electroweak gauge bosons are used to illustration of most likely decays.*

2.3.7 Conclusions

Since its emergence in the 1970s, theorists have given supersymmetry strong theoretical foundations. Despite this, there have been no experimental observations to support it [55]. This blow to the theory is usually set aside by supposing that supersymmetric particles must have masses which are so far beyond the energies accessible to existing experiments. Given an experiment with higher beam energies, however, these particles can be created. The LHC is now reaching these high beam energies, and so it is an exciting time for those working on supersymmetric models.

Chapter 3

The ATLAS Experiment

"All men naturally desire to know."
— Auctoritates Aristotelis

3.1 The Large Hadron Collider

The LHC is a particle accelerator located on the French-Swiss border (Figure 3.1) in the 27 km circumference existing large electron-positron (LEP) collider ring. It has been designed (when operating at its optimum) to collide proton beams together at a centre of mass energy, $\sqrt{s} = 14$ TeV. It also collides 5.5 TeV heavy ions, such as lead nuclei together for, ideally, about one month in each year. The higher the beam energy, the greater the energy available for the production of new particles. The LHC has been designed to reach a luminosity of 1.0×10^{34} cm^{-2}s^{-1}. Luminosity is a measure of beam intensity, proportional to the number of interactions of a given type. There will be $\sim 10^{11}$ protons in each bunch crossing, colliding at a rate of 40 MHz. Electron-positron colliders can offer high precision measurements, but they will be limited by their energy reach and it is harder to obtain high luminosities. Hadron colliders can relatively easily achieve both high energy and high luminosity. Hadron colliders are very good for discovery physics, at the risk of limiting precision measurement potential. The spread of parton momenta inside the protons means all energies can be simultaneously explored.

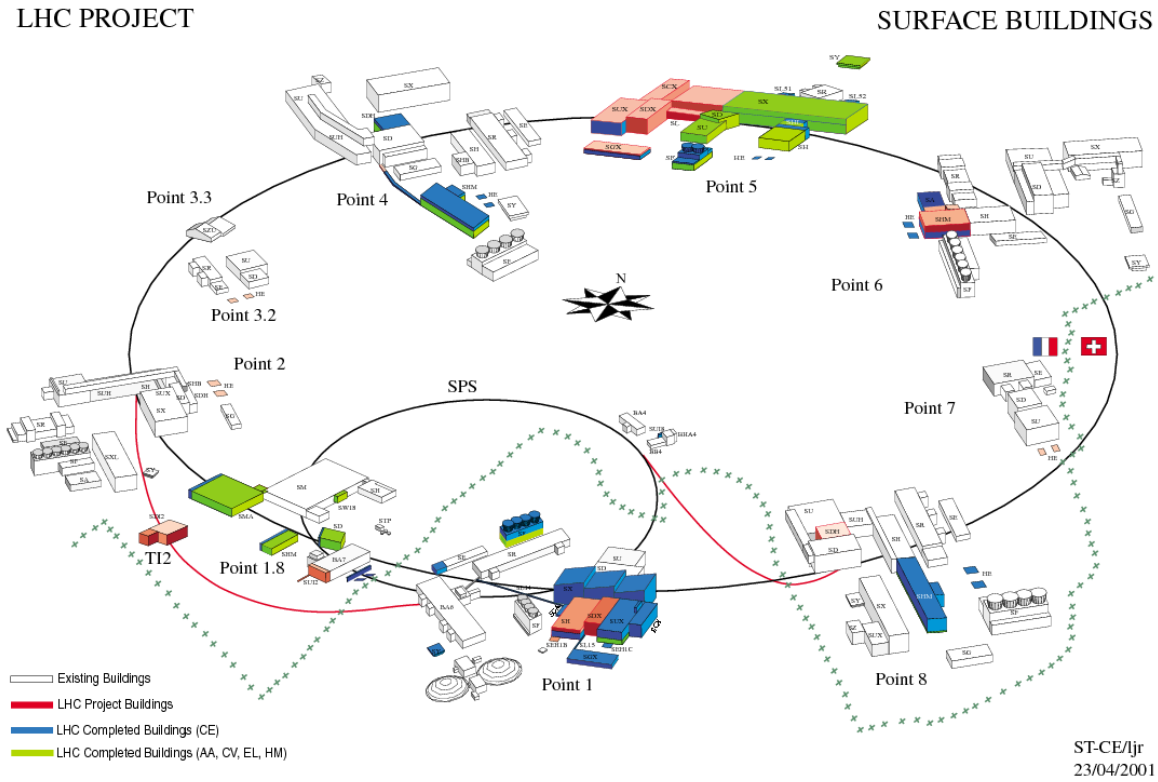

Figure 3.1: *The 27 km LHC located under the French-Swiss border and the four experiments: ATLAS, CMS, LHCb and Alice (from [56]). All "Project Buildings" are now in a completed state. The ATLAS experiment is located at "Point 1", Alice at "Point2", CMS at "Point 5" and LHCb at "Point 8". The French-Swiss border (as marked), places all experiments except ATLAS in France.*

The beams are forced into collision at four different points along the LHC experiment ring, each point housing its own experiment. Two of these, A Toroidal LHC Apparatus (ATLAS) and Compact Muon Solenoid (CMS), are discovery experiments searching for new physics (supersymmetry, evidence of extra dimensions and so on). The third, Large Hadron Collider beauty experiment (LHCb), is an experiment searching for new physics in rare b-decays and making precision measurements of $\mathcal{CP}$ violation (which is used to account for the excess of matter over anti-matter in the universe). The last, A Large Ion Collider (Alice), is a heavy-ion experiment investigating the quark-gluon plasma thought to exist a few millionths of a second after the big bang.

Protons are initially accelerated by the linear accelerator (LINAC). These $\sim$50 MeV protons are then boosted by 1.4 GeV before being fed into the Proton Synchrotron (PS) which brings their energies up to 25 GeV. Bunches of these protons are injected into the Super Proton Synchrotron (SPS) and accelerated over 12 turns to 450 GeV. The LHC performs the final acceleration, bringing their energies up to a maximum of 7 TeV per beam. In order to control the acceleration around the LHC ring, and keep the beam focused, the machine employs over 1300 dipole magnets (8.3 T), each cooled by a bath of superfluid helium (1.9 K), and 392 quadrupole magnets. For every interesting physics interaction there will be $\sim$20 underlying inelastic collisions occurring simultaneously, at design operation ("pile-up").

Following a successful start-up in late November 2009, the LHC collided protons together at $\sqrt{s}$ = 900 GeV to produce a dataset with an integrated luminosity of approximately 9 μb^{-1} [57]. By mid-March of the following year the LHC was primed for $\sqrt{s}$ = 7 TeV collisions. These collisions ran, with small intermissions, from mid-March through to early-November of the same year. Figure 3.2 illustrates the luminosity recorded by day by ATLAS for this $\sqrt{s}$ = 7 TeV run. This luminosity profile is a tribute to the hard work of the LHC beam engineers. The step-wise improvements to the luminosity gathered over a single day are immense and crucial to ATLAS recording a $\sqrt{s}$ = 7 TeV 2010 dataset with an integrated luminosity of $\sim$45 pb^{-1}, a luminosity sensitive to new physics scenarios. In the first two months of $\sqrt{s}$ = 7 TeV operation, the number of colliding bunch pairs varied from 1-2 (compared with the design number, 2808) with 1.1×10^{10} protons per bunch. The luminosity during this period was 0.1-1.2 $\times 10^{28}$ $cm^{-2}s^{-1}$ [58]. By the middle of October the LHC was delivering physics with a luminosity $> 10^{32}$ $cm^{-2}s^{-1}$, with as many as 312 bunches per beam. On Sunday

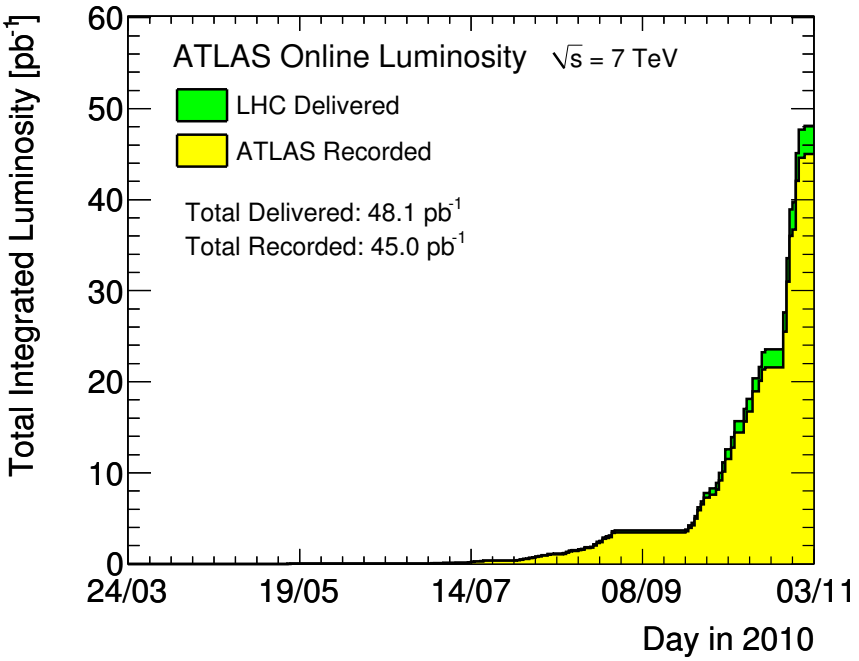

Figure 3.2: *Cumulative luminosity versus day in 2010 delivered to (green), and recorded by (yellow), the ATLAS experiment during stable beams at* $\sqrt{s} = 7$ TeV *(from [59]). The luminosity is determined from the counting rates measured by the ATLAS luminosity detectors calibrated using van-der-Meer beam-separation techniques. The systematic uncertainty on these luminosity measurements is estimated to be* 11%.

7th November 2010, heavy ions collided together in the LHC ring for the first time (see Figure 3.3, a first heavy ion collision event in Alice).

The LHC has the energy and luminosity required to explore a variety of new physics scenarios, the hope being that it will help answer many of the important questions posed by physicists during the last century. Where does mass come from? Why is there more matter than antimatter in the universe? The LHC experiments are starting to: (i) look for the Higgs, (ii) seek out physics beyond the standard model, (iii) precisely measure the mass of the top quark, (iv) make precision measurements of the electroweak parameters, (v) explore the physics of b quarks and (vi) measure the parameters in QCD. This list is by no means exhaustive. The physics programs on which the experiments have commenced are both unique and exciting. The results they will report over the next decade will be of great importance to fundamental physics.

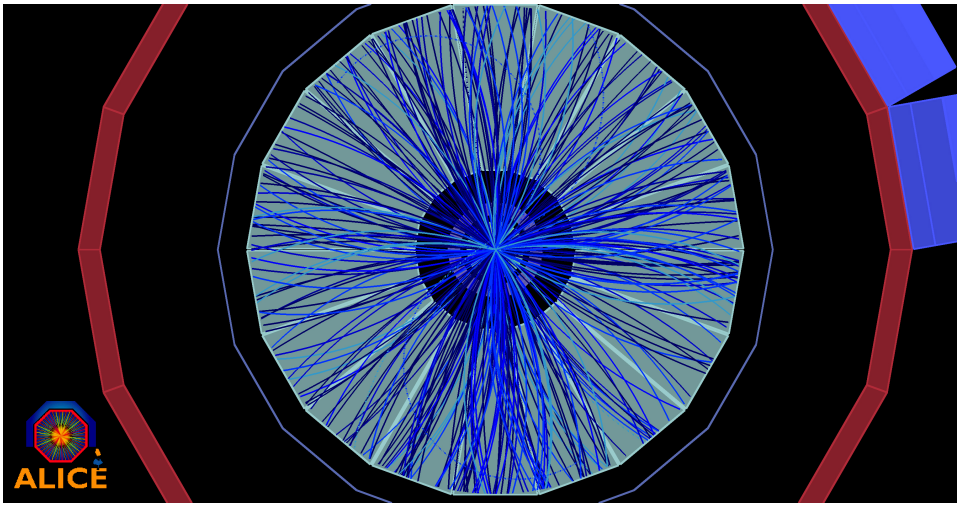

Figure 3.3: *An event from the first lead ion collisions in Alice at* $\sqrt{s} = 2.7$ TeV *per nucleon pair (from [60]). These collisions produced the highest temperatures and densities ever produced in an experiment, temperatures where even protons and neutrons melt resulting in a hot dense soup of quarks and gluons known as a quark-gluon plasma.*

3.2 The ATLAS Detector

3.2.1 Overview

The ATLAS experiment (Figure 3.4) is 64 m long and 25 m tall. ATLAS has four main systems (an inner detector, calorimeters, a muon system and a trigger system), each of which is divided into sub-systems (Figure 3.5). The "Inner Detector" (ID) is surrounded by a solenoid (red in Figure 3.5), sits closest to the beam-pipe and is designed to track charged particles and measure collision and decay vertices. The electromagnetic and hadronic calorimeters (yellow and green) surround the inner detector and measure energies. Charged particles deposit energy in the electromagnetic calorimeters and hadronic jets in the hadronic calorimeters. The muon detectors (blue) lie furthest away from the beam. A toroidal magnet system (grey) creates the azimuthal magnetic field. ATLAS detects high transverse momentum (p_T) leptons and jets. The electromagnetic calorimeters allow the ATLAS detector to identify and measure electrons and photons. Hadronic calorimetry (covering the whole of the detector) enables ATLAS to make accurate measurements of jets. The muon spectrometer makes high precision muon measurements. ATLAS also benefits from efficient tracking capabilities, large acceptance and good trigger systems. Full details of the topics to be discussed here, and the detector, are given in the ATLAS Technical Design Reports [61–66]. Full details of its expected performance

can be found in Ref. [67]. A brief overview of the key detector components follows.

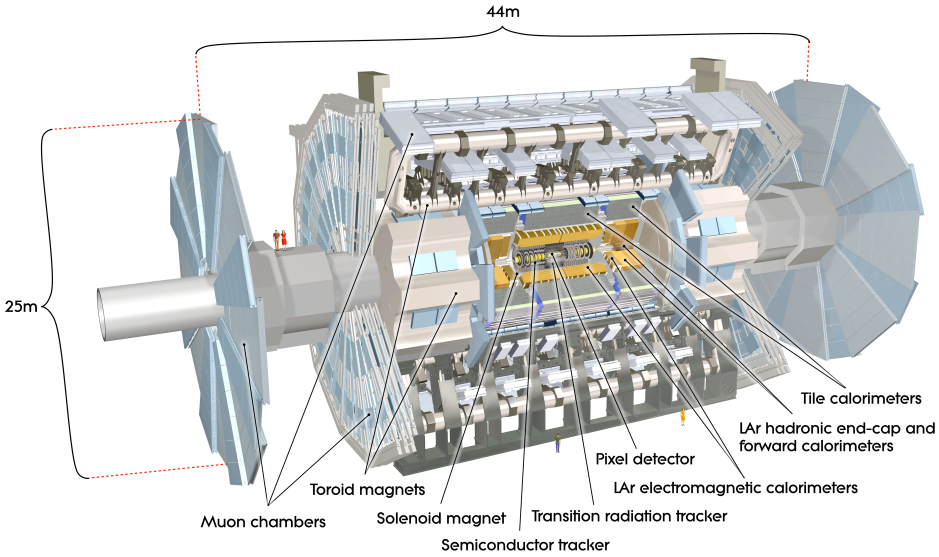

Figure 3.4: *An overall view of the ATLAS experiment, illustrating the great size of the experiment and the layout and positions of the main detector components (from [67]). The four illustrated people are drawn to highlight the scale of the image. Each detector component is well designed to detect a particular type of particle, the impressive magnet system forces charged particles to follow curved tracks for precision momentum measurements.*

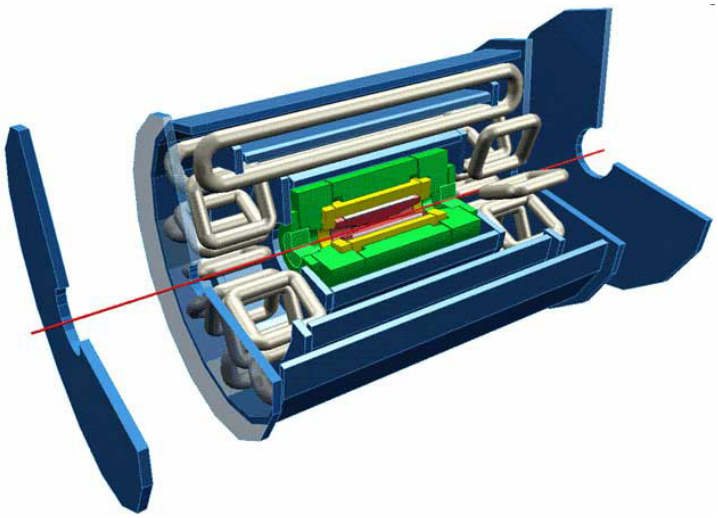

Figure 3.5: *Components of ATLAS, separated by colour to illustrate their scope and highlight the layered structure of the experiment (from [68]). The Inner Detector and beam-pipe (red), the calorimeters (yellow and green), the muon systems (blue) and the toroidal magnet system (grey) work together to reconstruct and identify the final state particles produced in collision events.*

In the circular LHC ring, the z-axis is defined by the beam direction and the $x-y$ plane transverse to this direction. The x-axis points towards the centre of the ring and the y-axis points vertically upwards. The distance measure R is the transverse radius from the beam-line. The azimuthal angle, ϕ, is measured around the beam axis. A polar angle, θ, is measured from the beam direction and used to calculate the angle measure "pseudorapidity" (Equation 3.1).

$$\eta = -\ln\tan(\theta/2) \tag{3.1}$$

This measure is not equal to the rapidity. Rapidity, y, is a Lorentz vector, Equation 3.2, with p_Z the component of the particle's momentum in the z-direction and E its energy, which conserves rapidity differences when they are boosted along the z-axis.

$$y = \tanh^{-1}\left(\frac{p_Z}{E}\right) \tag{3.2}$$

Since rapidity is difficult to measure (it involves the particle masses) the experiment settles for pseudorapidity which, in the relativistic limit, is a good approximation to rapidity. Pseudorapidity is also independent of boost, and expands the small angle θ range. The variable ΔR (Equation 3.3) gives distances in the pseudorapidity-azimuthal angle space. Here $(\Delta\eta)^2$ is the square of the difference in η between two points in the detector and $(\Delta\phi)^2$ the square of the difference in ϕ between the points.

$$\Delta R = \sqrt{(\Delta\eta)^2 + (\Delta\phi)^2} \tag{3.3}$$

ATLAS is approximately cylindrical in shape. It is important that there are detectors surrounding the whole of this cylinder so that the conservation (or rather the non-conservation) of momentum for entire events can be used to hint at the momentum of any "invisible" particles (neutrinos, and more exotic particles predicted by theories beyond the standard model). Of course, a completely enclosed cylinder is not realisable as the beam-pipe has to pass through the detector, and the various services, like cryogenics, need to reach the detector components. Allowing for this the coverage has however, been made as good as it can be (choosing between concentrating all the services into dead regions, and spreading them out throughout the detector). The central η regions of the detector are termed "barrel" regions, whilst the "forward" regions of the detector are those at high $|\eta|$, and served by "end-caps".

3.2.2 The Inner Detector

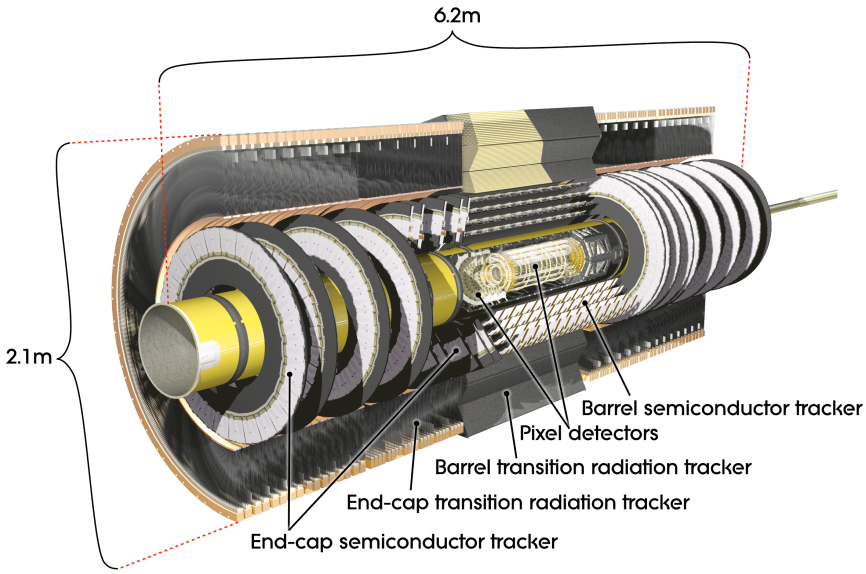

Figure 3.6: *The three main components of the ATLAS Inner Detector: the Semiconductor Tracker (SCT), Pixel Detectors and Transition Radiation Tracker (TRT) (from [67]). Each detector component has a central barrel, and two end-caps which cover the forward region. Detector design is based on the particle occupancy at different radii, the potential for radiation damage and costs.*

The ID (illustrated in Figure 3.6) is entirely contained within a 7 m long cylinder with a radius of 1.15 m. The solenoidal magnetic field which surrounds the ID has a strength of 2 T in the centre. The ID is designed to reconstruct charged particle tracks and vertices, contributing to the measurement of the momenta and charges of the particles it reconstructs. Closest to the beam-pipe, tracking, momentum and vertex measurements are made using discrete high resolution semiconductor pixel and strip detectors. The outer radii are served by continuous tracking elements. The highest granularity detection is needed closest to the beam-pipe to cope with the very large particle track density. Further away from the beam-pipe, where the particle occupancy is lower, reduced granularity detection suffices. The three detector components (the Pixel Detectors, the Semiconductor Tracker (SCT) and the Transition Radiation Tracker (TRT)) positioned at successively greater radii work together. The ID must provide high granularity track measurements without preventing accurate energy measurement. The more material the particles pass through, the worse the subsequent energy measurement will be.

The components of the ID are bombarded with a great deal of radiation during LHC running and will therefore eventually need replacing. Cost and reducing the severity of this damage are important design considerations. The three components are now discussed in more detail (all of which have a central barrel and two end-caps). The ID barrel extends to over ± 80 cm and the two end-caps cover the rest of the cavity to give coverage up to $|\eta| \leq 2.5$. Full details are given in the ATLAS Inner Detector Technical Design Report [69, 70].

Pixel Detectors

There are 140 million pixel detector elements in the ID. The pixels are responsible for the resolution of impact parameter measurements and the ability of the detector to find short-lived b quarks and τ leptons (particles detected by their secondary vertices). As the pixels lie in close proximity to the beam interaction point they must cope with a very high particle density flux and high radiation levels. Each pixel is just 50×400 µm in size. The pixel system is made out of three barrels and eight disks (four per side). There are just over 1500 identical modules in the barrel (each 62.4 mm $\times$ 22.4 mm) and ~ 1000 identical modules in the disks. Each module contains just under 50,000 individual pixels, grouped into 16×60 mm arrays. The disks lie between 12 cm and 19 cm from the beam, whereas the barrels sit at average radii of 5 cm, 9 cm and 12 cm. For further details see Ref. [63]. The inner most layer of the pixel detectors is termed the "b-Layer", and it is the most crucial detector component for tracking, vertexing and "tagging" b quarks.

Semiconductor Tracker

The are two planes of silicon strip detectors on each SCT module. By the time the particles reach the SCT the particle density is much reduced. The silicon is therefore arranged in strips. The strips contribute to the measurement of track momentum, impact parameters and vertex position. The SCT can make a total of eight precision measurements per track. Each silicon detector has an area of 6.36×6.40 cm^2 and 768 readout strips. The spatial resolution in $(R\phi, z)$ of the silicon detectors is 16 µm $\times$ 580 µm allowing tracks to be separated if they are more than 200 µm apart. There are four coaxial cylindrical barrels in the SCT, and two end-caps. Each end-cap has nine disks (these disks limit the η coverage of the SCT to $|\eta| < 2.5$). The innermost barrel sits at

a radius of 299 mm with the outer barrel at a radius of 514 mm.

Transition Radiation Tracker

The TRT is a straw tube tracker and the largest component of the ID, filling the majority of the ID cavity. The TRT is capable of making a large number of track position measurements (up to 36 hits per track). It therefore complements the pixel detectors and the SCT, giving enhanced momentum resolution to track measurements. The TRT contains over 370,000 4 mm diameter "straws". On average, a track travelling through the TRT will pass through 32 straws. Each straw is coated on the inside with aluminium (a high voltage cathode), threaded with a gold-plated tungsten wire (the anode wire) and filled with a mixture of 70% Xe, 27% CO_2 and 3% O_2. As charged particles pass through the gas, the liberated charge is collected by the anode wire. The passage of ionising particles through the TRT is recorded with a spatial resolution of approximately 170 µm. The TRT is however not just a straw drift tube tracker, but a vitally important transition radiation detector for electron identification. The straws are all packed together with a filling of polypropylene/polyethylene fibre radiator. This filling has an abruptly varying refractive index causing travelling ionising particles with high Lorentz gamma factor to emit X-ray radiation along their track (transition radiation, or "TR", photons). There are thus two components to the energy deposited in the TRT. The first is a contribution from ionisation losses, the second a contribution from transition radiation deposition.

The TRT uses double-threshold binary electronics to help distinguish between minimally ionising particles (e.g. pions) and prompt electrons. The low threshold setting ($\sim$250 eV) detects charge liberated by ionising particles, whilst the high threshold setting ($\sim$5 KeV) detects the higher charges produced by transition radiation photons. Whilst both electrons and pions produce transition radiation photons, the radiation rate is substantially higher for electrons. Electrons with an energy of 10 GeV have a Lorentz gamma factor $\sim 20,000$ whilst pions of similar energy have a Lorentz factor $\sim$74. The fraction of total hits on a track at high threshold is therefore an important and powerful variable for discriminating between electrons and pions (see Chapter 4).

Tracks are seeded by a combination of hits in the pixel detectors and the first layer of the SCT. These tracks are extended through the remaining layers of the SCT and selected tracks are continued into the TRT. The expected resolution of each primary

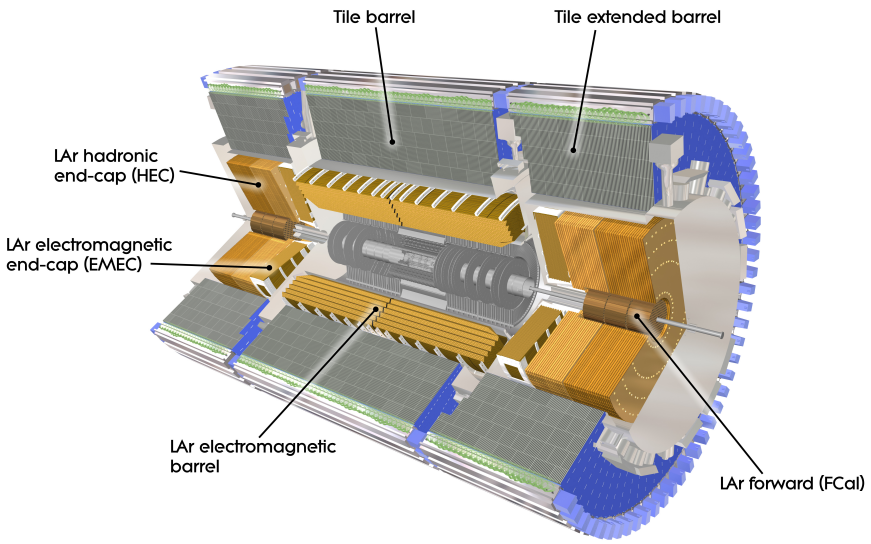

Figure 3.7: *An overview of the ATLAS calorimeters (from [68]). The electromagnetic calorimeters are LAr calorimeters with an accordion geometry. The electromagnetic calorimeter is made up of a barrel and two electromagnetic end-cap calorimeters (EMEC). The hadronic calorimeter end-caps (HEC) are LAr calorimeters and the barrel calorimeters, "tile" calorimeters (plastic scintillator plates, embedded in an iron absorber). Forward LAr calorimeters cover the region* $3.1 < |\eta| < 4.9$. *The LAr calorimeter system is contained in a cylinder of* 2.25 m *radius, and* ± 6.65 m *length along the beam axis. The tile calorimeter system is contained in a cylinder of radius* 4.23 m*, and total length* ± 6.10 m.

track parameter can be expressed as:

$$\sigma_X = \sigma_X(\infty)(1 \oplus p_x/p_T) \tag{3.4}$$

where, $\sigma_X(\infty)$ is the resolution expected for a particle of infinite momentum, p_x a constant and p_T the transverse momentum of the particle. For example, for the inverse track momentum $(1/p_T)$ ATLAS is expected to give a resolution parameterisation in the barrel with $\sigma_X(\infty) = 0.34$ TeV^{-1}, and $p_x = 44$ GeV.

3.2.3 Calorimeters

In common with most general purpose detectors, ATLAS has two different types of calorimeter [64]. The intrinsic resolution of these calorimeters improves with energy. The electromagnetic and hadronic calorimeters all sit outside the central solenoid (Figure 3.7). The barrel electromagnetic calorimeter is contained in a barrel cryostat sur-

rounding the whole ID cavity. The electromagnetic and hadronic calorimeters both occupy the region $|\eta| < 3.2$. The forward region ($3.1 < |\eta| < 4.9$) is served by forward liquid argon (LAr) calorimeters. The electromagnetic calorimeter is divided up into a barrel ($|\eta| < 1.475$) and two end-caps ($1.375 < |\eta| < 3.2$). A pre-sampler is placed in front of the main electromagnetic calorimeter (in the region $|\eta| < 1.8$), to correct for energy lost in the material before the calorimeter (lost in the inner detector, cryostats and coil upstream of the calorimeter). The hadronic calorimeter is also divided up into a barrel ($|\eta| < 1.7$) and two end-cap hadronic calorimeters ($1.5 < |\eta| < 3.2$). The hadronic calorimeter barrel is made out of a barrel ($|\eta| < 1.0$) and an "extended barrel" ($0.8 < |\eta| < 1.7$). The electromagnetic calorimeters are LAr calorimeters, with an accordion geometry. The hadronic barrel and extended barrel calorimeters are made out of plastic scintillator plates (or "tiles", as labelled on Figure 3.7). These plastic tiles are embedded in an iron absorber. The end-cap hadronic calorimeters, and the forward calorimeters, are LAr calorimeters. The larger rapidity regions require "intrinsically-hard" LAr technology to cope with the higher radiation flux.

The calorimeters contribute to the accurate measurement of both the position and energies of electrons and photons, and give both the energy and direction of jets. Energy measurements are made from the showers particles deposit inside the calorimeter. Electrons and photons incident on matter create cascades of particles both from pair production ($\gamma \to e^+e^-$) and bremsstrahlung ($e \to e\gamma$) processes. These electromagnetic showers are characterised longitudinally by their radiation length (X_0) and have a narrow transverse profile. Interactions between hadrons and dense materials produce cascades of particles with particle multiplication through successive inelastic hadron-nuclear interactions. The lateral spread of hadronic showers is greater than for electromagnetic showers, and the nuclear interaction length an order of magnitude greater than X_0. The calorimeters are referred to as sampling calorimeters. The material producing the shower is different to the material used to measure the shower. As a result of this the fractional resolution has a $1/\sqrt{E}$ dependence, a resolution dominated by sampling fluctuations.

Electromagnetic Calorimeter

The electromagnetic LAr calorimeter is illustrated in Figure 3.8. Its accordion geometry prevents "cracks" in coverage in the azimuthal ϕ direction. The electromagnetic calorimeters must have a large acceptance. The ID limits the useful region for preci-

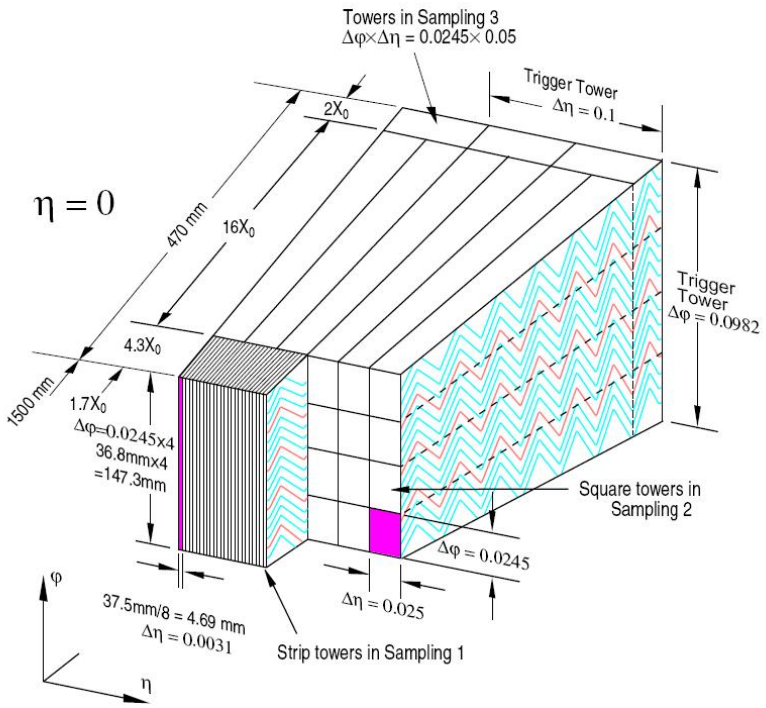

Figure 3.8: *A schematic view of the ATLAS electromagnetic calorimeter (from [64]). In the precision region, $|\eta| < 2.5$, the calorimeter is segmented into three different longitudinal sampling layers. The first, a "strip" layer has radiation thickness $\sim 6\ X_0$. The second, "middle" layer, has a thickness of $\sim 18\ X_0$. The third, "back" layer, has a thickness of $\sim 2\ X_0$. Also illustrated are the sizes of "tower" into which the electromagnetic calorimeter is divided, by layer. "Trigger towers" have much coarser granularity.*

sion physics with electrons to $|\eta| < 2.5$ and so the electromagnetic calorimeters have their best granularity in this region, with a coarser granularity for $|\eta| > 2.5$. The total electromagnetic calorimeter coverage is $0 < |\eta| < 4.9$. Despite the accordion geometry, there is an unavoidable region of transition between the barrel and end-cap calorimeters. Electrons and photons falling in this "transition region", $1.37 < |\eta| < 1.52$, are often not considered for physics analyses. The barrel calorimeter is made out of two identical half-barrels, separated by a tiny 6 mm gap at $|\eta| = 0$. In the region of the electromagnetic calorimeter devoted to precision physics ($|\eta| < 2.5$), the electromagnetic calorimeter is segmented into three different longitudinal "sampling" layers. The first sampling, or "strip" layer has a thickness of 6 X_0, and acts as a pre-shower detector, enhancing particle identification (γ/π^0 and e/π separation, etc.). It gives precise position measurement in η. The second sampling, or "middle" layer, is transversely segmented into square towers of size $\Delta\eta \times \Delta\phi = 0.025 \times 0.025$. The sizes of the towers in the back and strip layers are given in Figure 3.8. The total calorimeter thickness up to the end of the second sampling is 24 X_0. The final layer, or "back layer", is coarser in η, with thickness varying between 2 and 12 X_0.

The expected energy resolution in the electromagnetic calorimeter can be described using a stochastic term, α, and a constant term, c, $\sigma_E/E = (\alpha/\sqrt{E}) \oplus c$. The stochastic term is expected to be $\sim 10\%$, and the constant term $\sim 0.7\%$.

Hadronic Calorimeter

Forward jet reconstruction requires the hadronic calorimeters to cover the region up to $|\eta| < 4.9$. The technology used in the hadronic calorimeters varies as a function of η, depending on the radiation environment and physics and performance requirements. In the extended barrel and barrel regions, the calorimeters are made out of iron absorber placed amongst plastic scintillator plates (the active material). The tiles, each 3 mm thick, are placed perpendicular to the colliding beams and staggered in depth. In the hadronic end-caps, thick copper absorber plates are separated by LAr filled gaps. In the forward region the material is denser, an absorber matrix of tungsten fills the space between an array of grounded copper tubes. Solid tungsten electrodes run down the centre of these tubes and the electrodes are separated from the walls of tubes by a thick layer of LAr. Any remaining gaps in the forward hadronic calorimeter are filled with "inactive" LAr.

The resolution of jet energy measurement can be described using the functional form:

$$\frac{\sigma_E}{E} = \sqrt{\frac{a^2}{E} + \frac{b^2}{E^2} + c^2} \tag{3.5}$$

The expected stochastic term is $\approx 60\%\ \sqrt{\text{GeV}}$, the expected constant term $\approx 3\%$ and the noise term one which is expected to vary between 0.5 and 1.5 GeV. At energies under 100 GeV, the stochastic and noise terms are dominant.

3.2.4 The Magnet Systems

The magnet system in ATLAS is complex. It weighs in at 13,000 tonnes and operates at a temperature of 4.8 K, storing 1600 MJ of energy when operational. It consists of a central solenoid (Figure 3.9(c)) surrounding the inner detector, and a system of toroids. There is one barrel toroid (Figure 3.9(a)) and two end-cap toroids (Figure 3.9(b)). The magnet system creates the magnetic field for the muon spectrometer (with an average field strength of 0.6 T) and a 2 T central field in the inner detector (directed along the beam axis). The central solenoid has a diameter of 2.5 m and a length of 5.3 m, but a thickness of just 45 mm. The thinness of this coil reduces the amount of material the particles need to pass through before reaching the calorimeters. The toroids are all eight-coil toroids. They are positioned radially around the beam axis. These are 25 m long and 5 m wide in the barrel, and 5 m in length in the end-caps. Between them, these magnets cover the region $0 < |\eta| < 2.5$.

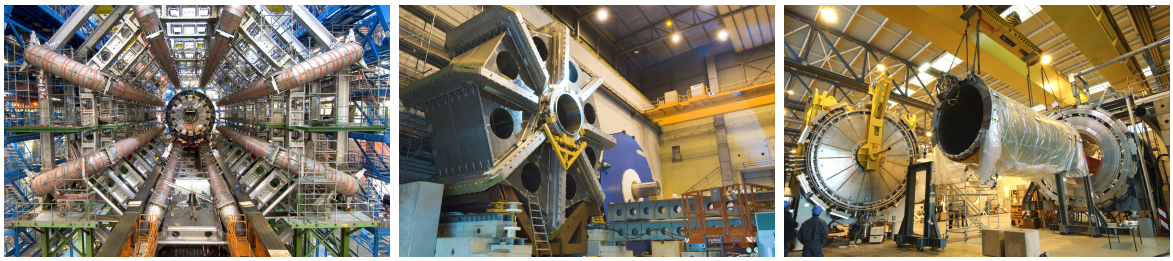

(a) (b) (c)

Figure 3.9: *The ATLAS Magnets (from [68]). The magnet system is composed of three air-coil toroids, one barrel (a), shown here inside the ATLAS cavern, and two end-caps (b), the one illustrated pre-installation. A thin solenoid surrounds the inner detector (c), shown here as it is placed inside the LAr calorimeter during installation.*

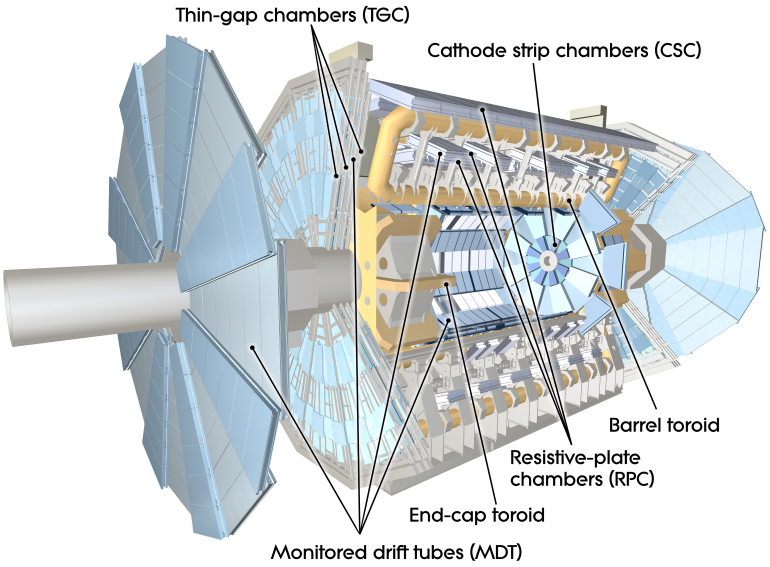

Figure 3.10: *The ATLAS Muon Spectrometer (from [68]). Precision measurement of track coordinates is made by the Monitored Drift Tubes (MDTs), covering most of the muon spectrometer's pseudorapidity range. The Cathode Strip Chambers (CSCs) cover points at large pseudorapidities, and points close to the interaction point. The Resistive Plate Chambers (RPCs) and Thin Gap Chambers (TGCs) form a separate trigger system.*

3.2.5 Muon Spectrometer

The high resolution ATLAS Muon Spectrometer (MS) [66] (Figure 3.10, and blue in Figure 3.5) has been designed to provide, over a wide range of p_T, η and ϕ, stand alone triggering and momentum measurement for muons. The magnetic field in the muon detectors is provided by the toroids. A large magnetic field over long distances is needed for good momentum measurement. The magnet system (grey in Figure 3.5) reaches 20 m in diameter and is 26 m long. The direction of the field is largely perpendicular to the muon trajectory, because of the azimuthal magnet system. The coils are maintained at an operating temperature of 4.5 K by liquid helium cryogenics. In the pseudorapidity range $|\eta| < 1.0$, the magnetic field is given by the eight-coil superconducting air core toroids. For $1.4 < |\eta| < 2.7$, muon tracks are bent by smaller end-cap magnets at both ends of the barrel toroid. In the intermediate region, $1.0 < |\eta| < 1.4$, the muons are deflected by a combination of barrel and end-cap fields. The magnetic system is designed to minimise resolution degradation from multiple scattering.

In the barrel region the muon chambers are arranged in three cylindrical layers (or "stations") around the beam axis. Chambers are installed vertically in the intermediate and end-cap regions. These stations are illustrated and labelled in Figure 3.10. Precision measurement of track coordinates in the principal bending direction of the magnetic field is given by the Monitored Drift Tubes (MDTs), covering most of the spectrometers pseudorapidity range. Larger pseudorapidities and points close to the interaction point are served by Cathode Strip Chambers (CSCs), which are higher granularity detection devices which can cope with both the increased occupancy and background bombardment. The separate trigger system (covering the range $|\eta| < 2.4$) is served by Resistive Plate Chambers (RPCs) in the barrel and Thin Gap Chambers (TGCs) in the end-caps. These chambers can also provide a "second-coordinate" measurement of track coordinates orthogonal to the precision measurement given by the MDTs and CSCs. Full details of the design and operation of these stations is given in Ref. [66].

3.2.6 The Trigger System

The ATLAS trigger systems have been designed to cope with 40 million collisions occurring each second, from bunches 25 ns apart. It has been designed to cope with these rates even when in addition to the signal events, there are $\sim$23 pile-up events. This means that its design ensures that an expected interaction rate close to 1 GHz can be reduced by a factor of 10^7 in order to write data to storage at a rate of $\sim$100 Hz. Figure 3.11 gives a schematic diagram of the ATLAS Trigger and Data Acquisition (TDAQ) system.

It is important that few signal events are accidentally thrown away. This is difficult as it is often the case that the most interesting and rarest signatures come with the smallest cross-sections or branching ratios. There are three levels to the ATLAS trigger. They act sequentially, improving the decision on whether to keep the event step by step. The higher trigger levels have access to more information, as with each level the steady drop in rate gives the subsequent level time to consider each event more carefully. The Level 1 trigger is a hardware trigger, based on coarse calorimeter and muon information. It uses this subset of detector parts to identify combinations of or the presence or absence of high-p_T muons, electrons, photons, jets and large missing energies. It must make its decision and pass it onto the front-end electronics in just 2.5 µs. The Level 2 Trigger, a software trigger, receives information from the Level 1 trigger about each event in

the "region of interest" (RoI) for the event. RoIs are regions of the detector containing potential trigger objects, there can be several per event. Using this information it can make a further decision about the event before it is passed to the final stage, a software trigger called the Event Filter. This final stage accesses the reconstructed events in their entirety and makes the final decision on which events to permanently store for offline analysis. The Level 1 Calorimeter Trigger is further detailed in Appendix A.

The $\sqrt{s} = 900$ GeV electron candidates studied in Chapter 4 were triggered using the Minimum Bias Trigger Scintillators. The candidate electron and Z boson events collected during $\sqrt{s} = 7$ TeV running (Chapters 4 and 5) were triggered using only the Level-1 Calorimeter Trigger. During later running, the higher level software triggers (Level-2 and the Event Filter) had been activated, and consequently are used for the analysis of the 35 pb^{-1} dataset described in Chapter 6. For this study the lowest unprescaled single electron and single muon triggers for 2010 data-taking were used. Full details of all triggers used for each analysis are given in the corresponding chapters.

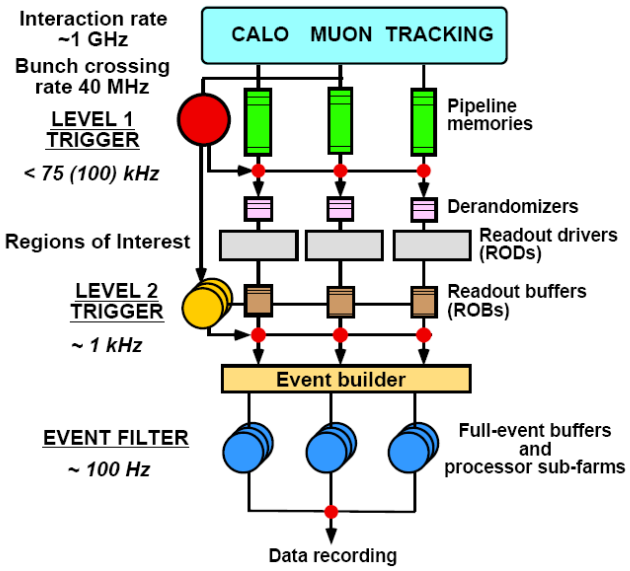

Figure 3.11: *A schematic overview of the ATLAS Trigger and DAQ system (from [61]). The trigger system is capable of producing a* 100 Hz *data rate for data recording from a* $\sim$1 GHz *interaction rate. The trigger system is a three tiered trigger system. The Level 1 Trigger (composed of a Level 1 Muon and a Level 1 Calorimeter trigger) reduces the rate to* $\sim$100 kHz*, a Level 2 Trigger with access to more information than the Level 1 Trigger further reduces this rate to* $\sim$1 kHz *before the Event Filter, with full access to the events, reduces it to* $\sim$100 Hz*.*

3.3 Simulating the Detector

The ATLAS software framework, `Athena` [71], provides a computer simulation of the ATLAS detector [72]. It simulates the response of the detector to different proton-proton collisions. The `Athena` software framework is needed, with event generators like `HERWIG` [73] and `PYTHIA` [74], to simulate Monte Carlo events on which physics analyses and performance studies can be performed. In the absence of real data these Monte Carlo events provide a way of "designing" new physics analyses and detailing and quantifying expected detector performance. In the presence of data, Monte Carlo provides an invaluable tool for comparisons between expectation and observation. Conventional python scripts (called `jobOptions`) are used to control an `Athena` application configuration at run-time.

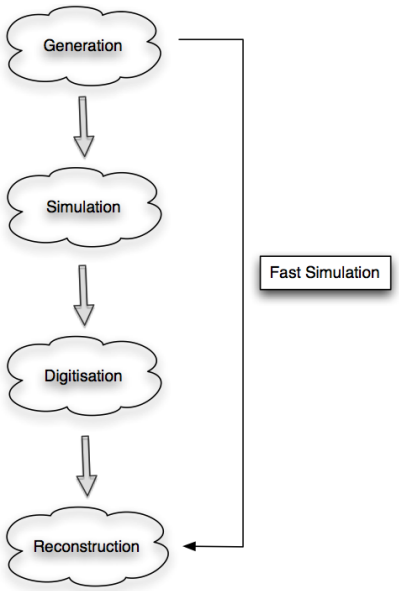

Figure 3.12: *The Full Monte Carlo production chain. Events generated using Monte Carlo generators are passed through a* `GEANT4` *[75] simulation of the ATLAS detector to produce hits. Hits are then digitised to produce digits which are reconstructed in the final step of the analysis chain. The full chain of steps can be bypassed using "fast" simulation.*

The production of simulated Monte Carlo events is a multi-stage process. The full chain of steps required for their production is illustrated in Figure 3.12. These steps are as follows:

- **Generation:** Generation refers to the production of particle four vectors from

specified physics processes.

- **Simulation:** Generated events are passed through a `GEANT4` [75] simulation of the ATLAS detector to produce `GEANT4` hits. These hits are a record of where each particle went in the detector (its path) and how much energy it deposited as it went. It simulates how the Monte Carlo events would behave if they were real events in the real detector. It simulates where they would go, which parts of the detector they would reach and, for instance, what the curvature of their paths would be as a result of the magnetic field.

- **Digitisation:** Digitisation is the process whereby the `GEANT4` hits from the simulation are subjected to the response of the detector. This produces "digits", such as times and voltages, as would be produced by a real particle in the real detector. The detector does not "see a muon" (or any other particle) rather it deduces its presence from the digits that the hardware records as a result of its flight.

- **Reconstruction:** Reconstruction is the process whereby the raw data digits, such as times and voltages, are reconstructed into tracks and energy deposits. This is where the software, as it does in the real detector, takes the voltages, times and other signals from the hardware in the detector and deduces the physics of what is happening. That is, what track the particle must therefore have been following and what its four-momenta was based on its track and energy deposit signals.

To simulate pile-up, hits from various types of event (signal, minimum bias, cavern background, beam gas and beam halo) must be overlaid. This is described in detail in Ref. [72]. Pile-up is simulated in the Monte Carlo used in Chapter 6.

Programs like `Atlfast` [76] and `AcerDET` [77] skip this "full" analysis chain. They take the generated events and apply resolution functions to the particles with appropriate parameterisations. The Monte Carlo analysis in Chapter 8 uses the `AcerDET` fast simulation software. The Monte Carlo analysis in Chapter 7 makes use of the full `Athena` framework for the generation of fully simulated events. The analyses in Chapters 4, 5 and 6 make use of both real data events, and fully simulated Monte Carlo.

3.4 Summary

Despite its size and complexity, the ATLAS detector is operating well and in-line with expectation. Chapter 4, a detailed study of electron candidates from $\sqrt{s} = 900$ GeV and $\sqrt{s} = 7$ TeV, will demonstrate how the detector components detailed here reconstruct and identify electrons, comparing early observations made from data with the initial expectations from Monte Carlo.

Part II

Data Studies

Chapter 4

Electron Reconstruction and Identification

"'Excellent,' I cried. 'Elementary,' said he."
— Arthur Conan Doyle, The Memoirs of Sherlock Holmes (1894), The Crooked Man

At the end of 2009, ATLAS enjoyed a series of stable LHC runs at $\sqrt{s} = 900$ GeV, successfully recording and analysing the many collisions which took place. A significant number of low-p_T electron candidates were reconstructed in these events. The majority of these candidates were predicted to be electrons from photon conversions and hadrons faking electrons. Whilst the transverse energies of the candidates observed in these data were well below those for which the reconstruction and identification algorithms had been optimised, these measurements provided quantitative tests of both the algorithms themselves and the reliability of the performance predictions in the transverse energy range from 2.5 GeV (the reconstruction threshold) to almost 10 GeV. The collision events analysed corresponded to a total integrated luminosity of approximately 9 μb^{-1} [57].

During the first few months of $\sqrt{s} = 7$ TeV operation, ATLAS collected data corresponding to an integrated luminosity of approximately 1 nb^{-1} [57]. The composition of this electron sample differed from the $\sqrt{s} = 900$ GeV sample. This sample contained candidates which were likely to be secondary electrons from conversions or hadrons faking electrons, but also a small ($\sim 1.5\%$) component of prompt electrons (the fraction of prompt electrons after "tight" selection, a selection designed to pick out prompt elec-

tron candidates and reject conversions, almost 50% of the sample). These $\sqrt{s} = 7$ TeV collision candidates also provided a test of reconstruction and identification algorithms and tests for higher-p_T electrons.

In this chapter the expected composition (in terms of the proportions of background electrons, hadronic fakes and prompt electrons in the sample) of these candidates is considered. Selected properties of these candidates (details of their track, the match between their cluster and track and the shape of their showers) are compared to the expectation from Monte Carlo. Electron identification in ATLAS involves making a series of cuts on discriminating track, "track-cluster match" and "shower shape" variables. There are three electron identification levels, each of which is successively more stringent. Each identification level is optimised to provide suitably high efficiencies for selecting prompt electrons, but also high rejection rates against fakes and background electrons. Comparing the properties of the electron candidates in terms of the variables used for their identification thus provides a first insight into how the expected selection efficiencies and rejections compare with reality.

This chapter exists neither to provide the most up to date status of performance, nor to outline the most recent electron identification cuts. Instead it exists to explain in detail the ideas and approaches to electron identification in ATLAS, illustrated by the very first $\sqrt{s} = 900$ GeV and $\sqrt{s} = 7$ TeV data observations and the identification cuts used at the time these illustrative plots were produced. These cuts are continually evolving such that the definition of the identification selections used for the $\sqrt{s} = 7$ TeV studies here are not identical to those which are used in latter chapters. This chapter opens with a review of the features of the ATLAS detector, as introduced in Chapter 3, which play the most important roles in electron identification and reconstruction. Details are then given of which cuts are used at each identification level, and a brief outline is presented of the expected performance of these cuts in terms of efficiencies for selecting prompt isolated and non-isolated electrons, and rates for rejecting electrons from conversions and hadrons faking electrons.

The work detailed in this chapter forms part of the first ATLAS data performance paper, Ref. [11], and a large part of one of the first ATLAS performance group conference notes, Ref. [2].

4.1 Reconstruction in ATLAS

Electrons produced in collisions leave curved tracks in the ID before depositing energy in the calorimeters. The cell energy deposits for an individual electron form a cluster. The cluster and associated track identify an electron candidate.

The electromagnetic calorimeter is finely segmented in both the lateral ($\eta \times \phi$ space) and longitudinal shower directions. At high energy, most of the electromagnetic shower energy is collected in the middle layer of the electromagnetic calorimeter. The strip layer in front of this is more finely grained in the η-direction (with a coarser granularity in ϕ) and can help discriminate between γs and π^0s. These two layers are complemented by the coarse granularity pre-sampler layer (covering the range $|\eta| < 1.8$) which can correct for energy lost in the material before the calorimeter. The back layer helps to correct for the tails of very highly energetic electromagnetic showers.

The ID provides precise track reconstruction. The SCT gives eight hits per track at intermediate radii, and the TRT as many as 35 hits per track (in the range $|\eta| < 2.0$) at the outer radii. The TRT is capable of discriminating between electrons and pions over a wide energy range (between 0.5 and 100 GeV). The b-Layer, located just outside the beam-pipe at a radius of 50 mm, provides precision vertexing.

Electron candidates falling in the transition region between the barrel and end-cap electromagnetic calorimeters (the fiducial region, $1.37 < |\eta| < 1.52$), are often ignored. The large amount of material in front of the first active calorimeter layers in this region results in poor electron reconstruction. Forward calorimeters give coverage of the range $3.1 < |\eta| < 4.9$, but electrons reconstructed in this region, termed "forward electrons", are not considered here.

Clusters are formed from a sliding window algorithm [78]. In this algorithm windows of fixed size in η and ϕ are slid across the $\eta - \phi$ grid of the LAr calorimeter. The sliding-windows are longitudinal towers of 3×5 cells of size 0.025×0.025 in $\eta \times \phi$ space. This corresponds to the granularity of the middle calorimeter layer (in the strip layer the size in $\Delta\eta$ is 0.0031, whereas in the back-layer it is 0.05, see Figure 3.8). These windows look for objects above predefined thresholds from which to form seeds. The seeds are

then used to build clusters. Each layer of the calorimeter is iterated over in order to define the energy and position of the cluster, to which corrections and calibrations are then applied. During calibration the electron clusters are rebuilt. The optimal size of these clusters in the electromagnetic barrel calorimeter is 3×7 cells in $\eta \times \phi$. In the electromagnetic end-cap calorimeters the optimal cluster size is 5×5 cells. The energy of each cluster is determined by summing four different contributions (estimated energy deposited in the material in front of the electromagnetic calorimeter, estimated energy in the chosen cluster size, external energy outside the cluster and the estimated energy deposit beyond the electromagnetic calorimeter). The electrons are reconstructed from the sliding window clusters if there is a suitable match with a track of $p_T > 0.5$ GeV. The "best" track is the one lying with an extrapolation closest in (η, ϕ) to the cluster barycentre in the middle electromagnetic calorimeter layer.

These reconstructed electron candidates are then subjected to an identification procedure designed to select true electrons efficiently whilst rejecting electrons from photon conversions and fake candidates.

4.2 Identification Algorithms

The baseline electron identification algorithms in ATLAS make a series of rectangular cuts on variables which can discriminate between isolated electrons, conversions and jets faking electrons. These variables are based on calorimeter, tracker and combined calorimeter-tracker information. ATLAS uses three different sets of reference cuts which are described as: "loose", "medium" and "tight". The choices of variables used for each set of reference cuts (including thresholds) vary over time, as understanding of the detector improves. In Table 4.1 examples of the variables used for loose, medium and tight electron identification are given. These are the set of variables and levels which were proposed for start-up and then used at $\sqrt{s} = 900$ GeV. When these cut values are optimised on Monte Carlo, the optimisation procedure is carried out in bins of cluster transverse energy (E_T) and η. The E_T distribution of a sample of electrons will depend on the composition of the sample. At different η different technologies are used in the detector, and the amount of material through which the candidates must pass changes.

Type	Description	Shorthand
Loose electron cuts		
Acceptance of the detector	$\|\eta\| < 2.47$ for electrons ($1.37 < \|\eta\| < 1.52$ excluded)	-
Hadronic leakage	Ratio of E_T in the 1st sampling of the hadronic calorimeter to E_T of the electromagnetic cluster (used over the range $\|\eta\| < 0.8$ and $\|\eta\| > 1.37$) Ratio of E_T in the hadronic calorimeter to E_T of the electromagnetic cluster (used over the range $\|\eta\| > 0.8$ and $\|\eta\| < 1.37$)	-
Middle layer of the electromagnetic calorimeter	Ratio in η of cell energies in 3 $\times$ 7 versus 7 $\times$ 7 cells.	R_η
	Lateral width of the shower	w_2
Medium electron cuts (in addition to the loose cuts)		
Strip layer of the electromagnetic calorimeter	Total lateral shower width (20 strips)	w_{stot}
	Ratio of the energy difference between the largest and second largest energy deposits over the sum of these energies	E_{ratio}
Track quality	Number of hits in the pixel detector (at least one)	-
	Number of hits in the pixels and SCT (at least seven)	-
	Transverse impact parameter (<5 mm)	d_0
Track matching	$\Delta\eta$ between the cluster and the track in the strip layer of the electromagnetic calorimeter	$\Delta\eta_1$
Tight electron cuts (in addition to the medium cuts)		
b-Layer	Number of hits in the b-Layer (at least one)	
Track matching	$\Delta\phi$ between the cluster and the track in the middle layer of the electromagnetic calorimeter	$\Delta\phi_2$
	Ratio of the cluster energy to the track momentum	E/p
TRT	Total number of hits in the TRT (used over the acceptance of the TRT, $\|\eta\| < 2.0$)	-
	Ratio of the number of high threshold hits to the total number of TRT hits (used over the acceptance of the TRT, $\|\eta\| < 2.0$)	-

Table 4.1: *Definition of variables used for electron identification. The "loose", "medium" and "tight" selections detailed here correspond to the early* $\sqrt{s} = 900$ GeV *definitions (as illustrated in the figures in this chapter). These cuts have evolved since, and will continue to evolve as detector performance for electrons is better understood. A not dissimilar table exists for photon candidates, where there are two selection levels "loose" and "tight" but no tracking cuts [2].*

The simplest selection, loose identification, cuts on the shapes of showers in the middle layer of the electromagnetic calorimeter, and on the fraction of cluster energy deposited in the layers of the hadronic calorimeter (see Table 4.1). Loose photon identification also uses cuts on these variables, with a shared set of thresholds, in order to provide a common ground for triggering. Although these loose cuts are shared, the electron candidates will consist of clusters associated to a loosely matching track whereas the photon candidate clusters will in general lack such a track. Electron candidates are required to lie within $|\eta| < 2.47$, the region covered by the calorimeter and precision region of the tracker.

The next level of selection, medium identification, builds on the loose electron selection, and additionally places requirements on the energy deposited in the strip layer of the electromagnetic calorimeter, the quality of the track and the match between track and cluster.

The highest level, tight identification, exploits the detector fully. The cuts at this level are designed to: (a) specifically reject charged hadrons (using the ratio between measured cluster energy and track momentum, E/p, and the fraction of high threshold hits in the TRT) and (b) reject background electrons from photon conversions (by requiring the presence of a hit on the track in the b-Layer, and rejecting candidates with a matching conversion vertex). At this selection level the track-matching cuts are also tightened.

4.3 Expected Performance

This section details the expected impact of applying each set of identification cuts successively on a sample of real and fake electrons, at the time these first observations were made. In Table 4.2, expected reconstruction efficiencies and rejections are given at each of the three different identification levels. This, and subsequent details of the expected performance, are taken from Ref. [2]. The efficiency is defined as the percentage of true electrons (lying within simple kinematic acceptance cuts on η and E_T) which are reconstructed and pass the three different levels of identification. Rejection is defined as the ratio of the number of true jets to the number of candidates which pass the given selection criteria [1]. These efficiencies and rejections are obtained from a Monte Carlo sample

[1] A truth jet is defined in this table as the sum of particle four-momenta in a cone with size $\Delta R = 0.4$.

of mainly di-jet events, but also a selection of events from important hard processes, like W and Z decay. In Table 4.2 the true electrons in the efficiency computation have $E_T > 20$ GeV and lie within $|\eta| < 2.5$. The η dependence of this efficiency, illustrated in Figure 4.1(a), demonstrates how efficiency is dependent on the amount of material in the inner detector and the electromagnetic calorimeter. Electrons in a lower-E_T region are considered in Figure 4.1(b). This figure illustrates that the efficiency at the level of medium identification is expected to rise sharply above 15 GeV, flattening out to a plateau of 90%. Table 4.2 also details the resulting composition of the di-jet sample at each successive level of identification. At the level of tight identification the sample is dominated by prompt electrons, isolated electrons from W and Z decays and non-isolated electrons from b and c decay. At the level of medium identification the sample is still dominated by background electrons (electrons from photon conversions and Dalitz decays). The $\sqrt{s} = 900$ GeV candidates considered in this chapter provide only a probe of electrons in the low-E_T region included in Figure 4.1(b), whilst the $\sqrt{s} = 7$ TeV electron candidates start just to infringe on transverse energies in the efficiency plateau.

	Efficiency (%)		Jet rejection	Sample composition (% of total)			
	$Z \to e^+e^-$	$b, c \to e$		Isolated electrons	Non-isolated electrons	Background electrons	Hadrons
Reconstructed	97.56 ± 0.03	-	91.5 ± 0.1	0.1	0.8	23.3	75.8
Loose	94.30 ± 0.03	36.8 ± 0.5	1066 ± 4	1.0	2.0	56.7	40.3
Medium	89.97 ± 0.03	31.5 ± 0.5	6821 ± 69	5.9	9.8	50.7	33.6
Tight	71.52 ± 0.03	25.2 ± 0.5	$(1.38 \pm 0.06) \times 10^5$	29.6	44.8	11.5	14.1

Table 4.2: *Expected electron reconstruction efficiency and jet rejection for a sample of events containing mainly di-jets, but also a selection of important hard processes like W, Z decay and heavy flavour decay (from [2]). These rejections and efficiencies are given for electrons passing an E_T threshold of* 20 GeV*. The efficiencies for reconstructing isolated electrons in Z decays are given in the second column and the efficiencies for reconstructing non-isolated electrons in heavy flavour decays ($b, c \to e$) are given in the third column. The total jet rejection includes rejections for hadron fakes and background electrons (from both photon conversions and Dalitz decays). In the last four columns the sample is broken down into four components: (i) isolated electrons from W, Z decays, (ii) non-isolated electrons from heavy flavour semi-leptonic decays, (iii) background electrons from photon conversions and Dalitz decays and (iv) the remaining hadronic component. These numbers were obtained from $\sqrt{s} = 10$ TeV Monte Carlo, without pile-up. The quoted errors are statistical.*

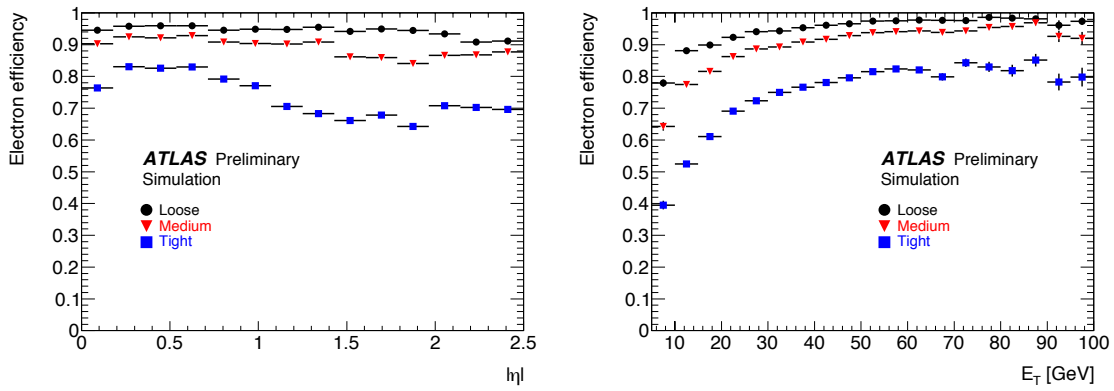

(a) (b)

Figure 4.1: *Expected electron efficiency versus $|\eta|$ (a) and E_T (b) shown for loose, medium and tight selection criteria (from [2]). The efficiency is defined as the ratio of the number of reconstructed electrons passing the identification criteria to the total number of electrons falling within acceptance. These figures were produced from $\sqrt{s} = 10$ TeV Monte Carlo, without pile-up.*

4.4 Event Samples

The results presented in this chapter are obtained from collision data samples collected at both $\sqrt{s} = 900$ GeV and $\sqrt{s} = 7$ TeV. These two samples are now detailed. At $\sqrt{s} = 900$ GeV all the events were triggered during times at which the LHC beams were stable using coincident signals from the two Minimum Bias Trigger Scintillators located in front of the end-cap electromagnetic calorimeters (which cover the pseudorapidity range, $2.09 < |\eta| < 3.84$). Events were selected for which the tracker, electromagnetic calorimeter and hadronic calorimeters recorded data with high quality and the solenoidal field was at its nominal value. The data sample obtained consists of 384,186 collision candidates and corresponds to an integrated luminosity of approximately 9 μb^{-1} [57]. The Monte Carlo event sample to which they are compared consists of 10^7 non-diffractive minimum bias events generated by the ATLAS central production teams with `PYTHIA`, using the ATLAS `mc09` tune [79] and the `MRSTLO` [80] parton distribution functions, simulated with `GEANT4` [75] and passed through full simulation of the ATLAS detector. The contribution from single and double diffractive events is negligible in this regime. In this sample all selected electron candidates have a cluster $E_T > 2.5$ GeV and a cluster η, measured in the middle layer of the calorimeter, satisfying $|\eta| < 2.47$. In the

remainder of this chapter E_T will refer to the transverse energy of the cluster and η to the pseudorapidity in the middle layer of the calorimeter.

For the data sample collected at $\sqrt{s} = 7$ TeV, the events considered were also those taken whilst the tracker, electromagnetic and hadronic calorimeters recorded data with high quality and the solenoidal field was at its nominal value. The sample contains about three million collision events, corresponding to an integrated luminosity of approximately 1 nb^{-1} [57]. These are compared to centrally produced non-diffractive minimum bias events generated with `PYTHIA`, using the ATLAS `mc09` tune [79] and the `MRSTLO` [80] parton distribution functions, simulated with `GEANT4` [75] and passed through full simulation of the ATLAS detector. The sample consisted of 2×10^7 events, generated at $\sqrt{s} = 7$ TeV. All events were required to contain at least one reconstructed primary vertex with at least three reconstructed tracks. The efficiency of this requirement for events containing at least one pre-selected electron candidate was found to be very close to 100% for both data and Monte Carlo. For a relatively small proportion of the selected data events ($\sim 25\%$), these were required only to satisfy the minimum bias trigger (a trigger expected to be effectively 100% efficient for minimum bias events). The remainder of events in the sample were triggered using the Level 1 Calorimeter Trigger (Appendix A) at its lowest possible threshold setting, 3 GeV (a trigger expected to be 98% efficient towards minimum bias events). The mixed triggers used in this sample of data reflect the changing luminosity profile with respect to time in the weeks and months shortly after LHC start-up. Events were required to have a raw cluster transverse energy above 4 GeV and a calibrated offline cluster transverse energy above 5 GeV. The pre-selected electrons were required to be associated to tracks containing at least ten TRT hits and four silicon hits, and lie within $|\eta| < 2.0$ (excluding the region $1.37 < |\eta| < 1.52$).

In what follows, the barrel region is defined as that covering $|\eta| < 1.37$ and the end-cap region that covering $1.52 < |\eta| < 2.47$. There are 879 candidates in the $\sqrt{s} = 900$ GeV sample before loose selection, and 128,909 in the $\sqrt{s} = 7$ TeV data sample before loose selection, but after the pre-selection described.

4.5 Electron Candidates

4.5.1 $\sqrt{s} = 900$ GeV Candidates

Table 4.3 presents the numbers of reconstructed electron candidates, over the full detector acceptance and in the two defined η regions, at the three levels of identification (the selection cuts were not optimised for such low-energy electron candidates). Figure 4.2 displays the E_T and η of all selected electron candidates. Both Table 4.3 and Figure 4.2 show agreement between data and simulation, given the large uncertainties expected in this kinematic regime.

The Monte Carlo sample is sub-divided (in all the figures displayed for $\sqrt{s} = 900$ GeV candidates) into the two dominant components: *(i) hadrons* and *(ii) electrons from conversions*, and normalised to data. The latter component corresponds to $\sim 33\%$ of all the electron candidates and is largely dominated by electrons from photon conversions. It also includes a small component ($\sim 3\%$) of background electrons from other sources, such as Dalitz decays, and an even smaller one ($< 1\%$) of prompt electrons from $b, c \to e$ decays. As can be seen in Table 4.3, the fractions of hadrons and conversions expected depends on the identification level, and the η-region chosen (see also Table 4.2 and Figure 4.1). This variation is a result of the distribution of material in the tracker, and specific kinematic features of the different backgrounds at low transverse energies.

The low statistics available do not allow quantitative comparisons of variables between data and simulation after tight selection cuts, for which the expectation is that a significant fraction of the electron candidates in Table 4.3 will be prompt electrons from b and c decay (see Table 4.2). Approximately 15% of the Monte Carlo electron candidates passing the tight cuts are expected to be prompt electrons, which means that three out of the twenty electron candidates passing tight cuts in the data would be expected to originate from heavy flavour decay. In the following, distributions will be compared between data and simulation for all selected candidates at $\sqrt{s} = 900$ GeV.

Electron candidates	All 879		Barrel 558		Endcap 321	
	Data (%)	Monte Carlo (%)	Data (%)	Monte Carlo (%)	Data (%)	Monte Carlo (%)
Loose	46.5 ± 1.7	50.9 ± 0.2 (40.0 ± 0.3)	47.3 ± 2.1	51.8 ± 0.3 (33.1 ± 0.4)	45.2 ± 2.8	49.5 ± 0.4 (51.2 ± 0.5)
Medium	10.6 ± 1.0	13.1 ± 0.2 (26.4 ± 0.6)	11.1 ± 1.3	12.9 ± 0.2 (19.5 ± 0.7)	9.6 ± 1.6	13.3 ± 0.3 (36.9 ± 1.0)
Tight	2.3 ± 0.5	2.4 ± 0.1 (37.9 ± 1.5)	1.6 ± 0.5	1.8 ± 0.1 (49.2 ± 2.2)	3.4 ± 1.0	3.3 ± 0.1 (28.7 ± 1.8)

Table 4.3: *Break down of the $\sqrt{s} = 900$ GeV candidates at the three levels of identification: the entire η-range, $|\eta| < 2.47$ is considered (left), as well as the η-ranges of the barrel (middle) and end-cap (right) electromagnetic calorimeters. The first row gives the total numbers of electron candidates reconstructed in data in these three different η-ranges. For each η-range, the percentages of identified loose, medium and tight candidates in data are compared to the precentages predicted by Monte Carlo. The numbers in brackets give the percentage of identified Monte Carlo electron candidates which are electrons from photon conversions or prompt electrons (the remainder are charged hadrons). The percentage errors are purely statistical binomial errors.*

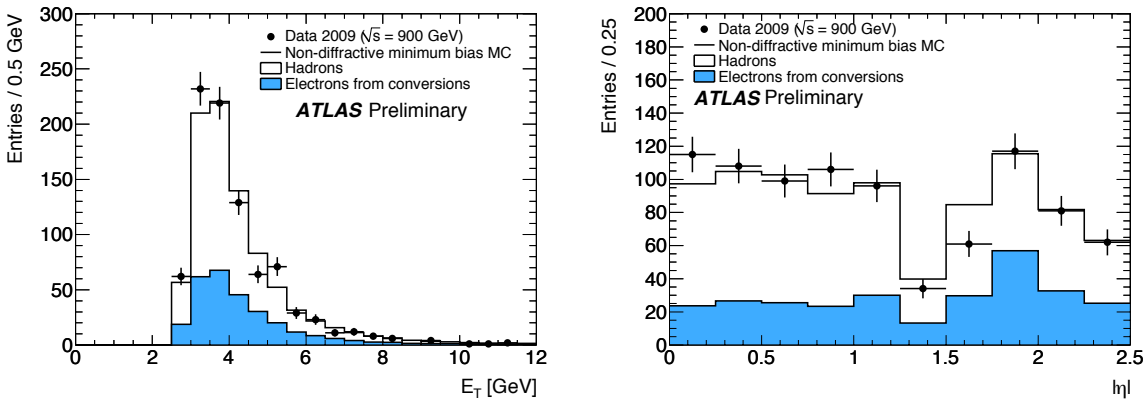

(a) (b)

Figure 4.2: *Cluster E_T (a) and $|\eta|$ (b) for all selected $\sqrt{s} = 900$ GeV electron candidates. The Monte Carlo is broken down into electrons from conversions (blue), and hadrons (white). The electrons from conversions component includes small components of background electrons from other sources and prompt electrons (3% and 1% respectively). The error bars on the data points are purely statistical $\sqrt{N}$ errors.*

4.5.2 $\sqrt{s} = 7$ TeV Candidates

Table 4.4 presents a break down of the $\sqrt{s} = 7$ TeV electron candidates in Monte Carlo. The fractions of each type of Monte Carlo electron passing pre-selection then loose, medium and tight identification selection are given. This table illustrates in detail the expected composition of the $\sqrt{s} = 7$ TeV electron sample. The prompt electron component rises from $\sim$4% of all the electrons in Monte Carlo at loose level, to almost 50% at tight. The conversion component holds steady over the three identification levels. There is no guarantee that the composition of the data sample will be identical. In Ref. [81] attempts are made to determine the composition of an inclusive electron sample at $\sqrt{s} = 7$ TeV through the exploitation of agreement (and also disagreement) between data and Monte Carlo in the variables which can be used to separate prompt electrons from conversions and charged hadrons. This is outside of the scope of what is considered here.

The η and E_T of the data candidates are given in Figure 4.3, and compared to Monte Carlo. In this figure, and all subsequent $\sqrt{s} = 7$ TeV figures, the Monte Carlo is

divided into the three dominant components: *(i) hadrons*, *(ii) electrons from conversions* and *(iii) prompt electrons*, and normalised to data. The agreement between data and Monte Carlo in both of these figures is good. Figure 4.3(b) illustrates the region of pseudorapidity which has been excluded ($1.37 < |\eta| < 1.52$).

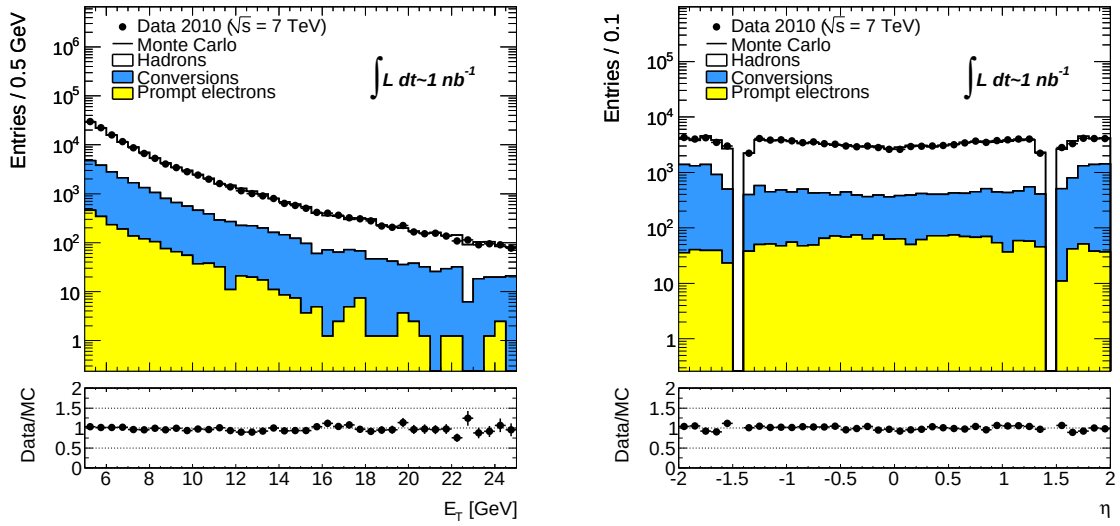

(a) (b)

Figure 4.3: *Cluster E_T (a) and $|\eta|$ (b) for all selected $\sqrt{s} = 7$ TeV electron candidates. The candidates with $|\eta| > 2.0$ are not considered in this chapter. The Monte Carlo is broken down into electrons from conversions (blue), hadrons (white) and prompt electrons (yellow). The error bars on the data points are purely statistical $\sqrt{N}$ errors.*

	Hadrons (%)	Conversions (%)	Prompt electrons (%)
Pre-selected	82.1 ± 0.1	16.3 ± 0.1	1.6 ± 0.1
Loose	67.5 ± 0.3	28.4 ± 0.3	4.1 ± 0.1
Medium	66.5 ± 0.5	22.8 ± 0.4	10.7 ± 0.3
Tight	29.6 ± 1.1	22.4 ± 1.0	48.1 ± 1.2

Table 4.4: *Break down of the* $\sqrt{s} = 7$ TeV *electron candidates in Monte Carlo at each identification level. The percentage of these Monte Carlo electron candidates which are electrons from photon conversions, hadrons and prompt electrons are given at each level of identification. The errors are purely statistical, binomial errors.*

The first $\sqrt{s} = 900$ GeV and $\sqrt{s} = 7$ TeV data electron candidates have been presented and initial comparisons have been made with Monte Carlo expectations. The agreement in E_T and η between data and Monte Carlo is sound. In Section 4.3 the reconstruction efficiencies and rejections expected at each of the three identification levels have been given (based on Monte Carlo truth studies of an unfiltered Monte Carlo sample of events, containing mainly di-jet events). The degree to which these efficiencies and rejections will be reproduced in data depends upon the extent to which the track, track-cluster and shower shape variables exploited at each identification level agree between data and Monte Carlo. The necessary efficiencies and rejections are optimised on Monte Carlo, using the expected behaviour of these variables for each of the key types of electron candidate. In the next section comparisons are made of these variables between data and Monte Carlo. The section will also highlight the ways in which these variables differ for the various types of electron candidate, and so provide an illustration of why the cuts listed in Table 4.1 are used to reject fake electrons and background electrons, whilst efficiently retaining prompt electrons.

4.6 Identification Variable Comparisons

4.6.1 Tracking and Track-Cluster Matching Variables

Electron reconstruction and identification, both at medium and tight identification levels, relies heavily on tracking. Figure 4.4 illustrates two of the track-cluster match variables used in electron identification for all electron candidates reconstructed in data and simulation at $\sqrt{s} = 900$ GeV. Figure 4.4(a) shows the difference in azimuth, $\Delta\phi_2$, between the track extrapolated to the middle layer of the electromagnetic calorimeter and the barycentre of the cell energies in this layer. A cut on the difference in η is used in medium identification, whilst a cut on $\Delta\phi_2$ is used at the level of tight identification. The difference in azimuth is sign-corrected to account for the opposite curvatures of electrons and positrons in the detector magnetic field, and the cuts applied to it are asymmetric. The cut is positioned so as to keep most of the candidates which have large negative $\Delta\phi_2$. The asymmetric tail of the distribution is more pronounced for the electron component than the hadron component as one would expect. The asymmetry arises from energy losses during bremsstrahlung in the tracker material. In contrast, the difference in η, $\Delta\eta_1$, between the track extrapolated to the strip layer of the electromagnetic calorimeter and the barycentre of the cell energies in this layer (Figure 4.4(b)),

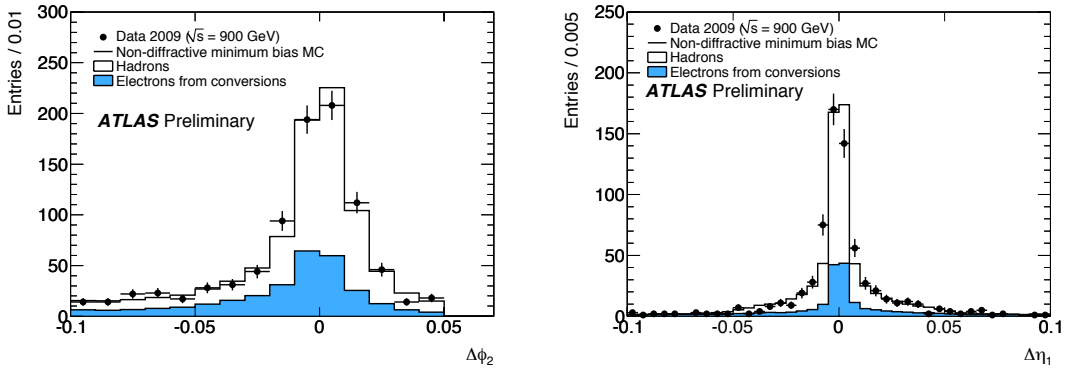

(a) (b)

Figure 4.4: *Distributions of track-cluster matching variables in ϕ (a) and η (b) for all electron candidates at $\sqrt{s} = 900$ GeV compared between data and simulation. The difference in ϕ, $\Delta\phi_2$ (a), is as measured in the middle layer of the calorimeter whilst the difference in η, $\Delta\eta_1$ (b), is as measured in the strip layer of the calorimeter. Monte Carlo is broken down into hadrons and electrons from conversions. The error bars on the data points are purely statistical $\sqrt{N}$ errors. Typical cuts on these two variables are: $|\Delta\phi_2| < 0.02$ and $|\Delta\eta_1| < 0.01$, the precise values varying as a function of p_T and η.*

is not asymmetric. Bremsstrahlung has no influence on the track-cluster match in the η-direction.

Figure 4.5 compares between data and simulation for all electron candidates in the $\sqrt{s} = 900$ GeV data the number of hits in the pixel detectors and the SCT, and the number of high threshold hits in the TRT. The agreement between data and simulation is good for all three distributions, despite the complications expected at these low energies from interactions with material in the detector and track reconstruction inefficiency. Figures 4.5(a) and 4.5(b) show the numbers of hits on the reconstructed tracks in the pixel and SCT detectors, respectively. As expected, a large fraction of the electrons from conversions in the simulation have tracks without hits in these detectors. A significant fraction of the hadrons also have no hits in these detectors. This could suggest that the track-matching algorithm is picking up tracks from secondaries in the TRT detector. Requirements are made on the number of pixel and silicon hits (at least one and at least seven, respectively) at the level of medium identification to reject electrons from conversions. The silicon hit distribution for the $\sqrt{s} = 7$ TeV candidates is illustrated in Figure 4.6(a), after the pre-selection requirement of candidates with at least four silicon

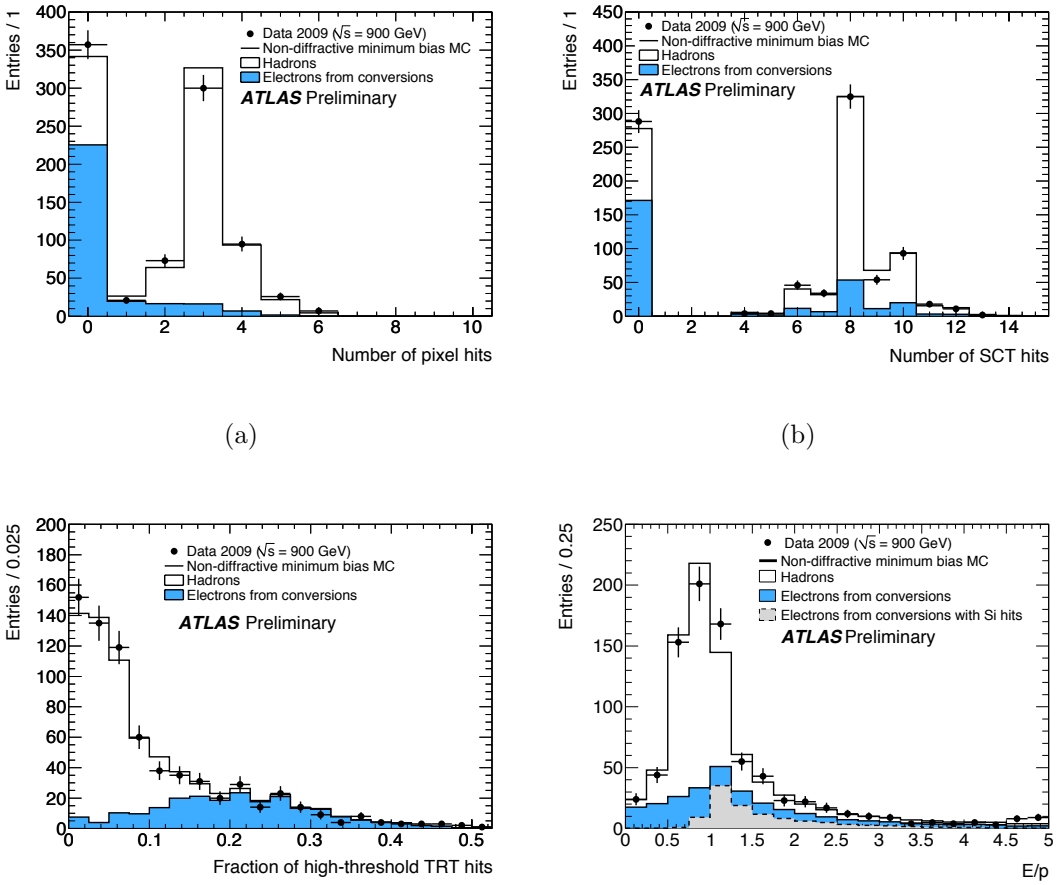

Figure 4.5: *Distributions of tracking variables for all electron candidates at* $\sqrt{s} = 900$ GeV *compared between data and simulation. Shown are the number of pixel (a) and SCT (b) hits on the electron track, the fraction of high threshold TRT hits for candidates with* $|\eta| < 2.0$ *and with a total number of TRT hits larger than ten (c) and the ratio of cluster energy to track momentum,* E/p *(d). Monte Carlo is broken down into hadrons and electrons from conversions. The error bars on the data points are purely statistical* $\sqrt{N}$ *errors. Typically, the ratio of* E/p *is required to lie between 1 and 3 for electrons selected at the tight identification level and the fraction of high-threshold hits is required to be* > 0.1 *(the precise values of these cuts vary with* η *and* p_T*).*

hits. This figure shows there is still reasonable agreement between data and simulation at higher energies. Conversions populate the lower end of this hit distribution.

Stringent requirements on the number of TRT hits, and the number of high threshold TRT hits, are not used until tight identification level where higher rejections and, in

particular, rejection against charged hadrons, are required. Figure 4.5(c) displays the fraction of high threshold TRT hits on the track for $\sqrt{s} = 900$ GeV electron candidates with $|\eta| < 2.0$ and greater than ten TRT hits. At low energies, electrons will give a non-optimal yield of transition radiation photons. Despite this, it is clear in Figure 4.5(c) that the agreement between data and simulation is good and that the expected hadron distribution is very different to the expected distribution from conversion electrons. As one would expect, conversions give tracks with a higher fraction of high threshold TRT hits than hadrons.

The power of the TRT is further demonstrated in Figure 4.6(b), which illustrates the fraction of high threshold TRT hits for loose $\sqrt{s} = 7$ TeV electron candidates. The fraction of prompt electrons in this sample of loose candidates will be significant. The proportion of hadron fakes and conversions in the sample will have been reduced by the loose identification cuts. There are very few hadrons with more than 10% high threshold hits. Figure 4.7 illustrates the number of these electron candidates which also satisfy tight identification selection cuts excluding the cut on the fraction of high threshold TRT hits (which is usually placed at ~ 0.1). This figure clearly shows that the hadrons still remaining at this level will be removed without too great a loss of signal prompt electrons by the well-placed cut on the fraction of high threshold TRT hits.

Tight electron candidates must satisfy requirements on not just $\Delta\phi_2$ and the numbers of TRT hits, but also on the ratio of cluster energy to track momentum, E/p. Figure 4.5(d) illustrates this ratio for all $\sqrt{s} = 900$ GeV electron candidates and for data and simulation. The corresponding $\sqrt{s} = 7$ TeV distribution for loose candidates is displayed in Figure 4.6(d). The expectation, for massless electrons, is that this distribution will peak at unity. Monte Carlo shows that the peak in this distribution from electrons is actually expected to lie slightly above unity. Bremsstrahlung losses in the tracker material give rise to the high tail in the E/p for electrons from conversions. Studies have shown this shift is not entirely due to bremsstrahlung losses [2]. An overestimate of the cluster energy, from the energy of nearby particles included in the cluster energy, shifts the peak to higher E/p values. The hadron component also appears to peak near unity, in fact just below it: hadrons which are reconstructed as electron candidates are those which have deposited most of their energy in the electromagnetic calorimeter at these low energies. Both these figures show that data is slightly shifted with respect to the Monte Carlo. This disagreement between the E/p seen in data and the expectation

from Monte Carlo is not yet fully understood.

At the level of medium identification, the $\Delta\eta_1$ cut is joined by a cut on the transverse impact parameter, d_0. Figure 4.6(c) illustrates the impact parameter for all $\sqrt{s} = 7$ TeV loose electron candidates. The agreement between data and simulation at these energies is good.

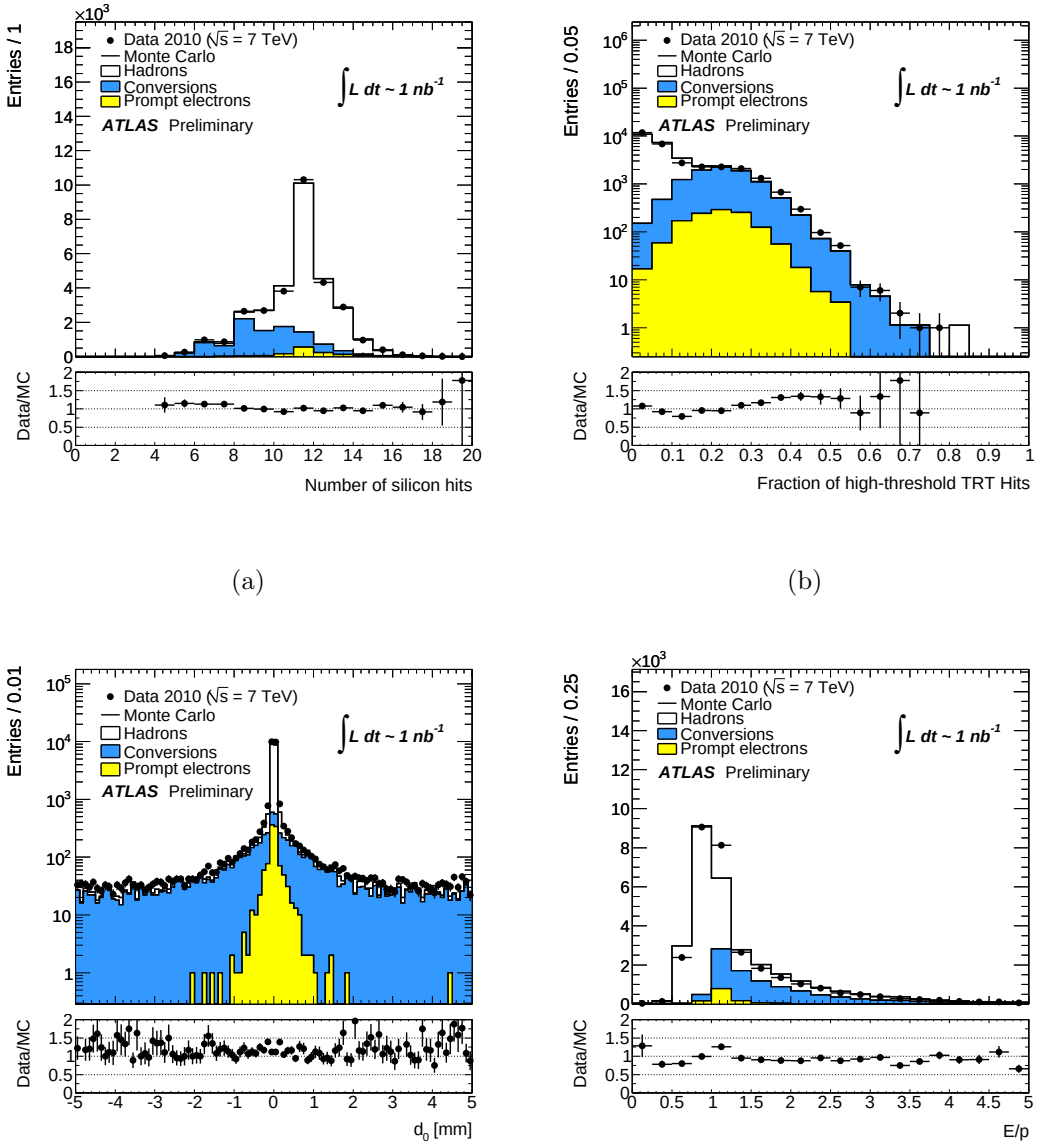

Figure 4.6: *Number of silicon hits (a), fraction of high threshold TRT hits (b), impact parameter d_0 (c) and E/p (d) at the level of loose identification for electron candidates at $\sqrt{s} = 7$ TeV. Monte Carlo is broken down into hadrons, electrons from conversions and prompt electrons. The error bars on the data points are purely statistical $\sqrt{N}$ errors.*

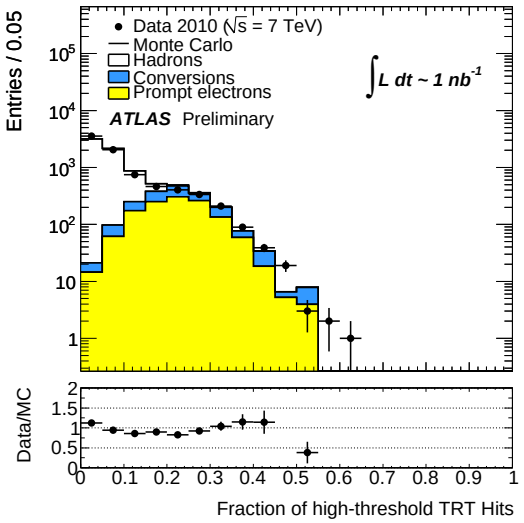

Figure 4.7: *Fraction of high threshold TRT hits for candidates passing all tight requirements, except that on this fraction, at* $\sqrt{s} = 7$ TeV. *At the tight level an* (η, p_T) *bin dependent cut is applied around* 0.1 *on the fraction of high threshold TRT hits. Monte Carlo is broken down into hadrons, electrons from conversions and prompt electrons. The error bars on the data points are purely statistical* $\sqrt{N}$ *errors.*

4.6.2 Shower Shape Variables

The fractions of energy deposited in successive layers of the electromagnetic calorimeter are denoted: (a) for the pre-sampler, f_0, (b) for the strip layer, f_1, (c) for the middle layer, f_2 and (d) for the back layer, f_3. Figure 4.8 illustrates the longitudinal shower development for tight $\sqrt{s} = 7$ TeV electron candidates in each layer of the electromagnetic calorimeter, based on the measured layer energies before cluster corrections are applied. There is reasonable agreement between data and Monte Carlo. Before any identification cuts are applied it is known that the fraction in the pre-sampler does not agree particularly well between Monte Carlo and data for values of f_0 greater than 0.6 [2]. This is likely to be a difference between simulation and data in the fraction of hadrons in the events. This disagreement is not seen at the tight identification level illustrated here. Although these figures illustrate nicely the development of the shower in the different calorimeter layers these variables are not used in electron identification.

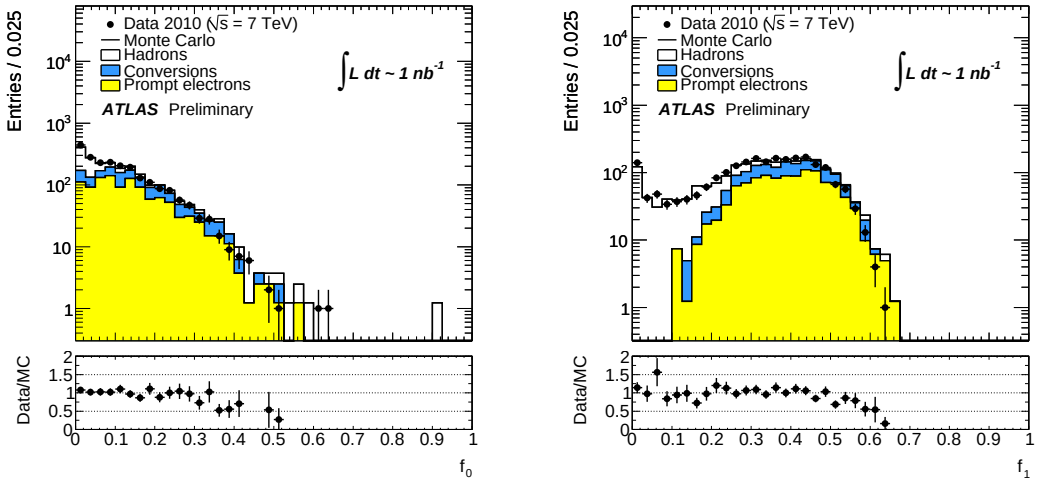

(a) (b)

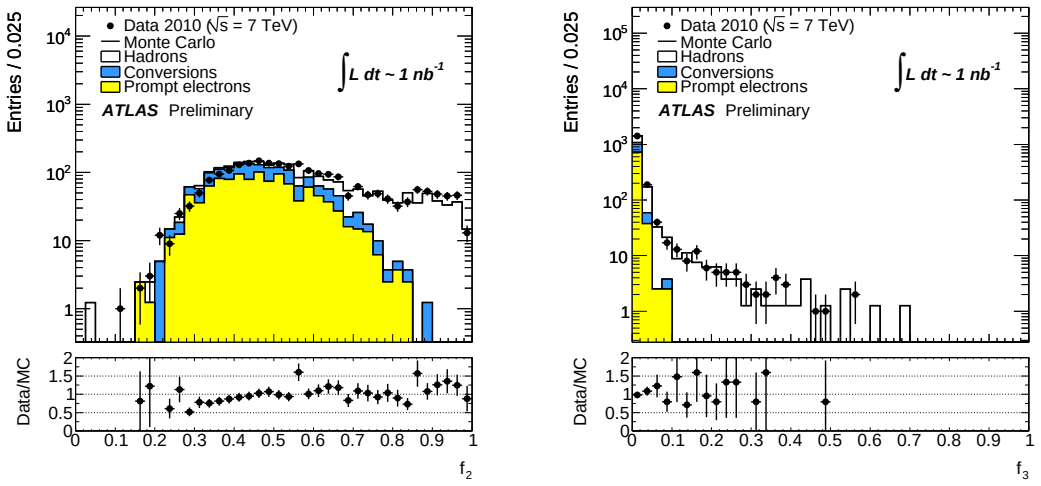

(c) (d)

Figure 4.8: *Sampling fractions in the different layers of the electromagnetic calorimeter, f_0 (a), f_1 (b), f_2 (c) and f_3 (d) at the level of tight identification cuts for $\sqrt{s} = 7$ TeV electron candidates . Monte Carlo is broken down into hadrons, electrons from conversions and prompt electrons. The error bars on the data points are purely statistical $\sqrt{N}$ errors.*

At the loose identification level, the fraction of energy which leaks from the electromagnetic calorimeter into the hadronic calorimeter is important, as is the lateral width of the shower in the middle layer of the electromagnetic calorimeter. At medium identification level further requirements are placed on the lateral width of the shower, but this time in the strip layer. The shapes of the electron showers are not considered further at the level of tight identification.

The fraction of the cluster energy deposited in the first layer of the hadronic calorimeter (or "hadronic leakage") by $\sqrt{s} = 7$ TeV candidates is shown in Figure 4.9(a) for all pre-selected candidates. The illustrated agreement is not particularly surprising since most of the electron candidates deposit energy in the first layers of the electromagnetic calorimeter (see Figure 4.8) and the noise dominates what energy leaks into the hadronic calorimeter. The lateral development of their showers, as detailed by the variables w_2, R_η and w_{stot} (described in Section 4.2 and in Table 4.1), is illustrated for candidates in Figures 4.9(b)-(d), w_{stot} illustrated for loose candidates. These variables all display small shifts between the shapes observed in data and those expected from simulation. The shower width w_2 is slightly larger in the data: preliminary studies by the ATLAS collaboration have shown that including the cross-talk between neighbouring middle layer cells ($\sim 0.5\%$) [82] in the simulation would explain part, but not all, of the observed difference [2]. It is very likely a complex interplay of factors is involved (the showering scheme in Monte Carlo and cross-talk being amongst the likely causes).

4.7 Conclusions

The data sample collected by ATLAS at $\sqrt{s} = 900$ GeV at the end of 2009 yielded just under 900 electron candidates with $E_T > 2.5$ GeV, before cuts were used to select them. The variables used to identify electron candidates have been qualitatively compared for these electron candidates with the expectation from Monte Carlo simulations. Most of these variables were found to be in remarkable agreement between data and simulation. The $\sim 130,000$ $\sqrt{s} = 7$ TeV candidates confirmed this, along with demonstrating the loose, medium and tight selection cuts. The ~ 1 nb^{-1} $\sqrt{s} = 7$ TeV sample also provided the first electrons with E_T as high as 25 GeV.

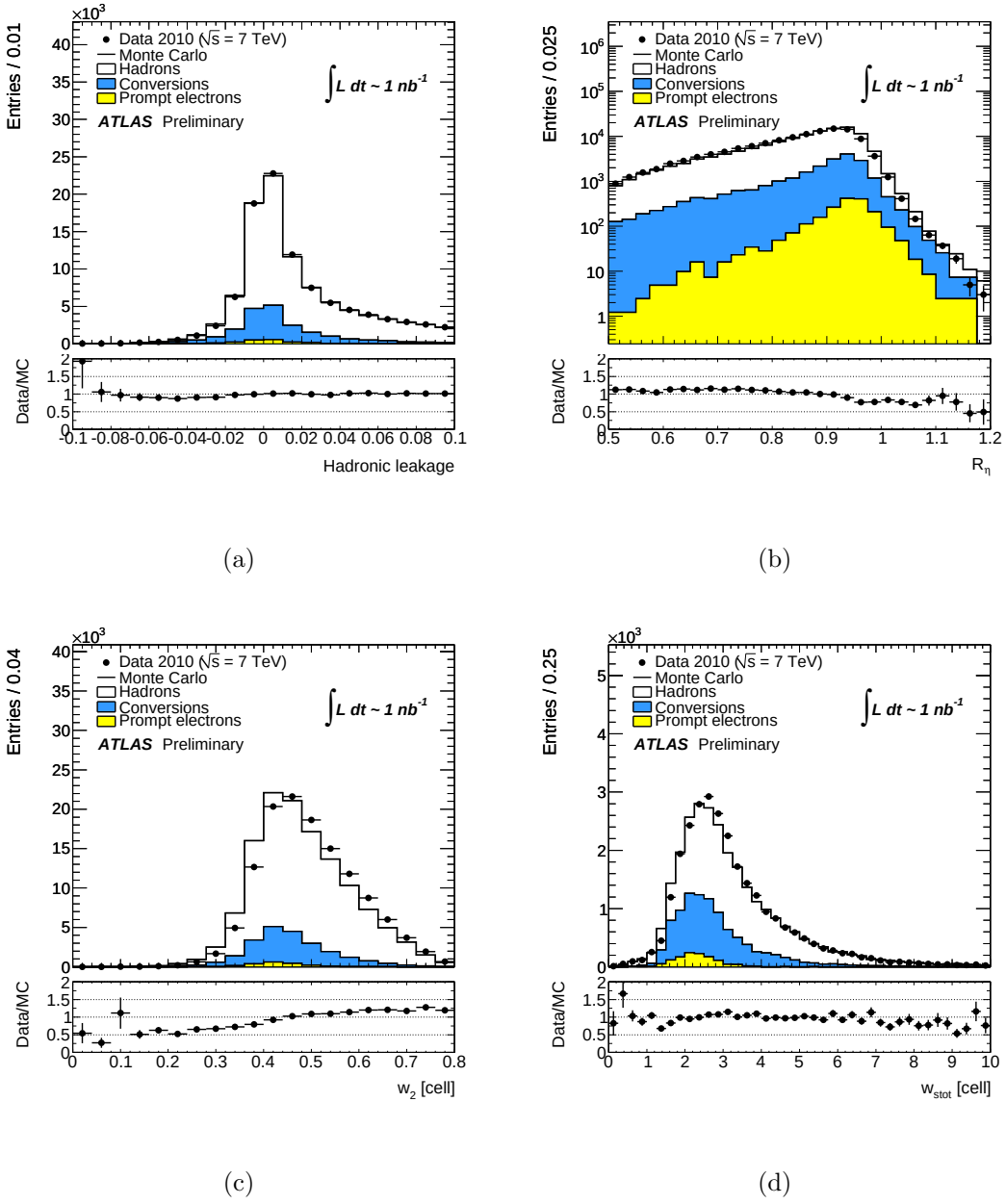

Figure 4.9: *Shower shape distributions compared between Monte Carlo and data. Shown are the hadronic leakage (a), R_η (b) and w_2 (c) at pre-selection and w_{stot} at the level of loose identification (d) for $\sqrt{s} = 7$ TeV electron candidates. Monte Carlo is broken down into hadrons, electrons from conversions and prompt electrons. The error bars on the data points are purely statistical $\sqrt{N}$ errors. Selected electrons must typically have hadronic leakage less than ~ 0.02, R_η above $0.8-0.9$, w_2 less than ~ 0.015 in η and a total lateral width < 3. These cut values vary as a function of p_T and η.*

Differences between data and expectations were found in both the lateral width of the showers and the ratio of cluster energy to track momentum. The selection efficiencies

at each identification level, and the rejections achieved against jets faking electrons and background electrons, are driven by a series of cuts including ones on these variables. The identification cuts used at each level were re-optimised by the ATLAS electron and photon performance group in response to the discrepancies observed here, and in later studies. As the luminosity collected increased these studies were broken down into studies of the discrepancies and agreements between these variables in the bins of E_T and η used for selection cuts, and the higher-E_T bins populated with candidates.

Although these discrepancies result in different selection efficiencies in data than one would expect from Monte Carlo, the differences are not significant enough to give rise to major differences in efficiencies and rejections. This remarkable agreement in early data comparisons confirmed that the ATLAS detector and the software algorithms devised are capable of efficiently selecting prompt electrons in the E_T ranges considered here whilst rejecting at each level the hadrons and background electrons. A full data-driven *quantitative* determination of the actual efficiencies for reconstructing electrons (as functions of E_T and η) followed later with the accumulation of increased statistics and the observation of the very first Z bosons (see Chapter 5).

Chapter 5

Observation of the First $Z \to e^+e^-$ Decays in ATLAS

"Where observation is concerned, chance favours only the prepared mind."
— Louis Pasteur, 7 December 1854

This chapter describes the first observations of $Z \to e^+e^-$ decays at ATLAS, one of two critical first steps in the planned ATLAS W and Z physics program. The study herein presents an observation of the Z boson at an integrated luminosity of ~ 220 nb^{-1} at $\sqrt{s} = 7$ TeV. The work detailed in this chapter formed a small part of one of the first ATLAS standard model conference notes, Ref. [5]

5.1 History

The W and Z bosons, propagators of the electroweak force, were first observed and measured in 1983 by the UA1 and UA2 collaborations (experiments at the CERN anti-proton proton collider) [40–43]. The W and Z bosons observed in ATLAS and CMS were the first of these bosons to be produced by a proton proton collider. The LEP collider was built to study the properties of the W and Z in detail. Colliding leptons together at specified energies, these machines were capable of producing very clean final states making identification of new particles far easier than at hadron colliders. Despite this, it was the hadron anti-proton proton collider that first discovered the W and Z bosons,

the discovery complicated but not hindered too much by an underlying event.

The Z bosons detected by UA1 were reconstructed by searching for the leptonic decays $Z \to e^+e^-$ and $Z \to \mu^+\mu^-$ and reconstructing the invariant mass, $m_{\ell\ell}$ (Equation 5.1), of the two leptons detected using their four momenta (p_ℓ^+ and p_ℓ^- respectively). This provides a very clean event by event measure of the mass of the Z, assuming a selection which minimises the background contamination from hadrons faking leptons and other physics processes. Attempts to measure the mass of the W were more difficult.

$$m_{\ell\ell}^2 = (p_\ell^+ + p_\ell^-)^2 \tag{5.1}$$

W bosons decay as $W^\pm \to e^\pm\nu$ and $W^\pm \to \mu^\pm\nu$, but unlike the charged leptons, the neutrinos remain undetected. Before a collision there is no momentum in the x and y directions. After the collision the momentum in the (x, y) plane must be conserved. If one adds up the transverse momentum components of all the visible particles in an event vectorially, the "missing" *transverse* momentum ($\mathbf{p}_T^{miss}$) required to make the sum zero should be equal to the *transverse* momentum of the undetected neutrino. The momentum in the z direction before the collision is not known, making it impossible to determine the missing *momentum* and hence the momentum of the undetected neutrino. Realistically, this vectorial sum will not exactly equal the p_T of the unobserved neutrino. There will be other sources of $\mathbf{p}_T^{miss}$ in the event (for example, dead calorimeter cells or gaps in the acceptance of the detector). The transverse mass of the W is given by Equation 5.2. In this equation E_T^ℓ and E_T^{miss} are the transverse energies of the observed lepton and "non-observed" energy respectively and $\mathbf{p}_T^\ell$ and $\mathbf{p}_T^{miss}$ the corresponding momentum two-vectors. The quantity E_T^{miss} is referred to as "missing transverse energy".

$$m_{T,W}^2 = 2(E_T^\ell E_T^{miss} - \mathbf{p}_T^\ell.\mathbf{p}_T^{miss}) \tag{5.2}$$

The transverse mass of the W has the property that,

$$m_{T,W}^2 \leq m_W^2. \tag{5.3}$$

It is therefore clear that on an event by event basis no W mass measurement is possible, but that looking at very many events should produce an upper bound on the W mass.

These two variables were used by ATLAS to reconstruct its first W and Z bosons (a couple of months apart, shortly after $\sqrt{s} = 7$ TeV collisions commenced in March 2010).

In the early 1990s, the e^+e^- colliders LEP and SLC measured the properties of the Z in great detail [83]. Then followed the first observations of the production of W bosons in pairs. The Tevatron has been accumulating W and Z bosons for many years. The consequence of the hard work of all these collaborations is very detailed information on the masses, widths and couplings of the W and Z, understanding of their production in proton-antiproton collisions and constraints on the proton parton density functions [84]. Existing knowledge will be vital for measurements of detector performance. The well measured Z width couplings should allow observed Zs in ATLAS to be used to determine reconstruction efficiencies and energy resolutions. The LHC is expected to produce W and Z bosons in abundance, benefitting from existing precision measurements, but also being able to make its own.

5.2 Candidate $Z \to e^+e^-$ Decays in the First 220 nb^{-1} of $\sqrt{s} = 7$ TeV Data

This chapter details the observation of 46 $Z \to e^+e^-$ candidates from a $\sqrt{s} = 7$ TeV data sample collected between March and July 2010 with an integrated luminosity of $\sim$220 nb^{-1}. The systematic uncertainty on this luminosity estimate is 11% [57].

In this chapter the observed Z bosons are compared to expectations based on Monte Carlo simulations. These Monte Carlo samples are detailed in Table 5.1, all were generated at $\sqrt{s} = 7$ TeV using the `PYTHIA` [74] Monte Carlo generator, the `MRSTLO` [80] parton distribution functions, simulated with `GEANT4` [75] and passed through a full simulation of the ATLAS detector by the central production teams. The quoted cross-sections $\times$ branching ratios for $W \to \ell\nu$ and $Z/\gamma^* \to \ell\ell$ are those calculated at next-to-next-to-leading order (NNLO) in QCD corrections by the ATLAS collaboration using the `FEWZ`

Monte Carlo Sample (relevant filter)	Cross-section × branching ratio (nb)	Luminosity (nb^{-1})
$Z \to e^+e^-$ ($m_{\ell\ell} > 60$ GeV)	0.989	4.8×10^6
$Z \to \mu^+\mu^-$ ($m_{\ell\ell} > 60$ GeV)	0.989	5.1×10^6
$Z \to \tau^+\tau^-$ ($m_{\ell\ell} > 60$ GeV)	0.989	2.0×10^6
$W \to e\nu$	10.45	6.7×10^5
$W \to \mu\nu$	10.45	6.7×10^5
$W \to \tau\nu \to \ell\nu\nu$ ($\ell = \mu, e$)	3.68	3.1×10^5
$t\bar{t}$ (semi-leptonic)	0.16	2.5×10^6
dijets ($p_T > 15$ GeV)	1.15×10^6	100

Table 5.1: *Signal and background Monte Carlo samples used in this chapter. Details are given of any relevant filters applied to the Monte Carlo, of the cross-section × branching ratio of each and of the integrated luminosity of each sample. Each sample was weighted to the luminosity of the data according to the cross-sections and luminosities listed in this table. The dijet samples were generated with a transverse momentum of the hard-scatter, p_T, greater than* 15 GeV. *Cross-sections for W and Z processes are quoted at next-to-next-to-leading order, whilst $t\bar{t}$ is only quoted at next-to-leading order (plus next-to-next-to-leading-log) and dijet processes with cross-sections to only leading order.*

program [85] with the `MSTW2008` parton distribution function set [84], and $m_{\ell\ell}$ of the $Z/\gamma^* \to \ell\ell$ decay is picked to be greater than 60 GeV. The uncertainty on these NNLO cross-sections is expected to be 3% (including factorisation and renormalisation scale, and parton distribution function uncertainties) [86–88]. All figures in this chapter are normalised to these cross-sections and luminosity.

The $\sqrt{s} = 7$ TeV event sample in this chapter consists only of data collected during times at which the LHC declared beams stable and the detector ready for collisions. Events were selected for which the tracker, electromagnetic calorimeter and hadronic calorimeters recorded data with high quality and the solenoidal field was at nominal magnetic field. This requirement ensures that the response and main criteria needed for the identification of electron candidates (see Chapter 4), and the energy and momentum computations do not deviate significantly from expectation. The events used were triggered with the Level 1 Calorimeter Trigger at a transverse energy threshold of 10 GeV (see Appendix A). Candidate events must also have at least one primary vertex with at least three tracks, and this primary vertex must be consistent with the

position of the beam spot. Electrons are selected offline with a cluster transverse energy, $E_T^{cl} > 20$ GeV and must pass medium selection criteria (see Chapter 4). These electrons must also satisfy $|\eta^{cl}| < 2.47$, and not fall within the transition region between the barrel and end-cap calorimeters ($1.37 < |\eta^{cl}| < 1.52$). The η^{cl} referred to here is the cluster η, a weighted pseudorapidity taking into account the recorded η in both the strip and middle layers of the electromagnetic calorimeters. At the time of observation, the reconstruction efficiency was expected (from Monte Carlo) to be 90% for true electrons, and the rejection against background jets passing this E_T^{cl} threshold estimated to be $\sim$6800 (see Table 4.2). Additional requirements are made on the expected quality of energy reconstruction in the liquid argon calorimeter in the vicinity of the electron candidates. Problematic regions of the calorimeter include: (i) regions affected by major high-voltage problems, (ii) regions affected by electronic front-end boards which do not provide an output signal and (iii) noisy isolated cells and cells producing no signal at all. Any candidates within a 3×3 (cells in $\Delta\eta \times \Delta\phi$ space) region surrounding a bad cell in the middle layer are rejected, as are any candidates which fall within a 3×7 region in the barrel or 5×5 region in the end-cap around a dead front-end board in either the presampler, strip layer or middle layer. Any events containing an electron rejected because of its cluster being near to such a region are rejected (to remove ambiguity from the analysis). A loss of acceptance of approximately 13% results from this requirement [4].

The candidate Z bosons are formed from the selected events by looking for electron-positron pairs in the events (events with more than two selected electrons are dismissed, but it is noted that no such tri-lepton or multi-lepton events were found in the sample). This selection gives a total of 51 e^+e^- pairs (where both electrons in the pair are medium and pass the $E_T^{cl} > 20$ GeV requirement). Of these 46 lie in the invariant mass range $66 < m_{e^+e^-} < 116$ GeV. The invariant mass of the pair, $m_{e^+e^-}$, is calculated from the two lepton four-momentum vectors. The four-momentum of each lepton is constructed from the well measured cluster energy, η_{tr} and ϕ_{tr} of the track, and a cluster $E_T^{cl'}$ formed from the cluster energy (E^{cl}) and η_{tr} (in contrast to the E_T^{cl} used to select the electron candidates). The triggered sample contained a total of $\sim 4 \times 10^6$ events. Of the backgrounds detailed, the main backgrounds to the observation of $Z \to e^+e^-$ are $Z \to \tau\tau$, $W \to e\nu$ and $t\bar{t}$ (though after selection, these are expected to make up just one-hundredth of the events observed).

The dijet background can be estimated using dijet Monte Carlo pairs for which both candidates satisfy the loose electron identification requirements (see Chapter 4), in the appropriate mass range, and data-derived loose to medium rejections for electrons (with $|\eta^{cl}| < 2.5$). The method to be applied is thus partially data-driven. The ratio of medium to loose electrons with $p_T > 20$ GeV, reconstructed using the standard electron algorithm and within the η acceptance of the detector is measured in data to be $0.15 \pm 0.01(stat.)$. The central loose to medium rejection, quoted here as its reciprocal, is consistent at the one-sigma level with the rejection measured from electrons in the dijet Monte Carlo, $0.14 \pm 0.01(stat.)$. In the region, $66 < m_{e^+e^-} < 116$ GeV, Monte Carlo predicts $14.2 \pm 3.4(stat.)$ QCD background events in the opposite-charge invariant mass distribution for loose lepton pairs. By applying the data-derived rejection factors to each electron in these pairs, a background estimate of $0.31 \pm 0.07(stat.) \pm 0.05(sys.)$ events in the opposite-charge distribution in the Z mass window is obtained. In the $66 < m_{e^+e^-} < 116$ GeV mass window the remaining sources of background ($W \to e\nu$: 0.06 events and $t\bar{t}$: 0.08 events in Monte Carlo) are expected to be a flat function of invariant mass. The background from $Z \to \tau\tau$ (0.04 events in Monte Carlo) drops off sharply as a function of invariant mass. These estimates give a total predicted background of $0.49 \pm 0.07(stat.) \pm 0.05(sys.)$ events.

In Figure 5.1(a) the E_T^{cl} of the electrons in the 46 data pairs are illustrated (electron and positrons combined in the same plot), with the pairs reconstructed in Monte Carlo. The agreement between data and Monte Carlo is reasonable. The two high E_T^{cl} electrons in the tail of the distribution are consistent with the integral of the expected number of events in the tail. The Monte Carlo is broken down into the dominant components: *(i)* $Z \to ee$, *(ii)* $Z \to \tau\tau$, *(iii)* $W \to e\nu$ and *(iv)* $t\bar{t}$. Given the small background expected from jet fakes in the medium channel, it is difficult to produce sufficient Monte Carlo to give a direct estimate of the QCD background. QCD Monte Carlo is therefore omitted from all the figures in this chapter. The remaining unillustrated backgrounds are all below the 10^{-3} level and the display of all backgrounds is suppressed in Figures 5.1(b) and 5.2. The transverse momentum, p_T^Z, of the 46 reconstructed and selected Z candidates is illustrated in Figure 5.1(b). The apparent high tail in the data p_T^Z distribution is not statistically significant (the Monte Carlo predicts 2.8 events with $p_T^Z > 60$ GeV). The invariant masses of the selected Z candidates are illustrated in Figure 5.2. These candidates give an invariant mass peak consistent with a Z invariant mass peak. There is only one same-sign di-electron pair in the wide invariant mass selection window used to make the opposite-sign di-electron pair observation. The Monte Carlo invariant mass

distribution in Figure 5.2 has not been normalised to data. As demonstrated in Chapter 4, a few of the variables used in the identification and reconstruction of electron candidates exhibit some discrepancies between data and Monte Carlo. The cuts used to identify the candidates here use the cuts on the variables optimised on Monte Carlo. The efficiency in data is therefore slightly lower than that anticipated in Monte Carlo. This expected discrepancy in reconstruction efficiencies between data and Monte Carlo is apparent in this figure, where no attempt to correct for this effect has been made. With a significant increase in the number of Z bosons observed, it will be possible to use them to make quantitative estimates of the electron reconstruction efficiency[1].

[1]This observation was made mid-2010. At the time of writing, mid-2011, "tag-and-probe" studies of some thousands of Z candidates have provided p_T and η dependent electron reconstruction efficiencies.

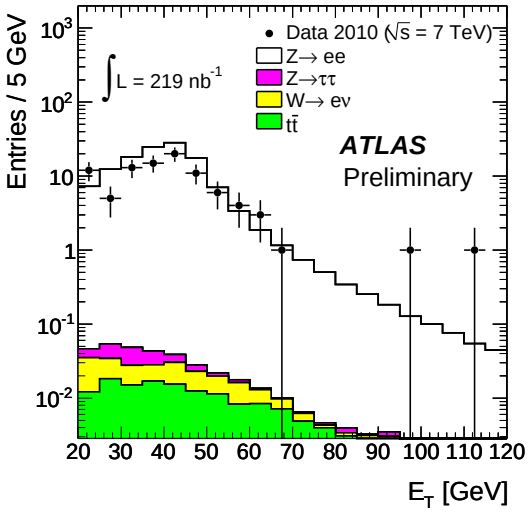

(a)

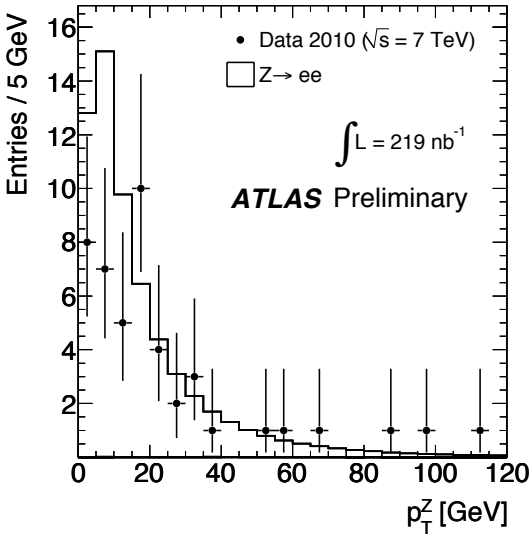

(b)

Figure 5.1: *Cluster E_T of electrons from reconstructed and selected $Z \to e^+e^-$ decays (a), and Z p_T (b). The E_T distribution begins to tail off in data at* $\sim$60 GeV *(much higher than in the low luminosity* $\sqrt{s} = 7$ TeV *sample of electron candidates in Chapter 4). Selected refers to the* $m_{e^+e^-}$ *of these candidates lying in the range* $66 < m_{e^+e^-} < 116$ GeV*. The one same-sign pair with* m_{ee} *in this range is not included in this figure. The apparent high tail in the data* p_T^Z *distribution (b) is not statistically significant (the integral in the tail above* 60 GeV *in the Monte Carlo is* 2.8 *events). The error bars on data in both distributions are statistical and correspond to* 68% *confidence intervals.*

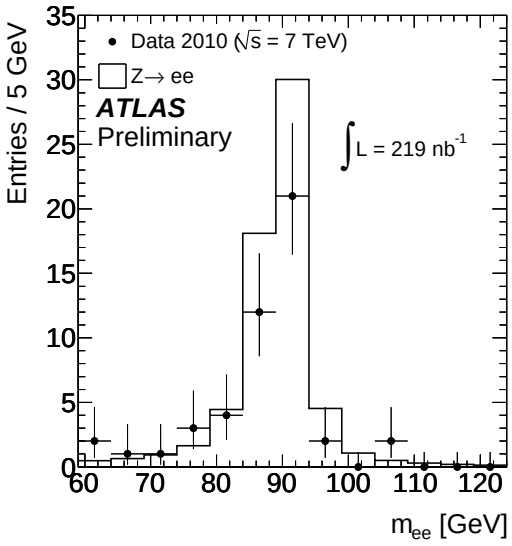

Figure 5.2: *The invariant mass distribution of the forty-six selected $Z \to e^+e^-$ events. In this figure the Monte Carlo is not normalised to data. The expected discrepancy in normalisation between observation and simulation arises from differences in efficiency between data and Monte Carlo. The differing efficiencies must account for the bulk of the normalisation difference, the uncertainty on the luminosity* (11%) *is not sufficient to explain it. The error bars on the data are statistical and correspond to* 68% *confidence intervals.*

5.3 Beyond 220 nb^{-1}

It is the hope that the continued observation and measurement of the W and Z bosons by ATLAS will provide new insights, tests of perturbative QCD calculations and precision measurement of W boson mass. It is expected that the well known Z will provide significant constraints on the performance of the CMS and ATLAS collider experiments at the LHC, exploiting detailed knowledge of its mass, width and leptonic decays. This includes constraints on detector energy, momentum scale, resolution, lepton identification, efficiency and triggers.

Chapter 6

Search for Supersymmetry in Events with Identical-Flavour Leptons

"'Curiouser and curiouser!' cried Alice."

— Lewis Carroll, Alice's Adventures in Wonderland (1865), ch. 2

This chapter details a search for supersymmetry in events with exactly two leptons and high missing transverse energy[1] in the full ATLAS 2010 $\sqrt{s} = 7$ TeV dataset. In particular, in this chapter, an excess of lepton-pairs with identical-flavour (e or μ) leptons over pairs with different-flavour leptons (beyond the standard model prediction) in these events is sought. This so-called "flavour subtraction" [89] analysis looks for decay chains in supersymmetric events which can only produce lepton-pairs with identical-flavour leptons. For instance, events containing the decay chains $\tilde{\chi}_2^0 \to \tilde{\ell}^{\mp}\ell^{\pm} \to \tilde{\chi}_1^0\ell^{\mp}\ell^{\pm}$ or $\tilde{\chi}_2^0 \to \tilde{\chi}_1^0\ell^{\pm}\ell^{\mp}$ are amongst those targeted by this search, whilst events in which the two leptons are produced by independent sparticle cascades are of lesser interest.

As already noted in the preface, this work, though the work of the author, was produced as part of a collaboration-wide analysis of two-lepton events in the 34.3 pb^{-1} $\sqrt{s} = 7$ TeV 2010 dataset[2]. Thus, this analysis makes use of partially data-driven background estimations obtained by other members of the collaboration for an inclusive anal-

[1] Missing transverse energy (E_T^{miss}) was introduced in Section 5.1.

[2] During the entire $\sqrt{s} = 7$ TeV 2010 data run, ATLAS recorded an integrated luminosity of 45 pb^{-1}. The total integrated luminosity of the data sample which passes requirements on the quality of the data, and the conditions of the beam and experiment is 34.3 pb^{-1}.

ysis of two-lepton events in this dataset [6, 7]. These partially data-driven background estimates and their uncertainties are used in tandem with additional Monte-Carlo-only background estimates, when setting limits. The setting of these limits, and use of these estimates in the context of a flavour subtraction, is solely the work of the author. It will be made clear in the text of this chapter which these estimates are, and when they are used.

The flavour subtraction analysis described in this chapter is one of the very first ATLAS searches for supersymmetry using events with lepton-pairs in data, Ref. [8]. There are two such first searches by the ATLAS experiment, the work in this chapter also contributing to the other, Ref. [6].

6.1 Motivation

If supersymmetric cascade decays are produced by collisions at the LHC then one potential way of searching for them is by looking for the presence of high missing transverse energy final states (arising from the production of un-detected neutralinos). High squark and gluino production cross-sections would give rise to energetic jets in the final states. Sparticle cascades are characterised not just by this high missing transverse energy and these energetic jets, but also by the presence of leptons. In supersymmetry, these leptons can be produced by slepton, gaugino or electroweak gauge boson decays. Supersymmetric particle cascade decays can give rise to events with identical-flavour lepton-pairs, with no corresponding different-flavour lepton-pair events. In this chapter a search is made for an excess, beyond that predicted by the standard model, of events with identical-flavour lepton-pairs and significant missing transverse energy. In this flavour subtraction analysis, backgrounds which possess equal branching ratios for the production of lepton-pairs of identical and different-flavour are "removed" by subtracting the number of observed different-flavour lepton-pairs, from the number of observed identical-flavour lepton-pairs.

The dominant standard model backgrounds to a two-lepton search in events with high missing transverse energy are generally ones for which the branching ratios for decays to identical-flavour lepton-pairs equal the branching ratios for decays to different-flavour lepton-pairs. Most notably this includes $t\bar{t}$ production. This dominates two-lepton searches and its estimation using data-driven approaches is generally made difficult by

the need to kinematically reconstruct the $t\bar{t}$ events to obtain a relatively clean control region. Flavour "asymmetric" backgrounds, which produce identical-flavour lepton-pairs and rarely different-flavour lepton-pairs, include Z/γ^*+jets events and WZ pair production events. The latter has a low cross-section, whilst the former is heavily suppressed by the requirement of high missing transverse energy. Therefore, the dominant background is one which naturally cancels in a flavour subtraction analysis. As well as benefitting from reduced backgrounds through this cancellation, the systematics associated with a search for an identical-flavour excess are small.

Identical-flavour lepton-pair events are expected to be of great utility for measuring the masses of supersymmetric particles. If an excess, beyond the excess predicted by the standard model, of identical-flavour lepton-pair events was discovered, mass measurements could be made through the end-points of various lepton-pair (with and without jet) invariant mass distributions formed from the leptons and jets in these events [56, 89–91]. The interest and usefulness of these channels and the flavour subtraction technique is, therefore, very likely to scale with luminosity.

This chapter will begin with a simple observation of the number of two-lepton events in data, which will be divided into six distinct categories based on the charge and flavour of the leptons in the pair. These observations will be compared with expectations based on Monte Carlo simulations. Various kinematic properties of the events will be illustrated for data and simulation. The methods used to quantify the identical-flavour excess in data, and set a limit on the identical-flavour excess from supersymmetry, will then be introduced. The Monte Carlo expectations, and data-driven estimations obtained from Ref. [7] will be used to predict the expected distribution of the identical-flavour excess in data. In this procedure the expected numbers of events in each channel will be needed not just to predict the mean expected excess, but also to predict the width of the expected distribution of identical-flavour excesses for a large number of hypothetical pseudo-experiments.

6.2 Signals

In this chapter model-independent limits are set on the mean excess of identical-flavour events from supersymmetric processes. The data are then used to exclude regions of

the parameter spaces of two specific supersymmetric model frameworks. Results are interpreted for model points from: (i) the mSUGRA/constrained MSSM framework (see Section 2.3.5), for comparison with previous experimental searches and (ii) a "5D-phenomenological grid", cast in a more general 24-parameter generic MSSM. In models for which R-parity is conserved, both high missing transverse energy and the presence of many high-p_T jets in the final state are generic model characteristics. The rate of lepton production is strongly model dependent. The signal points considered throughout this chapter were produced by the ATLAS collaboration, and the 5D-phenomenological grid devised by the collaboration, to give an appropriate grid in which to interpret multi-lepton searches for supersymmetry.

Within the mSUGRA/CMSSM framework, results are interpreted in the $m_0 - m_{1/2}$ plane[3] for a slice through this parameter space where $\tan\beta = 3$, $A_0 = 0$ and $\mu > 0$. At hadron colliders, the phenomenology is mostly dependent on m_0 and $m_{1/2}$, and so most searches for supersymmetry report their results in an $m_0 - m_{1/2}$ plane for fixed values of $\tan\beta$ and A. At the time of this search, the best mSUGRA sensitivity was that given by the Tevatron DØ tri-lepton search [92], one carried out in the same two-dimensional "slice" through the mSUGRA parameter space. The mSUGRA slice in $m_0 - m_{1/2}$ is spanned by 200 grid points[4] in the range $40 < m_0 < 1160$ GeV and $100 < m_{1/2} < 340$ GeV. A cluster of an additional 80 points in the region of this slice where $m_{\tilde{\chi}_2^0} \approx m_{\tilde{\ell}}$, which was not-excluded by the DØ tri-lepton search ($70 < m_0 < 140$ GeV and $160 < m_{1/2} < 240$ GeV), is also included.

In the MSSM 24-parameter model, the following parameters are fixed: $m_A = 1000$ GeV, $\mu = 1.5m$ (where m is the minimum of the gluino and squark masses), $\tan\beta = 4$, $A_t = \mu/\tan\beta$, $A_b = \mu\tan\beta$ and $A_\ell = \mu\tan\beta$ (where A_t, A_b and A_ℓ are the soft-breaking tri-linear couplings). These parameter choices reduce complications in the decay chain from heavy-flavour decays and give no left-right mixing. The chosen value of m_A serves to remove heavy higgs particles from the squark and gluino decay chains. The 3^{rd} generation sfermions are given masses of 2 TeV, whilst the 1^{st} and 2^{nd} generation squarks and sleptons are assumed to share common mass parameters. Consequently, the three gaug-

[3] As introduced in Section 2.3.5, m_0 and $m_{1/2}$ are the masses of the supersymmetric scalars and fermions at the scale of supersymmetry breaking, and $\tan\beta$ the ratio of vacuum expectations values of the two Higgs doublets in the model. The parameter A is the common tri-linear term and the sign of μ the higgsino mass term.

[4] A top mass of 172.5 GeV was picked by the ATLAS collaboration for all calculations when producing these signal points.

ino masses, the common squark mass and the common slepton mass remain as the free parameters in this 5D-phenomenological grid. The choice of mass hierarchy and μ ensure that $\tilde{\chi}_1^0$ is pure bino and $\tilde{\chi}_2^0$ is pure gaugino. The branching ratios for $\tilde{q}_L$ decay to $\tilde{\chi}_2^0$ and $\tilde{\chi}_1^+$ decay are 30% and 60% respectively. The $\tilde{q}_R$ decays always into $\tilde{\chi}_1^0$. Two grids with points satisfying these criteria are used: (a) PhenoGrid2 and (b) PhenoGrid3. In both cases for each pairing of squark and gluino mass, a favourable point and a less favourable point are conceived (a favourable point being one which is more likely to be observable). In PhenoGrid2, the less favourable case, a "compressed spectrum", arises from choosing $m_{\tilde{\chi}_2^0} = m - 50$ GeV, $m_{\tilde{\chi}_1^0} = m - 150$ GeV and $m_{\tilde{\ell}_L} = m - 100$ GeV. The more favourable "light LSP spectrum" is formed from points satisfying $m_{\tilde{\chi}_2^0} = m - 100$ GeV, $m_{\tilde{\chi}_1^0} = 100$ GeV and $m_{\tilde{\ell}_L} = m/2$ GeV. In PhenoGrid3, $m_{\tilde{\ell}_R}$ and $m_{\tilde{q}_R}$ are set to 2000 GeV, to boost the fraction of two-lepton events. Once again, for each squark and gluino mass in this grid, two points are produced for the compressed spectrum and the light LSP spectrum (satisfying the same hierarchies as set out for PhenoGrid2). The p_T of the leptons produced by decays in these grids is influenced by the mass difference between the $\tilde{\chi}_2^0/\tilde{\chi}_1^\pm$ and $\tilde{\ell}$ particles, and also the difference between the $\tilde{\chi}_1^0$ and $\tilde{\ell}$ masses. In both the compressed spectrum and light LSP grids the minimum mass difference is 50 GeV, but the maximum differences are 50 GeV and 200 GeV respectively. In the compressed spectrum the final state kinematics are soft, whereas in the light LSP scenario the spectrum of leptons (jets and E_T^{miss}) is harder. PhenoGrids 2 and 3 contain 72 points each, divided equally into points from the compressed spectrum and points from the light LSP spectrum. These grid points span the mass ranges $300 < m_{\tilde{g}} < 800$ GeV and $300 < m_{\tilde{q}} < 800$ GeV. Note that in PhenoGrid3 the number of kinematically allowed decay chains is limited.

Additionally, this chapter will refer by name to points "MSSMxx" and SU4 as illustrative individual model points. SU4 is an mSUGRA/CMSSM benchmark point chosen for its proximity to the Tevatron bound and its inclusion in the region for which 2010 data analyses are expected to be sensitive. The SU4 point has the mSUGRA parameters: $m_0 = 200$ GeV, $m_{1/2} = 600$ GeV, $A = -400$ GeV, $\tan\beta = 10$ and $\mu > 0$. The MSSMxx benchmark points are taken from the MSSM 24-parameter model. Each benchmark point has the same squark and gluino masses (400 GeV and 420 GeV respectively). The masses of the remaining free parameters are specified in Table 6.1.

	$m_{\tilde{g}}$	$m_{\tilde{q}}$	$m_{\tilde{\chi}_2^0}$	$m_{\tilde{\ell}}$	$m_{\tilde{\chi}_1^0}$
MSSM22	420	400	200	150	100
MSSM27	420	400	350	200	100
MSSM29	420	400	350	300	250

Table 6.1: *Benchmark points in the MSSM 24-parameter model. Each benchmark point is chosen to have a gluino mass of* 420 GeV *and a squark mass of* 400 GeV*. All masses are in units of* GeV*.*

6.3 Event Samples

6.3.1 Data

The data used in this analysis were collected between 24th June 2010, and the end of $\sqrt{s} = 7$ TeV running in late October 2010. These data correspond to the ATLAS data-taking periods "E" through to "I"[5]. Not all of the events in these five data-taking periods are analysed. Only those for which the LHC declared stable beams and the ATLAS detector was at nominal high voltage are considered. Additionally, the solenoid and toroid fields were required to be both on and nominal (for good muon and electron momentum measurements). The sub-detectors were also required to be recording data with good quality so that the electron, muon and jet identification and reconstruction algorithms can be relied upon to be giving results which do not deviate significantly from expectation. The total integrated luminosity of the data analysed is $\int \mathcal{L}\mathrm{dt} = 34.3$ pb^{-1}. Table 6.2 lists the luminosity of each data-taking period. In this search events are taken from both the `Egamma` and `Muon` streams.

6.3.2 Monte Carlo

All Monte Carlo samples used in this analysis were produced by the ATLAS central production teams. QCD dijet, heavy flavour and Drell-Yan di-lepton events were generated using `PYTHIA`[74], with the `MRST2007LO*` modified leading-order (LO) parton distribution

[5]The $\sqrt{s} = 7$ TeV data analysed in Chapters 4 and 5 are from data-taking period "A". In total the periods "A" through to "D" correspond to only 300 nb^{-1} of integrated luminosity and so comprise a luminosity less than 1% of that considered. These data are not analysed in this study (they correspond to data taken during a time when the trigger menu was rather different, and there was little pile-up) but would result in no further signal events.

Period	Run Numbers	$\int \mathcal{L}\mathrm{dt}$ (pb^{-1})
E	160387–161946	0.9
F	162347–162882	1.7
G	165591–166383	5.7
H	166466–166964	7.1
I	167575–167844	19.0
Total		34.3

Table 6.2: *The data-taking periods analysed in this chapter, with the integrated luminosity, $\int \mathcal{L}dt$, recorded in each after requirements on the quality of the data, and the experiment and collider conditions, have been imposed. In total,* 34.3 pb^{-1} *of integrated luminosity is analysed, the majority of which is from the data-taking period I.*

functions. Top quark pair-production and single top-quark production was simulated with `MC@NLO` [93–95], using the `CTEQ66` next-to-leading (NLO) parton distribution functions [96]. Samples of $W \to \ell\nu$+jets and $Z \to \ell\ell$+jets events were both produced in slices of the number of partons in the hard scattering process. These were generated at $\sqrt{s} = 7$ TeV using the `ALPGEN` [97] generator with the `CTEQ6L1` [98] parton distribution functions. Diboson events (WW, WZ and ZZ) were generated using `HERWIG` [73]. Fragmentation and hadronization for the `ALPGEN` and `MC@NLO` samples was performed with `HERWIG` [73], using `Jimmy` [99] for the underlying event model. Monte Carlo signal events were generated with `HERWIG++` [100]. A generator level filter on the invariant mass of the truth lepton-pair produced in the Drell-Yan events was used to remove any overlap between the `PYTHIA` Drell-Yan events and the `ALPGEN` $Z \to \ell\ell$+jets events. The supersymmetric particle spectra are calculated with `ISAJET` [101]. All Monte Carlo samples were produced using the ATLAS `mc09` parameter tune [79] and passed through a full `GEANT4` [75] simulation of the ATLAS detector. The signal samples are normalised using NLO cross-sections determined by members of the collaboration using `PROSPINO` [102], by hard-process. The top pair-production cross-section calculated at NNLO precision, 160 pb [103], is used, whilst the cross-sections for single-top ($s-$channel $t-$channel and $Wt-$channel) at NNLO precision: 0.47 pb, 7.0 pb, and 13.0 pb respectively, are used. The Z/γ^*+jets and W+jets cross-sections at NNLO are 1.07 nb [85] and 31.4 nb [104, 105] respectively, and those used in this analysis. At NLO, the diboson cross-sections are: 44.9 pb (WW), 18.0 pb (WZ) and 6.0 pb (ZZ) [106], again these are used in this study. The QCD and Drell-Yan samples are normalised to cross-sections at LO, as returned by `PYTHIA`.

In $\sqrt{s} = 7$ TeV data, in addition to the hard-scattering interaction, there are typically between one and three soft-scattering interactions. The majority of the Monte Carlo samples used in this study were generated with on average two primary interactions per event. The resulting distribution of additional good vertices for these events is Poisson distributed with a mean of one. The number of good primary vertices (defined as vertices associated with at least five tracks) for $\sqrt{s} = 7$ TeV data is illustrated in Figure 6.1(a) (black marker points), where it is compared with the distribution in Monte Carlo (red marker points). As expected the two distributions are very different[6]. The discrepancy between data and Monte Carlo is corrected for by re-weighting the primary vertex multiplicity distribution in Monte Carlo, to match that in data. In Figure 6.1(b) the necessary weights, as a function of the number of good primary vertices, are illustrated. After applying these weights, the resulting Monte Carlo good vertex distribution will, by construction, identically match the data[7]. For Monte Carlo samples generated with only one primary interaction vertex (the diboson and low-mass Drell-Yan samples), no pile-up weights are applied.

6.4 Object Definitions

Electrons reconstructed by the standard ATLAS electron reconstruction algorithms are selected if they satisfy medium electron identification requirements (see Chapter 4), have $p_T > 20$ GeV and $|\eta^{cl}| < 2.47$. Events are vetoed if any selected electron is found in the transition region of the electromagnetic calorimeter ($1.37 < |\eta^{cl}| < 1.52$). If any electron falls near a region of the detector with noisy or dead cells, high voltage or problematic front-end boards (as detailed in Chapter 5), then it is rejected. When, in the analysis, electrons are further required to be tight, this refers to the requirement that the electrons pass the tight electron identification requirements. When electrons are also required to be isolated, this refers to the requirement that the total transverse energy in a ΔR cone of 0.20 around the electron is less than 0.15 of the electron's p_T (calorimeter isolation). In the object definitions, electrons are required to be neither

[6]The Monte Carlo distributions illustrated, and thus the Monte Carlo events used to derive suitable weights to correct for the differences between data and Monte Carlo, are the events in both data and Monte Carlo which pass all but the $m_{\ell\ell}$ event selection criteria (see Section 6.6.2).

[7]After pile-up re-weighting a further weight correction is applied to each sample to restore the cross-sections to their original values. This additional re-weighting is necessary because the primary vertex distributions are not *exactly* identical for each sample (due to finite and limited statistics), and so the weights based on all the Monte Carlo may not precisely conserve each sample's cross-section. These additional weights do not deviate significantly from 1.

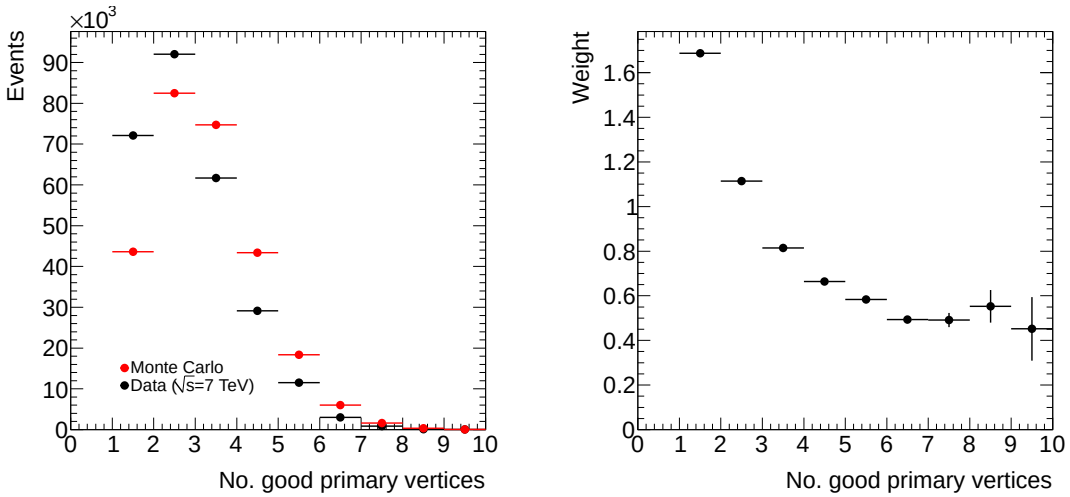

(a) (b)

Figure 6.1: *Re-weighting Monte Carlo to account for pile-up. The number of Monte Carlo (red) events and data (black) events as a function of the number of good primary vertices (defined as vertices associated with at least five tracks), before pile-up re-weighting (a). In this figure data is normalised to Monte Carlo. The weights applied to Monte Carlo to match the Monte Carlo distribution to the data (b).*

tight nor isolated. These two requirements are imposed after initial object selection and overlap removal but during later analysis.

Muons must be identified either in both the ID and MS systems (combined muons), or as a match between an extrapolated ID track and one or more segments in the MS. They must have $p_T > 20$ GeV and $|\eta| < 2.4$. The ID tracks must have a least one pixel hit, more than five SCT hits, and a number of TRT hits which varies as a function of η. Any selected combined muon must have a good match between ID and MS tracks, with the p_T measured by each system compatible with the resolution. The selected muons must be isolated with the total p_T in a cone of size 0.2 less than 1.8 GeV. In order to veto against cosmic muons, the distance between the z coordinate of the primary vertex and that of the extrapolated muon track at the point of closest approach to the primary vertex, $|z_\mu - z_{PV}|$, must be less than 10 mm.

Jets are reconstructed using the anti-k_T jet clustering algorithm [107] with a radius parameter, $R = 0.4$. Clusters of calorimeter cells, seeded by cells with energy significantly above the measured noise, are used as the input to this algorithm. Each cluster is treated as an $(E, \vec{p})$ four-vector with zero-mass, and the jet constructed as the four vector sum over these. The energy is first measured at the electromagnetic scale before the non-compensation of the calorimeter, upstream material and other effects are corrected for using p_T and η dependent calibration factors [108]. Jets are required to have $p_T > 20$ GeV and $|\eta| < 2.5$. If a jet and a selected medium electron are found within a distance $\Delta R < 0.2$ of one another, the jet is discarded. Furthermore, identified muons and medium electrons are discarded if they lie within a distance $\Delta R < 0.4$ of any remaining jet.

Missing transverse energy is calculated as the modulus of the vectorial sum of the p_T of all reconstructed objects (for jets this includes all jets with $p_T > 20$ GeV, but which lie within the full η coverage of the detector). To this vectorial sum, non-isolated muons and calorimeter clusters (built from cells significantly above noise thresholds) not belonging to reconstructed objects are added.

6.5 Estimation of Systematic Errors

Whilst a flavour subtraction analysis is only weakly sensitive to systematics, these are still taken into account. The uncertainty on the luminosity is taken to be 11% [57]. Uncertainties on the cross-section of 5% have been assumed for the Drell-Yan, Z/γ^*+jets, W+jets and diboson samples (consistent with the quoted uncertainties on these cross-sections in Refs. [85, 104–106]), with 100% uncertainty assigned to the dijet and heavy flavour QCD samples[8]. An uncertainty on the cross-section for $t\bar{t}$ of $^{+7\%}_{-9\%}$ is assigned, based on Refs. [109, 110].

Additionally, uncertainties on the scale and resolutions of the jets, electrons and muons in the events are considered. Uncertainties on the jet energy scale and jet energy resolution of $\sim \pm 7\%$ [111] and $\sim 14\%$ [112] respectively are assumed. In both cases these uncertainties are not flat in p_T and η. For the jet energy scale, the uncertainty is parameterised as a function of both p_T and η. When exploring uncertainties in the jet energy resolution, each jet is smeared according to a Gaussian distribution, with unit mean, and a width, sigma, a function of jet p_T. Electron scale and resolution, and muon resolution uncertainties are also considered. For the electron scale, a 3% uncertainty is applied for both upwards and downwards uncertainty on the scale to all electrons (regardless of their p_T and η). The electron resolution uncertainty is explored using a Gaussian with both p_T and η dependent sigma. The Gaussian uses an uncertainty on the electron resolution from the sampling term of 20%, and an uncertainty on the constant term of 100% in the barrel and 400% in the end-cap. The asymmetric resolution uncertainties applied to the MS and ID (extrapolated) components of the (combined) muon momentum are small and as described in Ref. [113].

A conservative uncertainty for the parton distribution functions of 5% is applied. Generated events are re-weighted according to Bjorken-x values of the interacting partons from the production process, and its scale Q^2 as given by the appropriate parton distribution function of the Monte Carlo, and those of the `CTEQ66` central NLO error set. The full set of eigenvectors of `CTEQ66` are considered and the errors combined according

[8]This uncertainty is motivated as an uncertainty on the fake-rate for QCD. Re-normalising each of these samples to match the data in a suitable control-region would require different scaling factors for each type of lepton-flavour pair. These scaling factors would be $\mathcal{O}(0.5)$. The QCD Monte Carlo samples are only used to produce illustrative figures, so this very conservative uncertainty simply provides a visual aid when looking at histograms of event variables.

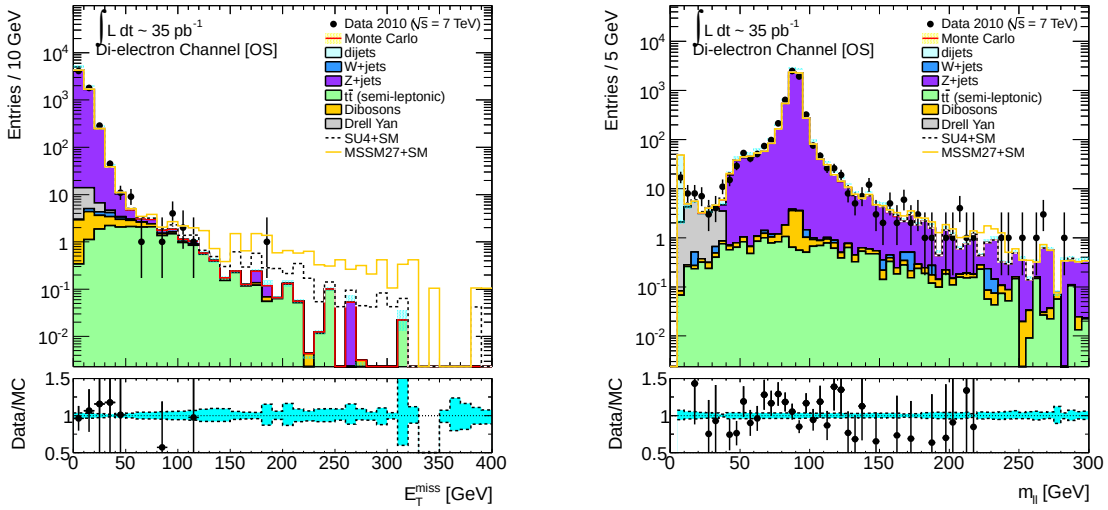

(a) (b)

Figure 6.2: *Parton distribution function uncertainties on E_T^{miss} (a) and $m_{\ell\ell}$ (b) for opposite-sign electron-pairs. A conservative uncertainty statistic of* 5% *could be applied based on these distributions. Errors on data points are* 68% *Poisson confidence limits and the error band on Monte Carlo is purely that given by parton distribution function re-weighting.*

to the "Master Equation" in Ref. [84]. This gives an estimate of the spread of NLO predictions, and an upper and lower uncertainty on the `CTEQ66` prediction. Figure 6.2 shows the effect of this procedure on example experimental distributions. In this figure the variation on the E_T^{miss} of selected electron-pair events and the $m_{\ell\ell}$ of opposite-sign electron-pairs, due to the parton distribution function re-weighting procedure, is illustrated by the cyan uncertainty band. The conservative error of $\sim$5% is assigned based on these figures. This parton distribution function uncertainty will be found to be a negligible error compared to those on the jet energy resolution and scale, and the statistical uncertainty.

Data-taking Period	Level 1 Item	Level 2 Trigger	Event Filter Trigger
E	L1_EM10	L2_g17_etcut	EF_g17_etcut
F-I	L1_EM10	L2_e15_medium	EF_e15_medium

Table 6.3: *Trigger chains and their corresponding L1, L2 and EF trigger items used for the different data-taking periods in this analysis. The electron triggers selected are all un-prescaled for the data-taking period in question, and importantly at an efficiency plateau for all electrons with* $p_T > 20$ GeV.

Data-taking Period	Trigger
E-F	EF_mu10_MSonly
G-H	EF_mu13
I	EF_mu13_tight

Table 6.4: *The muon triggers used for the different data-taking periods in this analysis. These muon triggers are all un-prescaled for the data-taking period for which they are chosen, and at an efficiency plateau for all muons with* $p_T > 20$ GeV.

6.6 Trigger and Event Selection

6.6.1 Trigger

In this study events are drawn from two separate streams: the `Egamma` stream and the `Muon` stream. Events in the `Egamma` stream are those which fired an electron or photon trigger, those in the `Muon` stream are events which fired a muon trigger. The electron triggers used, by data-taking period, are illustrated in Table 6.3. In Table 6.4 the equivalent details are given for the muon triggers. These triggers are all un-prescaled, and at the plateau for $p_T > 20$ GeV leptons (those considered in this analysis). For Monte Carlo, the EF_e10_medium and EF_mu10_MSonly triggers are used for electrons and muons respectively.

A scheme is adopted by which ee events are taken from the `Egamma` stream, $\mu\mu$ from the `Muon` stream and $e\mu$ events from the `Muon` stream only if they are events not triggered by an electron trigger (and thus should be in the `Egamma` stream).

6.6.2 Event Selection

Events are discarded if they contain a jet (with p_T at the electromagnetic scale greater than 10 GeV) which fails basic quality selection criteria designed to reject detector noise and non-collision backgrounds [114]. These criteria include requirements made on the fraction of energy in the electromagnetic calorimeter, the fraction of jet energy in the hadronic end-cap calorimeter, the minimum number of cells which contain at least 90% of the cluster energy, the fraction of LAr cells with a cell Q-factor greater than 5000, calorimeter timing information and the maximum energy fraction in one calorimeter layer. If any event contains a cosmic muon (classified as one which passes all event selection criteria, but has $|z_\mu - z_{PV}| > 10$ mm), or an electron in the transition region ($1.37 < |\eta^{cl}| < 1.52$), it is rejected. Further to this, events must contain at least one primary vertex associated to at least five tracks.

After the pre-selection described above, events are required to have exactly two selected leptons (satisfying the object definitions, and overlap-removal criteria, defined in Section 6.4). Events are further required to have two-leptons which satisfy $m_{\ell\ell} > 5$ GeV. Any electrons in the pair must be both tight and isolated (see Section 6.4). These events will fall into one of three flavour categories: (i) di-electron (ee), (ii) electron-muon ($e\mu$) and (iii) di-muon ($\mu\mu$). These lepton-pairs can be further classified as opposite-sign ($\ell^\pm\ell^\mp; \ell = e, \mu$) or same-sign ($\ell^\pm\ell^\pm; \ell = e, \mu$). Events in Monte Carlo which pass this selection, and contain electrons, are re-weighted using global event weights which correct for differences in electron reconstruction efficiencies between data and Monte Carlo. Events in the "signal region" are the events which satisfy $E_T^{miss} > 100$ GeV. Only the opposite-sign events are of interest to the flavour subtraction analysis. In Ref. [6] the same-sign events are studied in the same high-E_T^{miss} signal region, and the opposite-sign events also studied inclusively in a higher E_T^{miss} signal region ($E_T^{miss} > 150$ GeV).

The E_T^{miss} cut is only needed to suppress Z/γ^*+jets backgrounds. The remainder of the dominant standard model backgrounds will cancel after flavour subtraction. The choice of E_T^{miss} cut is one which significantly reduces the Z/γ^*+jets background, without reducing unnecessarily any signal significance. As the supersymmetric parameter space is a varied one, there is no characteristic missing energy distribution for supersymmetry and so detailed optimisation is neither necessary nor desirable. The E_T^{miss} cut is placed at 100 GeV, at which point, the Z/γ^*+jets background becomes negligible (Figure 6.6).

Approximately 12.5 million events are pre-selected from the `Egamma` stream, and approximately 10.7 million events are pre-selected from the `Muon` stream. Just under 10,000 of the pre-selected events in the `Egamma` stream contain electron-pairs, whilst just under 13,000 of those pre-selected in the `Muon` stream contain muon-pairs. Fewer than 200 electron-muon-pairs are found in these two streams. The pre-selected events are assumed to be dominantly Z/γ^*+jets events.

The major sources of standard model opposite-sign lepton-pairs are: Z/γ^*+jets, $t\bar{t}$ and WW, WZ and ZZ diboson pair production (WZ pair production is the most important, the $Z \to \ell^+\ell^-$ decay reconstructed in preference to one lepton from the W and one from the Z). Of these, Z/γ^*+jets will dominate, with $t\bar{t}$ and diboson pair production a much smaller contribution. After a hard E_T^{miss} cut is applied however, $t\bar{t}$ and WZ diboson events (both have not just opposite-sign lepton-pairs, but also invisible decay products which can give rise to higher missing transverse energies) will dominate. As well as these sources of true lepton-pairs, contributions can be expected from $W \to \ell\nu$+jets events and QCD jets. In the former case, one electron is a true electron from the $W \to \ell\nu$ decay, and a second is a jet faking an electron. In the case of QCD jets, two jets must fake an electron for this to be a contributing source. So despite the high cross-section for QCD jets expected, the contribution to the opposite-sign lepton-pair events from these processes will be small. Single top events can produce both fake sources of lepton-pair events (in the s and t-channel decays), and true sources of lepton-pairs (Wt-channel decays), but the cross-section for single top production is small.

The total numbers of opposite-sign data events, at pre-selection, event selection and signal selection, are compared with the expectations from Monte Carlo simulation in Table 6.5. In this table the agreement between data and Monte Carlo is reasonable. The Monte Carlo events in this table are simply weighted according to their cross-section, and to the luminosity of the data sample. The systematic errors on the event numbers in the signal region are detailed in Table B.1. There are 4, 13 and 13 data events[9] in the $e^\pm e^\mp$, $e^\pm \mu^\mp$ and $\mu^\pm \mu^\mp$ channels respectively after an E_T^{miss} cut of 100 GeV (these are reduced

[9]One of the $\mu^\pm \mu^\mp$ events has $E_T^{miss} \sim 600$ GeV. On closer inspection of this event, it is a likely cosmic candidate (the difference in angle ϕ between the two muons is approximately π). Estimates of the expected contamination due to "cosmics" (both from cosmic events alone, and cosmic events arriving in tandem with collision events), give predictions in the $e^\pm \mu^\mp$ and $\mu^\pm \mu^\mp$ channels consistent with zero [7]. Cosmic backgrounds are neglected in the flavour subtraction analysis presented in this chapter. Provided the rate of $\mu^\pm \mu^\mp$ cosmic events is greater than the rate of $e^\pm \mu^\mp$ cosmic events[115], neglecting the cosmic background rate will lead to a conservative limit.

to 1, 4 and 4 events after an E_T^{miss} cut of 150 GeV). The efficiency for reconstructing muons is greater than the efficiency for reconstructing electrons, and so the different numbers of observed two-lepton events before any E_T^{miss} cut (which are mainly Z/γ^*+jets events) is as expected. The $m_{\ell\ell}$ cut, designed to remove the overlap between leptons in cases where a muon produces an electron through bremsstrahlung and showering, has a negligible effect on both Monte Carlo and data. Single top events, though a negligible contribution before E_T^{miss} cuts are applied, are a surprisingly significant component of the expected signal region events. These single top events are almost all Wt-channel single top events, $bg \to W^-t$ where $W^- \to e^-\bar{\nu}$ and $t \to b\nu e^+$.

There are fewer sources of real standard model same-sign leptons, and most of the background events in these channels at high-E_T^{miss} contain fake leptons. Despite the charge requirement, Z/γ^*+jets events are still expected to be a major source of same-sign lepton-pair events. These same-sign events can be produced in one of two ways: (a) "tridents" and (b) charge mis-identification. In trident events one of the leptons from the $Z \to \ell^+\ell^-$ decay emits a photon in the tracking material through a hard external bremsstrahlung. This photon later converts into an e^+e^- pair. When the initial lepton, and the same-sign member of the converting pair are soft, the two hard reconstructed leptons in the event have the same-sign. For instance, if the ℓ^+ produces a photon, and this interacts later with a nucleus to produce a lepton-pair, $\ell^+ \to (\gamma)\ell^+ \to (\ell^-\ell^+)\ell^+$, and both the final state ℓ^+ are soft, the reconstructed final state will contain two negatively charged leptons. Similarly, $t\bar{t}$ events can be a source of tridents when one ℓ produced by the leptonic decay of the W bremsstrahlungs. The probability of charge mis-identification for an electron is $< 2\%$, but this is sufficient to give ~ 100 two-lepton events from $Z \to \ell^+\ell^-$ decays reconstructed as same-sign lepton-pairs (given the expectation of $\sim 6,000$ opposite-sign lepton-pairs from $Z \to \ell^+\ell^-$ decays, Table 6.5). The equivalent probability is distinctly lower for muons of medium-p_T.

$W \to \ell\nu$+jets, $t\bar{t}$ and diboson events can all contribute to the same-sign fake rate. In events producing both a $b\bar{b}$ pair and a $W \to \ell\nu$ decay, if either of the b jets decays semi-leptonically, the events can give two same-sign leptons. In $W \to \ell\nu$+jets events the light jets can fake electrons. In $t\bar{t}$ production one of the two W decays can be semi-leptonic ($W \to \ell\nu$) as can one of the b decays. In WZ and ZZ diboson pair production three or more leptons are produced. If one or more of these leptons are not reconstructed, the two which are can have the same sign. This is expected to be a small contribution as in WZ

(a) $e^{\pm}e^{\mp}$

	2 Leptons	$m_{\ell\ell} > 5$ GeV	$E_T^{miss} > 100$ GeV	$E_T^{miss} > 150$ GeV
Data	6250	6250	4	1
Z+jets	6023.09 ± 24.97	6023.09 ± 24.97	0.38 ± 0.16	0.20 ± 0.12
W+jets	2.45 ± 0.60	2.45 ± 0.60	0.00 ± 0.00	0.00 ± 0.00
Drell-Yan	22.5 ± 1.3	22.5 ± 1.3	0.0 ± 0.0	0.0 ± 0.0
$t\bar{t}$	20.2 ± 0.8	20.2 ± 0.8	3.7 ± 0.3	0.9 ± 0.2
Dibosons	11.88 ± 0.12	11.88 ± 0.12	0.30 ± 0.02	0.09 ± 0.01
Dijets	49.3 ± 5.3	49.3 ± 5.3	0.0 ± 0.0	0.0 ± 0.0
Single Top	1.6 ± 0.3	1.6 ± 0.3	0.1 ± 0.1	0.0 ± 0.0
Standard Model	6131.1 ± 25.6	6131.1 ± 25.6	4.5 ± 0.4	1.2 ± 0.2

(b) $e^{\pm}\mu^{\mp}$

	2 Leptons	$m_{\ell\ell} > 5$ GeV	$E_T^{miss} > 100$ GeV	$E_T^{miss} > 150$ GeV
Data	131	131	13	4
Z+jets	37.39 ± 1.98	37.39 ± 1.98	0.36 ± 0.16	0.08 ± 0.08
W+jets	2.75 ± 0.70	2.75 ± 0.70	0.00 ± 0.00	0.00 ± 0.00
Drell-Yan	0.0 ± 0.0	0.0 ± 0.0	0.0 ± 0.0	0.0 ± 0.0
$t\bar{t}$	51.7 ± 1.2	51.7 ± 1.2	9.8 ± 0.5	1.8 ± 0.2
Dibosons	12.77 ± 0.17	12.77 ± 0.17	0.36 ± 0.03	0.06 ± 0.01
Dijets	53.2 ± 35.0	53.2 ± 35.0	0.0 ± 0.0	0.0 ± 0.0
Single Top	4.5 ± 0.4	4.5 ± 0.4	0.8 ± 0.2	0.1 ± 0.0
Standard Model	162.3 ± 35.1	162.3 ± 35.1	11.3 ± 0.6	2.0 ± 0.3

(c) $\mu^{\pm}\mu^{\mp}$

	2 Leptons	$m_{\ell\ell} > 5$ GeV	$E_T^{miss} > 100$ GeV	$E_T^{miss} > 150$ GeV
Data	12774	12772	13	4
Z+jets	13006.96 ± 36.93	13006.96 ± 36.93	0.97 ± 0.29	0.15 ± 0.11
W+jets	0.64 ± 0.30	0.64 ± 0.30	0.00 ± 0.00	0.00 ± 0.00
Drell-Yan	56.7 ± 2.0	56.7 ± 2.0	0.0 ± 0.0	0.0 ± 0.0
$t\bar{t}$	34.8 ± 1.0	34.8 ± 1.0	7.0 ± 0.4	1.5 ± 0.2
Dibosons	23.94 ± 0.17	23.94 ± 0.17	0.61 ± 0.03	0.15 ± 0.01
Dijets	214.7 ± 61.1	214.7 ± 61.1	0.0 ± 0.0	0.0 ± 0.0
Single Top	3.4 ± 0.4	3.4 ± 0.4	0.7 ± 0.2	0.1 ± 0.1
Standard Model	13345.3 ± 71.4	13345.3 ± 71.4	9.2 ± 0.6	1.9 ± 0.2

Table 6.5: *Numbers of events in the opposite-sign channels at various stages of event selection, for the largest sources of standard model background. Errors on the Monte Carlo prediction are purely statistical.*

events the two leptons from the $Z \to \ell^+\ell^-$ decay are reconstructed in preference to one from the W and one from the Z. QCD and $b\bar{b}$ decays are potentially a very dangerous source of background events because they are produced with a very high cross-section.

The total number of same-sign data events at pre-selection and event selection are compared with Monte Carlo in Table 6.6. The systematic uncertainties on these numbers are detailed in Table B.2. There are no data events surviving the cut on E_T^{miss} in any of the three channels, consistent with the expectations from Monte Carlo at this luminosity. Before this requirement is made, Z/γ^*+jets dominate the $e^\pm e^\pm$ event counts (dominantly trident events). Fake same-sign lepton-pairs from QCD events are the next most significant contribution (but only account for 1.4% of the total). Heavy flavour QCD events are the dominant source of $\mu^\pm\mu^\pm$ events before the missing energy requirement is made.

In the figures which follow, comparisons are made between data and Monte Carlo for a variety of event variables after pre-selection and event selection. The Monte Carlo samples are weighted by cross-section and luminosity. The illustrated uncertainty band includes the uncertainties on each cross-section, the luminosity, energy scales and resolutions (as detailed in Section 6.5) and the statistical sum-of-weights uncertainty which arises from limited Monte Carlo statistics. All standard model Monte Carlo events are illustrated along with data and a signal point (the mSUGRA benchmark point, SU4) combined with the total standard model background for illustrative purposes.

Figure 6.3 illustrates for the opposite-sign and same-sign channels separately the p_T of the leading lepton in selected events, whilst Figure 6.4 illustrates the p_T of the sub-leading lepton in these events. The three opposite-sign channels are illustrated separately, whilst only the overall distribution for all three same-sign channels combined is shown. The statistics in the same-sign channel make the individual by-channel plots not particularly informative. The agreement between data and Monte Carlo is good across the p_T range for both identical-flavour opposite-charge channels, for both leading and sub-leading p_T. The same-sign distributions suffer from an expected lack of statistics, but there is no obvious disagreement between the distributions and as Table 6.6 illustrates, the observed numbers of selected same-sign two-lepton events are consistent with expectation. The $e^\pm\mu^\mp$ distributions, and all subsequent $e^\pm\mu^\mp$ distributions, show an

(a) $e^{\pm}e^{\pm}$

	2 Leptons	$m_{\ell\ell} > 5$ GeV	$E_T^{miss} > 100$ GeV
Data	62	62	0
Z+jets	66 ± 3	66 ± 3	0 ± 0
W+jets	0.5 ± 0.2	0.5 ± 0.2	0.0 ± 0.0
Drell-Yan	0.3 ± 0.2	0.3 ± 0.2	0.0 ± 0.0
$t\bar{t}$	0.4 ± 0.1	0.4 ± 0.1	0.1 ± 0.1
Dibosons	0.37 ± 0.02	0.37 ± 0.02	0.01 ± 0.00
Dijets	1.2 ± 0.8	1.2 ± 0.8	0.0 ± 0.0
Wbb	0.02 ± 0.02	0.02 ± 0.02	0.00 ± 0.00
Single Top	0.06 ± 0.04	0.06 ± 0.04	0.00 ± 0.00
Standard Model	68.80 ± 2.74	68.80 ± 2.74	0.14 ± 0.06

(b) $e^{\pm}\mu^{\pm}$

	2 Leptons	$m_{\ell\ell} > 5$ GeV	$E_T^{miss} > 100$ GeV
Data	11	5	0
Z+jets	2 ± 0	1 ± 0	0 ± 0
W+jets	6.5 ± 1.2	1.7 ± 0.6	0.1 ± 0.1
$t\bar{t}$	0.7 ± 0.1	0.6 ± 0.1	0.1 ± 0.1
Dibosons	0.84 ± 0.03	0.81 ± 0.03	0.03 ± 0.01
Dijets	0.0 ± 0.0	0.0 ± 0.0	0.0 ± 0.0
Wbb	0.12 ± 0.06	0.08 ± 0.05	0.03 ± 0.03
Single Top	0.09 ± 0.06	0.07 ± 0.06	0.00 ± 0.00
Standard Model	10.15 ± 1.25	4.49 ± 0.66	0.21 ± 0.08

(c) $\mu^{\pm}\mu^{\pm}$

	2 Leptons	$m_{\ell\ell} > 5$ GeV	$E_T^{miss} > 100$ GeV
Data	3	3	0
W+jets	0.2 ± 0.2	0.2 ± 0.2	0.0 ± 0.0
$t\bar{t}$	0.1 ± 0.1	0.1 ± 0.1	0.0 ± 0.0
Dibosons	0.45 ± 0.02	0.45 ± 0.02	0.02 ± 0.00
Dijets	3.1 ± 3.1	3.1 ± 3.1	0.0 ± 0.0
Single Top	0.05 ± 0.04	0.05 ± 0.04	0.00 ± 0.00
Standard Model	3.98 ± 3.14	3.98 ± 3.14	0.02 ± 0.00

Table 6.6: *Numbers of events in the same-sign channels at various stages of event selection, for the largest sources of standard model background. Errors on the Monte Carlo prediction are purely statistical. There are no Drell-Yan $e^{\pm}\mu^{\pm}$ or $\mu^{\pm}\mu^{\pm}$ events, nor any Wbb or Z+jets $\mu^{\pm}\mu^{\pm}$ events in the Monte Carlo.*

unsurprising disagreement at low-p_T (or in regions with significant QCD) between data and simulation. This region is dominated in Monte Carlo simulation by dijet events. The discrepancy arises from limitations in the modelling of the QCD fakes by Monte Carlo.

Figure 6.5 illustrates the invariant masses of all selected lepton-pairs. Discrepancies at low $m_{\ell\ell}$ in all three opposite-sign distributions are once again the result of a poor match between QCD dijets in simulation, and these events in data. Both the $e^{\pm}e^{\mp}$ and $\mu^{\pm}\mu^{\mp}$ distributions illustrate a clear peak at the mass of the Z, in agreement with the predicted width and mass from Z/γ^*+jets simulated events. The peak in the same region in the $\ell^{\pm}\ell^{\pm}$ distribution is populated by trident events. The E_T^{miss} of each selected event and the transverse mass formed from the leading lepton p_T and this E_T^{miss} are illustrated in Figures 6.6 and 6.7 respectively. The E_T^{miss} distribution illustrates the discriminatory power of a cut on this variable. The combined SU4 and standard model distribution is ever increasingly above the expectation from Monte Carlo alone as the distribution reaches out to higher E_T^{miss}. This is the only event variable used to define the signal region, and so the demonstrated agreement between Monte Carlo simulation and data in these figures is an important one.

The total number of jets in each event is illustrated in Figure 6.8. In the analysis presented in this chapter, no requirement is placed on the number of jets in the event. These figures illustrate the higher jet multiplicities expected in the presence of the signal point SU4. In these figures, Z/γ^*+jets and $t\bar{t}$ events dominate the tail of the spectrum. There are no significant deviations from expectation observed in these distributions, with the exception of those which result from poor modelling of the data events by the dijet QCD simulations.

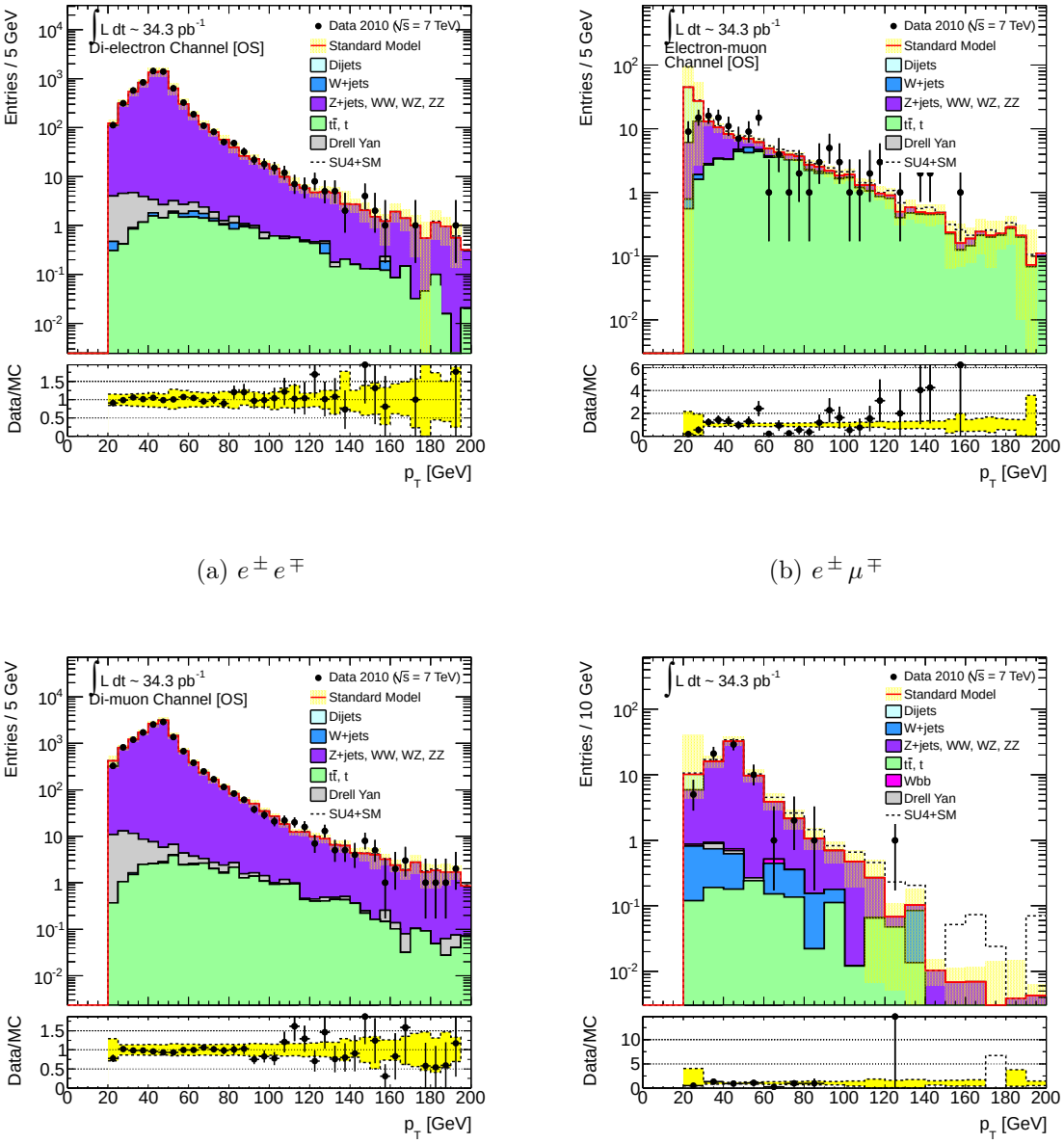

(a) $e^{\pm}e^{\mp}$ (b) $e^{\pm}\mu^{\mp}$

(c) $\mu^{\pm}\mu^{\mp}$ (d) $l^{\pm}l^{\pm}$

Figure 6.3: *Distributions of the p_T of the leading lepton in two-lepton events in data and Monte Carlo. The two-lepton events are divided into the three opposite-sign and a single same-sign charge channel, $e^{\mp}e^{\pm}$ (a), $e^{\mp}\mu^{\pm}$ (b), $\mu^{\mp}\mu^{\pm}$ (c) and $\ell^{\mp}\ell^{\mp}$ (d). Errors on data points are 68% Poisson confidence limits and the error band on Monte Carlo represents the statistical, jet energy scale and resolution, lepton energy scale and resolution, cross-section and luminosity uncertainties (as detailed in the text). In the bottom histogram the black data points, and the yellow uncertainty band, have been divided by the total Monte Carlo to show whether the fractional deviation of the data from the Monte Carlo lies within the uncertainty band. The red Monte Carlo line is the sum of all the Standard Model backgrounds.*

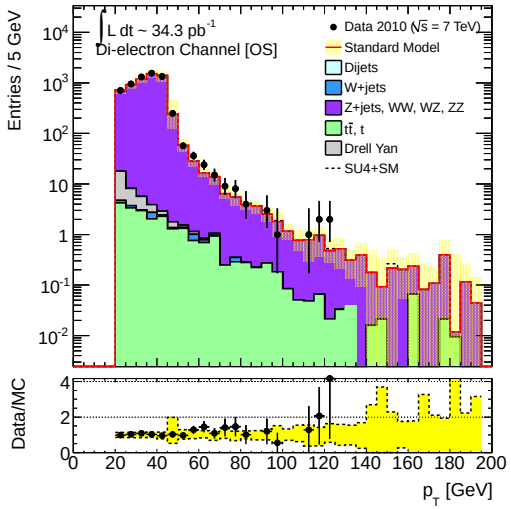

(a) $e^{\pm}e^{\mp}$

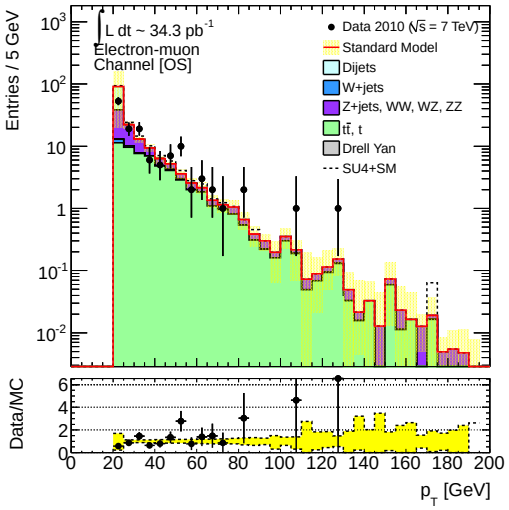

(b) $e^{\pm}\mu^{\mp}$

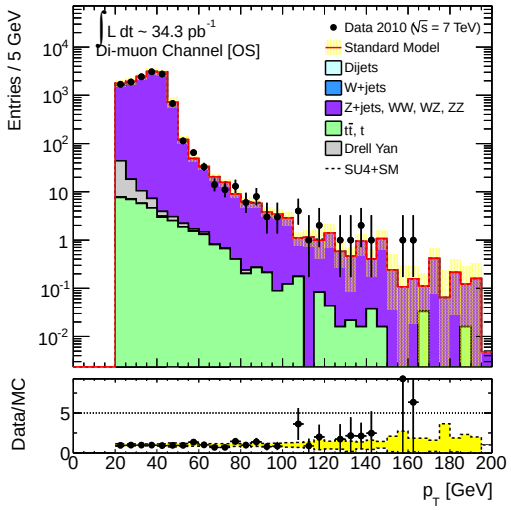

(c) $\mu^{\pm}\mu^{\mp}$

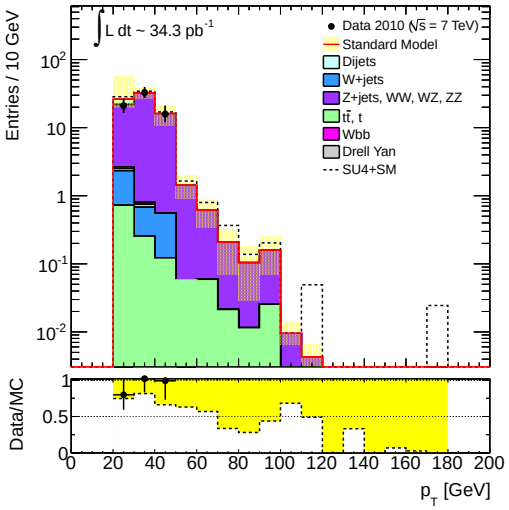

(d) $l^{\pm}l^{\pm}$

Figure 6.4: *Distributions of the p_T of the sub-leading lepton in two-lepton events in data and Monte Carlo. The two-lepton events are divided into the three opposite-sign and a single same-sign charge channel, $e^{\mp}e^{\pm}$ (a), $e^{\mp}\mu^{\pm}$ (b), $\mu^{\mp}\mu^{\pm}$ (c) and $\ell^{\mp}\ell^{\mp}$ (d). Errors on data points are 68% Poisson confidence limits and the error band on Monte Carlo represents the statistical, jet energy scale and resolution, lepton energy scale and resolution, cross-section and luminosity uncertainties (as detailed in the text). In the bottom histogram the black data points, and the yellow uncertainty band, have been divided by the total Monte Carlo to show whether the fractional deviation of the data from the Monte Carlo lies within the uncertainty band. The red Monte Carlo line is the sum of all the Standard Model backgrounds.*

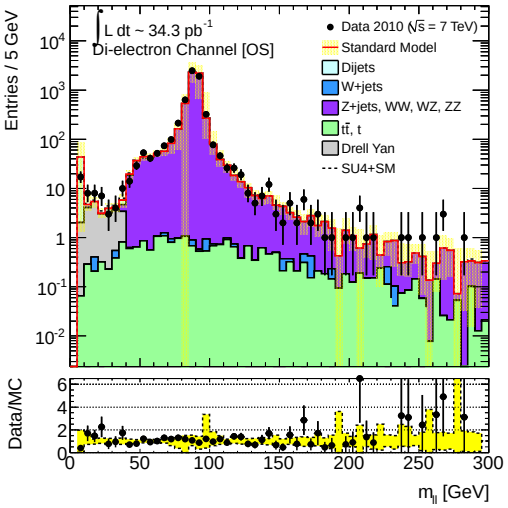

(a) $e^{\pm}e^{\mp}$

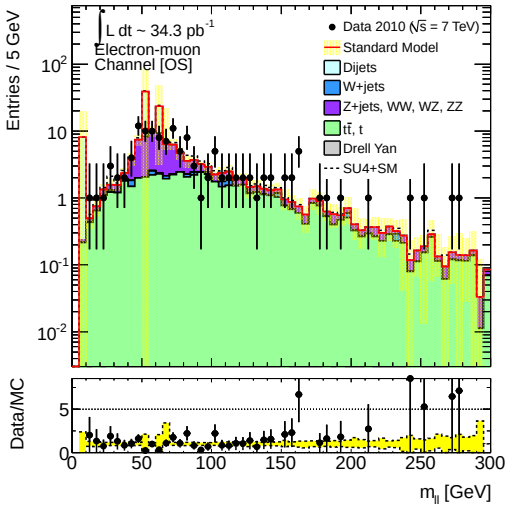

(b) $e^{\pm}\mu^{\mp}$

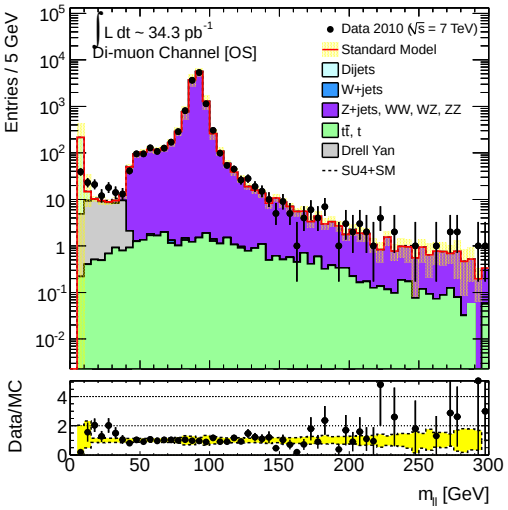

(c) $\mu^{\pm}\mu^{\mp}$

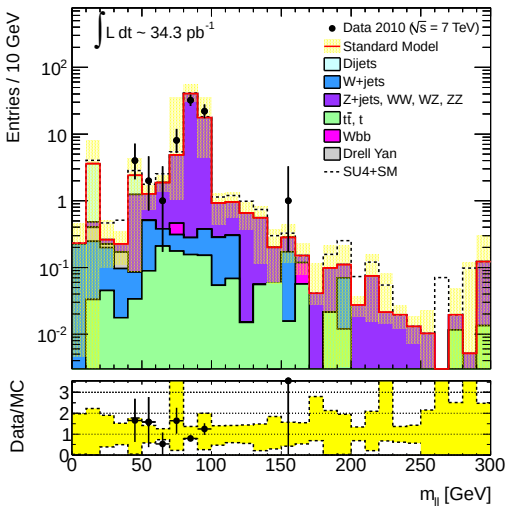

(d) $l^{\pm}l^{\pm}$

Figure 6.5: *Distributions of the invariant mass of the lepton-pair in two-lepton events in data and Monte Carlo. The two-lepton events are divided into the three opposite-sign and a single same-sign charge channel, $e^{\mp}e^{\pm}$ (a), $e^{\mp}\mu^{\pm}$ (b), $\mu^{\mp}\mu^{\pm}$ (c) and $\ell^{\mp}\ell^{\mp}$ (d). Errors on data points are 68% Poisson confidence limits and the error band on Monte Carlo represents the statistical, jet energy scale and resolution, lepton energy scale and resolution, cross-section and luminosity uncertainties (as detailed in the text). In the bottom histogram the black data points, and the yellow uncertainty band, have been divided by the total Monte Carlo to show whether the fractional deviation of the data from the Monte Carlo lies within the uncertainty band. The red Monte Carlo line is the sum of all the standard model backgrounds.*

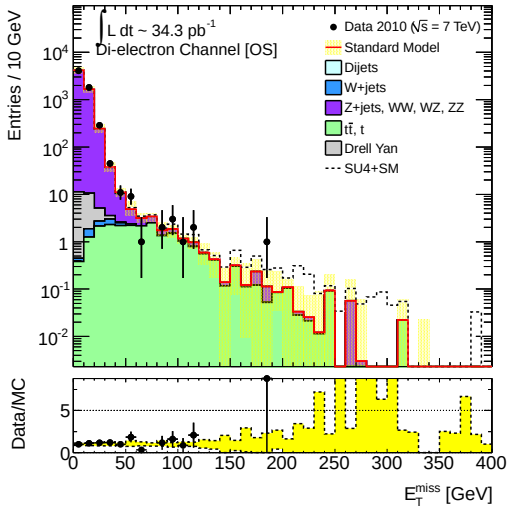

(a) $e^{\pm}e^{\mp}$

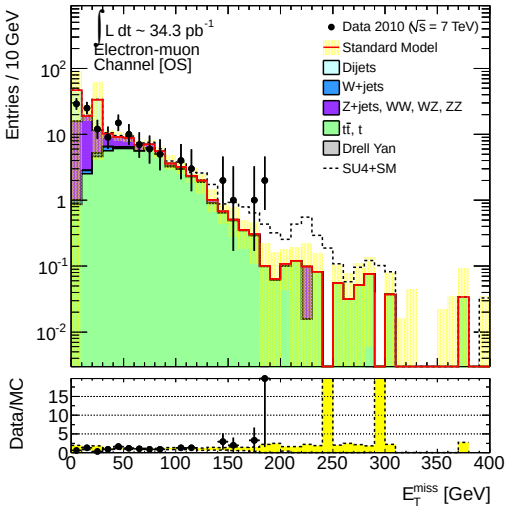

(b) $e^{\pm}\mu^{\mp}$

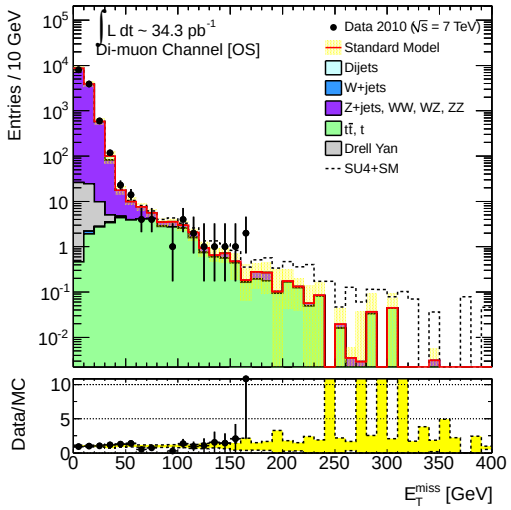

(c) $\mu^{\pm}\mu^{\mp}$

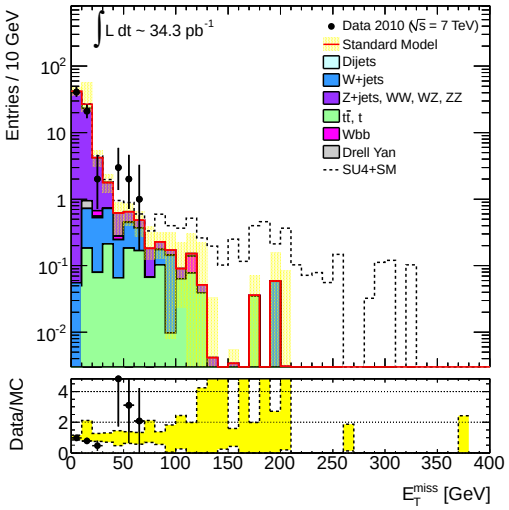

(d) $l^{\pm}l^{\pm}$

Figure 6.6: *Distributions of the transverse missing energy (E_T^{miss}) of two-lepton events in data and Monte Carlo. The two-lepton events are divided into the three opposite-sign and a single same-sign charge channel, $e^{\mp}e^{\pm}$ (a), $e^{\mp}\mu^{\pm}$ (b), $\mu^{\mp}\mu^{\pm}$ (c) and $\ell^{\mp}\ell^{\mp}$ (d). Errors on data points are 68% Poisson confidence limits and the error band on Monte Carlo represents the statistical, jet energy scale and resolution, lepton energy scale and resolution, cross-section and luminosity uncertainties (as detailed in the text). In the bottom histogram the black data points, and the yellow uncertainty band, have been divided by the total Monte Carlo to show whether the fractional deviation of the data from the Monte Carlo lies within the uncertainty band. The red Monte Carlo line is the sum of all the standard model backgrounds.*

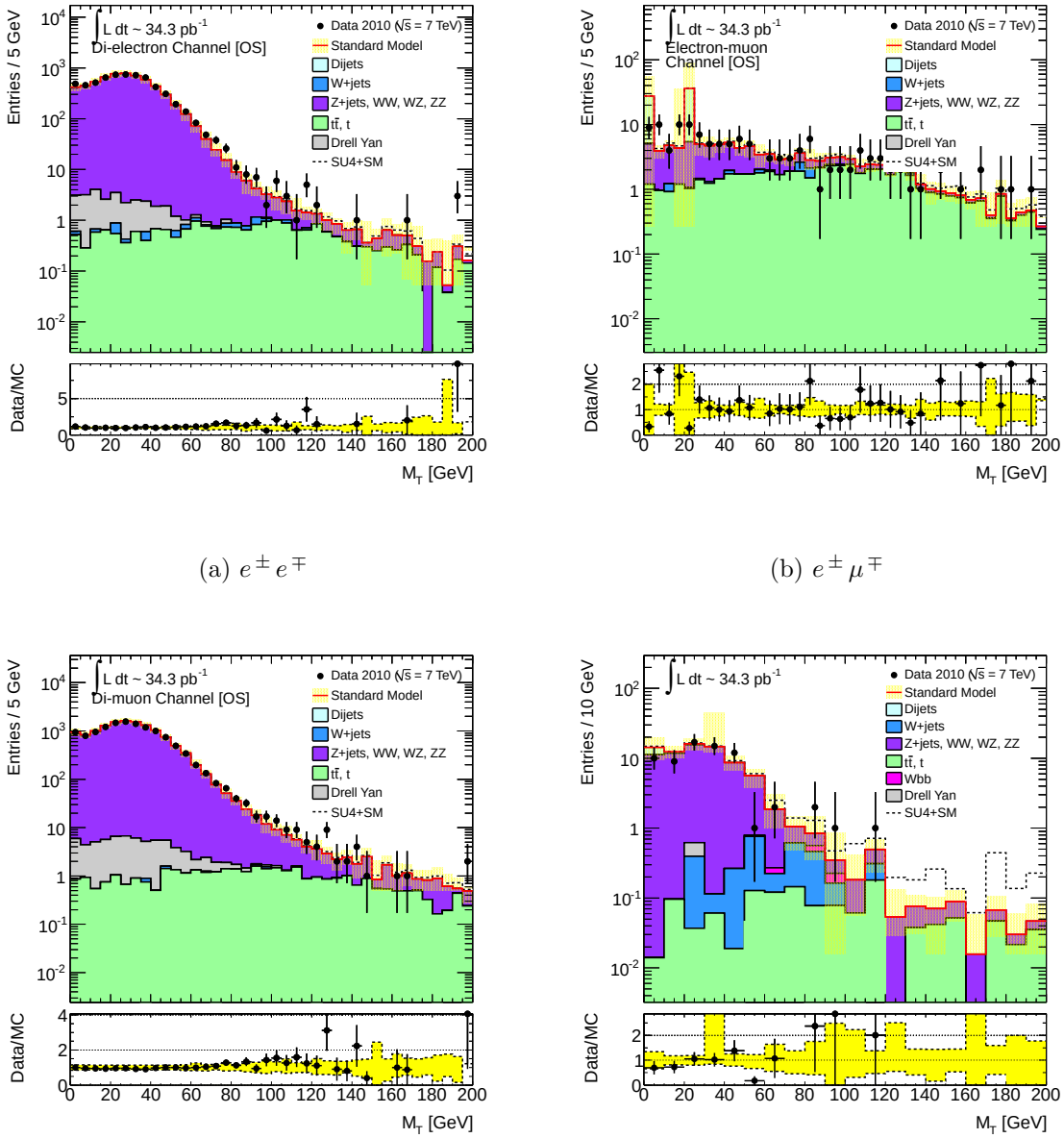

(a) $e^{\pm}e^{\mp}$ (b) $e^{\pm}\mu^{\mp}$

(c) $\mu^{\pm}\mu^{\mp}$ (d) $l^{\pm}l^{\pm}$

Figure 6.7: *Distributions of the transverse mass (M_T) of the highest p_T lepton and E_T^{miss} in two-lepton events in data and Monte Carlo. The two-lepton events are divided into the three opposite-sign and a single same-sign charge channel, $e^{\mp}e^{\pm}$ (a), $e^{\mp}\mu^{\pm}$ (b), $\mu^{\mp}\mu^{\pm}$ (c) and $\ell^{\mp}\ell^{\mp}$ (d). Errors on data points are 68% Poisson confidence limits and the error band on Monte Carlo represents the statistical, jet energy scale and resolution, lepton energy scale and resolution, cross-section and luminosity uncertainties (as detailed in the text). In the bottom histogram the black data points, and the yellow uncertainty band, have been divided by the total Monte Carlo to show whether the fractional deviation of the data from the Monte Carlo lies within the uncertainty band. The red Monte Carlo line is the sum of all the standard model backgrounds.*

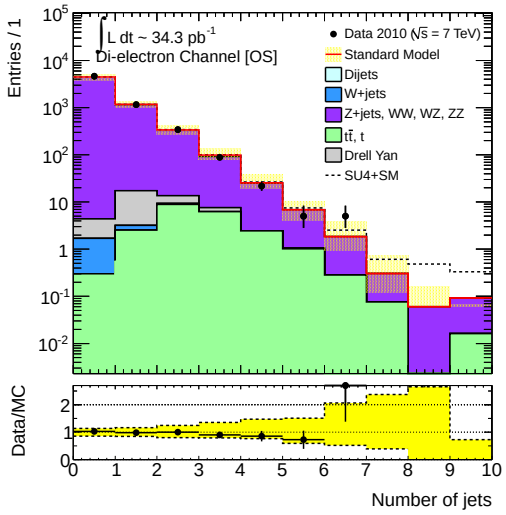

(a) $e^{\pm}e^{\mp}$

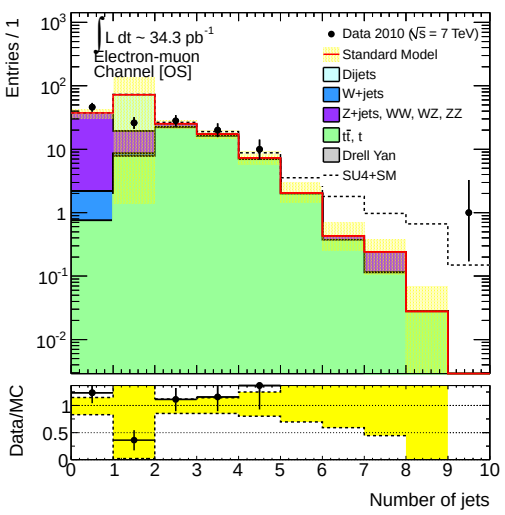

(b) $e^{\pm}\mu^{\mp}$

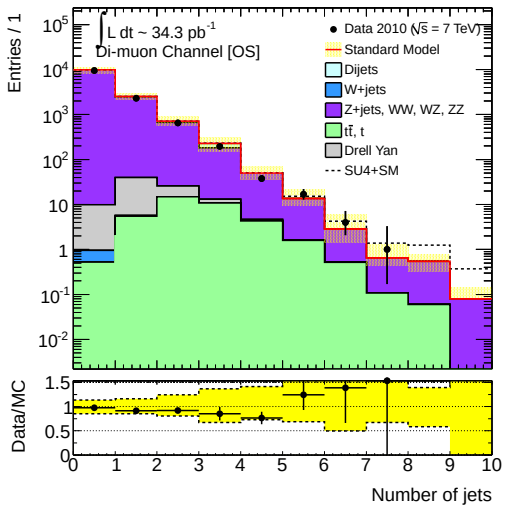

(c) $\mu^{\pm}\mu^{\mp}$

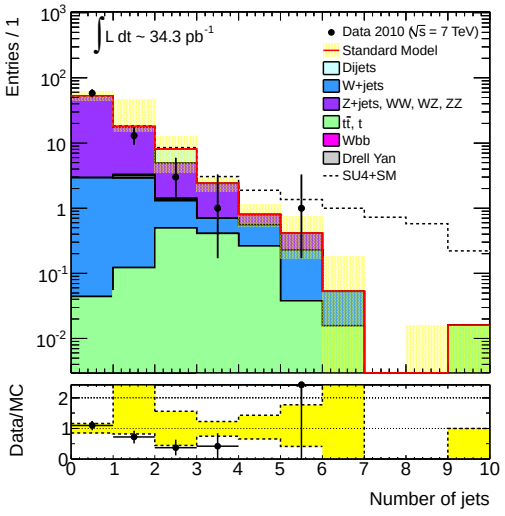

(d) $l^{\pm}l^{\pm}$

Figure 6.8: *Distributions of the total number of jets in the two-lepton events in data and Monte Carlo. The two-lepton events are divided into the three opposite-sign and a single same-sign charge channel, $e^{\mp}e^{\pm}$ (a), $e^{\mp}\mu^{\pm}$ (b), $\mu^{\mp}\mu^{\pm}$ (c) and $\ell^{\mp}\ell^{\mp}$ (d). Errors on data points are* 68% *Poisson confidence limits and the error band on Monte Carlo represents the statistical, jet energy scale and resolution, lepton energy scale and resolution, cross-section and luminosity uncertainties (as detailed in the text). In the bottom histogram the black data points, and the yellow uncertainty band, have been divided by the total Monte Carlo to show whether the fractional deviation of the data from the Monte Carlo lies within the uncertainty band. The red Monte Carlo line is the sum of all the standard model backgrounds.*

The final figure, Figure 6.9, illustrates the stransverse mass variable, M_{T2} [116], for opposite-sign lepton-pair events only. This variable, Equation 6.1, is particularly interesting for event topologies in which two particles of the same type are pair-produced and decay semi-invisibly.

$$m_{T2}^2 = \min_{\mathbf{q}_T^{\prime(1)}+\mathbf{q}_T^{\prime(2)}=p_T^{miss}} \left[\max\left(M_T^2(\mathbf{p}_T^{\alpha}, \mathbf{q}_T^{\prime(1)}; m_{\alpha}, m_{\chi}), M_T^2(\mathbf{p}_T^{\beta}, \mathbf{q}_T^{\prime(2)}; m_{\beta}, m_{\chi})\right)\right] \quad (6.1)$$

In this definition (see Figure 6.10), m_{χ} is the mass of the LSP (which may or may not be known, but can be guessed) and $\mathbf{p}_T^{\alpha,\beta}$ the transverse momenta of the two visible particles with masses $m_{\alpha,\beta}$ - labelled in the figure as the particles with momentum p_1 and p_2. The dummy variables $\mathbf{q}_T^{(1)}$ and $\mathbf{q}_T^{(2)}$ are the momenta of the two invisible particles (represented by the dashed lines in the figure), and must be constrained to equal the total missing transverse momentum in the event, p_T^{miss}. For these events, M_{T2}, formed from the observed decay products and the missing-p_T vector, is bounded from above by the mass of the pair-produced sparticles. One very clean source of two-lepton events in supersymmetry would be in events where sleptons are pair-produced. These pair-produced sleptons would both decay "semi-invisibly" into a neutralino-lepton-pair. These events, although unlikely, would show up very cleanly in these figures. The signal point illustrated shows no upper bound because the cross-section for slepton-pair production is negligible for this model. If, however, squarks and gluinos were too heavy to be produced at the $\sqrt{s} = 7$ TeV collision energies studied here, slepton-pair production would dominate. Figure 6.9(b) differs so greatly from Figures 6.9(a) and (c) because only the $t\bar{t}$ background is significant in the different-flavour distribution.

The opposite-sign two-lepton events are now studied in further detail and measurements are to be made of the identical-flavour excess in data, for comparison with the expected identical-flavour excess from standard model processes alone. The same-sign lepton-pairs are not analysed further, though limits on supersymmetry were set using these same-sign events in Ref. [6].

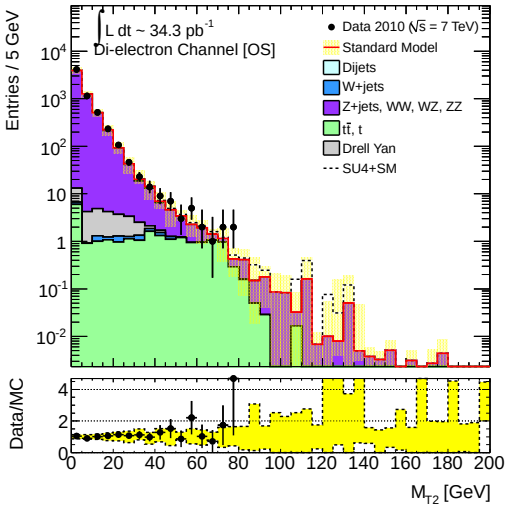

(a) $e^{\pm}e^{\mp}$

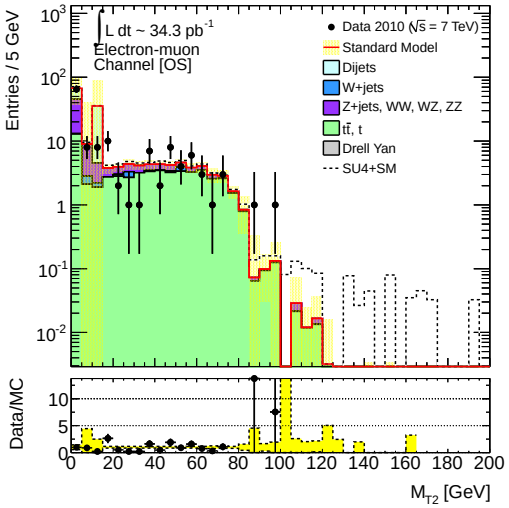

(b) $e^{\pm}\mu^{\mp}$

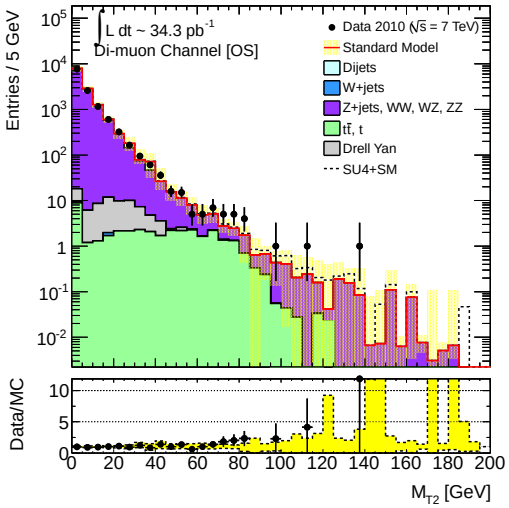

(c) $\mu^{\pm}\mu^{\mp}$

Figure 6.9: *Distributions of event M_{T2} in the two-lepton events in data and Monte Carlo. The two-lepton events are divided into the three opposite-sign channels, $e^{\mp}e^{\pm}$ (a), $e^{\mp}\mu^{\pm}$ (b) and $e^{\pm}\mu^{\pm}$ (c). Errors on data points are 68% Poisson confidence limits and the error band on Monte Carlo represents the statistical, jet energy scale and resolution, lepton energy scale and resolution, cross-section and luminosity uncertainties (as detailed in the text). In the bottom histogram the black data points, and the yellow uncertainty band, have been divided by the total Monte Carlo to show whether the fractional deviation of the data from the Monte Carlo lies within the uncertainty band. The red Monte Carlo line is the sum of all the standard model backgrounds.*

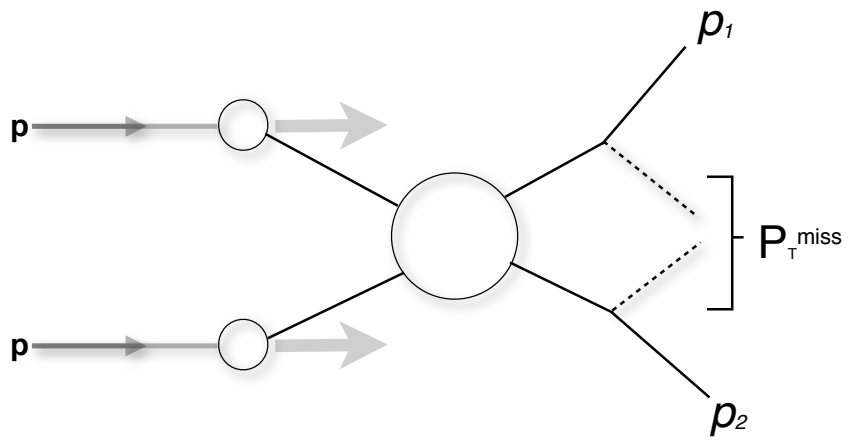

Figure 6.10: *Event topology for which the variable m_{T2} is useful. In events with this topology, two particles are pair-produced which both decay semi-invisibly. The visible decay products have momenta p_1 and p_2, whilst the invisibly decaying particles have combined missing transverse momentum of p_T^{miss}.*

6.7 A Method for Estimating the Identical-Flavour Excess

An observation has been made of the number of $e^{\pm}e^{\mp}$ events, $N(e^{\pm}e^{\mp})$, the number of $e^{\pm}\mu^{\mp}$ events, $N(e^{\pm}\mu^{\mp})$, and the number of $\mu^{\pm}\mu^{\mp}$ events, $N(\mu^{\pm}\mu^{\mp})$ in data in a high-E_T^{miss} signal region.

The identical-flavour excess, after flavour subtraction, in this data is to be quantified using a variable $\mathcal{S}$, given by Equation 6.2 where τ_e and τ_μ are the electron and muon trigger efficiencies respectively, and the triggers are assumed to be at the plateau for all $p_T > 20$ GeV leptons. This equation also takes into account the different electron and muon reconstruction efficiencies, ϵ_e and ϵ_μ respectively, whose ratio, ϵ_e/ϵ_μ, is defined as β. This quantity measures the excess of identical-flavour events (first and third terms) over different-flavour events (second term). This ratio must take into account differences in both reconstruction efficiencies and acceptance (and so although ϵ_e and ϵ_μ are referred to as efficiencies, the acceptance is included). This equation does not equal the excess of identical-flavour events exactly, rather it equals the number of excess identical-flavour events multiplied by the product of ϵ_e and ϵ_μ.

$$\mathcal{S} = \frac{N(e^{\pm}e^{\mp})}{\beta(1-(1-\tau_e)^2)} - \frac{N(e^{\pm}\mu^{\mp})}{1-(1-\tau_e)(1-\tau_\mu)} + \frac{\beta N(\mu^{\pm}\mu^{\mp})}{(1-(1-\tau_\mu)^2)} \tag{6.2}$$

The denominators on the identical-flavour terms include factors which correct for the loss of events in which both leptons of the same kind fail the appropriate trigger, the denominator of the different-flavour term correcting for the loss of events when neither the electron nor the muon trigger catches the $e\mu$ event.

In the presence of only the standard model, the mean value of $\mathcal{S}$ obtained, $\bar{\mathcal{S}}_b$, from selected identical-flavour and different-flavour lepton-pair events is expected to be small but non-zero. This asymmetry arises primarily from standard model processes which produce significant numbers of Z bosons (Z/γ^*+jets and WZ events) and which are not fully suppressed by the E_T^{miss} cut.

In Figure 6.11 the invariant mass distributions of lepton-pairs in selected events prior to applying the $E_T^{miss} > 100$ GeV requirement are presented for both the identical-flavour (a) and different-flavour (b) populations. Each event is weighted with the multiplicative factors in Equation 6.2. In the flavour subtraction, the weighted population of different-flavour events is subtracted from the weighted population of identical-flavour events to measure the identical-flavour excess.

6.8 Measurement of β, τ_e and τ_μ

6.8.1 Trigger efficiencies τ_e and τ_μ

The trigger efficiencies at the plateau, τ_e and τ_μ, for data and Monte Carlo are summarised in Table 6.7. These trigger efficiencies are the efficiencies for triggering on electrons and muons which satisfy the object definitions used in this analysis. The muon trigger efficiency in data has been obtained using independently triggered events in the `Egamma` stream. The trigger efficiency quoted is the percentage of muons in single-muon events in the `Egamma` stream, satisfying the object definition requirements, which also satisfy the appropriate muon trigger for the data-taking period. The quoted error is the binomial error on this efficiency. Conversely, the electron trigger efficiency in data was determined using electron candidates satisfying the object definition requirements in single-electron events in the `Muon` stream. In Monte Carlo, the procedure is repeated without the stream requirement.

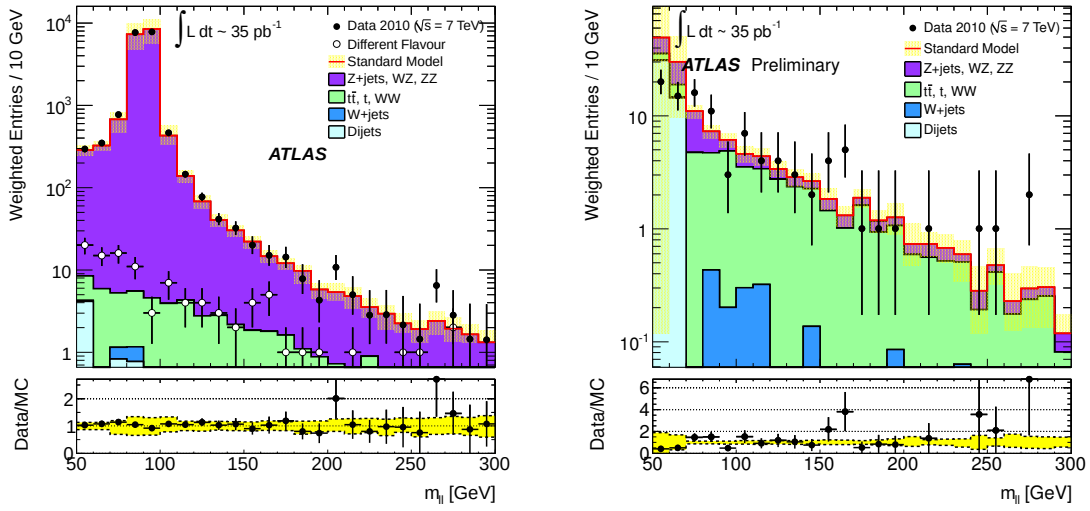

Figure 6.11: *The invariant mass distributions of lepton-pairs in selected events prior to applying the* $E_T^{miss} > 100$ GeV *requirement, weighted by the multiplicative factors in Equation 6.2. The distribution in (a) represents the identical-flavour terms in Equation 6.2 and the distribution in (b) represents the different-flavour term in this equation. The black data-points with error bars indicate the observed distributions in each case, with the open data-points in figure (a) showing the weighted different-flavour data distribution from figure (b) for comparison. The histograms indicate the background expectations obtained from the Monte Carlo samples normalised to luminosity and cross-section. The yellow uncertainty bands indicate the uncertainty on the Monte Carlo predictions from finite Monte Carlo statistics and uncertainties in cross-section, luminosity and jet and lepton energy scales and resolutions. The discrepancy between data and Monte Carlo in the different-flavour distribution arises from limitations in the modelling of QCD fakes by Monte Carlo simulation.*

	τ_e	τ_μ
Data	$(98.5 \pm 1.1)\%$	$(83.7 \pm 1.1)\%$
Monte Carlo	$(99.1 \pm 0.2)\%$	$(84.1 \pm 0.5)\%$

Table 6.7: *Trigger efficiencies in data (derived using an orthogonal sample of electron or muons as appropriate in an independent data stream) and Monte Carlo. These trigger efficiencies are over the barrel and end-caps.*

	$e^{\pm}e^{\mp}$	$e^{\pm}\mu^{\mp}$	$\mu^{\pm}\mu^{\mp}$
Data	6250	131	12774
Standard Model	6131 ± 26	162 ± 35	13345 ± 71
Data ($E_T^{miss} > 100$ GeV)	4	13	13
Standard Model ($E_T^{miss} > 100$ GeV)	4.5 ± 0.4	11.3 ± 0.6	9.2 ± 0.6

Table 6.8: *Numbers of events in each of the three opposite-sign channels before and after an E_T^{miss} cut of* 100 GeV. *Errors on the Monte Carlo predictions are purely statistical (see Table 6.5 for the break down of the Monte Carlo into individual background components).*

6.8.2 Estimation of β

The ratio of electron to muon reconstruction efficiencies times acceptances in both data and Monte Carlo is taken to be $0.69 \pm 0.03(sys.)$ (the statistical error is negligible). This ratio is obtained separately for data and Monte Carlo by isolating the selected opposite-sign identical-flavour pairs which satisfy the criteria: $80 < m_{\ell\ell} < 100$ GeV and $E_T^{miss} < 40$ GeV. The ratio of the number of pairs in this region which are $e^{\pm}e^{\mp}$ pairs to those which are $\mu^{\pm}\mu^{\mp}$ pairs should, after correcting for the different trigger efficiencies, and the ratio of efficiencies and acceptances, equal one. Solving this equation for β, using the derived τ_e and τ_μ above, separately for Monte Carlo and data, gives a measurement of β in both data and Monte Carlo. These measurements are equal to the accuracy quoted. This is not surprising as the muon reconstruction efficiency is known to match within $\sim 1\%$ between data and Monte Carlo, and the electron events in Monte Carlo have been re-weighted to correct for known efficiency discrepancies in data and Monte Carlo. Alternative studies in Ref. [7] confirm these estimates. The systematic assigned to the measurement of β is taken from studies in Ref. [7] which consider the variation in β measured using tag-and-probe for different Monte Carlo samples ($t\bar{t}$ and $Z \to \ell\ell$+jets, primarily).

6.9 Observation of $\mathcal{S}$ in Data

In data, 4, 13 and 13 events have been observed in the $e^{\pm}e^{\mp}$, $e^{\pm}\mu^{\mp}$ and $\mu^{\pm}\mu^{\pm}$ channels respectively. The expected numbers of events in these channels from Monte Carlo simulation are compared with these observations in Table 6.8. This table also summarises the expected numbers of two-lepton events from Monte Carlo in each channel, and compares

these expectations with the observed numbers of events in data. The observed numbers of signal events set a measurement of $\mathcal{S}$ in data of:
$\mathcal{S}_{obs.} = 1.98 \pm 0.15(sys._{\beta}) \pm 0.02(sys._{\tau_e}) \pm 0.06(sys._{\tau\mu})$ where the listed uncertainties are from the uncertainties on the respective efficiency parameters.

6.10 Analysis of the Expected $\mathcal{S}$ from the Standard Model

The Monte Carlo simulations, and partially data-driven predictions, of the numbers of events expected in each channel can be used to determine the expected mean value of $\mathcal{S}$ from standard model background events alone, $\bar{\mathcal{S}}_b$. Through toy experiments, these predictions will also give the width and shape of the expected distribution of $\mathcal{S}$ values obtained from a large number of hypothetical signal-free experiments. This width will be dominated by the Poisson fluctuations in the expected numbers of observed events in the three channels. Combined with hypothesised rates of supersymmetric event production in each channel, these background predictions will also predict the expected distribution of $\mathcal{S}$ values obtained in the presence of supersymmetry. These toy experiments will be used later to set an upper bound on $\bar{\mathcal{S}}_s$, the mean contribution to $\mathcal{S}$ from supersymmetry.

Background predictions will give a non-zero $\bar{\mathcal{S}}_b$, dominated by Z/γ^*+jets and diboson events. The range of expected $\mathcal{S}$ for a signal-free experiment will be dominated by the expected number of selected $t\bar{t}$ events in each flavour channel. The statistical Poisson fluctuations in each channel give the distribution of expected $\mathcal{S}$ a width which is significantly larger than the statistical and systematic uncertainties on $\bar{\mathcal{S}}_b$.

6.10.1 Partially Data-Driven Predictions

It has been noted that the degree to which $\bar{\mathcal{S}}_b$ is non-zero can be estimated. For this first estimation of $\bar{\mathcal{S}}_b$, contributions from single top and diboson events are estimated using Monte Carlo scaled to luminosity and cross-section (as in Figures 6.3 to 6.9). Contributions from Z/γ^*+jets, $t\bar{t}$ and events containing fake leptons (QCD jets and W+jets) are estimated using Monte Carlo normalised to the number of data events in an appropriate control region. The latter estimated contributions are obtained from Ref. [7], and the methods by which they are estimated briefly summarised below.

In Ref. [7], the Z/γ^* control region used selects lepton-pair events satisfying the same selection criteria as the signal region but with $E_T^{miss} < 20$ GeV and an additional requirement that $81 < m_{\ell\ell} < 101$ GeV.

The $t\bar{t}$ control region selects "top-tagged" lepton-pair events again satisfying the same selection criteria as signal candidates but with a looser missing energy requirement $60 < E_T^{miss} < 80$ GeV and an additional requirement of ≥ 2 jets with $p_T > 20$ GeV. The top-tagging requirement is imposed through the use of the variable m_{CT} [117] which can be calculated from the four-vectors of the selected jets and leptons:

$$m_{CT}^2(v_1, v_2) = \left[E_{\mathrm{T}}(v_1) + E_{\mathrm{T}}(v_2)\right]^2 - \left[\mathbf{p}_{\mathrm{T}}(v_1) - \mathbf{p}_{\mathrm{T}}(v_2)\right]^2 \tag{6.3}$$

where v_i can be a lepton, a jet, or a lepton-jet combination, transverse momentum vectors are denoted by $\mathbf{p}_{\mathrm{T}}$ and transverse energies E_T are defined as $E_T = \sqrt{p_{\mathrm{T}}^2 + m^2}$. This variable is bounded from above by analytical functions of the top quark and W masses. Top-tagged events are required to possess m_{CT} values calculated from combinations of jets and leptons consistent with the expected bounds from $t\bar{t}$ events, and also to possess lepton-jet invariant mass values consistent with top quark decays, as detailed in Ref. [118].

The contribution from events containing fake leptons is estimated using a method similar to that described in Ref. [119]. The electron and muon identification criteria are relaxed to obtain "looser" samples of leptons, dominated by fakes. This lepton selection is termed "loose" (but is not to be confused with loose electron identification, as introduced in Chapter 4). The observed events in data containing loose-loose, loose-tight, tight-loose and tight-tight lepton pairs are counted. The probabilities of loose real leptons passing the tight selection criteria are obtained from a Z control sample. The probabilities of loose fake leptons passing the tight selection criteria are obtained using several control samples dominated by QCD jet events. Linear equations are constructed which relate the observed event counts to the numbers of fake-fake, fake-real real-fake and real-real lepton pairs. Simultaneous solution of these four equations yields the expected contribution to the signal region from events containing fake leptons.

The resulting predictions for the numbers of events in each channel are given in Table 6.9. The dominant uncertainties in the partially data-driven background estimates

	$e^{\pm}e^{\mp}$	$e^{\pm}\mu^{\mp}$	$\mu^{\pm}\mu^{\mp}$
Data	4	13	13
Z/γ^*+jets	0.40 ± 0.46	0.36 ± 0.20	0.91 ± 0.67
Dibosons	0.30 ± 0.11	0.36 ± 0.10	0.61 ± 0.10
$t\bar{t}$	2.50 ± 1.02	6.61 ± 2.68	4.71 ± 1.91
Single top	0.13 ± 0.09	0.76 ± 0.25	0.67 ± 0.33
Fakes	0.31 ± 0.21	-0.15 ± 0.08	0.01 ± 0.01
Standard Model	3.64 ± 1.24	8.08 ± 2.78	6.91 ± 2.20

Table 6.9: *Expected numbers of standard model background events in the signal region for each of the three possible lepton flavour combinations. The estimates for single top and dibosons are as detailed in Section 6.10.2, whilst the remaining background estimates are from Ref. [7] which were obtained using the methods described in the text. The prediction of a negative number of fake events in the $e^{\pm}\mu^{\mp}$ channel is an artifact of the method (which involves the inversion of a four-by-four matrix) used to estimate their contribution. In the $e^{\pm}\mu^{\mp}$ column of this table, and in subsequent calculations and toy experiments involving the estimate in this channel, the estimated number of fakes is taken to be zero. The quoted errors include the statistical and systematic uncertainties on the predicted numbers of events. The systematic uncertainties on the diboson and single top estimates include the sources detailed in Section 6.5, as tabulated in Table B.1. The systematic uncertainty on the Z/γ^*+jets estimate from Ref. [7] includes the uncertainties due to jet energy scale and resolution, and choice of generator. The $t\bar{t}$ estimate from Ref. [7] includes jet energy scale and resolution uncertainties, uncertainties due to the choice of generator, uncertainties in the parton shower and those in initial-state and final-state radiation, and control region statistical uncertainties. The systematic uncertainties included in the fake rate estimate from Ref. [7] include uncertainties in the fake rate parameterisation, and uncertainties which arise from using a Bayesian Neural Network to predict the event rates in each channel. The probabilities for the Standard Model to fluctuate to the respective observation are $e^{\pm}e^{\mp}$ 48%, $e^{\pm}\mu^{\mp}$ 14% and $\mu^{\pm}\mu^{\mp}$ 6%.*

Process	$\bar{\mathcal{S}}_b$
Z/γ^*+jets	0.86 $\pm$ 0.33 (stat.) $\pm$ 0.74 (sys.)
Dibosons	0.51 $\pm$ 0.04 (stat.) $\pm$ 0.12 (sys.)
$t\bar{t}$	0.28 $\pm$ 0.61 (stat.) $\pm$ 0.13 (sys.)
Single top	-0.10 $\pm$ 0.23 (stat.) $\pm$ 0.08 (sys.)
Fakes	0.46 $\pm$ 0.31 (stat.) $\pm$ 0.10 (sys.)
Standard Model	2.06 $\pm$ 0.79 (stat.) $\pm$ 0.78 (sys.)

Table 6.10: *Expected mean $\mathcal{S}$ values for principal standard model processes estimated using the partially data-driven estimates in Ref. [7] (for all but single top and diboson backgrounds), together with their uncertainties (both statistical and systematic). The systematic uncertainty includes the (small and negligible) uncertainties on $\bar{\mathcal{S}}_b$ from uncertainties in the ratio of reconstruction efficiencies, and the trigger efficiencies. The estimates are obtained by using the predicted events in each channel detailed in Table 6.9, in Equation 6.2. See discussion in Appendix B and Table B.3 for a detailed break down of the systematic sources.*

arise from limited statistics in the control regions, theoretical uncertainties and from the jet energy scale and jet energy resolution uncertainties affecting the shapes of the Monte Carlo E_T^{miss} distributions [7]. The systematic errors on the Monte-Carlo-only estimates of single top and diboson backgrounds are dominated by the jet energy scale and resolution uncertainties (see Table B.1). The corresponding contributions to $\bar{\mathcal{S}}_b$ from each background are detailed in Table 6.10. Combining these estimates of $\bar{\mathcal{S}}_b$ for each background gives a data-driven prediction of $\bar{\mathcal{S}}_b = 2.06 \pm 0.79(stat.) \pm 0.78(sys.)$ for the standard model. The dominant contributions to $\bar{\mathcal{S}}_b$ are Z/γ^*+jets and diboson events, as expected. The estimated statistical and systematic uncertainties are comparable. The statistical and systematic uncertainties on this mean are small, and will be significantly smaller than the width of the distribution of hypothetical observed $\mathcal{S}$ from a large number of signal-free experiments (as will the systematic and statistical uncertainties on the width of the distribution itself, see Figure 6.12).

6.10.2 Monte-Carlo-Only Predictions

The predicted numbers of standard model events in the signal region from Monte Carlo simulations, scaled only to cross-section and luminosity, are detailed in Table 6.11. The corresponding contributions to $\bar{\mathcal{S}}_b$ from these Monte-Carlo-only estimates of the background are detailed in Table 6.12. The overall estimate of the mean, $\bar{\mathcal{S}}_b$, obtained from

	$e^{\pm}e^{\mp}$	$e^{\pm}\mu^{\mp}$	$\mu^{\pm}\mu^{\mp}$
Data	4	13	13
Z/γ^*+jets	0.38 ± 0.39	0.36 ± 0.20	0.97 ± 0.44
Dibosons	0.30 ± 0.11	0.36 ± 0.10	0.61 ± 0.10
$t\bar{t}$	3.72 ± 1.13	9.80 ± 2.50	6.99 ± 1.64
Single top	0.13 ± 0.09	0.76 ± 0.25	0.67 ± 0.33
Standard Model	4.53 ± 1.43	11.27 ± 2.58	9.23 ± 1.91

Table 6.11: *Expected numbers of standard model background events in the signal region for each of the three possible lepton flavour combinations from Monte Carlo simulations scaled to luminosity and cross-section. The quoted error includes systematic and statistical uncertainties. The systematic uncertainties on each estimate include the sources detailed in Section 6.5, as tabulated in Table B.1. In this table only the non-zero contributions from Monte Carlo are listed (for example, statistics were insufficient for any QCD dijet events pass the signal selection criteria). The single top and diboson estimates are also used in Table 6.9.*

	$\bar{\mathcal{S}}_b$
Z/γ^*+jets	0.89 $\pm$ 0.35 (stat.) $\pm$ 0.54 (sys.)
Dibosons	0.51 $\pm$ 0.04 (stat.) $\pm$ 0.12(sys.)
$t\bar{t}$	0.52 $\pm$ 0.76 (stat.) $\pm$ 0.53 (sys.)
Single top	-0.10 $\pm$ 0.23 (stat.) $\pm$ 0.08 (sys.)
Standard Model	1.82 $\pm$ 0.87(stat.) $\pm$ 1.10 (sys.)

Table 6.12: *Expected mean $\mathcal{S}$ values for principal standard model processes estimated using Monte Carlo normalised to luminosity and cross-section, together with their uncertainties (both statistical and systematic). The systematic uncertainty includes the (small and negligible) uncertainties on $\bar{\mathcal{S}}_b$ from uncertainties in the ratio of reconstruction efficiencies, and the trigger efficiencies. The estimates are obtained from the predicted events in each channel detailed in Table 6.11, used in Equation 6.2. In this table only the non-zero contributions from Monte Carlo are listed (for example, statistics were insufficient for any QCD dijet events to pass the signal selection criteria). See Tables B.4 and B.5 for a detailed break down of the systematic uncertainties.*

combining the individual background estimates, and their uncertainties, is:
$\bar{\mathcal{S}}_b = 1.82 \pm 0.87(stat.) \pm 1.10(sys.)$. The statistical uncertainty on this estimate of the mean is comparable to the systematic one. The systematic uncertainty is dominated by the jet scale and resolution uncertainties (see Table B.5).

Point	$\bar{\mathcal{S}}_s$
MSSM22	21.2 ± 1.5
MSSM27	26.7 ± 1.4
MSSM29	18.3 ± 1.3

Table 6.13: *Predicted $\bar{\mathcal{S}}_s$ for benchmark points in the MSSM 24-parameter framework. Errors on these Monte Carlo predictions are statistical only. The masses of these signal points are given in Table 6.1.*

6.11 Interpretation and Limits

The expected $\bar{\mathcal{S}}_s$ predicted from Monte Carlo for the three MSSM benchmark points are listed in Table 6.13. These predictions are substantially higher than the standard model predictions for $\bar{\mathcal{S}}$, $\bar{\mathcal{S}}_b$. In this section model independent limits will be set on $\bar{\mathcal{S}}_s$ using the observation in data and the estimates of the expected numbers of events in each channel. This data and these predictions will also be used to exclude regions of the parameter spaces of the frameworks described at the beginning of this chapter.

An observation has been made of $\mathcal{S}$ from the data, $\mathcal{S}_{obs}$. To ascertain whether this observation is consistent with expectation requires a consideration of more than the mean expected $\mathcal{S}$ from the standard model, $\bar{\mathcal{S}}_b$, but also an evaluation of the range of expected $\mathcal{S}$ values which arises from Poisson fluctuations in the potential numbers of events observed in each channel. For the particular $\mathcal{S}_{obs}$ observed here, its proximity to (both estimates of) $\bar{\mathcal{S}}_b$ clearly indicates that it is consistent. It is instructive, however, to consider what range of observed $\mathcal{S}$ would have been consistent.

Using the predicted numbers of standard model events in each channel as the mean numbers of $e^{\pm}e^{\mp}$, $e^{\pm}\mu^{\mp}$ and $\mu^{\pm}\mu^{\mp}$ events expected, the distribution of likely observed $\mathcal{S}$ in the absence of physics beyond the standard model can be established using pseudo-experiments. A single pseudo-experiment is set-up as follows ($N_b(e^{\pm}e^{\mp})$, $N_b(e^{\pm}\mu^{\mp})$ and $N_b(\mu^{\pm}\mu^{\mp})$ are the predicted numbers of standard model events in each flavour channel). The number of observed standard model $e^{\pm}e^{\mp}$, $e^{\pm}\mu^{\mp}$ and $\mu^{\pm}\mu^{\mp}$ events are taken as the three random numbers drawn from three Poisson distributions with means $\lambda_{b,e^{\pm}e^{\mp}}$, $\lambda_{b,e^{\pm}\mu^{\mp}}$ and $\lambda_{b,\mu^{\pm}\mu^{\mp}}$. To account for the systematic and statistical uncertainties on the estimates of the N_b, the λ_b are not trivially set to equal the N_b. Instead,

to obtain the λ_b for the pseudo-experiment, the N_b are decomposed into the separated background predictions, $N_{b,i}$ for background i, in each channel. The appropriate λ_b for each background, $\lambda_{b,i}$, are obtained by multiplying each $N_{b,i}$ in each channel by a series of random numbers drawn from various Gaussian distributions to account for each systematic and statistical uncertainty affecting the channel and the background i. The overall λ_b in each channel is then formed by summing over the resulting $\lambda_{b,i}$. Each Gaussian has unit mean, and a width equal to the fractional size of the uncertainty. Correlations between the different channels and the different backgrounds are fully taken into account by drawing only one random number (from a single Gaussian) for each uncertainty, but then appropriately scaling the drawn number before it is applied to a given background or channel. The β, τ_e and τ_μ measured by the psuedo-experiment are drawn from Gaussian distributions with means equal to the expected quantities, and sigma equal to the absolute uncertainties. The resulting $\mathcal{S}$ is then calculated using the total numbers of events observed in each channel.

The above procedure can be thought of very simply as a sequence of three steps. (i) In the first step, the mean number of background events in each channel and from each source is sampled (a first sampling). This sampling takes appropriate account of the correlations between uncertainties in the estimates of these means. (ii) The resulting total numbers of background events in each channel are used to construct three Poisson distributions. The second step is to draw the observed numbers of events from these Poisson distributions (a second sampling). (iii) Finally, β, τ_e and τ_μ are also sampled, and $\mathcal{S}$ constructed.

The distribution of $\mathcal{S}$ values obtained from one million signal-free experiments is given in Figure 6.12, using the predicted numbers of events in each channel derived partially from data (see Section 6.10.1, in particular Table 6.9). This figure illustrates the statements made in Section 6.10, that the shape of the distribution is dominated by statistical fluctuations in the event rates, and that the uncertainties on $\bar{\mathcal{S}}_b$ are negligible compared to the width of this distribution[10]. This observation of $\mathcal{S}_{obs}$ is an entirely likely measurement of $\mathcal{S}$ given the standard model predictions. The number of pseudo-experiments with $\mathcal{S} > \mathcal{S}_{obs}$ is 49.7%.

[10]The discrete probability distribution of the difference $n_1 - n_2$ between two statistically independent random variables N_1 and N_2 each Poisson distributed with means μ_1 and μ_2 respectively is the Skellam distribution [120]. The multiplicative scale factors in Equation 6.2 make $\mathcal{S}$ not purely Skellam distributed.

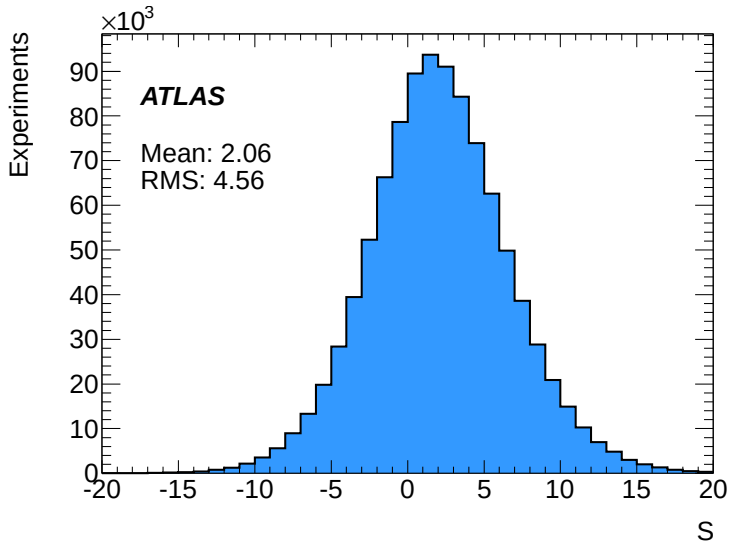

Figure 6.12: *Distribution of observed $\mathcal{S}$ values from a million hypothetical signal-free experiments. The shape is driven by statistical Poisson fluctuations in the expected rates of identical-flavour and different-flavour events, dominated by $t\bar{t}$ events. Statistical and systematic uncertainties on these event rates do not have a significant impact on the width. The width of this distribution is far greater than the statistical and systematic uncertainties on its mean, $\bar{\mathcal{S}}_b$.*

These pseudo-experiments can be modified to evaluate the probability of observing a given $\mathcal{S}$ in the presence of a hypothesised signal. The observed numbers of signal $e^{\pm}e^{\mp}$, $e^{\pm}\mu^{\mp}$ and $\mu^{\pm}\mu^{\mp}$ events are taken as the three random numbers drawn from three Poisson distributions with means $\lambda_{s,e^{\pm}e^{\mp}}$, $\lambda_{s,e^{\pm}\mu^{\mp}}$ and $\lambda_{s,\mu^{\pm}\mu^{\mp}}$. Systematic and statistical uncertainties are applied to the predicted N_s (where appropriate), taking account of correlations between the uncertainties in each channel on each background prediction, to obtain these λ_s.

To set a model-independent limit on $\bar{\mathcal{S}}_s$, the assumption is made that the branching ratios into $e^{\pm}e^{\mp}$ decays and $\mu^{\pm}\mu^{\mp}$ decays from supersymmetry are equal (i.e. $\frac{1}{\beta}\lambda_{s,e^{\pm}e^{\mp}} \approx \beta\lambda_{s,\mu^{\pm}\mu^{\mp}}$). Predicting an increasing contribution to the observed number of $e^{\pm}\mu^{\mp}$ events from supersymmetry, i.e. increasing $\lambda_{s,e^{\pm}\mu^{\mp}}$, for given $\lambda_{s,e^{\pm}e^{\mp}}$ and $\lambda_{s,\mu^{\pm}\mu^{\mp}}$, will change both the mean of the observed $\mathcal{S}$ distribution and its width. Equally, the distributions of observed $\mathcal{S}$ from two different sets of λ_s which predict the same $\bar{\mathcal{S}}_s$ will have identical mean, but differing width. The limits set on $\bar{\mathcal{S}}_s$ are therefore ones which depend upon the number of predicted signal events in all three channels. In addition to the assumption that identical-flavour rates are equal, assumptions must

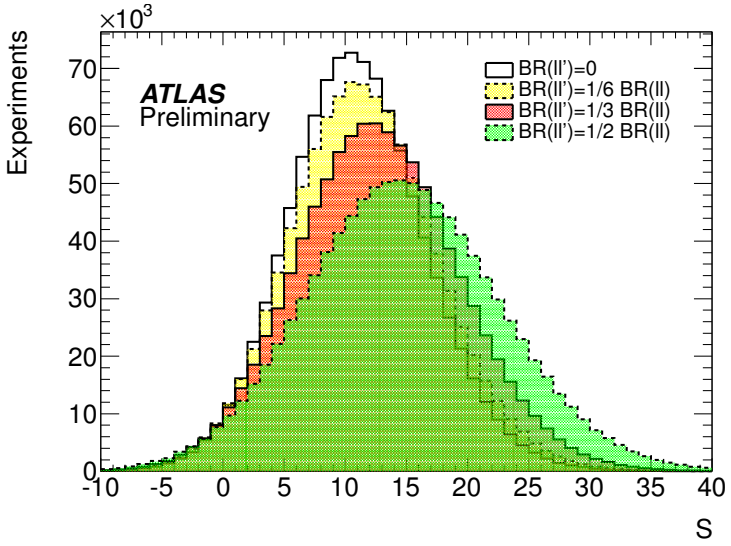

Figure 6.13: *Distribution of observed $\mathcal{S}$ values from four sets of a million hypothetical experiments in which a signal is present, for increasing branching ratio for supersymmetric decay to different-flavour leptons, and increasing $\bar{\mathcal{S}}_s$. In each case the expected numbers of supersymmetric events added to each channel (assuming equal branching fractions for $e^{\pm}e^{\mp}$ and $\mu^{\pm}\mu^{\mp}$) are set so that only 5% of experiments give a value of $\mathcal{S}$ less than our $\mathcal{S}_{obs}$. Adding supersymmetric events to each channel broadens the distribution and shifts the peak. Adding no net excess of identical-flavour events just broadens the distribution, as by construction $\bar{\mathcal{S}}_s$ does not change. The greater the relative branching ratio for decays into different-flavour leptons, the higher the upper limit on $\bar{\mathcal{S}}_s$. The predicted number of events in each channel from the standard model are obtained from the partially data-driven predictions.*

be made about the branching ratio into different-flavour lepton-pairs relative to the branching ratio into identical-flavour lepton-pairs.

In Figure 6.13 the distribution of observed $\mathcal{S}$ for four different sets of one-million hypothetical experiments are illustrated. These sets of experiments each assume a different ratio of different-flavour to identical-flavour lepton-pair branching fractions. The width of the distribution of observed $\mathcal{S}$ is given roughly by the square-root of the sum of the variances of the estimated number of background events in each channel. The limit on the $\bar{\mathcal{S}}_s$ obtained is therefore quite sensitive to the predicted rate of decays to $e^{\pm}\mu^{\mp}$. The greater the relative branching ratio into different-flavour lepton-pairs, the wider the distribution. The λ_s have been set in each set of experiments so that only 5% of experiments predict $\mathcal{S} < \mathcal{S}_{obs}$. The λ_s give a corresponding $\bar{\mathcal{S}}_s$. The limits in the four cases illustrated in Figure 6.13 are tabulated in the middle column of Table 6.14. The right column of this table also gives the equivalent limits if the standard model mean event

BR($l'l$):BR(ll)	Data-Driven	Monte-Carlo-Only
0	8.8	10.2
1/6	9.3	10.5
1/3	10.5	12.0
1/2	12.6	14.0

Table 6.14: *Observed limit on $\bar{\mathcal{S}}_s$ obtained using the data-driven estimates of the contributions in each channel from standard model background, and the Monte-Carlo-only estimates of the contributions in each channel from standard model background. The observed limits assume that the rates of production of $e^{\pm}e^{\mp}$ and $\mu^{\pm}\mu^{\mp}$ events from supersymmetric processes are the same. Limits are given for increasing relative branching ratio to different-flavour lepton-pairs.*

rates (and their uncertainties) are taken from Monte-Carlo-only. The limits are slightly weaker in the Monte-Carlo-only case. The estimated numbers of $t\bar{t}$ in each channel are greater if Monte Carlo is normalised to luminosity and cross-section than if Monte Carlo is normalised to data using the described control region. The distribution of expected $\mathcal{S}$ if the Monte-Carlo-only predictions are used is therefore wider, and hence the limit slightly weaker.

The data and predicted numbers of background events can exclude regions of various parameter spaces. The $N_s(e^{\pm}e^{\mp})$, $N_s(e^{\pm}\mu^{\mp})$ and $N_s(\mu^{\pm}\mu^{\mp})$ from which the λ_s can be obtained are taken from Monte Carlo. The uncertainties on these event rates for the signal include the theoretical uncertainties on the factorisation and renormalisation scales, experimental jet energy scale and resolution uncertainties and uncertainties on the lepton reconstruction efficiencies; the size of these uncertainties for each signal point having been estimated by members of the ATLAS collaboration, Ref[7]. For each model point, the N_s and their uncertainties as input to one million pseudo-experiments give a distribution of possible $\mathcal{S}$ values. The percentage of these experiments with $\mathcal{S} < \mathcal{S}_{obs}$ gives the probability of the signal and background hypothesis being falsely rejected. If the probability of being falsely rejected is $< 5\%$, the point is excluded at 95% confidence, and the signal plus background hypothesis rejected.

The points excluded and not excluded in the $m_0 - m_{1/2}$ mSUGRA/CMSSM plane at 95% confidence are illustrated in Figure 6.14, whilst those in the 5D-phenomenological grid are illustrated in Figure 6.15. The limits in the mSUGRA/CMSSM plane exclude a

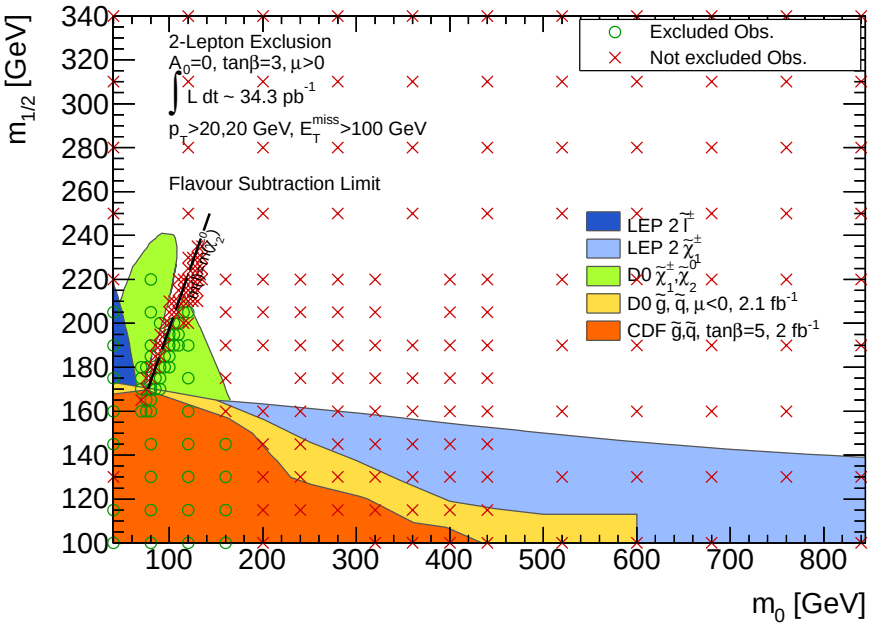

Figure 6.14: *Points excluded and not excluded at 95% confidence in a slice through the mSUGRA/CMSSM models with $A_0 = 0$, $\tan\beta = 3$ and $\mu > 0$, illustrated in the $m_0 - m_{1/2}$ plane. The existing limits shown are those from previous experiments [92, 121–123]. Note: The illustrated $\tilde{q}\tilde{g}$ DØ limit assumes $\mu < 0$. The line $m_{\tilde{\ell}} = m_{\tilde{\chi}_2^0}$ is marked on this figure. For $m_{\tilde{\ell}}$ just less than $m_{\tilde{\chi}_2^0}$ (the left-hand side of this line) the lepton from the $\tilde{\chi}_2^0 \to \tilde{\ell}^{\pm}\ell^{\mp}$ decay is soft. The latest ATLAS exclusion limits [55, 124, 125] from searches using jets, one-lepton and b jets are not detailed on this figure. Similarly, the latest results by the CMS collaboration are omitted [126].*

region of parameter space at low $m_0 - m_{1/2}$ roughly similar that excluded by the Tevatron experiments (the best limit in this region arising from their tri-lepton, $\tilde{\chi}_1^{\pm}, \tilde{\chi}_2^0$, search). The "missing" wedge in the DØ exclusion, which is also observed in this analysis, is just to the left of the $m_{\tilde{\chi}_2^0} = m_{\tilde{\ell}}$ line. For $m_{\tilde{\ell}}$ just less than $m_{\tilde{\chi}_2^0}$ (the left-hand side of this line) the lepton from the $\tilde{\chi}_2^0 \to \tilde{\ell}^{\pm}\ell^{\mp}$ decay is soft. In a search for all opposite-sign two-leptons, without flavour subtraction, the expectation is that this wedge will be attenuated (see Ref. [6]). Whilst the favour subtraction analysis is specifically searching for decays with flavour correlations, in an inclusive analysis the two leptons can be from chargino decays, or a hard lepton can be picked up from the other side of the decay. In the 5D-phenomenological grid a discontinuity is marked where $m_{\tilde{g}} = m_{\tilde{q}}$. When $m_{\tilde{g}} < m_{\tilde{q}}$, gluinos decay into a chargino or a neutralino, and two jets. A significant fraction of these decays are to the neutralino plus two jet final state. This reduces the branching fraction for decays into leptons.

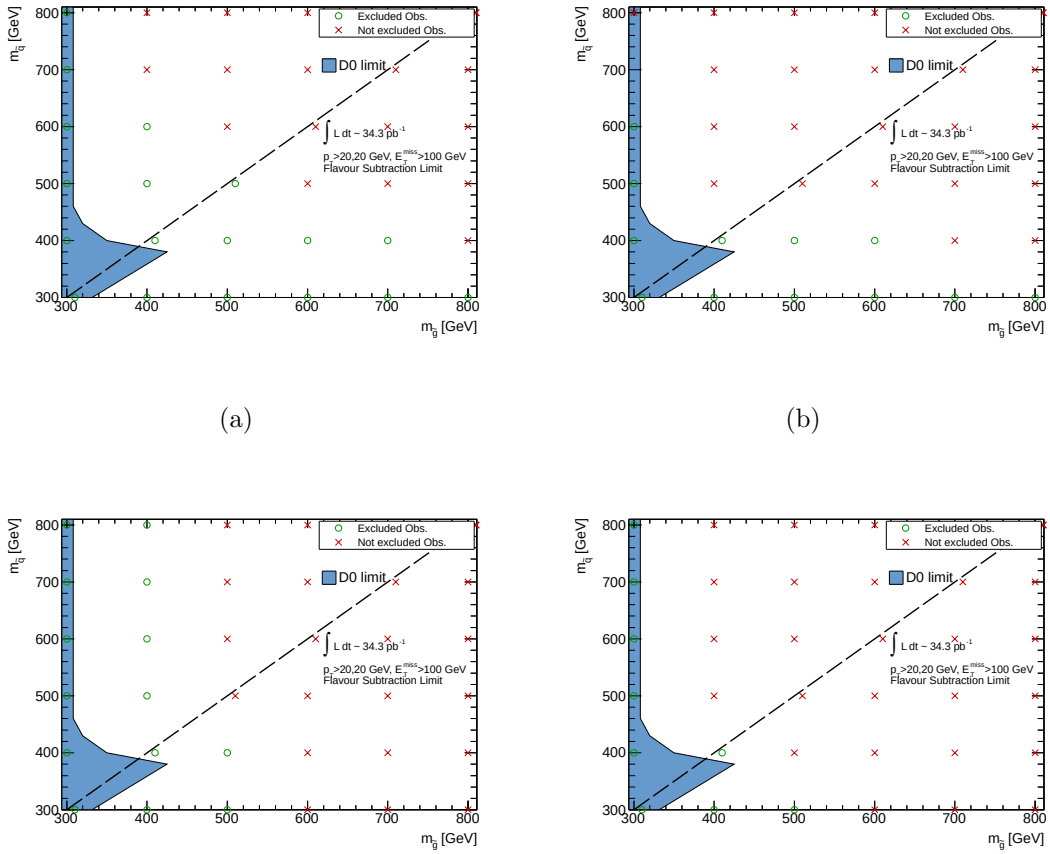

(a) (b)

(c) (d)

Figure 6.15: *Points excluded and not excluded at* 95% *confidence in the 5D-phenomenological grid presented in the* $m_{\tilde{g}} - m_{\tilde{q}}$ *plane for both the "light neutralino" PhenoGrid2 (a) and PhenoGrid3 (c) grids, and the "compressed spectrum" PhenoGrid2 (b) and PhenoGrid3 (d) grids. The line* $m_{\tilde{q}} = m_{\tilde{g}}$ *is marked on each of these figures. This line marks a discontinuity in branching ratios at* $m_{\tilde{q}} = m_{\tilde{g}}$*. When* $m_{\tilde{g}} < m_{\tilde{q}}$*, gluinos decay into a chargino or neutralino plus two jets. A significant fraction of these decays are to the neutralino plus two jet final state. This reduces the branching fraction of decays into leptons. The DØ limit is illustrative, but is based on a* $\tilde{g}\tilde{q}$ *search [122] so it is not a particularly suitable limit for comparison. This search, Ref. [8], the ATLAS inclusive search in Ref. [6] and a CMS search reported in Ref. [127], are the first experimental exclusions based on observations of two-lepton events in* $\sqrt{s} = 7$ TeV *data.*

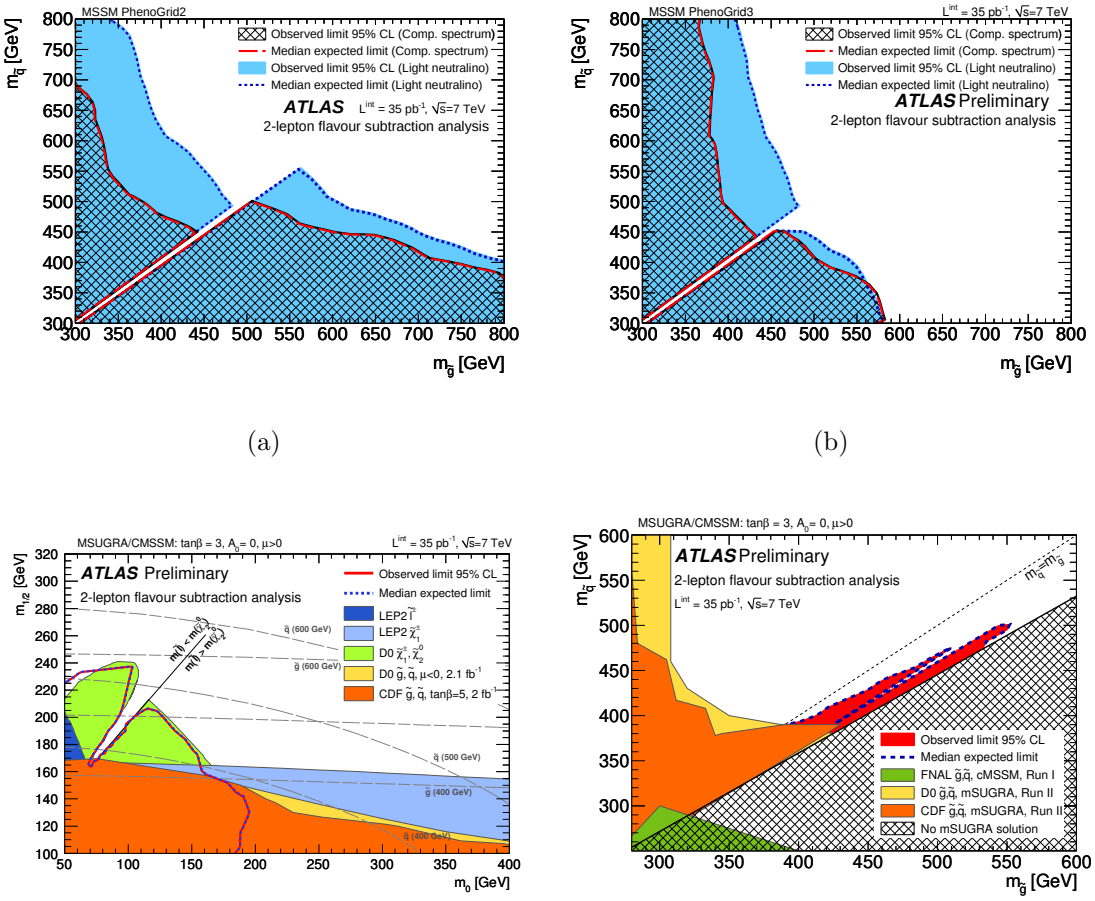

Figure 6.16: *"As released" observed exclusion limits for PhenoGrid2 (a), PhenoGrid3 (b) and mSUGRA (c),(d) (from Refs. [8] and [128]). The mSUGRA limits are presented in the $m_0 - m_{1/2}$ (c) and $m_{\tilde{g}} - m_{\tilde{q}}$ (d) planes. The p-value of each point has been calculated using the described toy experiments. These p-values have been converted into significances. The contour is the 95% confidence limit interpolated in these significances.*

It is possible to take these grids and the p-values of the excluded and not-excluded points to interpolate a contour in the significance. This was done to produce exclusion limits for publication by a member of the ATLAS collaboration. These interpolated contours are illustrated for both PhenoGrids and the mSUGRA parameter space in Figure 6.16. For PhenoGrid2 "compressed spectrum" ("light neutralino") models and $m_{\tilde{g}} = m_{\tilde{q}} + 10$ GeV, the 95% confidence lower limit on $m_{\tilde{q}}$ is 503 (558) GeV. For PhenoGrid3 the equivalent limits are 453 (454) GeV, at 95% confidence.

6.12 Conclusions

This chapter has presented the results of a flavour subtraction technique applied to the 2010 $\sqrt{s} = 7$ TeV ATLAS dataset to search for an excess of events containing opposite-sign identical-flavour lepton-pairs and significant missing transverse energy. Data corresponding to an integrated luminosity of 34.3 pb^{-1} has been analysed. No significant excess has been observed, allowing limits to be set on the parameters of the minimal supergravity framework, and also those of a phenomenological supersymmetric parameter space. An exclusion in the mSUGRA/CMSSM framework has been set which is similar to the Tevatron experiment's tri-lepton search exclusion. A model-independent limit has also been set on $\bar{\mathcal{S}}_s$, the mean contribution to the introduced quantity $\mathcal{S}$ (simply the number of excess identical-flavour events, multiplied by detector acceptances and efficiencies) from supersymmetry. This limit is robust and excludes at 95% confidence excesses $\bar{\mathcal{S}}_s > 12.6$ at 34.3 pb^{-1}, in models with equal branching ratios for decays to $e^{\pm}e^{\mp}$ and $\mu^{\mp}\mu^{\pm}$, and a relative branching ratio for different-flavour lepton-pair events to those of identical-flavour of 50%. The analysis presented is one which will scale very favourably with luminosity. This search, Ref. [8], the ATLAS inclusive search in Ref. [6] and a CMS search reported in Ref. [127], are the first experimental exclusions based on observations of two-lepton events in $\sqrt{s} = 7$ TeV data.

Part III

Monte Carlo Studies

Chapter 7

R-parity Violation with Jet Signatures

"Why, sometimes I've believed as many as six impossible things before breakfast."
— Lewis Carroll, Through the Looking-Glass (1872), ch.1

This chapter demonstrates how jet substructure techniques can be used to reconstruct experimentally challenging decays expected in certain R-parity violating supersymmetric scenarios. A model in mSUGRA parameter space is chosen and R-parity is violated by setting the λ''_{112} term in the superpotential (Chapter 2) to be non-zero. This permits the decay $\tilde{\chi}_1^0 \to qqq$, a decay which is likely to be difficult to detect in busy hadronic detector environments. In RPC supersymmetric scenarios, the presence of invisible particles in the final state complicates the reconstruction of the particle spectrum, but the large missing energy signature provides an efficient way of rejecting standard model background. In the RPV scenario here the final states are in principle completely reconstructable, but the experimental handle of high missing energy is absent.

In many supersymmetric decay chains, the long cascades give rise to high-p_T leptons. Previous studies of R-parity violating supersymmetry have exploited this leptonic signature as a means of identifying the decay, and more importantly as a means of reducing the standard model background [129]. In Ref. [129] both the $\tilde{\chi}_1^0$ and $\tilde{\chi}_2^0$ are reconstructed from cascade decays of a left-handed squark which is assumed to decay in a sequence of successive two-body decays that at one stage produces a right-handed

slepton ($\tilde{q}_L \rightarrow \tilde{\chi}_2^0 q \rightarrow \tilde{l}_R \ell q \rightarrow \tilde{\chi}_1^0 \ell\ell q$). The $\tilde{\chi}_1^0$ decays into three jets, and it is thus reconstructed by calculating the invariant masses of all possible three jet combinations in the final state. Addition of two final state leptons into this invariant mass then yields the possible $\tilde{\chi}_2^0$ candidates. Cutting a "window" into the resulting possible $\tilde{\chi}_2^0 - \tilde{\chi}_1^0$ space selects the combinations likely to be true decay chains, and the selected decay chains give an observable $\tilde{\chi}_1^0$ mass peak.

The method demonstrated in this chapter avoids the need for three-jet combinatorics, and does not rely on leptons being produced alongside the decaying $\tilde{\chi}_1^0$. It was originally proposed by J.M. Butterworth, G.P. Salam, A. Raklev and J.R. Ellis [130], in a study performed without detector simulation. This method exploits jet substructure to pick out the subset of highly boosted $\tilde{\chi}_1^0$ decays from the hadronic background. The three jets from the boosted $\tilde{\chi}_1^0$ become more collimated and, given an appropriately "sized" jet reconstruction algorithm, are thus reconstructed as single jets. The substructure of the resulting single jets can be used to determine which of the single jets are likely to be composed of three merged "sub-jets". Similar methods have been suggested as viable means of reconstructing hadronic W decays in elastic W-W scattering [131]. This method is tested in this chapter for use in ATLAS, using Monte Carlo events produced using full ATLAS detector simulation. The potential for a discovery of this type of RPV supersymmetry with ATLAS, using this technique, with up to 1 fb^{-1} of $\sqrt{s} = 10$ TeV data is gauged. It should be noted that whilst this method is tested here for use with R-parity violating supersymmetric decays, the same method could also be applied to any hadronically-decaying massive-particle resonance.

The work in this chapter is also described in one of the few $\sqrt{s} = 10$ TeV public ATLAS notes on supersymmetry, Ref. [13].

7.1 Motivation

Before presenting the analysis, it is beneficial to digress and discuss the possible motivations for exploring models which violate R-parity given that its introduction has so far only been motivated as a way of preventing proton decay (Chapter 2). The addition of R-parity violating terms, which violate baryon number (B) and lepton number (L), would seem at odds with observation. No baryon and lepton number violating processes

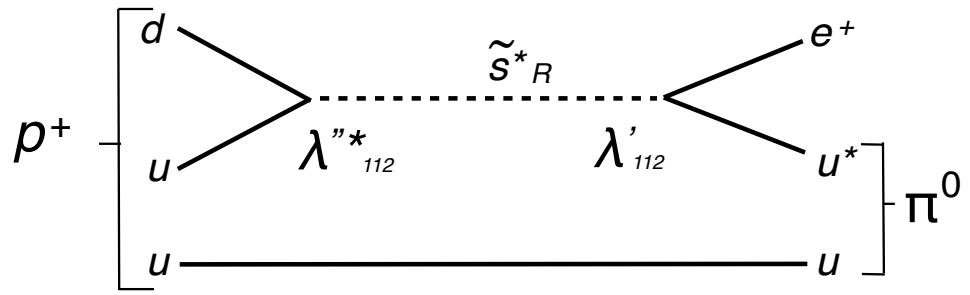

Figure 7.1: *Decay of the proton. In R-parity violating supersymmetric scenarios, non-zero and unsuppressed $\lambda^{'}$ and $\lambda^{''}$ couplings could give rise to a short proton-lifetime. This decay, which gives the final state $e^{+}\pi^{0}$, is one possible decay mode. Other decay modes include decays with $e^{+}K^{0}$, $\mu^{+}\pi^{0}$ and similar final states. The final state is dependent on the relative sizes of $\lambda^{'}$ and $\lambda^{''}$.*

have been observed experimentally. Proton decay, which would violate both baryon and lepton numbers by one unit, is the very obvious experimental consequence that has never been observed.

The R-parity violating terms, as introduced in Chapter 2, are again:

$$W = \frac{1}{2}\lambda^{ijk} L_i L_j \bar{e}_k + \lambda^{'ijk} L_i Q_j \bar{d}_k + \mu^{'i} L_i H_u + \frac{1}{2}\lambda^{''ijk} \bar{u}_i \bar{d}_j \bar{d}_k \tag{7.1}$$

If both $\lambda^{'}$ and $\lambda^{''}$ couplings were present and unsuppressed then the proton would have a very short lifetime. The proton would be able to decay, for example, into an $e^{+}\pi^{0}$ final state as illustrated in Figure 7.1. The allowable decay modes depend upon the relative sizes of the $\lambda^{'}$ and $\lambda^{''}$ components. For squark masses of $\sim$1 TeV, and couplings of order unity, the proton could decay in a fraction of a second [52]. This therefore sets bounds on $\lambda^{'ijk}$ and $\lambda^{''11k}$. For each $i = 1, 2$; $j = 1, 2$; $k = 2, 3$, at least one of $\lambda^{'ijk}$ and $\lambda^{''11k}$ must be extremely small. The upper-bounds placed on these couplings by proton decay are treated in detail by Ref. [132]. A review of the bounds on all the R-parity violating couplings, based on observations not just of proton decay but also of ν–$\bar{\nu}$ oscillation, ν_e-Majorana mass, neutrino-less double β decay and a variety of other processes, is given in Ref. [133].

The only motivation given so far for the introduction of R-parity as a symmetry is to ensure the stability of the proton. The introduction of this symmetry is not, however, the only way to prevent proton decay. "Baryon-parity" can conserve baryon number,

forbidding just the interactions $\bar{u}_i\bar{d}_j\bar{d}_k$, but allowing R-parity violation via the $L_iQ_j\bar{d}_k$ and $L_iL_j\bar{e}_k$ operators [134]. In many Grand Unified Theories and string theory there is no preference for either R-parity conservation or R-parity violation [134]. From the theoretical understanding of unification, there is no clear preference. It is thus very important to search experimentally for both R-parity conserving and R-parity violating decays, particularly given the very different phenomenologies they predict at colliders. R-parity violation has even been put forward as a potentially favoured solution to various experimentally observed discrepancies between observation and standard model predictions [133, 135]. In 1997, the ALEPH collaboration observed an excess in the number of events in the $e^+e^- \to 4$ jets channel [136]; many attempts to explain this anomaly by invoking R-parity violating couplings were made [133, 137–139].

7.2 The $k_\perp$ Algorithm and Jet Substructure

This section describes the $k_\perp$ algorithm [140]. This is the algorithm chosen to reconstruct jets in this study, and the algorithm which gives the necessary handle on jet substructure needed to select jets formed from merged sub-jets. It runs over the collection of calorimeter clusters in each event, and for cluster k and pair of clusters (k, l), it calculates the resolution variables (Equations 7.2 and 7.3):

$$d_{kB} = p_{Tk}^2 \tag{7.2}$$

$$d_{kl} = \min(p_{Tk}^2, p_{Tl}^2) R_{kl}^2 / R^2 \tag{7.3}$$

where p_{Tk} is the transverse momentum of cluster k with respect to the beam axis and R_{kl}^2 the separation in $\eta - \phi$ space between the clusters k and l, as defined in Equation 7.4. R is the "radius parameter", varied to change the "size" of the jets.

$$R_{kl}^2 = (\eta_k - \eta_l)^2 + (\phi_k - \phi_l)^2 \tag{7.4}$$

The precise definition of these three quantities (d_{kB}, d_{kl} and R_{kl}^2) control how the $k_\perp$ algorithm behaves in the soft and collinear limits. The choice of definitions, or scheme, is not expected to make a significant difference to the highly boosted jets of interest to this study. This ΔR angular scheme (Equation 7.4) is chosen in this study to match the choice made in Ref. [130].

The $k_\perp$ algorithm finds the smallest of d_{kB} and d_{kl}. If d_{kl} is the smallest then k and l are combined into a single object with momentum p_{kl}. If d_{kB} is smallest the object is merged with the beam-pipe object. This process is repeated until all objects have been included as jets. The parameter R in Equation 7.3 is normally of order one and plays a similar role to the R parameter in cone algorithms. Higher R parameters worsen the jet mis-reconstruction, because of the increased "junk" which may be included in the jet, but potentially improve the signal efficiency in this study by reconstructing greater numbers of neutralino candidates as single jets. An R parameter of 0.7 is chosen as it gives a sufficiently high signal efficiency, at the risk of overestimating reconstructed particle masses by including extra material in the jets. The choice of R parameter has not been optimised and so it may be the case that a slightly smaller R, or equally larger R, would improve the ratio of signal to background. The way that the p_{kl} of the new combined objects is calculated depends on the specified recombination scheme. The "E scheme" is chosen and in this scheme the four momenta of the two objects, k and l, are simply added linearly to form the four momenta p_{kl}.

The scale at which jets from two or more very collimated partons separate into their sub-jets is reflected in the values of d_{kl} calculated in the jet-finding algorithm. The proposed variable y, defined as $y = d_{kl}/m^2$ where m is the jet mass, is used to isolate the signal from the background [130]. Given that the hadronic resonance is of unknown mass, a scale invariant method is needed to pick out the decay. The $k_\perp$ distance, d_{kl}, is the relative transverse momentum distance between the merged objects. Any cuts purely on the d_{kl} values would tend to bias the search, as this cut would be dimensional. The variable y is dimensionless and satisfies this requirement. For any decaying mother particle, the interesting mergers are the final ones. Effectively the sequence of y values records the distance between the merged jet constituents. The value y_1 is defined as the scaled d_{kl} value from the last merging and y_2 as the scaled d_{kl} value from the penultimate merging. These two mergings are of interest because the $\tilde{\chi}_1^0$ has a 3-body decay.

This technique relies on the decaying particle, in this case the $\tilde{\chi}_1^0$, having sufficient boost to decay into three jets which "merge" to form a single jet. Figure 7.2 illustrates a measure of the pseudo-cone radius as a function of neutralino p_T for the three signal neutralino decay products (at parton level). The radius plotted is the smaller of the circumradius formed by the three jets (the relevant triangle used in the calculation of the circumradius having sides of length R_{ij} as defined in Equation 7.4) and half the

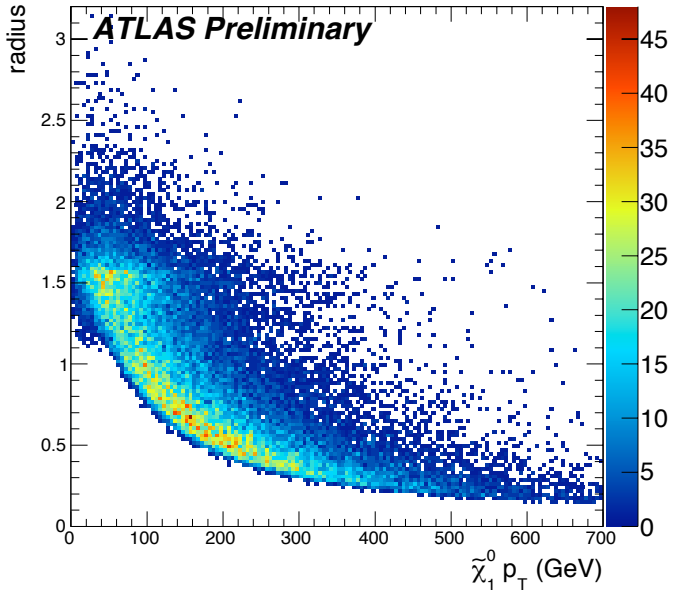

Figure 7.2: *Pseudo cone-radius as a function of neutralino p_T. The neutralino in the SPS1a mSUGRA point has a mass, $m_{\tilde{\chi}_1^0} \sim 96$ GeV. As neutralino p_T increases, the three jets from its decay become more collimated. For a neutralino mass of* 100 GeV*, the jets form a "cone" with radius ~ 0.6. The "larger" the jets formed, the higher the signal efficiency for finding neutralino decays but the amount of "junk" included in the jet greater.*

largest of the R_{ij}. This figure demonstrates that as the neutralinos become more boosted the degree of jet collimation increases.

7.3 Monte Carlo

This method is illustrated on the mSUGRA bulk benchmark point SPS1a [141]. The sparticle masses in this model are relatively light. The neutralino of interest, $\tilde{\chi}_1^0$, has a mass $m_{\tilde{\chi}_1^0} = 96.1$ GeV. The R-parity violating coupling, λ''_{112} is set to 0.001, and is the only coupling chosen to be non-zero. The SPS1a mSUGRA point was chosen for its reasonably high cross-section (17.4 pb at LO) but "difficult" dominant final state. By this it is meant that the choice of λ'' ensures a final decay with no heavy flavours or displaced vertices. In principle, heavy flavours and displaced vertices could provide an additional handle on the signal. SPS1a, or the "Snowmass" point, has the mSUGRA parameters: $m_0 = 100$ GeV, $\tan\beta = 10$, $A_0 = -100$, $m_{1/2} = 250$ GeV and $\mathrm{sgn}\,\mu > 0$. Selected sparticle masses are given in Table 7.1 for this point. The squark and gluino

masses are $\sim$500 and 600 GeV respectively. As Table 7.1 shows, these masses are much heavier than the $\tilde{\chi}_1^0$ mass and so the $\tilde{\chi}_1^0$ will be appropriately boosted.

$\tilde{\chi}_1^0$	$\tilde{\chi}_2^0$	$\tilde{g}$	$\tilde{u}_R$	$\tilde{u}_L$	$\tilde{d}_R$	$\tilde{d}_L$	$\tilde{\ell}_R$	$\tilde{\ell}_L$	h^0
96.1	176.8	595.2	520.4	537.2	520.1	543.0	143.0	202.1	114.0

Table 7.1: *Masses of selected particles in* GeV *in the SPS1a mSUGRA point. The squark masses are* $\sim 500 - 600$ GeV *and the lightest neutralino,* $\tilde{\chi}_1^0$*, much lighter at* 96.1 GeV*. This gives a scenario in which the produced* $\tilde{\chi}_1^0$ *are highly boosted.*

This particular coupling, $\lambda''_{112} = 0.001$, is actually ruled out by current experimental bounds [142, 143]. However, this method should be applicable to other combinations of $(i, j, k) = 1, 2$, many of which have much looser bounds. Given that this chapter is a test of a method, and given that any other combination of $(i, j, k) = 1, 2$ would give equivalent results, it is not of too much concern that this coupling is ruled out. The results here serve as a proof of principle, not an optimised study with a predicted search reach.

The standard model backgrounds to be considered include: $t\bar{t}$, dijets, $W \to \ell\nu$+jets and $Z \to \ell\ell$+jets. The dijet samples were generated using the `PYTHIA` [74] Monte Carlo generator with the `CTEQ6L1` [98] parton distribution functions. These dijet samples were generated in slices of $\hat{p}_T$, the transverse momentum of the two partons involved in the scattering process, for $\hat{p}_T > 17$ GeV, with total LO cross-section of 1.4×10^{12} fb. The $Z \to \ell\ell$+jets and $W \to \ell\nu$+jets samples were generated using the `ALPGEN` [97] Monte Carlo generator with the `CTEQ6L1` [98] parton distribution functions. The total cross-sections for $W \to \ell\nu$+jets and $Z \to \ell\ell$+jets production are 4.1×10^7 fb and 3.6×10^6 fb respectively at LO. The Z+jets and W+jets samples were both produced in slices of the number of partons in the hard scattering process. The semi-leptonic and fully-hadronic $t\bar{t}$ events were generated, with cross-sections of 202,860 fb and 170,740 fb respectively, using the `MC@NLO` [144] Monte Carlo generator to simulate the hard process, a generator including full NLO QCD corrections, `HERWIG` [73] for parton showering and fragmentation and `Jimmy` [99] for the underlying event. The `CTEQ6M` [145] NLO parton distribution function set is used. For these studies SPS1a RPV signal events were generated using the `PYTHIA` [74] Monte Carlo generator (using the older `PYTHIA` showering scheme). During reconstruction, locally-calibrated topological clusters [146] (clusters formed from an

algorithm which adds neighbouring cells with energy above a threshold to a seed cell iteratively) were built from calorimeter cells and passed as input to the $k_\perp$ algorithm using an R parameter of 0.7. All samples were generated at $\sqrt{s} = 10$ TeV and passed through the full `GEANT4` [75] simulation of the ATLAS detector by the ATLAS central production team.

7.4 Method

7.4.1 Particle Identification

The reconstructed particles used in this analysis are selected and identified as follows. Electrons are selected which have $p_T > 10$ GeV, and $|\eta| < 2.5$. These electrons must pass medium identification cuts (see Chapter 4). Muons are selected which have $p_T > 10$ GeV, and $|\eta| < 2.5$. The selected muons must pass a cut on the matched tracking fit between the ID and the outer muon systems of $\chi^2 < 100$. The energy deposited within a cone $\Delta R = \sqrt{(\Delta\phi)^2 + (\Delta\eta)^2} = 0.2$ around the muon is required to be less than 10 GeV. The selected photons must have $p_T > 10$ GeV and $|\eta| < 3.5$, passing "tight" photon selection. Taus with $p_T > 20$ GeV and $|\eta| < 3.5$ are selected. These must also have a likelihood discriminant of the jet-τ hypothesis greater than -6 [147]. All jets with $p_T > 20$ GeV and $|\eta| < 5.0$ are selected. Reconstructed objects passing the above cuts are declared as overlapping if they fall within: (i) $\Delta R = 0.2$ of each other for any two non-jet objects or (ii) $\Delta R = 0.3$ if one object is a jet. Electrons are selected first, then photons, muons and finally jets.

7.4.2 Offline Selection

Defining y_1 and y_2, as the y values from the last and penultimate merging of the jets, the following offline cuts are made: (i) require at least four jets in the event, with the four highest-p_T jets having $|\eta| < 2.5$, (ii) two of these jets must have $p_T > 275$ GeV, (iii) for both of these jets, $y_2 > -0.17y_1 + 0.08$ and (iv) there must be two further jets both with $p_T > 135$ GeV.

The first high-p_T jet cut (ii) is used to select highly boosted jets, likely to be neutralino candidates. Given that the signal events of interest are supersymmetric, there should

be two decay chains and each decay chain should end in an LSP. Thus two high-p_T jets are required because it is reasonable to expect two neutralino candidates for each signal event. The $y_{1,2}$ cut (iii) is chosen to eliminate a significant proportion of the background by exploiting the substructure of boosted jets which are formed by the merging of the three sub-jets (see Figure 7.5). These cuts look for structure in the most relevant jet mergings, the last two. The rejection achieved using these hard p_T cuts and structure cuts is not alone sufficient to obtain a significant signal. In order to achieve higher background rejection an additional cut (iv) is proposed, which requires the presence of two further jets with $p_T > 135$ GeV. This cut exploits the properties of the rest of the supersymmetric decay chain. Approximately 40% of neutralinos are produced directly by the decay of a squark. The decay of a squark to a neutralino produces an additional quark jet. Two non-neutralino jets are therefore expected in many of the RPV supersymmetric events. Even in longer decay chains, it is still likely a jet will have been produced somewhere in the cascade. These extra cuts maintain high signal efficiency therefore but further increase dijet background rejection.

7.4.3 Online Trigger

Triggers are required which will pass signal events efficiently, whilst significantly reducing the proportion of background events. In what follows the following convention is adopted: `nJxx` is a trigger requiring `n` jets with $p_T >$`xx` GeV and `JExx` a trigger asking for a jet with energy greater than `xx` GeV. Signal events are expected to have multiple high-p_T jets in the final state. The most useful triggers for this analysis are therefore the single (`Jxx`), multijet (`3Jxx`, `4Jxx`) and total jet energy (`JExx`) triggers. Table 7.2 tabulates the trigger efficiencies for a selection of these jet triggers. The first efficiency is the efficiency for passing all the supersymmetric events, the second is the efficiency for passing the subset of supersymmetric events which survive event selection.

From the efficiencies in Table 7.2, it is clear that the ATLAS trigger system has several un-prescaled jet triggers that should pass signal events with very high efficiency. The efficiency after selection is most relevant and should be near to 100% for the best triggers. Though an explicit trigger selection was not used for the results shown in subsequent sections, these numbers show that they will not be degraded due to losses of events at the trigger level. The most suitable triggers are the multijet triggers. If the rates for these triggers were found to be unexpectedly high, and so then prescaled by ATLAS,

Trigger	Prescale	Efficiency before selection (%)	Efficiency after selection (%)
J350	1	50.0	82.7
3J180	1	56.0	98.3
4J95	20	77.6	99.6
3J60	1000	95.0	99.6
J265	15	75.5	99.6
4J125	1	55.8	99.6
JE280	2	91.0	100
JE340	1	83.2	100

Table 7.2: *Trigger efficiencies for various jet triggers as given by the SPS1a signal point. The trigger efficiencies are given before selection, and after selection. The most relevant trigger efficiency, after selection, is near* 100% *for a good proportion of the triggers. Importantly, there are near* 100% *efficient triggers which are expected to be un-prescaled during ATLAS data-taking.*

the un-prescaled single jet trigger could also be used[1]. This would only yield a slight decrease in the significance of results. This would also be the most suitable trigger for a boosted particle decay in lower jet multiplicity events.

7.5 Results

The numbers of events by type passing each offline cut are given in Table 7.3. The masses and transverse momenta of all jets, in events which satisfy the first selection criterion, are illustrated in Figure 7.3 for each type of event. The distribution of jet p_T against mass for signal events features a vertical band at a mass of approximately 100 GeV (around the peak of the heavy neutralino resonance), for jets with transverse momenta above 250 GeV. In contrast, the distribution for standard model background events shows no such structure. For standard model background events, the bulk of the jet-mass distribution lies at low-p_T and low-mass. Therefore, the p_T cut applied in the second offline selection criterion should select jets in the signal produced by heavy

[1]This analysis was completed in June 2009. As of April 2011, the expected lowest un-prescaled Jxx trigger is J250, and the lowest un-prescaled 3Jxx trigger, 3J75. The event filter for jet triggers was not used during the 2010 $\sqrt{s} = 7$ TeV run.

particle decays preferentially. This can be illustrated further by projecting these jets onto the jet mass axis, as shown in Figure 7.4. In this projection the neutralino mass resonance is very visible. Jets from the decay of highly-boosted W bosons and top quarks also cause noticeable mass resonances near their respective masses. In all three cases these peaks are positioned higher than the true particle masses (96.1 GeV, $\sim$90 GeV and 175 GeV). This is a direct result of using a high R-parameter. The jet-algorithm has clustered more than just the three quarks from $\tilde{\chi}_1^0$ decay into the single jets. Clean-up procedures do exist which attempt to remove some of the "junk" in jets. These are not used here as the aim of this exercise is not a precise determination of the neutralino mass, but rather a demonstration that ATLAS has the necessary resolution required to exploit jet substructure in this way. Dijets are the dominant source of standard model background at this stage. This source must be reduced by several orders of magnitude before the identified interesting mass peaks are experimentally detectable.

The necessary reduction is achieved by the third event selection criterion. Finding an appropriate choice of cut requires a careful study of the jet y values for signal and background events. Figure 7.5 illustrates the correlation between the y values from the last and penultimate mergings for each event topology for jets with $p_T > 275$ GeV. The dashed line on these distributions marks the chosen y value cut. Events with y values above this line are accepted, whilst events below are rejected. In supersymmetric events, both y_1 and y_2 are widely distributed, much more so than in the standard model events. This is an expected result, the dominant dijet background should not exhibit

	At least four jets	Two jets with $p_T > 275$ GeV	$y_2 > -0.17y_1 + 0.08$ for both jets	Two extra jets with $p_T > 135$ GeV
SPS1a	14,577	5,849	792	347
$t\bar{t}$	2.3×10^5	$2,000$	200	1
dijets	3.2×10^9	1.1×10^6	1.8×10^4	$1,100$
W+jets	$1,500$	20	20	0
Z+jets	1.9×10^4	210	2	1

Table 7.3: *Numbers of events passing each offline cut, for SPS1a and each standard model background (assuming an integrated luminosity of* 1 fb^{-1}*). The cuts in each row are sequential and cumulative. The event selection cuts reduce the dijets by a factor* $\sim 10^6$*, with much smaller impact on the number of signal SPS1a events. Event counts are rounded to appropriate illustrative numbers of significant figures, only SPS1a event counts are exactly as counted in the Monte Carlo.*

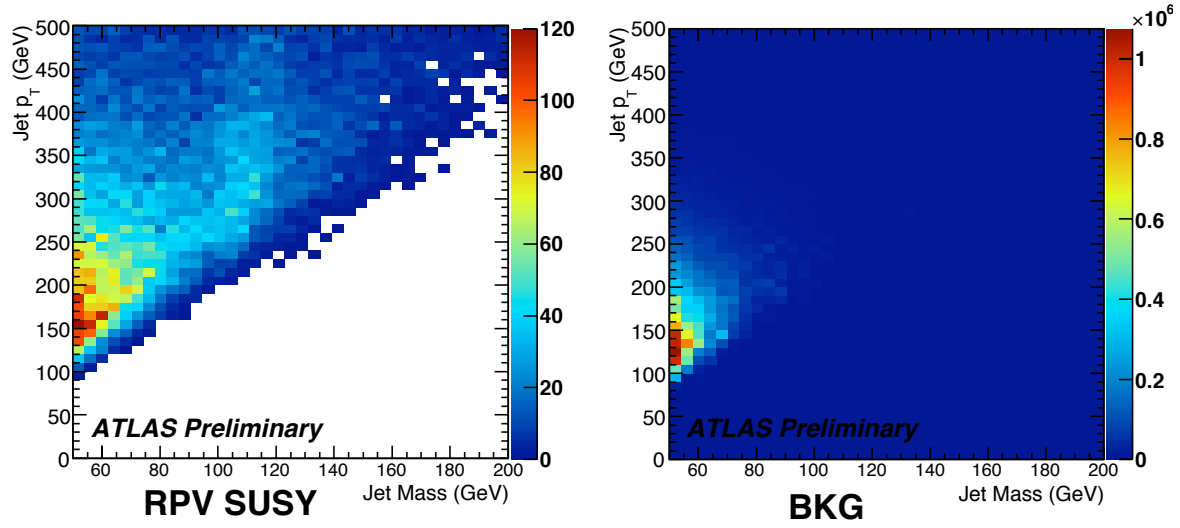

Figure 7.3: *Jet p_T vs. jet mass for jets in supersymmetric events (left) and standard model events (right) with at least four jets lying in the range $|\eta| < 2.5$, for 1 fb^{-1} of integrated luminosity at $\sqrt{s} = 10$ TeV. There is clear structure present in the strip at $\sim$100 GeV in supersymmetric events, which is not present in the standard model background distribution. Note: as marked, the z-axis for the background events has a scale of 10^6.*

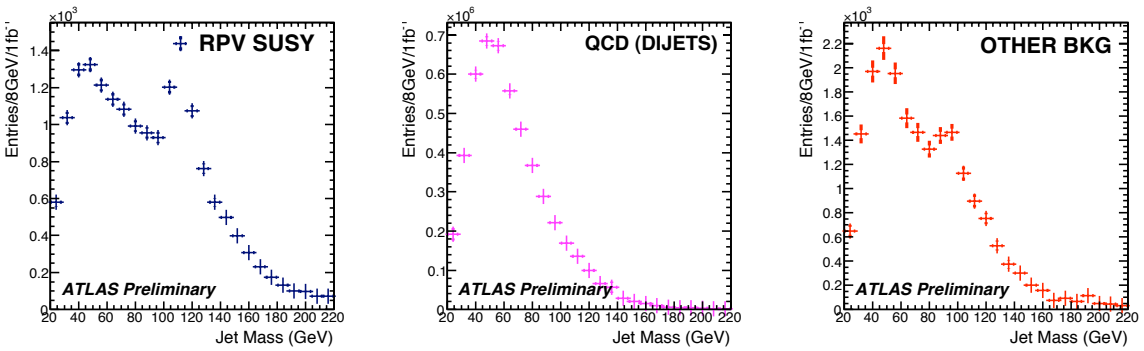

Figure 7.4: *Jet mass distributions of jets with $p_T > 275$ GeV in events with at least four jets with $|\eta| < 2.5$, for 1 fb^{-1} of integrated luminosity at $\sqrt{s} = 10$ TeV. For SPS1a events (left), the jet mass distribution peaks near the mass of the neutralino ($\sim$100 GeV), for dijet events (middle) the distribution steadily decays after the distribution turn-on, whilst for Z+jets, W+jets and $t\bar{t}$ events (right) the distribution peaks just above the top ($\sim$174 GeV) and W/Z masses (80 − 90 GeV). The error bars are statistical sum-of-weights squared errors. Note the y-axis scales: 10^6 for dijet QCD events, but 10^3 for the RPV point and other standard model backgrounds.*

any particularly strong structural features.

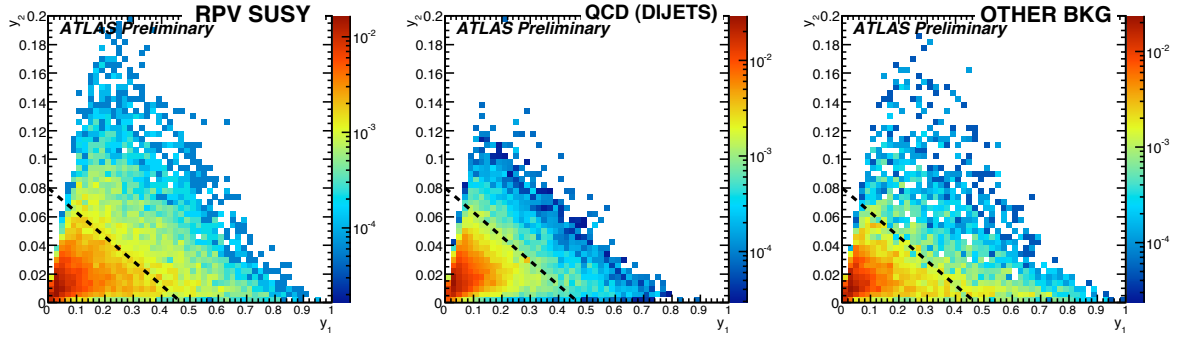

Figure 7.5: *Distributions of y_2 vs. y_1 for jets with $p_T > 275$ GeV in supersymmetric and standard model background events with at least four jets (distributions normalised to unity). Distributions are for an integrated luminosity of* 1 fb^{-1} *at* $\sqrt{s} = 10$ TeV. *The line illustrated is the line* $y_2 = -0.17y_1 + 0.08$, *events above which are accepted and events below which are rejected.*

This y value cut does not provide the necessary rejection against QCD backgrounds alone. The chosen y value cut of $y_2 > -0.17y_1 + 0.08$ must be supplemented with the fourth listed cut, the requirement that there be a 3rd and 4th jet each with $p_T > 135$ GeV. The masses of the two highest-p_T jets remaining, after the substructure and additional jet p_T cuts are applied, are illustrated in Figure 7.6. These additional event selection cuts have had some impact on signal efficiency, but the impact of these cuts is greatest away from the signal jet mass peak (which has only decreased by a factor of ten). This reduction compares favourably with the large suppression of QCD jets at a level of 10^3 across the distribution. In Figure 7.7, the p_T distribution of jets in the signal sample passing the event selection cuts is also given. This distribution illustrates the transverse momentum range of the jets selected as neutralino candidates.

Comparing the resulting dijet background and signal mass distribution (Figure 7.8) directly, it is clear that there are comparable numbers of signal and background events after cuts. Moreover, there remains a very clear peak in the signal distribution at the mass of the neutralino. The QCD mass distribution suffers from low statistics, due to the limited Monte Carlo datasets available. At least an order of magnitude more simulated QCD events would be needed to reduce significantly the high event weights. The errors expected from an integrated luminosity of 1 fb^{-1} are better modelled by the Poisson errors, which are shown in Figure 7.8 as the smaller of the two sets of vertical

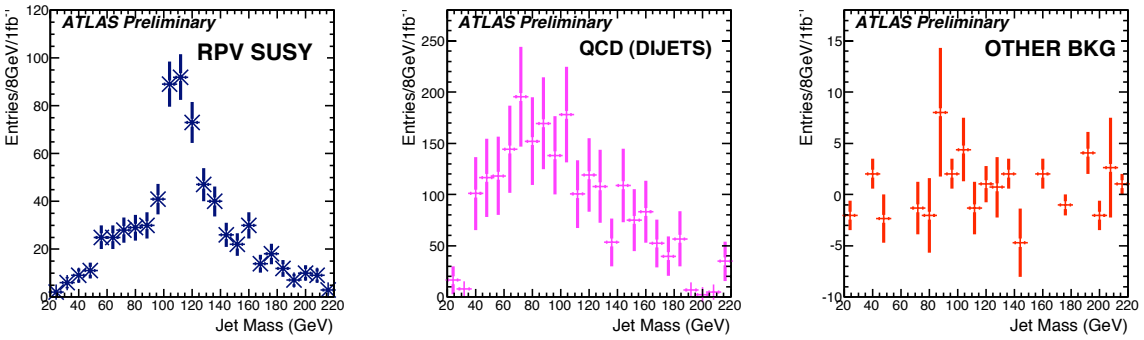

Figure 7.6: *Jet mass for jets with* $p_T > 275$ GeV *and* $y_2 > -0.17y_1 + 0.08$ *in events passing all event selection cuts, at an integrated luminosity of* 1 fb^{-1} *at* $\sqrt{s} = 10$ TeV. *The jets peak at a mass near the neutralino mass in SPS1a events (left). The jet mass distributions for dijet events (middle) and W+jets, Z+jets and* $t\bar{t}$ *events (right) are also shown. The error bars are statistical sum-of-weights squared errors.*

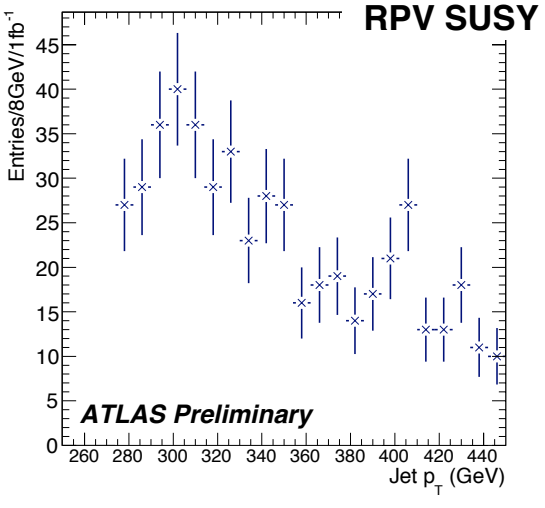

Figure 7.7: *Jet* p_T *for jets with* $p_T > 275$ GeV *and* $y_2 > -0.17y_1 + 0.08$ *in signal events passing all event selection cuts, at an integrated luminosity of* 1 fb^{-1} *at* $\sqrt{s} = 10$ TeV. *The error bars are statistical sum-of-weights squared errors.*

error bars. For this model point, the background has been reduced to a level at which it is of manageable size, one which is comparable to the signal. This suggests that models (whether supersymmetric or otherwise) which can pair produce states with mass greater than $\sim$100 GeV, with transverse momenta similar to those of Figure 7.7, and where those states subsequently decay to three jets, are likely to be observable at ATLAS. The difficulty in realising this analysis in data is that it would require a sound understanding of the QCD background distribution.

The shape and post-selection cross-section of the QCD background are the main systematic uncertainties in this analysis. For example, were the QCD background to be twice as large, any signal significance would drop by a factor of $\sqrt{2}$. The shape of the mass distribution may also change. The steeper the slope of the QCD background distribution towards high mass, the greater the signal cross-section needed to obtain high signal significance. If the background were flatter, evidence for a signal peak would be obtainable at much lower signal cross-sections or with more QCD background. The cuts chosen have not been fully optimised, rather they serve to illustrate the suitability of the method.

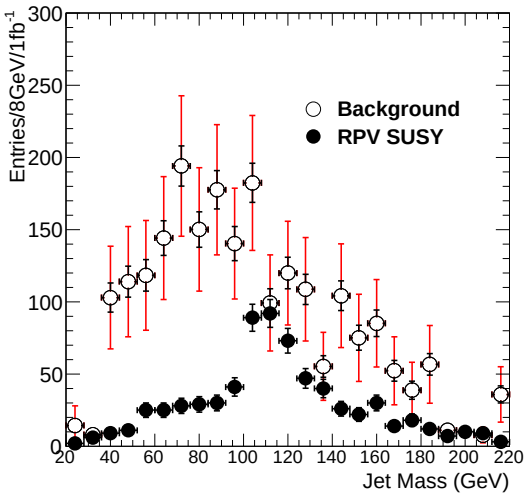

Figure 7.8: *Jet mass for jets with* $p_T > 275$ GeV *and* $y_2 > -0.17y_1 + 0.08$ *in events passing all event selection cuts, at an integrated luminosity of* 1 fb^{-1} *at* $\sqrt{s} = 10$ TeV. *The error bars are statistical sum-of-weights squared errors, on which (smaller) Poisson* $\sqrt{N}$ *errors are drawn.*

7.6 Summary

This chapter has demonstrated the technique described in Ref. [130] for reconstructing heavy-particle decays into three-jets by exploiting the substructure of the single jets formed when these decays are boosted. This approach has been illustrated using R-parity violating $\tilde{\chi}_1^0 \to qqq$ supersymmetric decays where the exploitation of jet substructure preferentially selects the jets from boosted neutralino decays over QCD jets, the dominant source of standard model background. The demonstration suggests that if such decays were present in data, they may be observable in the ATLAS detector. To perform this analysis on data, a thorough estimation of the QCD background shape would be required and a complete evaluation of the systematic uncertainties necessary.

Chapter 8

Measuring Slepton Masses and Mixings

"Slow and steady wins the race."
— Aesop, The Hare and the Tortoise

Physicists do not have an understanding of the smallness nor the hierarchy in the standard model flavour parameters, and this makes flavour physics interesting. Flavour physics also holds a key to understanding theories beyond the standard model. If supersymmetry is discovered at the LHC, then studying its flavour properties (the masses and mixings of the sleptons and squarks) may shed light not only on the underlying structure of supersymmetry and supersymmetry breaking, but may also very well lead to a big step forward in the understanding of the standard model flavour parameters. In this chapter, new steps toward a quantitative analysis of the actual prospects for supersymmetric flavour measurements at the LHC are undertaken. A number of alternative, earlier studies of lepton flavour violation at the LHC [148–156] also exist. This chapter investigates how many sleptons it might be possible to find at the LHC and how precisely their masses might be determined, whilst also making tentative steps towards measurements of their flavour decompositions. In what follows lepton flavour is violated meaning that the measurement of the flavour decomposition in the model chosen is both interesting and non-trivial.

Any such analysis is only feasible in the event of discovering supersymmetry, but it is also only realisable towards the latter stages of an experiments run. The study that follows considers as much as 100 fb^{-1} integrated luminosities worth of experimental data, at high centre of mass collision energy. The approach taken is not to select a wide variety of supersymmetric models and explore the potential measurements that could be made from each, but to instead pick one particular model with relevant characteristics, shared by a variety of models, and show that in some, well-motivated cases, answering these questions may be possible.

In Ref. [9] hybrid supersymmetric models are constructed in which sfermion masses receive both flavour conserving gauge-mediated contributions and flavour violating gravity-mediated contributions governed by a $\text{U}(1) \times \text{U}(1)$ horizontal symmetry. A particular realisation of one of these models is analysed in this chapter. Significant flavour mixing for sleptons and sneutrinos is expected in these models. A more detailed summary of these types of model is given in Refs. [9, 10]. Only the experimental features, relevant to the tests of experimental observability which follow, are highlighted in this chapter. The techniques developed will be also applicable to models with other forms of hybrid supersymmetry breaking [157, 158] and other similar frameworks where these important features are also realised. In these models, the LSP is the gravitino, and the NLSP, a charged slepton, is metastable. Not only is there no missing energy associated with the NLSP but, in principle, the supersymmetric decay chains are fully reconstructable. The charged sleptons will leave curved and detectable tracks in a detector yielding the ability to measure both their momentum and their speed (by charting the progress of the track through the detector, their "time-of-flight"). In the model selected the majority of the slepton mass splittings are large enough to be observable, and a selection of the flavour mixings are significant. These features will benefit any attempt to measure masses and mixings.

The analysis in this chapter is published in Ref. [10], and the "Shifted Peak" method used in this chapter published in Ref. [15].

8.1 Flavour and Supersymmetry

The soft-supersymmetry breaking terms in the supersymmetric Lagrangian introduce many new parameters, not present in the standard model. There are a total of 105 masses, phases and mixing angles in the MSSM Lagrangian that have no counterpart in the ordinary standard model. This arbitrariness in the supersymmetric Lagrangian is a result of supersymmetry breaking, rather than of supersymmetry itself. The unknown details of the MSSM are contained in the soft-supersymmetry breaking terms of the Lagrangian.

Fortunately the new parameters introduced by soft-supersymmetry breaking are parameters which imply $\mathcal{CP}$ violation or flavour mixing and experimental results severely restrict these types of parameter. The flavour mixing parameters are of relevance to the work in this chapter and so a brief discussion of the constraints on the flavour parameters is now given. Consider the 3×3 matrix in family space, $\mathbf{m^2_{\tilde{e}}}$. If this matrix is not diagonal in the basis of sleptons whose superpartners are the right-handed parts of the standard model mass eigenstates e, μ, τ, ($\tilde{e}_R$,$\tilde{\mu}_R$,$\tilde{\tau}_R$) then the slepton mass states are not identical to the flavour states. Slepton mixing will occur, and individual lepton numbers will not be conserved. No longer are there three right-handed sleptons, selectron-right, smuon-right and stau-right each with a unique mass. Instead the mass states are each mixtures of the flavour states. Experiment gives a limit on the components of the $\mathbf{m^2_{\tilde{e}}}$ matrix.

The process, $\mu \to e\gamma$ can arise from a non-zero value of $-\mathbf{m^2_{\tilde{e}}}_{21}\tilde{\mu}^*_R\tilde{e}_R$ (the degree of $\tilde{e}$ and $\tilde{\mu}$ in $\tilde{\ell}_1$, Figure 8.1(a)). The experimental limit on the branching ratio for $\mu \to e\gamma$ is currently 1.2×10^{-11} at 90% confidence [159]. It can be shown [52] that if a random right-handed slepton squared-mass matrix $\mathbf{m^2_R}$ were picked with "random" entries of comparable size, then the predicted rate would be larger than the experimental bound, even if slepton and bino masses were shifted as high as 1 TeV. If the superpartners are lighter, it is even harder to make a prediction which gives a branching ratio within the experimental limit. Left and right-handed sleptons with different flavours are mixed in Figure 8.1(b). The elements of the left-handed slepton squared-mass matrix $\mathbf{m^2_L}$ will also contribute to the rate of $\mu \to e\gamma$ (Figure 8.1(c)).

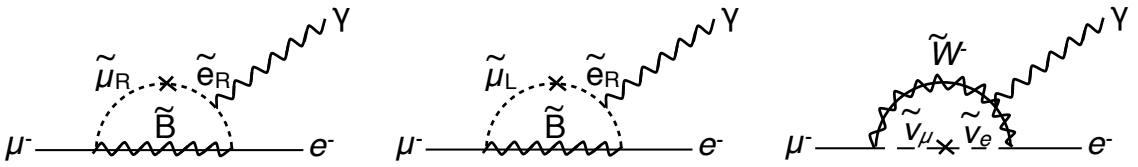

(a) (b) (c)

Figure 8.1: *Loop diagrams contributing to $\mu^- \to e^-\gamma$ in models with lepton flavour violating soft supersymmetry breaking parameters. The experimental limits on $\mu \to e\gamma$ decay severely constrain the flavour violating terms of the soft-supersymmetry breaking supersymmetric Lagrangian. The new parameters introduced by soft-supersymmetry breaking are parameters implying either $\mathcal{CP}$ violation or flavour mixing.*

Therefore it is clearly the case that any model which wishes to violate lepton flavour and introduce a non-diagonal ($\mathbf{m^2_{\tilde{e}}}$) must remain within these bounds convincingly. In the most general models where the left-handed and right-handed sleptons with different lepton flavours can mix, even finding evidence for this left-right mixing is useful[1].

8.2 The Model

In Figure 8.2 the masses and flavour compositions of the sleptons in the particular model studied are given (for more details see Refs. [9, 10]). The six sleptons are labelled $\tilde{\ell}_i$ with $i = 1, 2, 3, 4, 5, 6$. In this naming scheme the lightest slepton is named $\tilde{\ell}_1$ and the heaviest, $\tilde{\ell}_6$. These sleptons are the mass eigenstates, each of which is a combination of the six possible flavour states ($\tilde{e}_R$, $\tilde{\mu}_R$, $\tilde{\tau}_R$, $\tilde{e}_L$, $\tilde{\mu}_L$ and $\tilde{\tau}_L$).

In this model, sleptons $\tilde{\ell}_{1,2,3}$ are dominantly right-handed, whilst the sleptons $\tilde{\ell}_{4,5,6}$ are dominantly left-handed. Left-right mixing in these sleptons is negligible, with the exception of a small amount of this mixing in $\tilde{\ell}_3$ and $\tilde{\ell}_5$ which carry small τ_L and τ_R components respectively. The lightest two sleptons are predominantly a selectron and a smuon. This particular feature is a favourable one. Other features of this model are not so favourable: (i) the two lightest sleptons are quasi-degenerate, with a mass splitting of roughly 5 GeV, (ii) the mixing of these two sleptons is small and (iii) one of the

[1]It is of note that it is not just mixing between different right-handed flavour states which gives flavour violation, but also mixing between different right and left-handed flavour states.

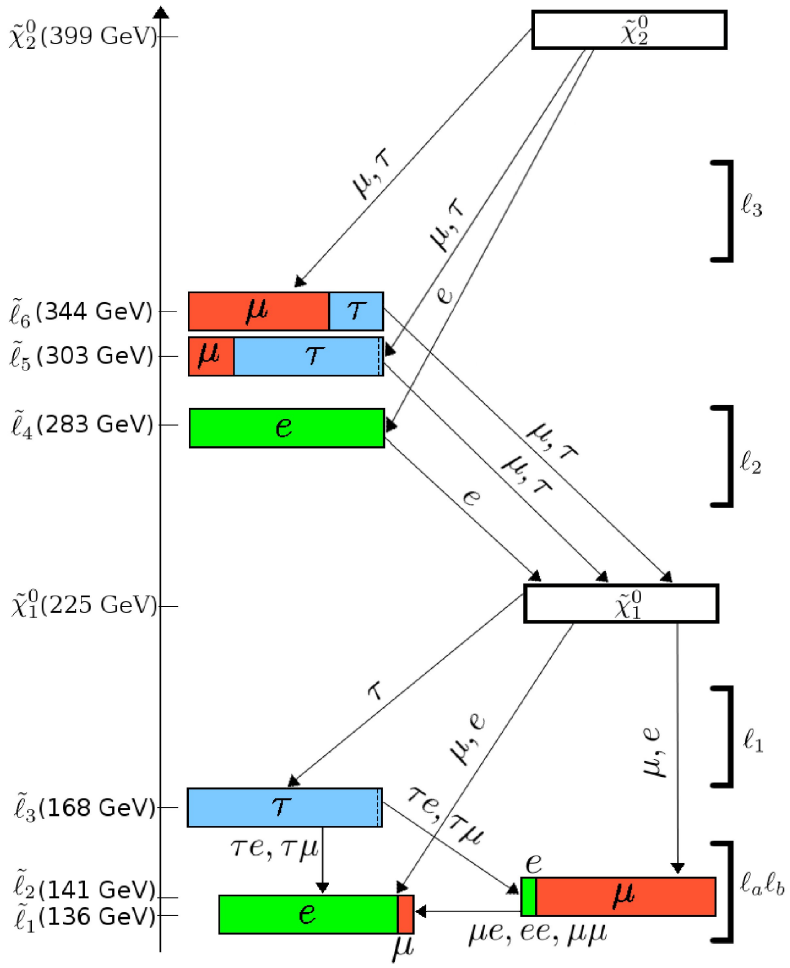

Figure 8.2: *The masses and flavour compositions of the six sleptons (from [10]). All decays involving sleptons which start with the decay of the heaviest of the two lightest neutralinos, are illustrated. The leptons which result from these common decay modes are also detailed. The labels ℓ_1, ℓ_2 and ℓ_3 refer to the single leptons produced at each step of the decay, these will be used later in the text. Sleptons $\tilde{\ell}_{1,2,3}$ are dominantly right-handed, with the dotted line in $\tilde{\ell}_3$ illustrating the small $\tilde{\tau}_L$ component. The sleptons $\tilde{\ell}_{4,5,6}$ are dominantly left-handed, with the dotted line in $\tilde{\ell}_5$ illustrating the small $\tilde{\tau}_R$ component. Left-right mixing in the other sleptons is negligible.*

remaining sleptons is an almost pure stau, so that its decays always involve taus which are hard to reconstruct.

8.3 Event Generation

Signal events are generated with centre-of-mass energy $\sqrt{s} = 14$ TeV using `HERWIG` [73, 160] and passed through a generic LHC detector simulation, `AcerDET 1.0` [77]. The package `AcerDET` is configured as follows: electrons and muons are selected with $p_T > 6$ GeV and $|\eta| < 2.5$. Electrons and muons are considered to be isolated if they are separated from other leptons and jets by $\Delta R > 0.4$, and if less than 10 GeV of energy is deposited in a cone of $\Delta R = 0.2$. The lepton momentum resolutions chosen are parameterised from the results of Full Simulation of the ATLAS detector [67]; the electrons are smeared according to a pseudorapidity-dependent parametrisation, while muons are smeared according to the results for $|\eta| < 1.1$. The LO 2-to-2 supersymmetric cross-section determined by `HERWIG` with `CTEQ5L` parton distribution functions is 1.154 pb. A total of 115,400 events are generated, corresponding to 100 fb^{-1} of data. `AcerDET` does not take into account lepton reconstruction efficiencies. Therefore a reconstruction efficiency of 90% is applied by-hand to the muons and a reconstruction efficiency of 77% to the electrons giving 0.86 as the ratio of electron to muon reconstruction efficiencies.

In a real detector (or full simulation thereof), the passage of a long-lived charged slepton, like the $\tilde{\ell}_1$, through it would produce a visible, curved track. A measurement of the curvature of this track could be used to determine the $\tilde{\ell}_1$ momentum-to-charge ratio, which could be used to determine its momentum under the assumption that all heavy tracks have unit charge. If the $\tilde{\ell}_1$ arrival time was also measured, these two pieces of information could be used to determine the $\tilde{\ell}_1$ speed. The measurements of momentum and speed could then be combined to determine the track mass. A measurement of the mass of the $\tilde{\ell}_1$, would constitute the primary signature for new physics in the signal events. Since `AcerDET` is not a full detector simulation, it does not produce track objects or speed "measurements" associated with the long-lived sleptons. Therefore it is necessary to augment `AcerDET` by incorporating additional parameterisations for $\tilde{\ell}_1$ momentum and speed measurements into this analysis. Resolutions for these measurements are taken from Ref. [161], a study based on ATLAS Muon Resistive Plate Chamber

timings[2]. The reconstructed $\tilde{\ell}_1$ momentum is modelled by taking the momentum from Monte Carlo truth and then "smearing" the magnitudes of the $\tilde{\ell}_1$ 3-momentum, $p \equiv |\vec{p}_{\tilde{\ell}_1}|$, and speed β, by Gaussian distributions with $\sigma_p/p = 0.05$ and $\sigma_\beta = 0.02$, respectively. The slepton's energy and direction are not smeared. Only sleptons with $\beta > 0.6$ are taken to to reconstructed, sleptons moving any slower are unlikely to reach the muon chambers in time to be registered in the same bunch crossing. In these signal events, 95% of sleptons have a speed, β, greater than 0.6.

In all that follows, the expressions like "$\tilde{\ell}_1$ momentum" and "β" refer to these smeared ("reconstructed") quantities, rather than the Monte Carlo truth.

8.4 Analysis

In this section, the approach used to measure the mixings and masses of the six sleptons is outlined, and the results of applying this are then illustrated. As the NLSP is a metastable charged particle (reconstructed as described in Section 8.3), in principle the entire decay chain is fully reconstructible (that is, the four-momentum of each particle in the decay chain is known). The goal of this analysis is therefore to reconstruct the various superpartners, starting with the slepton NLSP, by working step-by-step up the various decay chains (Figure 8.2), constructing the various invariant mass distributions. In this section each invariant mass distribution constructed is motivated, and the resulting interpretation of each distribution given. In the concluding section a more detailed interpretation is given, in terms of flavour mixings.

Tau leptons are ignored, and instead only deductions and measurements of masses and mixings from observing electrons and muons are made. Tau reconstruction is expected to be poor in comparison to electron and muon reconstruction, and it is for this reason that this method does not rely on it. It is hoped that with 100 fb^{-1}, sufficient understanding of tau lepton performance will be available to supplement these methods.

[2]Note that an alternative parametrisation, based on ATLAS Muon Drift Tube fits [162], could equally well have been used. The resolution obtained here may not reflect the maximum potential realisable.

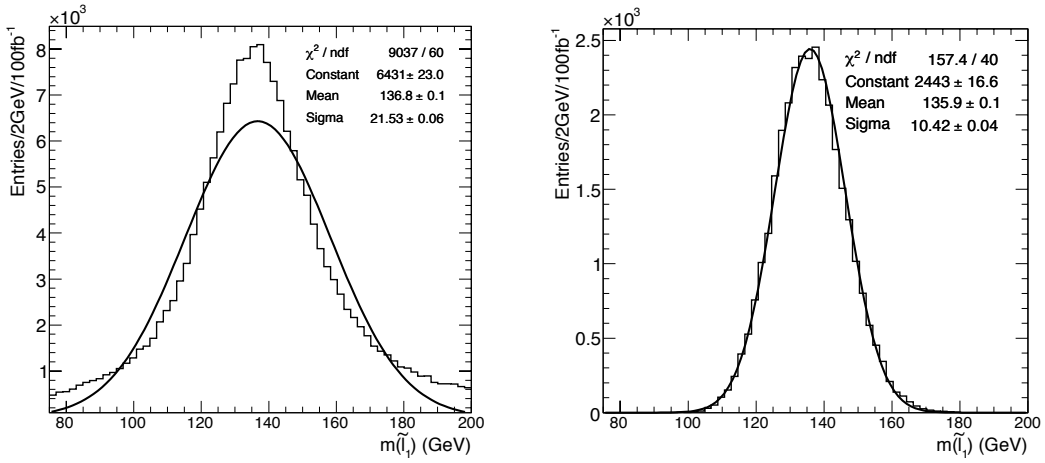

(a) $\beta > 0.6$ (b) $0.6 < \beta < 0.8$

Figure 8.3: *Reconstructed $\tilde{\ell}_1$ masses from events with slepton speed, $\beta > 0.6$ (a) and $0.6 < \beta < 0.8$ (b). The histograms are the distributions, and the solid lines are Gaussian fits with means and standard deviations as indicated. The Gaussian fit for (a) is poor and is shown for comparison only. The $\tilde{\ell}_1$'s 3-momentum magnitudes $p \equiv |\vec{p}_{\tilde{\ell}_1}|$ and speeds have been smeared by Gaussian distributions with $\sigma_p/p = 0.05$ and $\sigma_\beta = 0.02$, respectively. These two smeared quantities are combined to give the $\tilde{\ell}_1$ mass.*

8.4.1 The Slepton NLSP ($\tilde{\ell}_1$)

In each event, it is expected that direct reconstruction of the $\tilde{\ell}_1$ momentum, speed, and mass using the slow charged track signature described in Section 8.3 will be relatively straightforward. Only sleptons with speeds in the range $0.6 < \beta < 0.8$ are considered. The lower bound restricts the study to $\tilde{\ell}_1$ likely to arrive in the same bunch-crossing, whilst the upper bound is expected to effectively distinguish supersymmetric events from standard model background [163–165], and also to play a crucial role in improving the resolution of the $\tilde{\ell}_1$ mass measurement. Of the sleptons with $\beta > 0.6$, 15% have $\beta < 0.8$ and so pass this extra restriction. The reconstructed mass distribution is shown in Figure 8.3 before and after the application of the upper β bound. As expected, even ignoring background that will enter the $\beta > 0.6$ distribution, a better measurement of slepton mass is obtained if just the slowest sleptons are considered. After the $0.6 < \beta < 0.8$ requirement on the slepton's speed, it is assumed that the efficiency for reconstructing $\tilde{\ell}_1$ is 100%.

A measurement of $m_{\tilde{\ell}_1} = 135.9 \pm 0.1$ GeV is obtained from the Gaussian fit[3] to the distribution of slepton masses given in Figure 8.3(b). For any given event, the slepton mass is measured to an accuracy of the order of 10 GeV. The integrated luminosity of 100 fb^{-1} is sufficient to allow a measurement of the $\tilde{\ell}_1$ mass with much smaller statistical error ($\sim$0.1 GeV). The measured mean agrees well with the underlying true $\tilde{\ell}_1$ mass. Such agreement was to be expected as no sources of systematic offsets were introduced in the smearing process. Realistically, the fitted mean reconstructed $\tilde{\ell}_1$ mass will be subject to some systematic offset, even after all attempts to calibrate the detector have been completed. The size and direction of such an offset, however, cannot be known in advance. In this analysis, no attempt is made to simulate systematic offsets. The quoted errors in this rest of this chapter are statistical uncertainties only.

The high precision mean mass measurement can be used to "reduce" some of the momentum and time-of-flight measurement errors in individual events. Each component of the four-momentum of every slow charged particle is scaled by a single constant so that the corresponding mass matches exactly the mean mass obtained from the fit to the mass distribution. This event-by-event rescaling process is necessary to give sufficient resolution to enable a determination of the masses of sparticles heavier than the NLSP. After this rescaling, the smeared and rescaled momentum is centred on the true momentum with a full-width half-maximum of 27 GeV and root-mean-squared (r.m.s) of 9.9 GeV, and the corresponding energy difference distribution has a full-width half-maximum of 31 GeV and r.m.s of 9.4 GeV.

8.4.2 The Lightest Neutralino ($\tilde{\chi}_1^0$) and Next-to-Lightest Slepton ($\tilde{\ell}_2$)

The next particles to reconstruct are the next two lightest sleptons, $\tilde{\ell}_{2,3}$. Figure 8.2 shows that the dominant $\tilde{\ell}_{2,3}$ decays are three-body decays. In principle, given an ideal detector, the $\tilde{\ell}_{2,3}$ decays could be reconstructed by looking at the three-particle invariant mass distributions which result from combining the reconstructed $\tilde{\ell}_1$ with all possible combinations of two further leptons which give a charged $\tilde{\ell}_{2,3}$ candidate. Since taus are not reconstructed in this analysis, the $\tilde{\ell}_3$ cannot be reconstructed in this way (see Section 8.4.3 for a discussion of $\tilde{\ell}_3$).

[3]The fits here, and all other fits in this chapter were performed using `RooFit` [166].

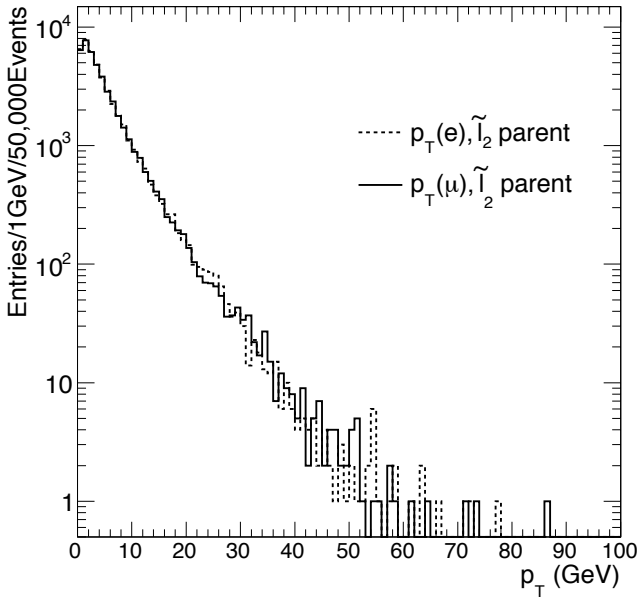

Figure 8.4: *The true p_T distribution of leptons ($\ell = e, \mu$) from the three body decays $\tilde{\ell}_2 \to \ell\ell\tilde{\ell}_1$. This figure illustrates that $\sim 90\%$ of all electrons and muons have $p_T < 10$ GeV. Leptons with $p_T < 10$ GeV are termed "soft" leptons, and provide more of a reconstruction challenge than higher p_T ("hard") leptons.*

Unfortunately, direct reconstruction of $\tilde{\ell}_2$ is also impossible as $\tilde{\ell}_1$ and $\tilde{\ell}_2$ are nearly degenerate. This near-degeneracy produces very low-p_T leptons when the $\tilde{\ell}_2$ decays. In Figure 8.4 the true p_T of all leptons produced in the three-body $\tilde{\ell}_2$ decays is plotted. This illustrates that $\sim$90% of all electrons and muons have $p_T < 10$ GeV. Leptons with $p_T < 10$ GeV, henceforth decsribed as "soft" leptons, pose a greater challenge to reconstruction than higher-p_T ("hard") leptons. Though not impossible to reconstruct, this analysis chooses to seek out an alternative method of reconstruction. To determine the mass and mixings of the $\tilde{\ell}_2$, indirect measurements must therefore be relied upon. Encouragingly, indirect measurement of the $\tilde{\ell}_2$ mass is found to be possible during $\tilde{\chi}_1^0$ reconstruction. In what follows reconstruction of the $\tilde{\chi}_1^0$ is described and an explanation given of how it can be used to detect the $\tilde{\ell}_2$, and measure its mass.

Figure 8.2 shows that the neutralino can decay to any one of the three light sleptons. First consider neutralino decays to $\tilde{\ell}_1$ and $\tilde{\ell}_2$, with the $\tilde{\ell}_2$ subsequently decaying to $\tilde{\ell}_1$ via a 3-body decay. Since the leptons involved in this 3-body decay, $\ell_{a,b}$, are typically soft, they will usually go undetected, so that the only particles actually observed in both these chains are the final $\tilde{\ell}_1$ and the hard lepton, ℓ_1, coming from the original neutralino decay. It is therefore possible to define two main categories of neutralino decay, direct and indirect. The latter is further divided into two subcategories, which are to be named "OS indirect" and "SS indirect", based on whether the final $\tilde{\ell}_1$ has the opposite or same sign as the lepton ℓ_1. Throughout this section, subscripts on the leptons are as given in Figure 8.2.

Explicitly, these decays are:

1. Direct decays of $\tilde{\chi}_1^0$ to the slepton NLSP: $\tilde{\chi}_1^0 \to \tilde{\ell}_1^{\pm}\,\ell_1^{\mp}$
2. Indirect decays of the $\tilde{\chi}_1^0$ to the slepton NLSP via $\tilde{\ell}_2$, $\tilde{\chi}_1^0 \to \tilde{\ell}_2^{\pm}\,\ell_1^{\mp}$, followed by a three-body $\tilde{\ell}_2$ decay of one of the following types:
   - $\tilde{\ell}_2^{\pm} \to \tilde{\ell}_1^{\pm}\,\ell_a^{\pm}\,\ell_b^{\mp}$ opposite-sign (OS) indirect
   - $\tilde{\ell}_2^{\pm} \to \tilde{\ell}_1^{\mp}\,\ell_a^{\pm}\,\ell_b^{\pm}$ same-sign (SS) indirect

Note that in the instance of a direct decay, the $\tilde{\ell}_1$ and the lepton ℓ_1 must be oppositely charged, whereas in indirect decays, it is possible for these two species to have the same charge. Any detection of the same-sign events described above would be direct evidence

for the Majorana nature of the neutralino (see also Chapter 6). If a hard lepton p_T cut is applied, only the lepton ℓ_1 should be observed. These different channels are now considered in detail.

Direct and OS indirect $\tilde{\chi}_1^0$ decays: measurement of the lightest neutralino ($\tilde{\chi}_1^0$) and next lightest slepton ($\tilde{\ell}_2$) masses

For both the direct and OS indirect decays, the $\tilde{\ell}_1$ and the lepton ℓ_1 have charges of opposite sign. The signatures for these channels are therefore identical and unavoidably reconstructed in tandem, when the invariant mass distribution of all $\tilde{\ell}_1^{\pm}\ell_1^{\mp}$ pairs is formed.

In what follows, all OS $\tilde{\ell}_1^{\pm}\, e^{\mp}$ and $\tilde{\ell}_1^{\pm}\, \mu^{\mp}$ combinations are identified and the invariant masses $m_{\tilde{\ell}_1^{\pm} e^{\mp}}$ and $m_{\tilde{\ell}_1^{\pm} \mu^{\mp}}$ reconstructed. When the OS $\tilde{\ell}_1$ and lepton are from a direct decay, the expectation is an exact reconstruction of the $\tilde{\chi}_1^0$ mass, to within experimental errors. However, when the $\tilde{\ell}_1$ is produced by an indirect decay, correct reconstruction of the $\tilde{\chi}_1^0$ is not expected, as the two soft leptons produced in the decay $\tilde{\ell}_2^{\pm} \to \tilde{\ell}_1^{\pm}\, \ell_a^+ \ell_b^-$ are missing (provided the lepton p_T is high enough). Nevertheless, such events contain valuable information: as shown in Appendix C and Ref. [15], the $\tilde{\ell}_1$-lepton invariant mass then exhibits a "shifted peak", positioned somewhat lower than the neutralino mass, by an amount,

$$E_{\text{shift}} \simeq \frac{M^2 + m_1^2}{2Mm_1}\Delta m \ . \tag{8.1}$$

Here M is the neutralino mass, the mean of the $\tilde{\ell}_1\ell_1$ invariant mass distribution, m_1 is the reconstructed mean of the $\tilde{\ell}_1$ mass, and $\Delta m \equiv m_{\tilde{\ell}_2} - m_{\tilde{\ell}_1}$. The model parameters predict an $E_{\text{shift}} \simeq 5.6$ GeV. The mass difference, Δm, can be deduced from a measurement of this shift, and so the mass of the $\tilde{\ell}_2$ determined indirectly.

The OS $\tilde{\ell}_1^{\pm}\ell_1^{\mp}$ invariant mass distributions are illustrated in Figure 8.5 for two differing cuts on lepton p_T, $p_T > 10$ GeV and $p_T > 30$ GeV. The harder of these two p_T cuts effectively removes the soft leptons produced in three-body $\tilde{\ell}_{2,3}$ decays that had not already failed reconstruction. These distributions (and those that follow) can be decomposed into the sum of an exponentially falling background and one or more Gaussian peaks. The exponentially falling background is designed to model the combinatoric

background from supersymmetric events (there is no guarantee that the leptons combined with the $\tilde{\ell}_1^{\pm}$ are indeed ℓ_1 and not ℓ_2 or ℓ_3, or even a lepton from the other "side" of the event). This fitting function takes the form

$$\frac{dN}{dm} = N_{\text{tot}} \left[\left(1 - \sum_i f_i \right) (-a_i) e^{a_i m} + \sum_i f_i \sqrt{\frac{2}{\pi}} \frac{1}{\sigma_i} e^{-\frac{(m-\bar{m}_i)^2}{2\sigma_i^2}} \right] , \tag{8.2}$$

where N_{tot} is the total number of events in the distribution, a_i is the exponential decay parameter with units of GeV^{-1}, f_i is the fraction of the total number of events in peak i, and $\bar{m}_i$ and σ_i are the center and width of peak i.

The peak position in the $\tilde{\ell}_1^{\pm} e^{\mp}$ distribution is indeed different to the $\tilde{\ell}_1^{\pm} \mu^{\mp}$ peak position: a heavier one at 225.1 GeV is observed in the $\tilde{\ell}_1^{\pm} e^{\mp}$ distribution, corresponding to the true neutralino mass, and the lower shifted peak centred at 220.6 GeV is observed in the $\tilde{\ell}_1^{\pm} \mu^{\mp}$ distribution. In the model considered, each one of these distributions really contains both these peaks, but because of the flavour compositions of $\tilde{\ell}_1$ and $\tilde{\ell}_2$, the $\tilde{\ell}_1^{\pm} e^{\mp}$ sample is dominated by direct decays, and therefore seems to exhibit just the unshifted peak at $\sim$225 GeV, while the $\tilde{\ell}_1^{\pm} \mu^{\mp}$ sample is dominated by indirect decays, and therefore seems to exhibit just the shifted peak at $\sim$220 GeV. In a general model, with larger mixings, a double-peak structure would be seen, which might be harder to disentangle. Then, however, the SS decays become important. These can only originate from indirect decays, and thus will cleanly exhibit the shifted peak only, with no contamination from direct decays.

SS indirect $\tilde{\chi}_1^0$ decays: a clean measurement of the next lightest slepton ($\tilde{\ell}_2$) mass

The SS $\tilde{\ell}_1^{\pm} \ell^{\pm}$ sample cleanly probes the indirect neutralino decays through $\tilde{\ell}_2$, and so its invariant mass distribution should exhibit just the neutralino shifted peak. All SS $\tilde{\ell}_1^{\pm}\, e^{\pm}$ and $\tilde{\ell}_1^{\pm}\, \mu^{\pm}$ combinations are formed and the invariant masses $m_{\tilde{\ell}_1^{\pm} e^{\pm}}$ and $m_{\tilde{\ell}_1^{\pm} \mu^{\pm}}$ reconstructed. This is done for two cuts on lepton p_T: $p_T > 10$ GeV and $p_T > 30$ GeV. The invariant mass distributions are shown in Figure 8.6, and indeed, only the neutralino shifted peak at around 219 GeV is observed in both distributions. It is not surprising that the peaks in these distributions are somewhat lower than the shifted peak in Figure 8.5(b). The SS pairs necessarily come from neutralino decays through $\tilde{\ell}_2$, which only exhibit the shifted peak, whereas the OS $\tilde{\ell}_1 \mu$ sample, although

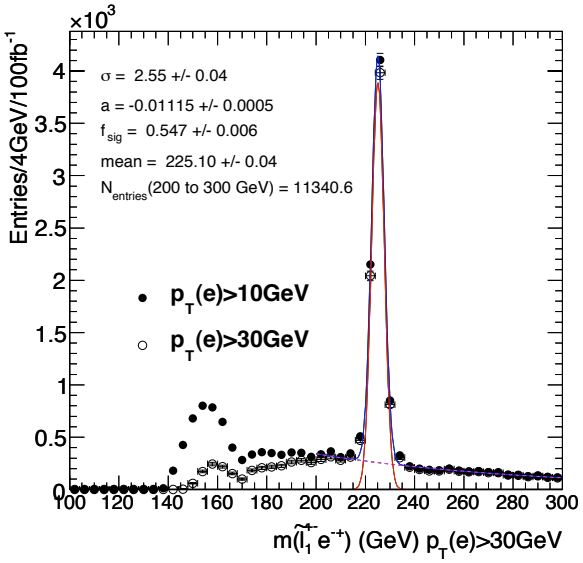

(a) $\ell = e$

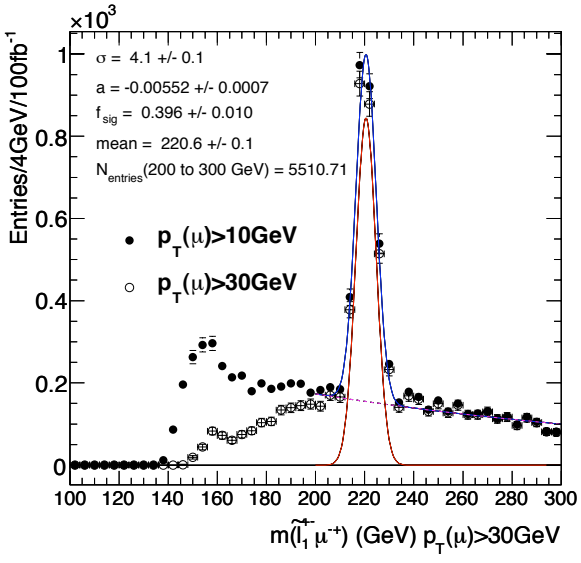

(b) $\ell = \mu$

Figure 8.5: *Invariant mass distributions of all OS* $\tilde{\ell}_1^{\pm}\,\ell^{\mp}$ *pairs for* $\ell = e$ *(a) and* $\ell = \mu$ *(b), requiring lepton* $p_T > 10$ GeV *and* $p_T > 30$ GeV. *The* $p_T > 30$ GeV *distributions in the range* 200 GeV $< m(\tilde{\ell}_1^{\pm}\,\ell^{\mp}) <$ 300 GeV *have been fitted with a Gaussian peak on top of an exponentially decaying background as given by the solid and dashed curves, respectively. The fit parameters, defined in Equation 8.2, are as indicated on the figures.*

dominated by such decays, also contains some events in which the neutralino decays directly to $\tilde{\ell}_1$. The latter lead to the correct neutralino peak at 225 GeV.

The intention was to be able to measure the $\tilde{\ell}_2$ indirectly using indirect SS and indirect OS χ_1^0 decays. In Figure 8.5(a) the invariant mass distribution of $\tilde{\ell}_1^{\pm} e^{\mp}$ pairs is illustrated. This distribution peaks at 225.10 ± 0.04 GeV. This peak is expected to be a combination of pure $\tilde{\chi}_1^0$ from direct decays and "off-reconstructed" $\tilde{\chi}_1^0$ from indirect decays. The $\tilde{\ell}_1^{\pm} \mu^{\mp}$ distribution of Figure 8.5(b) peaks at a mass roughly 5 GeV lower. In Figure 8.6 it is seen that both SS slepton-lepton invariant mass distributions have a mean close to the lower of the two OS peak positions. These demonstrate a measurement consistent with Appendix C and Ref. [15]: nearly degenerate $\tilde{\ell}_1$ and $\tilde{\ell}_2$ with the $\tilde{\ell}_1$ having a much greater selectron component than the $\tilde{\ell}_2$ (seen from the minimal contamination of the $\tilde{\chi}_1^0$ peak in the $\tilde{\ell}_1^{\pm} e^{\mp}$ distribution). With this hypothesis it is possible to identify the position of the higher peak, namely the $\tilde{\ell}_1^{\pm} e^{\mp}$ peak, as the $\tilde{\chi}_1^0$, yielding a $\tilde{\chi}_1^0$ mass of 225.10 ± 0.04 GeV.

It is cleaner to extract E_{shift} from the SS distributions, as these come only from indirect decays. In Figure 8.6(b), the shifted peak is at 219.39 ± 0.06 GeV. This gives an E_{shift} measurement of 5.71 ± 0.07 GeV. Using Equation 8.1, $\Delta m = 5.06 \pm 0.06$ GeV, and so $m_{\tilde{\ell}_2} = 141.0 \pm 0.1$ GeV. Note that the statistical uncertainty on $m_{\tilde{\ell}_2}$ is dominantly from the statistical uncertainty on $m_{\tilde{\ell}_1}$.

Since the shifted neutralino peak appears in both the $\tilde{\ell}_1^{\pm} \mu^{\pm}$ and $\tilde{\ell}_1^{\pm} e^{\pm}$ invariant mass distributions, there is strong evidence that $\tilde{\ell}_2$ has both smuon and selectron components. Similarly, since peaks are present in both the $\tilde{\ell}_1^{\pm} e^{\mp}$ and $\tilde{\ell}_1^{\pm} \mu^{\mp}$ distributions, it is possible to conclude that $\tilde{\ell}_1$ has both selectron and smuon components. It is still unclear whether these states also have stau components. The cleanest "flavour" measurement that can be extracted is one based on the SS shifted neutralino peaks in Figure 8.6, since these are only sensitive to $\tilde{\ell}_2$. If it is assumed that the neutralino couplings to the first two generations are the same, then dividing the number of events N_{SSe} in the $\tilde{\ell}_1 e$ peak of Figure 8.6(a) by the number of events $N_{SS\mu}$ in the $\tilde{\ell}_1 \mu$ peak of Figure 8.6(b), and adjusting for the different reconstruction efficiencies for electrons and muons, the ratio of selectron to smuon components of $\tilde{\ell}_2$ is found to be

$$|U_{2e}/U_{2\mu}|^2 = N_{SSe}/N_{SS\mu} = 0.071 \pm 0.010 \ , \tag{8.3}$$

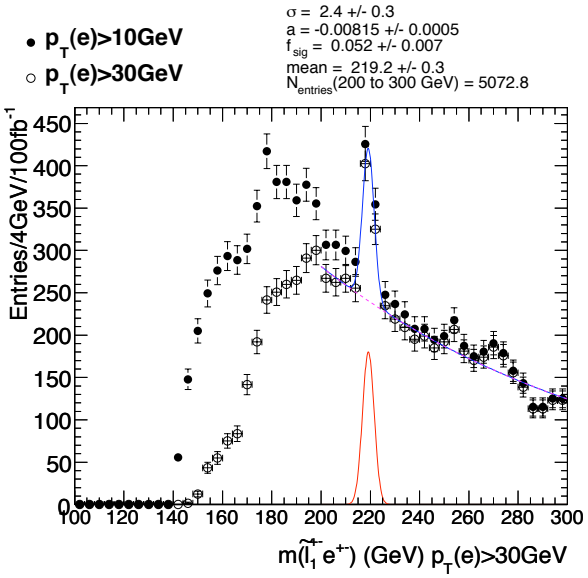

(a) $\ell = e$

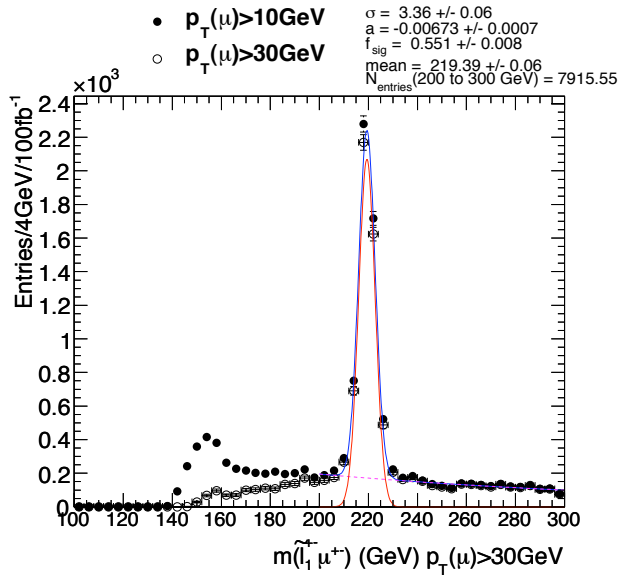

(b) $\ell = \mu$

Figure 8.6: *Invariant mass distributions of SS* $\tilde{\ell}_1^{\pm}\,\ell^{\pm}$ *pairs for* $\ell = e$ *(a) and* $\ell = \mu$ *(b), requiring lepton* $p_T > 10$ GeV *and* $p_T > 30$ GeV. *The* $p_T > 30$ GeV *distributions in the range* 200 GeV $< m(\tilde{\ell}_1^{\pm}\,\ell^{\pm}) <$ 300 GeV *have been fitted with a Gaussian peak on top of an exponentially decaying background as given by the solid and dashed curves, respectively. The fit parameters, defined in Equation 8.2, are as indicated on the figures.*

in good agreement with the input model.

The existence of only one shifted neutralino peak in the $\tilde{\ell}_1 e$ and $\tilde{\ell}_1 \mu$ distributions indicates that there is no such third slepton which is close in mass to $\tilde{\ell}_1$ and significantly composed of selectron or smuon components.

8.4.3 Indirectly Reconstructing the Remaining Light Slepton ($\tilde{\ell}_3$)

Figures 8.5 and 8.6 both show a small peak around 160 GeV. This peak corresponds, at least partially, to $\tilde{\ell}_3$. Decays of $\tilde{\ell}_3$ to $\tilde{\ell}_1$ are dominantly $\tilde{\ell}_3 \to \tilde{\ell}_1 e\tau$. The tau decay could give another charged lepton, but this charged lepton would typically be softer than the original electron produced in the $\tilde{\ell}_3$ decay. Thus, when the invariant mass of this electron paired with the $\tilde{\ell}_1$ is formed, it should display a peak somewhat below the $\tilde{\ell}_3$ mass, much like the shifted neutralino peak discussed in the previous section. An analogous peak should also occur for $\tilde{\ell}_1 \mu$ pairs, coming either from direct $\tilde{\ell}_3 \to \tilde{\ell}_1 \mu\tau$ decays, or from indirect decays through $\tilde{\ell}_3 \to \tilde{\ell}_2 \mu\tau$. The 160 GeV peaks in both these distributions start at around 140 GeV, which, is the $\tilde{\ell}_2$ mass. Another peak around 140 GeV, originating from $\tilde{\ell}_2 \to \tilde{\ell}_1$ decays with one soft lepton is also to be anticipated. In a real detector, smearing effects would then make it hard to conclusively establish the identity of the 160 GeV peak. The lack of a direct observation of a third slepton is entirely to be expected for the spectrum used here, and for an analysis not attempting to reconstruct taus.

8.4.4 Reconstructing the Heavy Sleptons ($\tilde{\ell}_{4,5,6}$)

Once the $\tilde{\chi}_1^0$ is reconstructed, it can be used as a base for reaching higher up the decay chain. As is evident in Figure 8.2, the heavier sleptons decay dominantly through $\tilde{\ell}_{4,5,6} \to \tilde{\chi}_1^0 \ell_2$. Since no heavy slepton is purely stau in the model used here, all three of the sleptons are in principle accessible.

All $\tilde{\ell}_1^{\pm}\, \ell_1^{\mp}$ combinations which lie within 2σ of the mean of the $\tilde{\ell}_1^{\pm}\, \ell_1^{\mp}$ invariant mass distributions of Figure 8.5 are combined with another lepton $\ell' = e, \mu$ to obtain $(\tilde{\ell}_1^{\pm}\, \ell_1^{\mp})\ell'$ invariant mass distributions. Hereafter $\tilde{\ell}_1 \ell_1$ will be enclosed in parentheses to indicate a

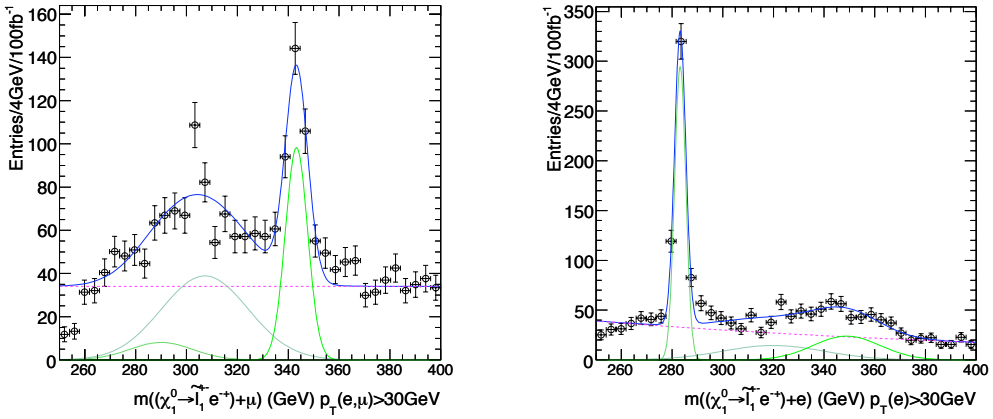

(a) $(\ell_1, \ell') = (e, \mu)$ (b) $(\ell_1, \ell') = (e, e)$

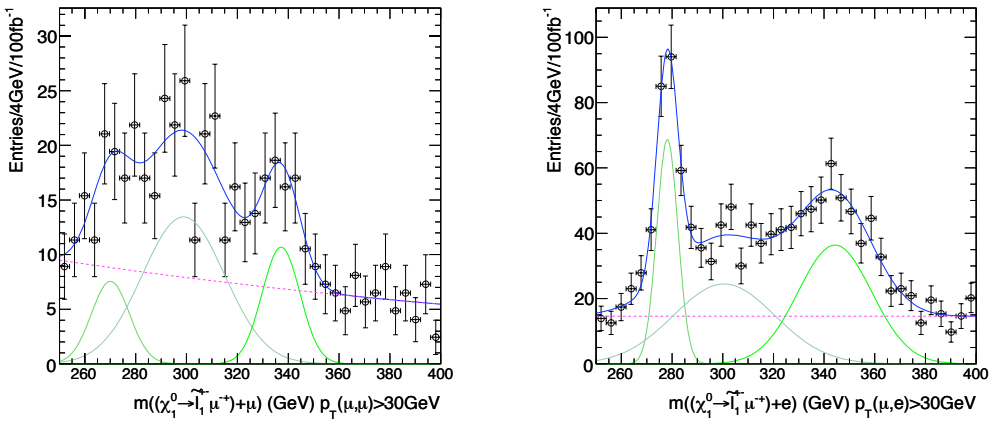

(c) $(\ell_1, \ell') = (\mu, \mu)$ (d) $(\ell_1, \ell') = (\mu, e)$

Figure 8.7: *Invariant mass distributions of* $(\tilde{\ell}_1^{\pm}\ \ell_1{}^{\mp})\ell'$*, where the* $\tilde{\ell}_1^{\pm}\ell_1^{\mp}$ *pair reconstructs the* $\tilde{\chi}_1^0$ *as described in the text, and* $(\ell_1, \ell') = (e, \mu)$ *(a),* (e, e) *(b),* (μ, μ) *(c), and* (μ, e) *(d). Both* ℓ_1 *and* ℓ' *are required to have* $p_T > 30$ GeV*. These distributions in the range* $250\ \text{GeV} < m(\tilde{\chi}_1^0\ell') < 400\ \text{GeV}$ *have been fitted with Gaussian peaks on top of an exponentially decaying background as given by the solid and dashed lines respectively.*

$\tilde{\ell}_1$-lepton pair that reconstructs the $\tilde{\chi}_1^0$. Both ℓ_1 and ℓ' are required to have $p_T > 30$ GeV. These invariant mass distributions essentially give the invariant mass, $m_{\tilde{\chi}_1^0\ell'}$. These are illustrated, with fitted peaks, in Figure 8.7.

All combinations of SS $\tilde{\ell}_1$-lepton pairs with invariant masses falling within 2σ of the SS primary $\tilde{\ell}_1$-lepton invariant mass distribution means can also be combined with another lepton. The resulting invariant mass distributions, with fitted peaks, are illustrated in Figure 8.8. Again both leptons are required to have $p_T > 30$ GeV. These combinations give a poorer reconstruction of the $\tilde{\ell}_{4,5,6}$ than the OS combinations, since SS $\tilde{\ell}_1\ell_1$ pairs reconstruct not the neutralino mass but the neutralino shifted peak, but these plots are included for completeness. The combinatoric background is larger in the SS distributions than the OS distributions, since they include combinations of $\tilde{\ell}_1$ plus two leptons with charges summing to either ± 1 or to ± 3, whereas the OS plots only include the former.

In principle, the invariant mass distributions of $(\tilde{\ell}_1\ell)\ell'$ combinations contain much information about $\tilde{\ell}_{4,5,6}$. However, the combinatoric supersymmetric background makes the identification of the peaks challenging. The cleanest peaks are those obtained from the OS combinations $(\tilde{\ell}_1^{\pm} e^{\mp})\ell'$, where the $\tilde{\ell}_1^{\pm} e^{\mp}$ pair reconstructs the $\tilde{\chi}_1^0$, as shown in Figures 8.7(a) and 8.7(b). The OS combinations, $(\tilde{\ell}_1^{\pm} \mu^{\mp})\ell'$, in Figures 8.7(c) and 8.7(d) also yield useful information, although the peaks are not as clean. Similarly, useful but not particularly clean peaks are found in the SS invariant mass distributions in Figure 8.8.

When the invariant mass distributions of $\tilde{\chi}_1^0 e^{\pm}$ combinations for $\tilde{\chi}_1^0$ reconstructed from $\tilde{\ell}_1^{\mp} e_1^{\pm}$ are considered (Figure 8.7(b)), a very clear peak is obtained which identifies $\tilde{\ell}_4$. The mean value of the fitted peak is 283.2 ± 0.1 GeV. The peak near the $\tilde{\ell}_6$ mass produced by considering these combinations is questionable and contains far fewer events than the $\tilde{\ell}_4$ peak. The $\tilde{\ell}_5$ peak is negligible. This strongly suggests that $\tilde{\ell}_4$ has a dominant selectron component. The invariant mass distributions of $\tilde{\chi}_1^0 e^{\pm}$ combinations for $\tilde{\chi}_1^0$ reconstructed from $\tilde{\ell}_1^{\mp} \mu_1^{\pm}$ (Figure 8.7(d)) are not as convincing, but the repeated presence of a dominant peak near $\tilde{\ell}_4$ further supports $\tilde{\ell}_4$ having a strong selectron component.

When the invariant mass distributions of $\tilde{\chi}_1^0 \mu^{\pm}$ combinations are considered (Figure 8.7(a)), one peak is present, which identifies the $\tilde{\ell}_6$. An additional excess of events at a lower mass could be evidence for $\tilde{\ell}_5$. In Figure 8.8(c) a similar excess, shifted to lower mass, supports the hypothesis that this excess of events is more than just a fluctuation of the background and is indeed $\tilde{\ell}_5$. The lack of evidence for a selectron component in these two states has already been described. The mass of the clear heavier peak, $\tilde{\ell}_6$,

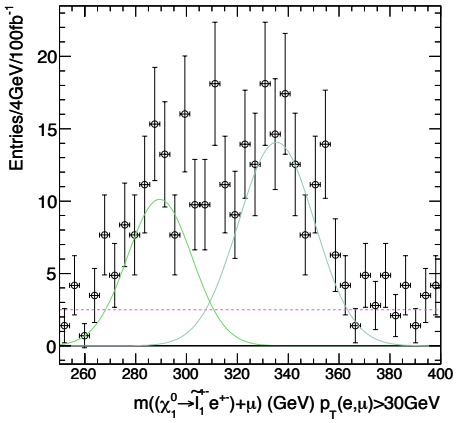

(a) $(\ell_1, \ell') = (e, \mu)$

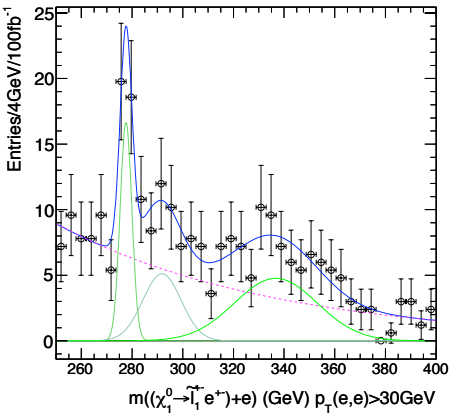

(b) $(\ell_1, \ell') = (e, e)$

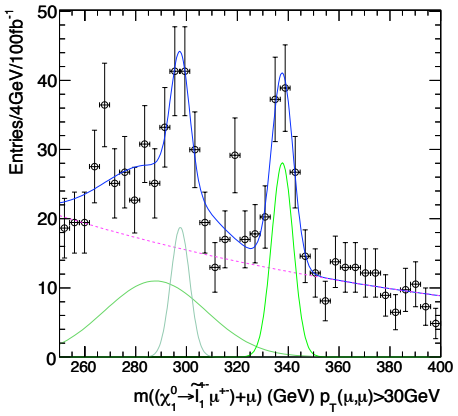

(c) $(\ell_1, \ell') = (\mu, \mu)$

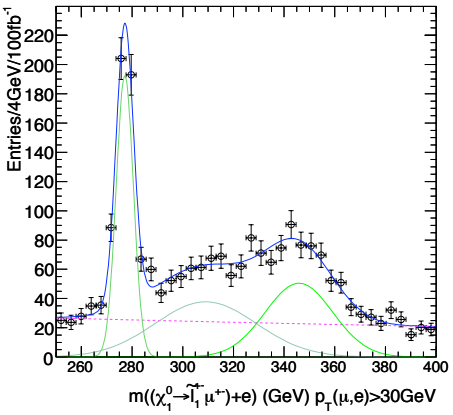

(d) $(\ell_1, \ell') = (\mu, e)$

Figure 8.8: *Invariant mass distributions of* $(\tilde{\ell}_1^{\pm}\ \ell_1{}^{\pm})\ell'$*, where the* $\tilde{\ell}_1^{\pm}\ell_1^{\pm}$ *pair does not exactly reconstruct the* $\tilde{\chi}_1^0$ *as described in the text, and* $(\ell_1, \ell') = (e, \mu)$ *(a),* (e, e) *(b),* (μ, μ) *(c) and* (μ, e) *(d). Both* ℓ_1 *and* ℓ' *are required to have* $p_T > 30$ GeV*. These distributions in the range* $250\ \text{GeV} < m(\tilde{\chi}_1^0\ell') < 400\ \text{GeV}$ *have been fitted with Gaussian peaks on top of an exponentially decaying background as given by the solid and dashed contours, respectively.*

is 343.3 ± 0.5 GeV. If the excess at lower mass is from $\tilde{\ell}_5$, then this describes a mass of 307 ± 5 GeV. These two masses are a reasonable measure of the true slepton masses given that the model for the background in this instance is not ideal. A greater number of events would be needed to truly believe that the excess near 305 GeV is the $\tilde{\ell}_5$ and not a fluctuation of the background.

Assuming that $\tilde{\chi}_2^0$ is predominantly gaugino, and that $\tilde{\ell}_5$ and $\tilde{\ell}_6$ have identical quantum numbers, only phase space effects can give rise to different $\tilde{\chi}_2^0$ branching ratios for the two sleptons. Since it is known that $\tilde{\ell}_{5,6}$ have negligible selectron components, they can only be smuon-stau mixtures. The ratio of the number of events in the $\tilde{\ell}_5$ peak to the number of events in the $\tilde{\ell}_6$ peak of Figure 8.7(a) therefore gives the smuon-stau mixing in these states up to the phase-space factor. Although the compounded reconstruction errors and ignorance of systematics make exact results from this analysis suspect, it is possible to conclude that this mixing is $\mathcal{O}(1)$, if the excess of events near 307 GeV is labelled as a $\tilde{\ell}_5$ mass peak.

8.4.5 Reconstructing the Heavier Neutralino ($\tilde{\chi}_2^0$)

With every step up the chain, the reconstruction errors compound, making $\tilde{\chi}_2^0$ reconstruction much harder than $\tilde{\chi}_1^0$ reconstruction. In this analysis no attempt is made to reconstruct the heavier neutralino. Nevertheless, it is noted that imposing the additional constraint that some lepton combinations reconstruct the $\tilde{\chi}_2^0$ may provide additional constraints on the flavour mixings of the heavy sleptons.

8.5 Conclusions

The best measurements of slepton masses and mixings obtained for this model are summarised in Table 8.1. Of the six sleptons, the masses of four: $\tilde{\ell}_1$, $\tilde{\ell}_2$, $\tilde{\ell}_4$ and $\tilde{\ell}_6$ have been convincingly determined. The $\tilde{\ell}_2$ mass has been determined indirectly using the neutralino shifted peak, whereas the other sleptons have been found by direct measurement. There is evidence in this analysis for the existence of the $\tilde{\ell}_5$, though statistics prevent a firm observation. The existence of the $\tilde{\ell}_3$ has been hinted at, but its mass cannot be measured in this analysis because it is dominantly stau, with a mass in close proximity to that of the $\tilde{\ell}_2$.

	True	Measured	Observation
$\tilde{\ell}_1$	135.83 GeV	135.9 ± 0.1 GeV	direct observation of $\tilde{\ell}_1$ with $0.6 < \beta(\tilde{\ell}_1) < 0.8$ (Figure 8.3(b))
$\tilde{\chi}_1^0$	224.83 GeV	225.10 ± 0.04 GeV	$\tilde{\chi}_1^0$ peak in the $\tilde{\ell}_1^{\pm} e^{\mp}$ invariant mass distribution (Figure 8.5(a))
$\Delta m(\tilde{\ell}_{1,2})$	4.95 GeV	5.06 ± 0.06 GeV	$\tilde{\ell}_1^{\pm} e^{\mp}$ minus $\tilde{\ell}_1^{\pm} \mu^{\pm}$ peak positions (Figure 8.5a, Figure 8.6(b))
$\tilde{\ell}_4$	282.86 GeV	283.2 ± 0.1 GeV	peak in $(\tilde{\ell}_1^{\mp} e^{\pm})e$ invariant mass distribution (Figure 8.7(b))
$\tilde{\ell}_5$	303.41 GeV	307 ± 5 GeV	peak in $(\tilde{\ell}_1^{\mp} e^{\pm})\mu$ invariant mass distribution (Figure 8.7(a))
$\tilde{\ell}_6$	343.53 GeV	343.3 ± 0.5 GeV	peak in $(\tilde{\ell}_1^{\mp} e^{\pm})\mu$ invariant mass distribution (Figure 8.7(a))
$\lvert U_{2e}/U_{2\mu}\rvert^2$	0.069	0.071 ± 0.010	$N(\tilde{\ell}_1^{\pm} e^{\pm})/N(\tilde{\ell}_1^{\pm} \mu^{\pm})$ (Figure 8.6)

Table 8.1: *Best measurements of slepton masses and mixings. The measurement for $\tilde{\ell}_5$ is given under the assumption that the excess of events is indeed a mass resonance, and not a fluctuation of the background. References are given to the appropriate figure, discussions in the text detail how these measurements were obtained. The errors are statistical errors only. In this study, no attempt is made to detail systematic uncertainties.*

This success highlights that for fully reconstructible supersymmetric decay chains ending in stable charged NLSPs, the adopted approach of "working up" the decay chain and reconstructing successive invariant mass distributions is a promising way of measuring slepton masses. Additionally, even very small mass splittings may actually be measurable, if indirect methods can be exploited.

The best mixing measurement made has been of the $e-\mu$ ratio in $\tilde{\ell}_2$ (Equation 8.3). If $\tilde{\ell}_{1,2}$ are assumed to be selectron-smuon mixtures, with no stau components, then

$$\begin{pmatrix} \tilde{\ell}_1 \\ \tilde{\ell}_2 \end{pmatrix} = \begin{pmatrix} \cos\theta_{12}^R & \sin\theta_{12}^R \\ -\sin\theta_{12}^R & \cos\theta_{12}^R \end{pmatrix} \begin{pmatrix} \tilde{e}_R \\ \tilde{\mu}_R \end{pmatrix} . \tag{8.4}$$

With this assumption, the measurement of Equation 8.3 implies

$$\sin^2\theta_{12}^R = 0.066 \pm 0.009 . \tag{8.5}$$

The assumption that $\tilde{\ell}_{1,2}$ have no stau component cannot be tested directly in an analysis that does not look at τ leptons. It is interesting to ask whether this assumption can be approximately tested. With some mild assumptions about the model, it can be shown that $\tilde{\ell}_1$ and $\tilde{\ell}_2$ can only have *equal* stau components, i.e., $|U_{1\tau}| = |U_{2\tau}|$. It is not possible to exclude, however, $|U_{1\tau}| = |U_{2\tau}| \neq 0$ (see discussion in Ref. [10], which is beyond the scope of this chapter).

The measured masses and mixings are very close to those of the underlying input model. The charged NLSP is a crucial ingredient in this analysis, yet the model chosen also has some unfavourable features. The two lightest sleptons were almost degenerate, and the $e-\mu$ mixing in these sleptons small. The $\tilde{\ell}_3$ was almost pure $\tilde{\tau}$, with mass close to the $\tilde{\ell}_{1.2}$ which gave a peak in the NLSP plus e, μ distributions very close to the $\tilde{\ell}_2$ peak. No information from tau leptons has been used. Given these difficult features and the pessimistic assumption about taus, the amount of information extracted is encouraging.

This chapter has demonstrated that under favourable, but not overly optimistic, circumstances, it may be possible to make measurements of slepton masses and mixings at the LHC using these techniques. To apply these techniques to real data, measurements would be needed to confirm the observed events were indeed supersymmetric. Addition-

ally, a full consideration of the standard model backgrounds remaining despite the initial requirement of a slow charged track would be needed, accompanied by full treatment of the systematic uncertainties which would impact an analysis of this type.

Part IV

Close

Chapter 9

Conclusions

The programme of research presented in this thesis was commenced just two weeks after a magnet quench the on 19th September 2008 left the LHC non-operational for just over a year. The LHC was repaired by late 2009, and ran at $\sqrt{s} = 900$ GeV for the rest of that year. By March 2010 the LHC had used a brief shutdown to re-optimise and make preparations to deliver collisions at $\sqrt{s} = 7$ TeV. These collisions ran until the end of October of the same year. It is these datasets which have been analysed herein, and the work presented in this thesis is consequently varied. The very first electron candidates and Z bosons in ATLAS have been illustrated. The analysis of the 2010 dataset in the search for supersymmetry in two-lepton events is one of the main pieces of research described in this thesis. Conclusions have also been drawn from Monte Carlo studies carried out during the year between the magnet quench and first $\sqrt{s} = 900$ GeV collisions.

In Chapter 4, the remarkable agreement between data and expectations based on simulation at $\sqrt{s} = 900$ GeV and $\sqrt{s} = 7$ TeV of the electron properties used in reconstruction and identification, has been presented. Chapter 5 recorded the observation of the very first Z bosons in ATLAS, these among the first candidate Zs ever produced in a proton-proton collider. The only major discrepancy between expectation and observation in this chapter was that alluded to in Chapter 4, a difference in the electron reconstruction efficiency expected from simulated Monte Carlo and that found for data. The final data chapter, Chapter 6, presented a search in the full 2010 $\sqrt{s} = 7$ TeV dataset for supersymmetry in final states with two leptons and high missing transverse energy. In this dataset no excess of identical-flavour lepton-pairs, over those of different-

flavour, above that expected by the standard model, was observed. This observation was then used to exclude parts of the mSUGRA/CMSSM framework and a phenomenological grid cast in the 24-parameter MSSM framework. Model independent limits were also set on the mean identical-flavour excess, multiplied by detector acceptances and efficiencies, from supersymmetric events at 95% confidence. This search, and those reported in Ref. [6] and Ref. [167] by ATLAS and CMS respectively, are the first searches for supersymmetry using events with two leptons in $\sqrt{s} = 7$ TeV data. The final two chapters presented the results of the Monte Carlo studies undertaken before data taking. Chapter 7 demonstrated the feasibility of jet substructure techniques for reconstructing boosted particles which decay into jets, whilst Chapter 8 demonstrated the potential for measurements of slepton masses and mixings in supersymmetry at high integrated luminosity with the LHC.

At the time of writing (April 2011), ATLAS is once again taking data and just like during 2010, data at $\sqrt{s} = 7$ TeV. The LHC experiments are exploring physics at energies never before reached by particle colliders. The 2011 data run is expected to deliver the first 1 fb^{-1} of data by July. This thesis is therefore only a taste of what is to come in the search for supersymmetry, with discoveries perhaps just around the corner.

Appendix A

Monitoring the Level 1 Calorimeter Trigger

This Appendix begins with a brief overview of the Level 1 Trigger, with a particular emphasis on the Level 1 Calorimeter Trigger. It summarises the tools written by the author to monitor the Level 1 Calorimeter Trigger under the guidance of Pete Faulkner from the University of Birmingham. This chapter details only the contributions made by the author to the already existing framework of monitoring and does not give tools or features existing previously. The software monitoring tools were written in `c++` and `Python` within the software framework `Athena` [71]. The tools developed by the author were tested and developed using `RAW` data files (these contain the events formatted as output from the trigger system, totalling $\sim$1.6 Mb per event [71]). Files were used from old collision and cosmic runs, sometimes necessitating the need to "fake" potential problems where no examples were to hand. The majority of the illustrative histograms used in this Appendix are those produced during local testing from old `RAW` files - either for a cosmic run, or a single beam run - rather than examples of plots seen at Point 1 with the monitoring software running, or after a run on the offline Data Quality monitoring webpages.

A.1 Overview

The Level 1 Trigger must select events from an input rate of $\sim$1 GHz at a maximum rate of $\sim$100 kHz. The Level 1 Trigger searches for exclusive signatures that could

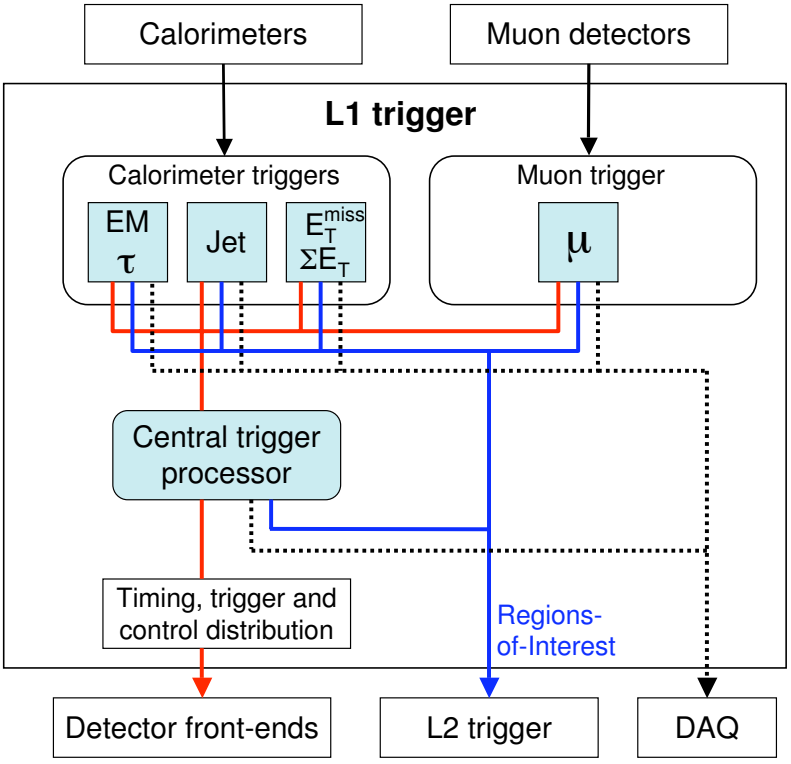

Figure A.1: *The Level 1 Calorimeter Trigger Decision (from [168]). This schematic diagram of the Level 1 Calorimeter Trigger illustrates the components which form the trigger decision. Calorimeter information is used by the calorimeter triggers to select events with high missing energy, energetic jets or electrons. The muon triggers, retrieving information from the muon chambers, select events with muons. All information is then processed by the central trigger processor, which is capable of pre-scaling triggers when their rate is too high.*

identify high-p_T electrons, photons, muons and taus, and searches for missing energy, jets and high total transverse energy. The system uses reduced granularity data from the muon chambers and both the electromagnetic and hadronic calorimeters. The muon triggers exploit the RPCs in the barrel and TGCs in the end-caps. Electrons, muons, jets, missing energy and taus are triggered using calorimeter information. Detector data can be held in a buffer for up to 2.5 µs whilst the Level 1 Calorimeter Trigger makes it decision. If a particular bunch crossing passes the Level 1 Accept criteria (L1A), the data is kept. There are three main components to the Level 1 trigger decision (Figure A.1):

- **Level 1 Muon Trigger (L1Muon)**
- **Level 1 Calorimeter Trigger (L1Calo)**
- **Central Trigger Processor (CTP)**

The CTP must process the results from both the Muon and Calorimeter Triggers. It implements the current "trigger menu" (the list of triggers on which decisions are to be made for the given run), based on results received from the L1Calo and L1Muon trigger systems. The CTP is capable of pre-scaling menu items when a trigger rate becomes too high.

The Level 1 Calorimeter Trigger takes its input from $\sim$7200 analogue trigger towers. These are reduced granularity trigger towers, most of which are 0.1×0.1 in $\Delta\eta \times \Delta\phi$. The Level 1 Calorimeter Trigger sits in USA15. It has three main sub-systems, as illustrated in Figure A.2: the pre-processor (magenta), the jet energy processor (yellow) and the cluster processor (blue). These sub-systems are:

- **Pre-processor:** This digitises analogue trigger-tower signals.
- **Cluster Processor:** This processor is designed to identify candidate electrons, photons and taus with high E_T (i.e. E_T above programmable thresholds specified for the trigger menu).
- **Jet/Energy-sum Processor:** This operates on "jet-elements", of coarser granularity than those used by the CP.

The "hit multiplicities" counted by the jet-energy processor and the cluster-processor for different objects are sent to the CTP.

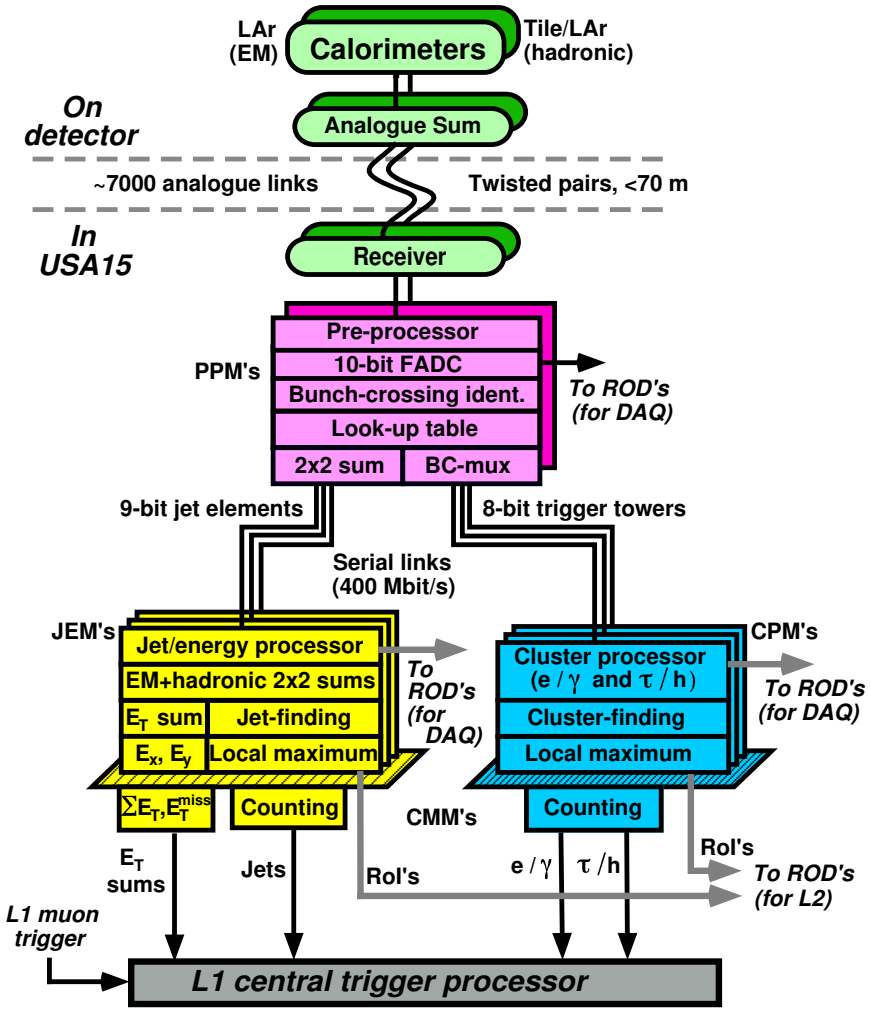

Figure A.2: *An overview of the Level 1 Calorimeter Trigger (from [168]). The real time data paths are shown in black, the readout paths in grey. The three main components: the pre-processor (PPM), jet/energy processor (JEM) and cluster processor (CPM) are illustrated.*

A.2 The Pre-processor Module

The PPM (magenta in Figure A.2) must digitise the analogue trigger tower signals, then use a digital filtering technique to associate the pulses with the right bunch crossing. The PPM then carries out: (i) pedestal subtraction, (ii) final E_T calibration, (iii) noise suppression and (iv) the masking of all problematic channels. These tasks are all performed using a "look-up table".

The PPM must convert energy "E" $\rightarrow$ transverse energy "E_T". The signal pulse (Figure A.3) is sampled at a rate of 40 MHz using a 10-bit flash-ADC, the sample pulse being taken over 5 bunch crossings. The pedestal is set at 32 ADC counts. The pulse is assigned to a bunch crossing using a Finite Input Response filter (FIR, Figure A.4), then a peak finder. The FIR filter "sharpens" the pulse before it enters the peak finder. The flash-ADC count is converted into a measure of E_T using a look-up table, or LUT. The net result of this is the conversion of the 10-bit ADC value to an 8-bit value of the trigger tower E_T in MeV. Any further use of the term "LUT" will refer to the mean final E_T of the trigger tower (not to be confused with a look-up table containing many values).

A.3 Monitoring

The Level 1 Calorimeter is a vitally important part of the ATLAS detector during data taking. It must be operating correctly at all times in order to guarantee that interesting events are fed to the Level 2 Trigger and then the Event Filter and if appropriate, stored for offline analysis. The Level 1 Calorimeter Trigger is a hardware trigger and as such susceptible to crate or module failures which will impact its performance. There is therefore a need to monitor its performance both in an online sense in the ATLAS Control Room during a run and an offline sense, retrospectively, when checking the "Data Quality" of a run. All ATLAS detector systems and subsystems must in fact be monitored both in the offline and online sense. This monitoring involves the writing of tools which produce histograms. These histograms are produced both offline and online and are designed to provide a visual, and relatively easily interpretable, means of ascertaining whether or not a particular system or subsystem is behaving as anticipated. This section details the tools written by the author to produce histograms for viewing both

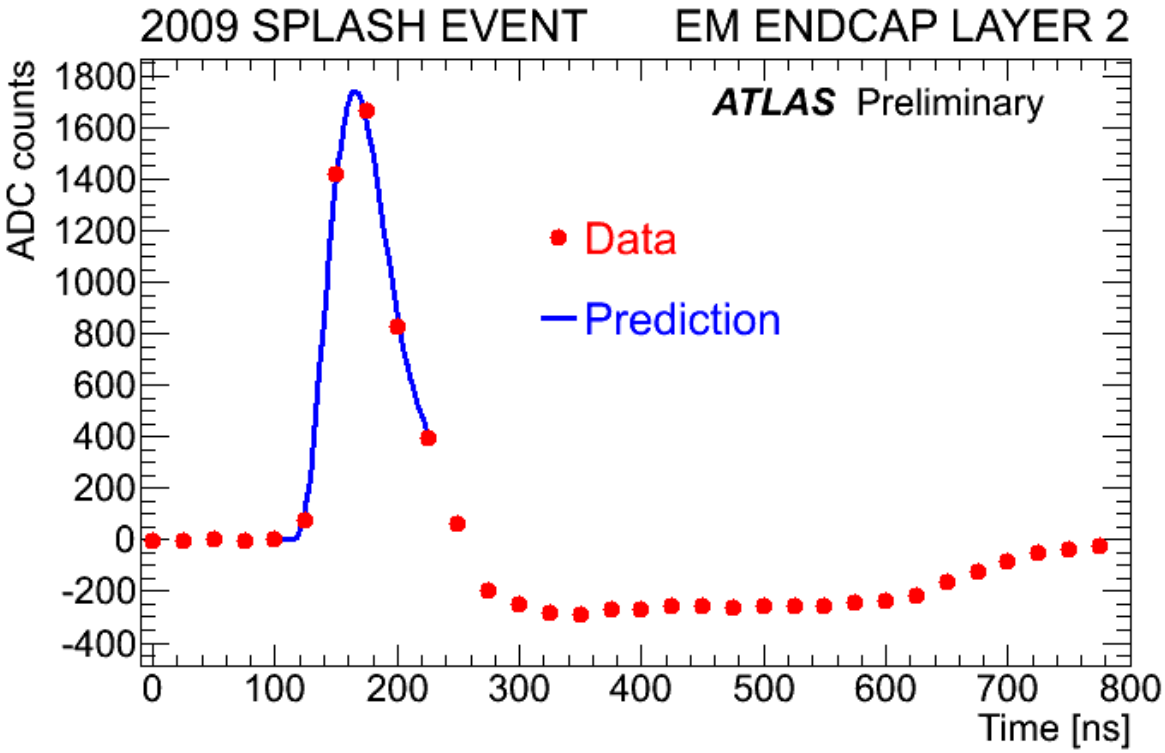

Figure A.3: *LAr pulse from a splash event (from [169]). The pulse lasts a very many number of bunch crossings, the LAr reading out over 32 bunch crossings. The undershoot at the end of the pulse is characteristic of LAr pulses (a tile pulse does not have such an undershoot).*

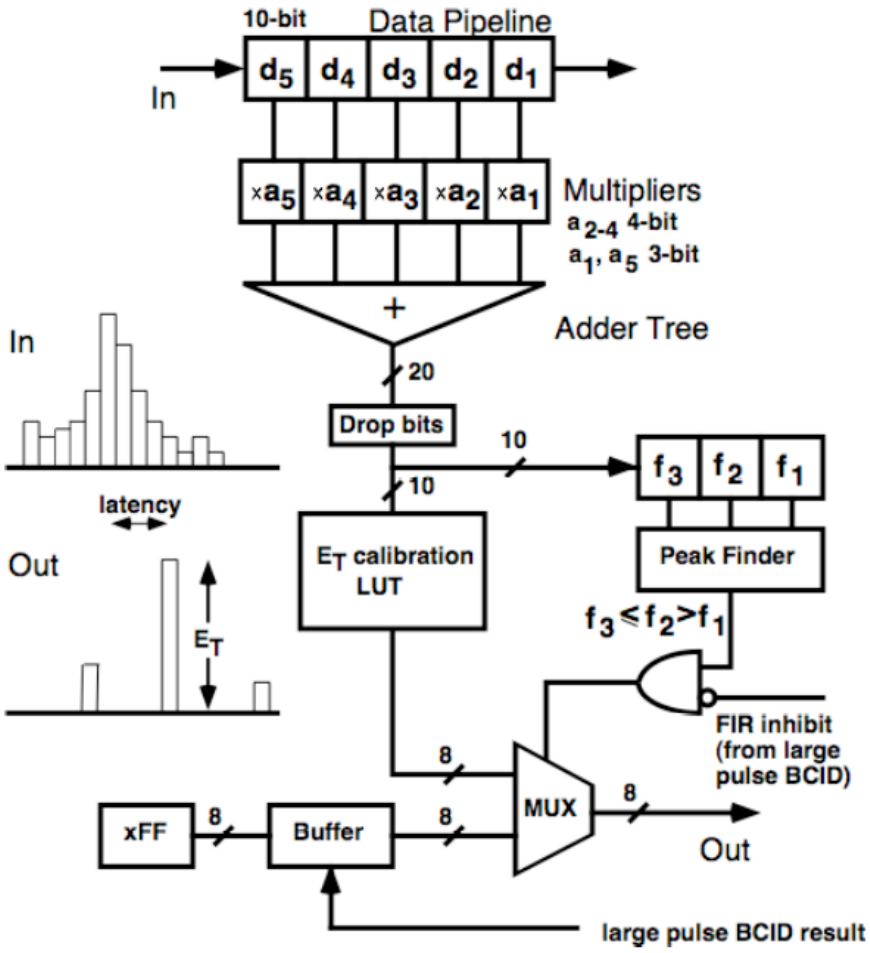

Figure A.4: *The Level 1 Calorimeter Finite Impulse Response filter (from [168]). The Finite Impulse Response filter "sharpens" the calorimeter pulse before it enters a peak finder which assigns the pulse to the correct bunch crossing.*

offline and online, to monitor the performance and behaviour of the Level 1 Calorimeter Trigger.

A.3.1 LUT Monitoring

The tools exist to "simulate" the calculation of the LUT (as described above). This simulation has certain key ingredients: (i) any simulation of the LUT must be able to synchronise signals from a given bunch crossing (cables are not all the same length and so time-of-flight and signal path lengths may differ), (ii) once a trigger tower is assigned to a bunch crossing, this must be used as an address for the look-up table, (iii) this look-up table must then tune the transverse energy scaling using a linear transformation and pedestal subtraction, (iv) small signals need to be set to zero, saturated signals set to full scale and (v) the simulation must take account of both problematic and dead channels, making sure that any signal in these channels is set by the software to zero. This simulation of the LUT calculation is a model of how the actual Level 1 Calorimeter hardware acquires the value of the trigger tower E_T.

The existence of this LUT simulation allows the trigger tower energy, as determined by the hardware, to be checked and consequently additions to the Level 1 Calorimeter Monitoring package were made to produce histograms comparing simulated LUT with the actual "data" LUT. The majority of these histograms take the form of $\eta - \phi$ maps, eight in total (four for the electromagnetic calorimeter towers, and four for the hadronic calorimeter towers). These histograms are made so that each bin in the two-dimensional $\eta - \phi$ map represents a different trigger tower. Each of the four histograms is an "error histogram", designed to be empty in the most likely case - that a run or the period of the run for which the histogram was filled, reports no trigger tower with a difference between simulated and data LUT values. The four types of error histogram are separately used to display:

- channels with a data LUT, but simulated LUT equal to zero
- channels with a simulated LUT, but data LUT equal to zero
- channels where data LUT equals simulated LUT
- channels where data LUT does not equal simulated LUT, and both are non-zero

Channels are identified by their η and ϕ values. An entry into any of these histograms will give a corresponding entry in a "MismatchEventNumbers" histogram (four in total, two crates per histogram) where the channel containing an error is identified not by its η and ϕ value, but by the crate and module in which it sits. Only the first few errors in each channel are recorded, and they are recorded by writing the numbers of the events containing the errors in the appropriate histogram bins. Up to a total of ten errors are recorded for each channel. The error summary histograms serve to give an example of an event with an error associated with a particular crate and module. An example of an $\eta - \phi$ error map is given in Figure A.5(a), and an example of a summary plot, for crates 6 and 7, is given in Figure A.5(b). The simulation of the LUT can fail when there are more than seven time slices in the trigger tower. Therefore events are only considered to be giving an "error" when there is zero data, non-zero simulation but also fewer than seven time slices in the trigger tower.

A.3.2 Pedestal Monitoring

Histograms have also been designed to monitor the pedestal value - comparing the actual pedestal for a run, and during a run, with the recorded pedestal value in the database. These include run summary histograms to appear in the offline and online worlds, and instantaneous and worst pedestal monitoring histograms to appear online only. These histograms also take the form of $\eta - \phi$ maps, each bin representing a different trigger tower. Run summaries record the average difference between the observed pedestal and the pedestal value in the database over the entire run (Figure A.6(a)). A second histogram records the r.m.s of this difference, calculated similarly over the entire run (Figure A.6(b)). Instantaneous measures look to display the average difference between the pedestal value in the database and the observed current pedestal over the most recent n events (set to a default of 400, but can be changed using the appropriate `jobOptions` files for the setup). The worst difference for an n event period is recorded in the worst pedestal difference histograms. Separate histograms are given for the electromagnetic and hadronic calorimeters.

Initially, the recorded pedestal value for each trigger tower is retrieved from a database. All trigger towers without a signal in them (i.e. zero data LUT) and which aren't disabled are considered. For each time slice of each trigger tower, the difference is then calculated between the ADC value and the looked up pedestal. The average of this difference is

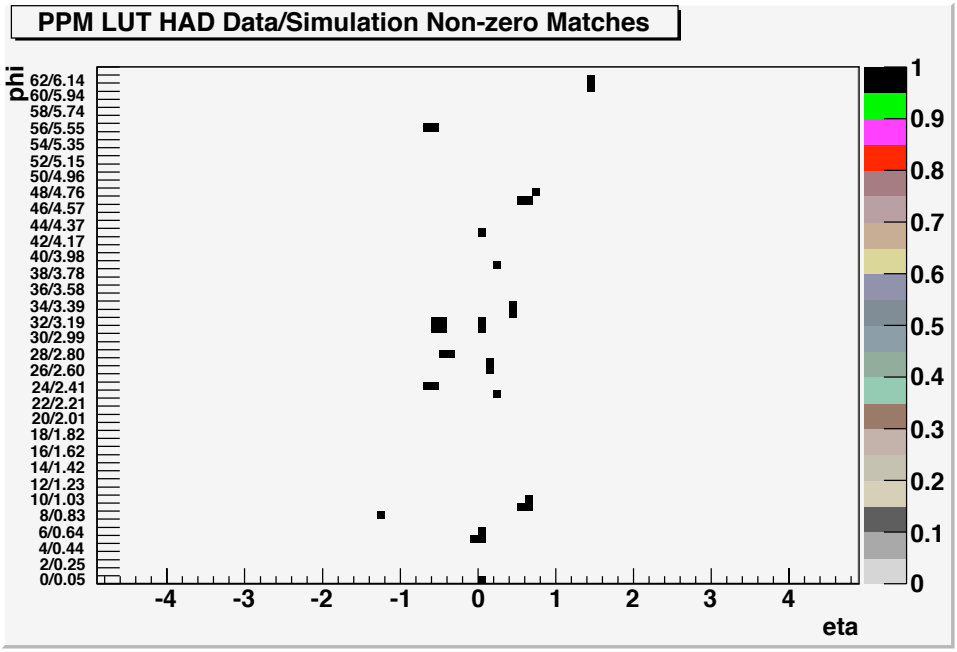

(a)

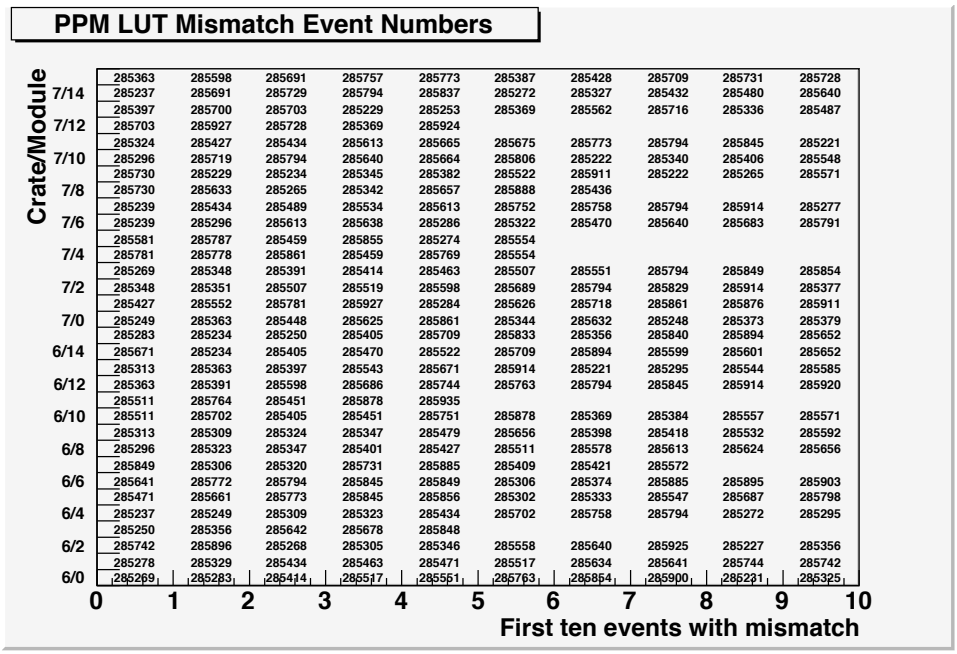

(b)

Figure A.5: *An example showing the $\eta-\phi$ simulated LUT vs data non-zero mismatch plot (a), and an example mismatch error summary plot, for non-zero mis-matches (b). Note that (b) (and also (a)) is not a histogram from a genuine run; instead infrequent errors have been faked in order to populate this histogram and give a clear visualisation of how it would look in the event of (an unrealistically large number of) errors, in a variety of channels.*

then recorded over the whole run in the appropriate histogram bin for each channel. At the same time the r.m.s of this difference is calculated, and the r.m.s for each trigger tower over the entire run recorded in the appropriate histogram bin. The instantaneous histograms are filled continuously during a run. At any one time, these histograms will be seen by the shifter to contain somewhere between the 200 and 400 most recent events when n is set to its default value. The mean histogram must show the average of the difference between the observed pedestal and the value of it in the database over these events only, similarly the r.m.s histogram must record the r.m.s of this difference over these events only. Figure A.7 outlines how the instantaneous histograms are produced, via an unseen histogram which is not "booked". Before these histograms are cleared, the worst absolute difference is extracted and if this is greater than the current worst difference for the channel, this difference is recorded in the worst difference histogram.

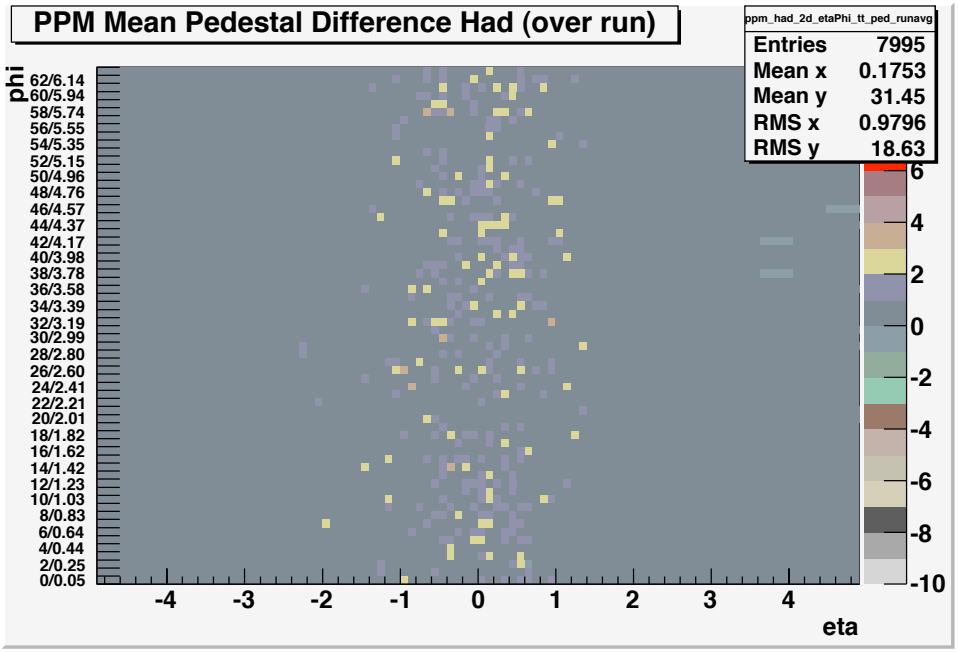

(a)

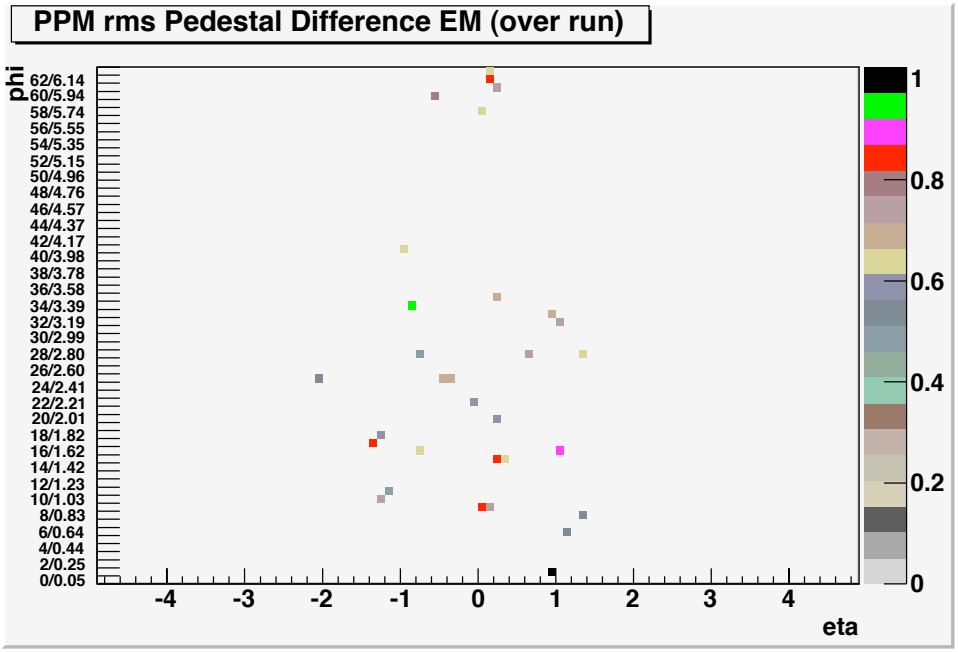

(b)

Figure A.6: *Average difference between observed pedestal and pedestal value in the database, over an entire run (a), and the r.m.s of this difference, also averaged over an entire run (b) (in both these histograms, the "run" is actually only a very small run of tens of test events).*

Event(s)	(1) *Booked histogram*	(2) *Unseen histogram*
0 - 200	fill	fill
200	(i) clear, (ii) fill with events from (2)	clear
200 - 400	fill	fill
400	(i) clear, (ii) fill with events from (2)	clear
400 - 600	...	...
...	...	...

Figure A.7: *An illustration of how the "instantaneous" histograms of the average pedestal value and the r.m.s of this difference are filled. At any one time, the shifter will see these histograms contain somewhere between the* 200 *and* 400 *most recent events. This illustration takes the value of n to be* 400 *(the default). The cycle repeats itself every* 200 *(generally* $\frac{n}{2}$*) events.*

A.3.3 Comparison of Level 1 Calorimeter Energy with Calorimeter Energy

The recorded E_T in a trigger tower (i.e. the LUT) takes integer values. This transverse energy should agree (with a precision of order 5 GeV) with the total reconstructed E_T of all the calorimeter cells from which a trigger tower is composed. The monitoring tool designed to monitor the difference between the so-called "L1Calo" energy and the "calo" energy was re-written by the author. These changes included: (i) bringing the η and $\eta - \phi$ binning in line with the other monitoring tools, (ii) switching the tool to use the most appropriate tools for retrieving and combining the calorimeter cells to reconstruct the calo energy of a trigger tower and (iii) adding some additional histograms to compare the two quantities.

A.3.4 Data Quality

A distinction has already been made between offline and online histograms. The histograms described here are all implemented in the `TrigT1CaloMonitoring` package. These histograms can then be displayed in the ATLAS Control Room for experts and online shifters to study, or they can be looked at offline. A set of the available histograms can also be used for Data Quality assessment, a part and perhaps the most important part of the offline world. Histograms for Data Quality assessment are displayed on a webpage (Figure A.8). Which histograms are displayed on this webpage is controlled

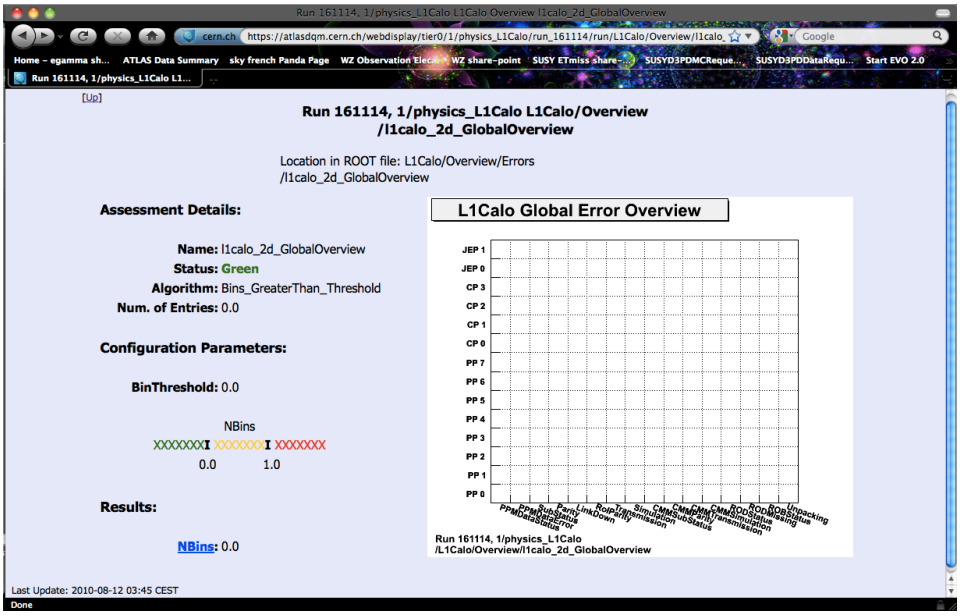

Figure A.8: *A screenshot of the ATLAS Data Quality Web Display. The displayed histogram will be flagged green (as is the case for the run displayed) if it is empty, and red if it is non-empty. This "Global Error Overview" Level 1 Calorimeter Monitoring histogram records the errors in the Level 1 Calorimeter hardware, for a given run, by type.*

by "`han`" [170] configuration files. The author was one of the people responsible for updating this configuration file. The `han` configuration file can give the details of not just which histograms to display, but also whether or not to display a reference histogram (a histogram illustrating the expected form of the histogram), and which algorithms to apply to the histograms. The most used algorithm for the Level 1 Calorimeter histograms displayed is an "is empty" algorithm applied to error histograms. The algorithm checks whether or not these histograms are empty. If the histogram is empty, the histogram is flagged green. An error histogram with entries will be flagged red.

Appendix B

Detailed Break Down of Systematic Uncertainties in the Search for Supersymmetry in Events with Identical-Flavour Leptons

This appendix details the systematic uncertainties from the sources described in Section 6.5 on the numbers of events with $E_T^{miss} > 100$ GeV in the Monte Carlo event samples analysed in Chapter 6. The uncertainties on these numbers for the opposite-sign lepton-pairs are given in Table B.1 and the uncertainties on these numbers for the same-sign lepton-pairs are given in Table B.2. For Monte Carlo samples with low statistics in the signal region (particularly Z/γ^*+jets), the "error on the error" for each systematic uncertainty will be quite large.

A detailed break down of the overall systematic uncertainty on $\bar{\mathcal{S}}_b$ calculated using the partially data-driven background estimates in Ref. [7] and the Monte-Carlo-only estimates for single top and dibosons, is given in Table B.3. Note that the s-channel and t-channel contributions to the single top Monte Carlo event rate are negligible. These two channels are taken into account by the fake component estimated from data, and so only the estimate of single top events in the Wt-channel is needed from Monte Carlo. In the "other$_{sys.}$" column, the uncertainties given are those which are particular to each data-driven background estimation, and are therefore not correlated between backgrounds. For $t\bar{t}$ this includes the uncertainties due to the choice of the generator,

(a) $e^{\pm}e^{\mp}$

	Events	$JES_{\uparrow}$	$JES_{\downarrow}$	JER	$E_{e,\uparrow}$	$E_{e,\downarrow}$	res_e	$\mu_{MS,\uparrow}$	$\mu_{MS,\downarrow}$	$\mu_{ID,\uparrow}$	$\mu_{ID,\downarrow}$	Lumi.	σ	pdf.	Total.	Stat.
Z+jets	0.383	0.129	-0.058	0.251	0.197	0.001	0.059	0	0	0	0	0.042	0.019	0.019	0.353	0.163
$t\bar{t}$	3.718	0.872	-0.665	0.145	0.257	-0.408	-0.043	0	0	0	0	0.409	0.186	0.186	1.089	0.311
Dibosons	0.303	0.089	-0.061	0.012	0.046	-0.031	0.003	0	0	0	0	0.033	0.015	0.015	0.108	0.019
Single Top	0.127	0	0	0	0.056	0	0	0	0	0	0	0.014	0.006	0.006	0.059	0.064

(b) $e^{\pm}\mu^{\mp}$

	Events	$JES_{\uparrow}$	$JES_{\downarrow}$	JER	$E_{e,\uparrow}$	$E_{e,\downarrow}$	res_e	$\mu_{MS,\uparrow}$	$\mu_{MS,\downarrow}$	$\mu_{ID,\uparrow}$	$\mu_{ID,\downarrow}$	Lumi.	σ	pdf.	Total.	Stat.
Z+jets	0.356	0.100	-0.117	-0.058	0	0	0	0	0	0	0	0.039	0.018	0.018	0.139	0.161
$t\bar{t}$	9.799	1.646	-1.946	-0.086	0.730	-0.641	0.086	0.010	-0.022	0.006	0	1.078	0.490	0.490	2.445	0.530
Dibosons	0.359	0.084	-0.049	0.022	0.025	-0.022	0.005	0.005	-0.002	0.007	0	0.039	0.018	0.018	0.103	0.028
Single Top	0.755	0.138	0.019	0.035	0.054	-0.023	-0.028	0	0	0	0	0.083	0.038	0.038	0.184	0.172

(c) $\mu^{\pm}\mu^{\mp}$

	Events	$JES_{\uparrow}$	$JES_{\downarrow}$	JER	$E_{e,\uparrow}$	$E_{e,\downarrow}$	res_e	$\mu_{MS,\uparrow}$	$\mu_{MS,\downarrow}$	$\mu_{ID,\uparrow}$	$\mu_{ID,\downarrow}$	Lumi.	σ	pdf.	Total.	Stat.
Z+jets	0.972	0.238	-0.131	-0.073	-0.041	-0.131	-0.057	0	-0.098	0	0	0.107	0.049	0.049	0.329	0.286
$t\bar{t}$	6.985	0.827	-1.233	0.137	0.233	-0.373	-0.050	0	-0.068	0.013	0.013	0.768	0.349	0.349	1.588	0.443
Dibosons	0.605	0.056	-0.024	0.006	0.014	-0.005	-0.001	0.016	-0.003	0.004	-0.002	0.067	0.030	0.030	0.100	0.027
Single Top	0.674	0.263	0	-0.027	-0.019	-0.027	0	0	0	0	0	0.074	0.034	0.034	0.280	0.176

Table B.1: *Numbers of events in the signal region ($E_T^{miss} > 100$ GeV) for each opposite-sign channel, with a break down of the absolute systematic error. The systematics detailed are as described in Section 6.5.* $JES_{\uparrow/\downarrow}$ *denotes the "up" / "down" systematic error due to uncertainty in the jet energy scale and* JER *denotes the systematic error due to uncertainty in the jet energy resolution.* $E_{e,\uparrow/\downarrow}$ *denotes the systematic error due to the electron energy-scale, whilst* res_e *denotes the systematic error due to the electron energy resolution. The columns headed* $\mu_{MS/ID,\uparrow/\downarrow}$ *detail the systematic error resulting from uncertainties in the MS and ID momentum components respectively. The abbreviation* "Lumi." *is short for the uncertainty resulting from the systematic uncertainty on the luminosity estimate,* "pdf." *is short for the uncertainty resulting from parton distribution function re-weighting and "σ" denotes the systematic error resulting from uncertainties on the cross-sections. The largest members of the* $JES_{\uparrow/\downarrow}$, $\mu_{MS/ID,\uparrow/\downarrow}$ *and* $E_{e,\uparrow/\downarrow}$ *pairs are used to compute the total systematic,* "Total.". *Also quoted is the statistical uncertainty (*"Stat."*). Only the Monte Carlo contributions which are non-zero are detailed for each channel.*

(a) $e^{\pm}e^{\pm}$

	Events	JES$_{\uparrow}$	JES$_{\downarrow}$	JER	E$_{e,\uparrow}$	E$_{e,\downarrow}$	res$_e$	$\mu_{MS,\uparrow}$	$\mu_{MS,\downarrow}$	$\mu_{ID,\uparrow}$	$\mu_{ID,\downarrow}$	Lumi.	σ	pdf.	Total.	Stat.
$t\bar{t}$	0.12	0.01	-0.01	0.01	0	0	0	0	0	0	0	0.01	0.01	0.01	0.02	0.06
Dibosons	0.015	0.005	-0.006	0.003	0	-0.001	0.001	0	0	0	0	0.002	0.001	0.001	0.007	0.004

(b) $e^{\pm}\mu^{\pm}$

	Events	JES$_{\uparrow}$	JES$_{\downarrow}$	JER	E$_{e,\uparrow}$	E$_{e,\downarrow}$	res$_e$	$\mu_{MS,\uparrow}$	$\mu_{MS,\downarrow}$	$\mu_{ID,\uparrow}$	$\mu_{ID,\downarrow}$	Lumi.	σ	pdf.	Total.	Stat.
W+jets	0.06	0	0	0	0	0	0	0	0	0	0	0.01	0	0	0.01	0.06
$t\bar{t}$	0.08	0	-0.03	0	0	0	0	0	0	0	0	0.01	0	0	0.03	0.06
Dibosons	0.035	0.008	-0.010	0.002	0.001	-0.006	0.002	-0.001	0	0	0	0.004	0.002	0.002	0.013	0.005
Wbb	0.03	0	0	0	0	0	0	0	0	0	0	0	0	0	0	0.03

(c) $\mu^{\pm}\mu^{\pm}$

	Events	JES$_{\uparrow}$	JES$_{\downarrow}$	JER	E$_{e,\uparrow}$	E$_{e,\downarrow}$	res$_e$	$\mu_{MS,\uparrow}$	$\mu_{MS,\downarrow}$	$\mu_{ID,\uparrow}$	$\mu_{ID,\downarrow}$	Lumi.	σ	pdf.	Total.	Stat.
W+jets	0	0.13	0	0	0	0	0	0	0	0	0	0	0	0	0	0
$t\bar{t}$	0	0	0.01	0	0	0	0	0	0	0	0	0	0	0	0.01	0
Dibosons	0.021	0.001	-0.004	0	0.001	-0.002	0	0	-0.001	0	0	0.002	0.001	0.001	0.005	0.004

Table B.2: *Numbers of events in the signal region ($E_T^{miss} > 100$ GeV) for each same-sign channel in the signal region, with a break down of the systematic error. The systematics detailed are as described in Section 6.5.* JES$_{\uparrow/\downarrow}$ *denotes the "up" / "down" systematic error due to uncertainty in the jet energy scale and* JER *denotes the systematic error due to uncertainty in the jet energy resolution.* E$_{e,\uparrow/\downarrow}$ *denotes the systematic error due to the electron energy-scale, whilst* res$_e$ *denotes the systematic error due to the electron energy resolution. The columns headed* $\mu_{MS/ID,\uparrow/\downarrow}$ *detail the systematic error resulting from uncertainties in the MS and ID momentum components respectively. The abbreviation* "Lumi." *is short for the uncertainty resulting from the systematic uncertainty on the luminosity estimate,* "pdf." *is short for the uncertainty resulting from parton distribution function re-weighting and "σ" denotes the systematic error resulting from uncertainties on the cross-sections. The largest members of the* JES$_{\uparrow/\downarrow}$, $\mu_{MS/ID,\uparrow/\downarrow}$ *and* E$_{e,\uparrow/\downarrow}$ *pairs are used to compute the total systematic,* "Total.". *Also quoted is the statistical uncertainty (*"Stat."*). Only the Monte Carlo contributions which are non-zero are detailed for each channel.*

and uncertainties in the modelling of initial state and final state radiation, for fakes this includes uncertainties on the predictions which arise from uncertainties in the electron and muon fake rates, and for Z+jets this includes the uncertainties from varying the control-region chosen and the choice of generator [7]. The luminosity, parton distribution function, jet energy scale and resolution, electron scale and resolution and β uncertainties are all uncertainties which are perfectly correlated between the backgrounds. These are each summed linearly to give the uncertainty from each of these systematics on the total standard model estimate. The cross-section uncertainties are not correlated between the backgrounds, and are therefore added in quadrature. The systematics due to the ID and MS muon momentum measurements, and the trigger efficiency uncertainties, are neglected as they are small. Finally, the estimates for each source of uncertainty on the overall estimate, $\bar{\mathcal{S}}_b$, are added in quadrature to give the total systematic uncertainty on the partially data-driven estimate[1].

Table B.4 details the contribution to $\bar{\mathcal{S}}_b$ from each Monte Carlo sample scaled to luminosity and cross-section with a break down of the systematic uncertainties. The overall systematic error from jet, electron and muon scale and resolution uncertainties in Table B.4, is decomposed further in Table B.5. The uncertainties in each column are assumed to be perfectly correlated between the backgrounds, with the exception of the cross-section uncertainties. The overall uncertainty due to scale and resolution uncertainties in the penultimate column of Table B.4 is not perfectly correlated between the backgrounds, but the individual scale and resolution uncertainties of which this is composed are. Perfectly correlated uncertainties are added linearly between the backgrounds, whilst those which are not assumed to be perfectly correlated are added in quadrature. This gives the overall estimate of the uncertainty on $\bar{\mathcal{S}}_b$ quoted for the Monte-Carlo-only estimate.

[1]Note that for single top, some entries in the table are negative. The negative sign is included in the table to make clear the cases where, as one uncertainty is explored, two different background components change in different directions i.e. there are negative correlations. This ensures that when each column is added up, the resulting uncertainty is the same as what it would have been had the background not been decomposed into its components.

	$\bar{\mathcal{S}}_b$	$\mathcal{L}_{sys.}$	$\text{pdf}_{sys.}$	$\sigma_{sys.}$	$\text{other}_{sys.}$	JES	JER	E_e	res_e	$\beta_{sys.}$	Stat.
Single Top	-0.10	-0.01	-0.01	-0.01	-	0.05	-0.05	0.01	0.03	0.01	0.23
Dibosons	0.51	0.06	0.03	0.03	-	0.08	0.00	0.05	0.00	0.00	0.04
Fakes	0.46	-	-	-	0.10	-	-	-	-	0.02	0.31
$t\bar{t}$	0.34	-	-	-	0.12	0.05	0.00	-	-	0.01	0.61
Z/γ^*+jets	0.86	-	-	-	0.49	0.16	0.53	-	-	0.00	0.33
Standard Model	2.06	0.05	0.02	0.03	0.52	0.34	0.48	0.06	0.03	0.05	0.80

Table B.3: *Break down of the uncertainties on the partially data-driven prediction for $\bar{\mathcal{S}}_b$, from all sources of systematics. The column headed "$\mathcal{L}_{sys.}$" details the uncertainty resulting from uncertainty on the luminosity estimate, that headed "$\text{pdf}_{sys.}$" the systematic resulting from uncertainties in the parton distribution functions and that headed "$\sigma_{sys.}$" the systematic resulting from uncertainties in the cross-sections.* JES *denotes the maximum of the "up" and "down" systematic errors due to uncertainty in the jet energy scale and* JER *denotes the systematic error due to uncertainty in the jet energy resolution.* E_e *denotes the maximum of the "up" and "down" systematic errors due to the electron energy-scale, whilst* res_e *denotes the systematic error due to the electron energy resolution. These sources of systematic uncertainty are as described in Section 6.5. The column headed "other_{sys}" details uncertainties which are specific to each background estimate, as described in the text. Also quoted is the statistical uncertainty ("*Stat.*")*

	$\bar{S}_b$	$\mathcal{L}_{sys.}$	pdf_{sys}	σ_{sys}	β_{sys}	$\tau_{e,sys}$	$\tau_{\mu,sys}$	$\text{scale}_{sys.}$	Total sys.	stat.
$t\bar{t}$	0.52	0.057	0.026	0.036	0.017	0.0029	0.0081	0.52	0.53	0.76
Dibosons	0.51	0.056	0.025	0.025	0.00039	9.9e-05	0.00073	0.099	0.12	0.043
Drell Yan	0	0	0	0	0	0	0	0	0	0
Z+jets	0.89	0.098	0.044	0.044	0.0052	9.3e-05	0.0012	0.52	0.54	0.35
W+jets	0	0	0	0	0	0	0	0	0	0
Dijets	0	0	0	0	0	0	0	0	0	0
Single Top	-0.096	-0.011	-0.0048	-0.0048	0.012	0.00023	0.00079	0.079	0.081	0.23

Table B.4: *Predicted composition of background in the flavour subtracted signal region. The various components which make up the total systematic,* Total sys.*, are detailed. The term "$\mathcal{L}_{sys.}$" denotes the uncertainty resulting from the luminosity uncertainties,* "pdf" *is short for the uncertainty resulting from parton distribution function re-weighting and "σ" denotes the systematic error resulting from uncertainties in the cross-section. The column labelled "$\text{scale}_{sys.}$" includes the jet, electron and muon scale and resolution uncertainties, as detailed in Table B.5. The $\text{pdf}_{sys.}$ and σ_{sys} uncertainties are approximate and indicative. The pdf_{sys} is a conservative uncertainty obtained by varying the parton distribution function sets as detailed in the text. The σ_{sys} is an additional uncertainty used to give an approximate uncertainty on the normalisation that arises from sources other than varying the parton distribution function used. These two uncertainties are negligible compared to $\text{scale}_{sys.}$ and thus have no significant impact on the analysis. The columns "$\beta_{sys.}$" and "$\tau_{e/\mu,sys.}$" detail the uncertainties due to the various efficiencies.*

	$\bar{\mathcal{S}}_b$	JES_{up}	JES_{down}	JER	$\text{E}_{e,up}$	$\text{E}_{e,down}$	res_e	$\mu_{MS,up}$	$\mu_{MS,down}$	$\mu_{ID,up}$	$\mu_{ID,down}$	$\text{scale}_{sys.}$
Z+jets	0.89	0.26	-0.06	0.37	0.26	-0.09	0.05	0.00	-0.07	0.00	0.00	0.52
$t\bar{t}$	0.52	0.20	0.11	0.39	-0.19	-0.21	-0.18	-0.01	-0.03	0.00	0.01	0.52
Dibosons	0.51	0.08	-0.06	-0.00	0.05	-0.03	-0.00	0.01	0.00	-0.00	-0.00	0.10
Single Top	-0.10	0.05	-0.02	-0.05	0.01	0.00	0.03	0.00	0.00	0.00	0.00	0.08
Total SM	1.82	0.59	-0.02	0.71	0.13	-0.33	-0.11	-0.00	-0.09	-0.00	0.01	0.99

Table B.5: *Break down of the uncertainty on the subtraction from scale and resolution uncertainties. The various systematics are detailed, then combined together to give a total uncertainty (expressed as an absolute uncertainty). The systematics detailed are as described in Section 6.5.* $\text{JES}_{\uparrow/\downarrow}$ *denote the "up" and "down" systematic error due to uncertainty in the jet energy scale and* JER *denotes the systematic error due to uncertainty in the jet energy resolution.* $\text{E}_{e,\uparrow/\downarrow}$ *denotes the systematic error due to the electron energy-scale, whilst* res_e *denotes the systematic error due to the electron energy resolution. The columns headed* $\mu_{MS/ID,\uparrow/\downarrow}$ *detail the systematic error resulting from uncertainties in the MS and ID momentum components respectively.*

Appendix C

The "Shifted Peak"

This appendix outlines an indirect method for determining the mass difference between two nearly degenerate particles, $\tilde{\ell}_1$ and $\tilde{\ell}_2$, with mass difference, $\Delta m \equiv m_2 - m_1 \ll m_1$ where m_1 and m_2 are the masses of $\tilde{\ell}_1$ and $\tilde{\ell}_2$ respectively. If the mass of $\tilde{\ell}_1$ is known, the mass of $\tilde{\ell}_2$ can be determined using this method. Further details of this result, and its full derivation, are given in Ref. [15]. This method is applicable to any scenario in which:

1. the four-momentum of the $\tilde{\ell}_1$ can be measured,
2. $\tilde{\ell}_2$ can only decay to $\tilde{\ell}_1$,
3. $\tilde{\ell}_1$ and $\tilde{\ell}_2$ are produced by the decay of a common mother particle.

If Δm is small, $\tilde{\ell}_2$ cannot be directly reconstructed because some of its decay products will be very soft, undetectable, particles. It is for this reason that the following indirect means of determining the mass of $\tilde{\ell}_2$, through the mass difference between it and $\tilde{\ell}_1$, was proposed.

In this appendix this method is tested on two sleptons, $\tilde{\ell}_1$ and $\tilde{\ell}_2$, with a difference in mass, $\Delta m \equiv m_2 - m_1 \ll m_1$. The $\tilde{\ell}_1$ is meta-stable as is common in certain supersymmetric models [9, 171, 172] which explain the masses and mixings of the standard model charged leptons and neutrinos in terms of broken flavour symmetries [173]. In gauge-mediated supersymmetry breaking models [174], and in large regions of the parameter space of models with gravity-mediated supersymmetry breaking [175] a meta-stable $\tilde{\ell}_1$ is also predicted. Since the meta-stable $\tilde{\ell}_1$ leaves a track in the muon systems

of large detectors, its momentum can often be measured. The time-of-flight of the $\tilde{\ell}_1$ can be measured by tracking the flight of the particle through these muon systems, allowing a measurement to be made of its velocity. If both the speed and time-of-flight of the $\tilde{\ell}_1$ are known, its four-momentum can be completely determined. The entire event is therefore fully reconstructible (all particles in the decay chains of interest are observed, and their four-momenta are known).

In these models the $\tilde{\chi}_1^0$ can decay to $\tilde{\ell}_1$ or $\tilde{\ell}_2$. If direct decays to $\tilde{\ell}_1$ are used to reconstruct the neutralino, the invariant mass distribution will peak at the neutralino mass (given no systematic experimental offset). A proportion of the time, the neutralino will decay indirectly to $\tilde{\ell}_1$, proceeding via $\tilde{\ell}_2$, which undergoes a three-body decay to $\tilde{\ell}_1$ and two soft leptons. Typically these leptons have energies of the order of Δm and so may remain undetected in a hadron collider experiment. If they are undetected, the neutralino decays $\tilde{\chi}_1^0 \to \tilde{\ell}_1$ and $\tilde{\chi}_1^0 \to \tilde{\ell}_2$ have the same topology.

It will be shown that reconstructing the $\tilde{\chi}_1^0$ using this shared topology, gives two peaks: one at the neutralino mass M, and one slightly shifted to a lower value by an amount $E_{\text{shift}} \sim \Delta m$. If this shift in neutralino mass peak can be measured, it provides evidence for two slepton states lighter than the neutralino, with a mass difference roughly given by E_{shift}. Furthermore, if the two particles in question are scalars, Δm can be determined in terms of E_{shift}, m_1, and the neutralino mass M. If M and m_1 are known, Δm and then $\tilde{\ell}_2$ can be calculated. This method has been termed the "Shifted Peak" method, the peak being shifted by an amount $\sim \Delta m$ from the true neutralino mass resonance.

C.1 Test Case

Rather than simulate a realistic supersymmetric model, `HERWIG` [73, 160] is used to specify a model which contains only the processes of interest, namely sparticles produced through $\tilde{q}\tilde{q}$, $\tilde{q}\tilde{g}$, and $\tilde{g}\tilde{g}$ pair production, followed by the cascade decays $(\tilde{g} \to)\tilde{q} \to \tilde{\chi}_1^0 \to \tilde{\ell}_{1,2}$. The chosen particle masses are (where all squarks are degenerate): $m_{\tilde{g}} = 650$ GeV, $m_{\tilde{q}} = 450$ GeV, $M = m_{\tilde{\chi}_1^0} = 225.2$ GeV, $m_2 = m_{\tilde{\ell}_2} = 139.9$ GeV and $m_1 = m_{\tilde{\ell}_1} = 134.9$ GeV. All remaining sparticles are made to be very heavy, and so are inaccessible to colliders. Additionally, $\tilde{\ell}_1 = \tilde{e}_R$, $\tilde{\ell}_2 = \tilde{\mu}_R$, and $BR(\tilde{\chi}_1^0 \to \tilde{\ell}_1) = BR(\tilde{\chi}_1^0 \to \tilde{\ell}_2)$, as appropriate for the case of a gaugino $\tilde{\chi}_1^0$ and right-handed sleptons.

The simulation of these events follows an identical procedure to that described in Chapter 8. Events are generated at $\sqrt{s} = 14$ GeV and passed through a generic LHC detector simulation, `AcerDET1.0` [77]. `AcerDET` is configured as follows: electrons and muons are selected with $p_T > 6$ GeV and $|\eta| < 2.5$. Electrons and muons are considered to be isolated if they lie at a distance greater than $\Delta R > 0.4$ from other leptons or jets and if less than 10 GeV of energy is deposited in a cone of $\Delta R = 0.2$. The lepton momentum resolutions used are according to the performance results of ATLAS full simulation [67]. The electrons are smeared according to a pseudorapidity-dependent parameterisation, whilst muons are smeared according to the results for $|\eta| < 1.1$. `AcerDET` does not take into account lepton reconstruction efficiencies. A reconstruction efficiency of 90% to the muons and a reconstruction efficiency of 77% to the electrons is applied "by hand". This gives 0.86 as the ratio of electron to muon reconstruction efficiency.

In total, 20,000 events (before any cuts or requirements are imposed) are considered, corresponding to 40,000 $\tilde{\chi}_1^0$ decays. The cross section for the events of interest and for the parameters chosen is ~ 50 pb (as returned by `HERWIG`), and so the event samples assume an integrated luminosity of $\mathcal{L} \sim 0.4$ fb^{-1}. In a more realistic model, only a fraction ϵ of all supersymmetric events will satisfy the event criteria, giving an assumed integrated luminosity is 0.4 fb$^{-1}/\epsilon$.

The $\tilde{\ell}_1$ are treated in exactly the way described in Chapter 8. That is, it is reasonable to consider only sleptons with $\beta > 0.6$, those with β less than this will not arrive in the same bunch crossing. Placing an upper limit on β improves the mass resolution (which tends to degrade as β approaches unity). Therefore $\tilde{\ell}_1$ candidates are required to have velocity, $0.6 < \beta < 0.8$. Also as in Chapter 8, the $\tilde{\ell}_1$ momenta $|\vec{p}_{\tilde{\ell}_1}|$ are taken from truth and smeared by a Gaussian with $\sigma = 0.05|\vec{p}_{\tilde{\ell}_1}|$ and each β is smeared by a Gaussian with $\sigma = 0.02$ (see the results in Ref. [161]). The resulting $\tilde{\ell}_1$ mass distribution is given in Figure C.1. From this point onwards, the measurement of m_1 is taken to be 134.9 GeV, the true mass of the $\tilde{\ell}_1$. The Gaussian fit gives 135.0 ± 0.1 GeV, consistent with this. The four-momentum components of each $\tilde{\ell}_1$ are scaled to give the exact value of the measured $\tilde{\ell}_1$ mass, 134.9 GeV.

To eliminate the soft leptons from $\tilde{\ell}_2$ decays, each selected lepton is required to have $p_T > 30$ GeV. The p_T distribution of these soft leptons is shown in Figure C.2, from which it can be seen that such a cut is indeed a reasonable choice. This cut is the same

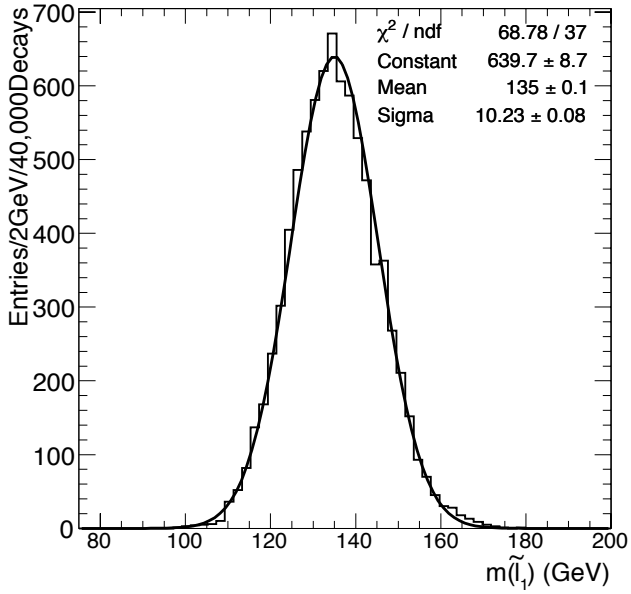

Figure C.1: *Reconstructed* $\tilde{\ell}_1$ *with* $0.6 < \beta < 0.8$ *after smearing* $\tilde{\ell}_1$ *momenta with a Gaussian with* $\sigma = 0.05|\vec{p}_{\tilde{\ell}_1}|$ *centred on the true momentum and* β *with a Gaussian with* $\sigma = 0.02$. *The mass of the* $\tilde{\ell}_1$ *is measured to be* 135.0 ± 0.1 GeV, *consistent with the true* $\tilde{\ell}_1$ *mass of* 134.9 GeV.

as that which is applied in Chapter 8.

C.2 Description of the "Shifted Peak" Method

The derivation which follows is taken from Ref. [15]. The neutralino will decay into $\tilde{\ell}_1$ in one of two ways:

1. Direct decay to $\tilde{\ell}_1$,

$$\tilde{\chi}_1^0 \to \tilde{\ell}_1^{\pm} \ell_1^{\mp} \ . \tag{C.1}$$

2. Decay to $\tilde{\ell}_2$,

$$\tilde{\chi}_1^0 \to \tilde{\ell}_2^{\pm} \ell_2^{\mp} \ , \tag{C.2}$$

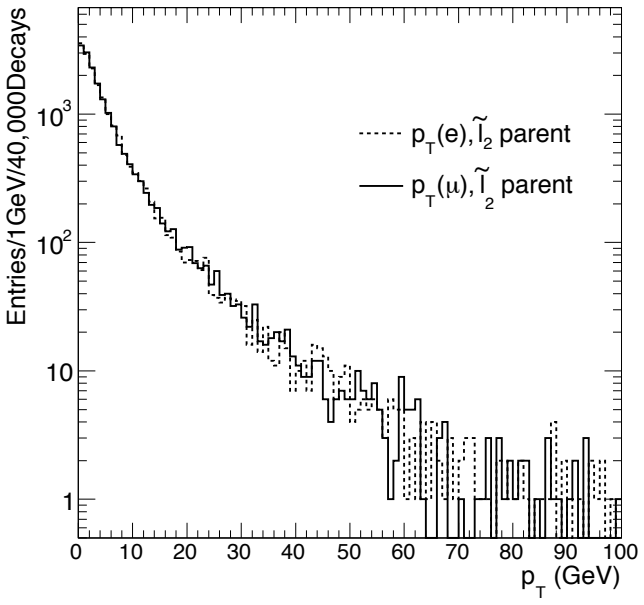

Figure C.2: *The p_T distribution of leptons produced by the three-body decays of $\tilde{\ell}_2$. A hard p_T cut is applied at* 30 GeV *to eliminate soft leptons from the three-body $\tilde{\ell}_2$ decays.*

followed by one of the two three-body decays [176, 177]

$$\tilde{\ell}_2^{\pm} \rightarrow \tilde{\ell}_1^{\pm} X^{\pm\mp} , \tag{C.3}$$

$$\tilde{\ell}_2^{\pm} \rightarrow \tilde{\ell}_1^{\mp} X^{\pm\pm} , \tag{C.4}$$

where $X^{\pm\mp}$ contains two opposite-sign (OS) leptons, and $X^{\pm\pm}$ contains two same-sign (SS) leptons. These pairs are denoted by X to emphasise that they are soft and so should not pass the chosen lepton p_T cut ($p_T > 30$ GeV).

The observed particles are the hard lepton (ℓ_1 or ℓ_2) from Equation C.1 or C.2, and the long-lived slepton ($\tilde{\ell}_1$) from Equation C.1, C.3 or C.4. It is therefore possible to form two different reconstructed invariant mass distributions:

$$\begin{aligned} m^2_{\tilde{\ell}\ell_1} &\equiv \left(p_{\tilde{\ell}_1} + p_{\ell_1}\right)^2 , \\ m^2_{\tilde{\ell}\ell_2} &\equiv \left(p_{\tilde{\ell}_1} + p_{\ell_2}\right)^2 . \end{aligned} \tag{C.5}$$

where p_a is the four-momentum of particle a. The $\tilde{\ell}_1$ and ℓ_2 can either have the same charges, or opposite charges. The $\tilde{\ell}_1$ and ℓ_1 must have opposite charges. For the first

case,

$$m_{\tilde{\ell}\ell_1} = M \ , \tag{C.6}$$

and so the invariant mass distribution peaks at the correct neutralino mass. However, because of the missing soft leptons, for the second case,

$$m_{\tilde{\ell}\ell_2} \neq M \ , \tag{C.7}$$

and the peak of the $m_{\tilde{\ell}\ell_2}$ distribution is shifted from M to $M - E_{\rm shift}$.

A peak in the invariant mass distribution, $m_{\tilde{\ell}_1^\pm \ell_2^\pm}$, formed from events with a SS lepton and slepton pair, can only result from reconstructing decays of the type described by Equation C.2. This distribution will therefore exhibit just one peak with a shift, $E_{\rm shift}$, from the true neutralino mass peak. The analogous OS distribution will contain both the type of events specified in Equation C.1 and those specified in Equation C.2. The OS distribution will therefore exhibit a double peak structure with the two peaks separated by an amount $E_{\rm shift}$.

If leptons ℓ_1 and ℓ_2 have different flavour, the SS distributions will not be required in order to separate out a purely shifted peak. For illustration, the $\tilde{\ell}_1 = \tilde{e}$ and $\tilde{\ell}_2 = \tilde{\mu}$, and so $\ell_1 = e$ and $\ell_2 = \mu$. To calculate the peak shift $E_{\rm shift}$, denote the $\tilde{\ell}_1$ energy by E_1, then,

$$m^2_{\tilde{\ell}_\mu} = M^2 - m_2^2 + m_1^2 - 2p_\mu \cdot p_X \ . \tag{C.8}$$

The masses of the leptons are neglected. In the $\tilde{\ell}_2$ rest frame, with the $x-y$ plane taken to be the plane of the muon and dilepton three-momenta, $\vec{p}_\mu$ and $\vec{p}_X$, and the $\hat{x}$-axis as the muon direction, the four-momenta of the hard muon and the soft dilepton are then given by

$$p_\mu = \frac{M^2 - m_2^2}{2m_2}(1, \hat{x}) \ , \tag{C.9}$$

$$p_X = \left(m_2 - E_1, -\hat{n}\sqrt{{E_1}^2 - m_1^2}\right) \ , \tag{C.10}$$

respectively, where $\hat{n} = (\cos\theta, \sin\theta, 0)$. Substituting Equations C.9 and C.10 into Equa-

tion C.8 yields,

$$m^2_{\tilde{\ell}_\mu} = m_1^2 + \frac{M^2 - m_2^2}{m_2}\left(E_1 - \cos\theta\sqrt{E_1^2 - m_1^2}\right), \tag{C.11}$$

with E_1 and $\cos\theta$ varying independently in the intervals

$$E_1 \in \left[m_1, \frac{m_2^2 + m_1^2}{2m_2}\right], \tag{C.12}$$

$$\cos\theta \in [-1, +1]\ . \tag{C.13}$$

If the condition that $\Delta m \ll m_1$ is imposed E_1, at leading order in Δm, is given in Equation C.12,

$$\frac{m_2^2 + m_1^2}{2m_2} \approx m_1\left(1 + \frac{1}{2}x^2\right), \tag{C.14}$$

where

$$x \equiv \frac{\Delta m}{m_1}\ . \tag{C.15}$$

E_1 can therefore be parameterised as,

$$E_1 = m_1\left(1 + \frac{1}{2}ax^2\right), \tag{C.16}$$

where $0 \leq a \leq 1$, and varies from event to event. To leading order in the mass splitting,

$$m^2_{\tilde{\ell}_\mu} - M^2 \sim -\left[(M^2 + m_1^2) + \cos\theta\sqrt{a}(M^2 - m_1^2)\right]x\ . \tag{C.17}$$

The peak shift, E_{shift} is defined by the peak of the $m^2_{\tilde{\ell}_\mu}$ distribution to be

$$E_{\text{shift}} = M - \sqrt{m^2_{\tilde{\ell}_\mu}|_{\text{ peak}}}\ . \tag{C.18}$$

Recalling that $a \leq 1$, the second term of the right-hand side of Equation C.17 will always be smaller than the first by a minimum of:

$$\frac{M^2 - m_1^2}{M^2 + m_1^2}\ . \tag{C.19}$$

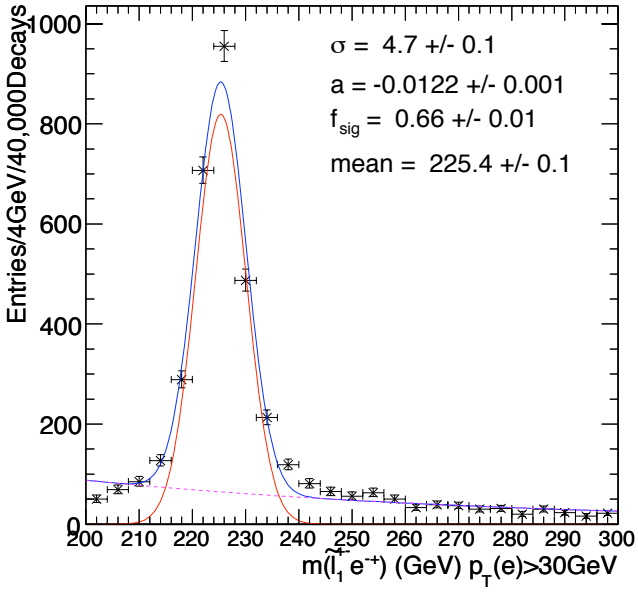

Figure C.3: *The $\tilde{\ell}_1^{\pm} e^{\mp}$ invariant mass distribution, for leptons with $p_T > 30$ GeV. The fit parameters σ, a, $f_{\rm sig}$, and mean are defined in Equation C.21.*

Therefore a good estimate of the mass splitting Δm can be obtained from the relationship,

$$E_{\rm shift} \sim \frac{M^2 + m_1^2}{2Mm_1} \Delta m \ . \tag{C.20}$$

An overview of the NLO calculation of this shift can be found in Ref. [15].

C.3 Results

The $m_{\tilde{\ell}_1 e}$ and $m_{\tilde{\ell}_1 \mu}$ invariant mass distributions can be reconstructed by forming all OS $\tilde{\ell}_1^{\pm} e^{\mp}$ and $\tilde{\ell}_1^{\pm} \mu^{\mp}$ pairings for leptons with $p_T > 30$ GeV. Equation C.20 predicts that $\widehat{m}_{\tilde{\ell}_1 e} - \widehat{m}_{\tilde{\ell}_1 \mu} = 5.6$ GeV (with $\widehat{m}_{\tilde{\ell}_1 e} = m_{\tilde{\chi}_1^0} = 225.2$ GeV and $\widehat{m}_{\tilde{\ell}_1 \mu} = 219.6$ GeV).

These invariant mass distributions are shown in Figures C.3 and C.4. These two distributions are separately decomposed into two pieces by fitting each with the sum of an exponentially falling background underneath a Gaussian distribution which takes the

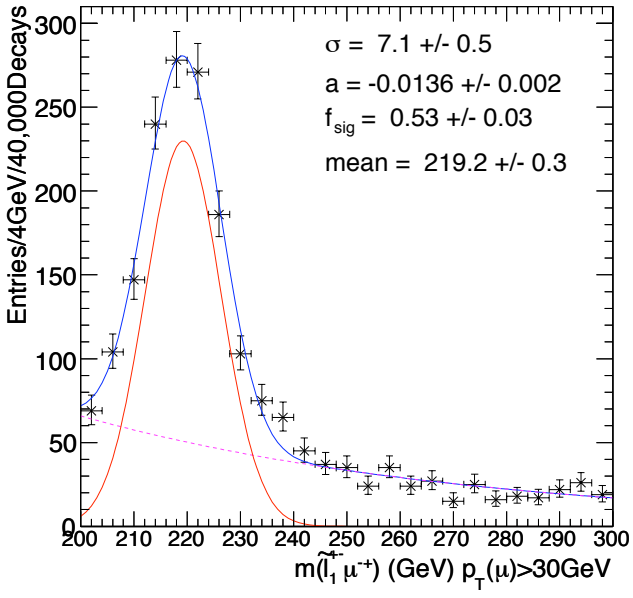

Figure C.4: *The $\tilde{\ell}_1^{\pm}\mu^{\mp}$ invariant mass distribution, for leptons with $p_T > 30$ GeV. The fit parameters σ, a, $f_{\rm sig}$, and mean are defined in Equation C.21.*

form,

$$\frac{dN}{dm} = N_{\rm tot}\left[(1-f_{\rm sig})|a|e^{am} + f_{\rm sig}\sqrt{\frac{2}{\pi}}\frac{1}{\sigma}e^{-\frac{(m-\text{mean})^2}{2\sigma^2}}\right] , \tag{C.21}$$

where a and mean have units of GeV^{-1} and GeV, respectively. The means of the Gaussian components then give,

$$\begin{aligned} \widehat{m}_{\tilde{\ell}e} &= 225.4 \pm 0.1 \text{ GeV} , \\ \widehat{m}_{\tilde{\ell}\mu} &= 219.2 \pm 0.3 \text{ GeV} . \end{aligned} \tag{C.22}$$

Using Equation C.20 and the peak positions given in Equation C.22, it can be inferred that the selectron and the smuon are split in mass by

$$\Delta m = 5.5 \pm 0.3 \text{ GeV} . \tag{C.23}$$

This compares well with the true 5 GeV mass difference between the sleptons.

Colophon

This thesis was made in LaTeX 2_ε using the "hepthesis" class [178].

Bibliography

[1] R. Brun and F. Rademakers, *ROOT: An object oriented data analysis framework*, Nucl. Instrum. Meth. **A389** (1997) 81--86.

[2] The ATLAS Collaboration, *Electron and photon reconstruction and identification: expected performance at high energy and results at 900 GeV*, ATLAS-CONF-2010-005, cds:1273197.

[3] The ATLAS Collaboration, *Observation of $W \to l\nu$ and $Z \to ll$ production in proton-proton collisions at $\sqrt{s} = 7$ TeV with the ATLAS detector*, ATLAS-CONF-2010-044.

[4] The ATLAS Collaboration, *Measurement of the $W \to l\nu$ production cross-section and observation of $Z \to ll$ production in proton-proton collisions at $\sqrt{s} = 7$ TeV with the ATLAS detector*, ATLAS-CONF-2010-051.

[5] The ATLAS Collaboration, *Measurement of the $Z \to ll$ production cross section in proton-proton collisions at $\sqrt{s} = 7$ TeV with the ATLAS detector*, ATLAS-CONF-2010-076.

[6] The ATLAS Collaboration, *Search for supersymmetric particles in events with lepton pairs and large missing transverse momentum in $\sqrt{s} = 7$ TeV proton-proton collisions with the ATLAS experiment*, submitted to EPJC Letters , arXiv:1103.6214 [hep-ex].

[7] The ATLAS Collaboration, *SUSY searches with dileptons and high missing transverse momentum*, ATL-PHYS-INT-2011-030, cds:1341811.

[8] The ATLAS Collaboration, *Search for an excess of events with an identical flavour lepton pair and significant missing transverse momentum in $\sqrt{s} = 7$ TeV proton-proton collisions with the ATLAS detector*, submitted to EPJC Letters , arXiv:1103.6208 [hep-ex].

[9] J. L. Feng, C. G. Lester, Y. Nir, and Y. Shadmi, *The Standard Model and Supersymmetric Flavor Puzzles at the Large Hadron Collider*, Phys. Rev. **D77** (2008) 076002, arXiv:0712.0674 [hep-ph].

[10] J. L. Feng et al., *Measuring Slepton Masses and Mixings at the LHC*, JHEP **01** (2010) 047, arXiv:0910.1618 [hep-ph].

[11] The ATLAS Collaboration, *Performance of the ATLAS Detector using First Collision Data*, JHEP **1009** (2010) 056, arXiv:1005.5254 [hep-ex].

[12] C. S. Cowden, S. T. French, J. A. Frost, and C. G. Lester, *Discovering the lightest Neutralino in R-parity Violating SUSY with non-zero λ''_{112} using Jet Substructure and the $k_\perp$ Algorithm*, ATL-PHYS-INT-2009-039, cds:1167947.

[13] The ATLAS Collaboration, *A method for discovering heavy particles decaying into single boosted jets with substructure using the $k_\perp$ algorithm*, ATL-PUB-PHYS-2009-076, cds:1177832.

[14] S. T. French (on behalf of the ATLAS Collaboration), *R-parity violation with jet signatures at the ATLAS detector*, ATL-PHYS-PROC-2009-089, cds:1205821.

[15] J. L. Feng, S. T. French, C. G. Lester, Y. Nir, and Y. Shadmi, *The Shifted Peak: Resolving Nearly Degenerate Particles at the LHC*, Phys. Rev. **D80** (2009) 114004, arXiv:0906.4215 [hep-ph].

[16] The ATLAS Collaboration, *Early supersymmetry searches with jets, missing transverse momentum and one or more leptons with the ATLAS Detector*, ATLAS-CONF-2010-066.

[17] The ATLAS Collaboration, *Search for new physics in multi-body final states at high invariant masses with ATLAS*, ATLAS-CONF-2010-088.

[18] M. Kobayashi and T. Maskawa, *CP Violation in the Renormalizable Theory of Weak Interaction*, Prog. Theor. Phys. **49** (1973) 652--657.

[19] J. J. Thomson, *Cathode rays*, Phil. Mag. **44** (1897) 293--316.

[20] C. D. Anderson, *The Apparent Existence of Easily Deflectable Positives*, Science **76** (1932) 238--239.

[21] C. D. Anderson and S. H. Neddermeyer, *Cloud Chamber Observations of Cosmic Rays at 4300 Meters Elevation and Near Sea-Level*, Phys. Rev. **50** (1936) 263--271.

[22] M. L. Perl et al., *Evidence for anomalous lepton production in e^+e^- annihilation*, Phys. Rev. Lett. **35** (1975) 1489--1492.

[23] M. L. Perl et al., *Properties of Anomalous $e\mu$ Events Produced in e^+e^- Annihilation*, Phys. Lett. **B63** (1976) 466.

[24] M. L. Perl et al., *Properties of the Proposed τ Charged Lepton*, Phys. Lett. **B70** (1977) 487.

[25] C. L. Cowan, F. Reines, F. B. Harrison, H. W. Kruse, and A. D. McGuire, *Detection of the free neutrino: A Confirmation*, Camb. Monogr. Part. Phys. Nucl. Phys. Cosmol. **14** (2000) 38--42.

[26] F. Reines and C. L. Cowan, *Detection of the free neutrino*, Phys. Rev. **92** (1953) 830--831.

[27] F. Reines, C. L. Cowan, F. B. Harrison, A. D. McGuire, and H. W. Kruse, *Detection of the free anti-neutrino*, Phys. Rev. **117** (1960) 159--173.

[28] C. L. Cowan, F. Reines, F. B. Harrison, H. W. Kruse, and A. D. McGuire, *Detection of the free neutrino: A Confirmation*, Science **124** (1956) 103--104.

[29] C. L. Cowan, F. Reines, F. B. Harrison, H. W. Kruse, and A. D. McGuire, *Detection of the free neutrino: A Confirmation*, Camb. Monogr. Part. Phys. Nucl. Phys. Cosmol. **1** (1991) 41--46.

[30] G. Danby et al., *Observation of High-Energy Neutrino Reactions and the Existence of Two Kinds of Neutrinos*, Phys. Rev. Lett. **9** (1962) 36--44.

[31] The DONUT Collaboration, K. Kodama et al., *Observation of τ-neutrino interactions*, Phys. Lett. **B504** (2001) 218--224, arXiv:hep-ex/0012035.

[32] E. D. Bloom et al., *High-Energy Inelastic e p Scattering at 6-Degrees and 10- Degrees*, Phys. Rev. Lett. **23** (1969) 930--934.

[33] M. Breidenbach et al., *Observed Behavior of Highly Inelastic electron-Proton Scattering*, Phys. Rev. Lett. **23** (1969) 935--939.

[34] The SLAC-SP-017 Collaboration, J. E. Augustin et al., *Discovery of a Narrow Resonance in e^+e^- Annihilation*, Phys. Rev. Lett. **33** (1974) 1406--1408.

[35] The E598 Collaboration, J. J. Aubert et al., *Experimental Observation of a Heavy Particle J*, Phys. Rev. Lett. **33** (1974) 1404--1406.

[36] S. W. Herb et al., *Observation of a dimuon resonance at 9.5 GeV in 400 GeV proton - nucleus collisions*, Phys. Rev. Lett. **39** (1977) 252--255.

[37] The D0 Collaboration, S. Abachi et al., *Search for high mass top quark production in $p\bar{p}$ collisions at $\sqrt{s} = 1.8$ TeV*, Phys. Rev. Lett. **74** (1995) 2422--2426, arXiv:hep-ex/9411001.

[38] The CDF Collaboration, F. Abe et al., *Observation of top quark production in $\bar{p}p$ collisions*, Phys. Rev. Lett. **74** (1995) 2626--2631, arXiv:hep-ex/9503002.

[39] The TASSO Collaboration, R. Brandelik et al., *Evidence for Planar Events in e^+e^- Annihilation at High- Energies*, Phys. Lett. **B86** (1979) 243.

[40] The UA1 Collaboration, *Experimental observation of isolated large transverse energy electrons with associated missing energy at $\sqrt{s} = 540$ GeV*, Phys. Lett. **B122** (1983) 103--116.

[41] The UA1 Collaboration, *Experimental observation of lepton pairs of invariant mass around 95 GeV/c^2 at the CERN SPS collider*, Phys. Lett. **B126** (1983) 398--410.

[42] The UA2 Collaboration, *Observation of single isolated electrons of high transverse momentum in events with missing transverse energy at the CERN anti-p p collider*, Phys. Lett. **B122** (1983) 476--485.

[43] The UA2 Collaboration, *Evidence for $Z \to e^+e^-$ at the CERN anti-p p collider*, Phys. Lett. **B129** (1983) 130--140.

[44] Particle Data Group Collaboration, *Review of particle physics*, Phys. Lett. **B33** (1970) 1--127.

[45] P. W. Higgs, *Broken Symmetries and the Masses of the Gauge Bosons*, Phys. Rev. Lett. **13** (1964) 508--509.

[46] F. Englert and R. Brout, *Broken Symmetry and the Mass of Gauge Vector Mesons*, Phys. Rev. Lett. **13** (1964) 321--322.

[47] The Super-Kamiokande Collaboration, Y. Fukuda et al., *Measurements of the Solar Neutrino Flux from Super-Kamiokande's First 300 Days*, Phys. Rev. Lett. **81** (Aug, 1998) 1158--1162.

[48] The Super-Kamiokande Collaboration, Y. Fukuda et al., *Evidence for oscillation of atmospheric neutrinos*, Phys.Rev.Lett. **81** (1998) 1562--1567, arXiv:hep-ex/9807003 [hep-ex].

[49] R. Hempfling, *Neutrino Masses and Mixing Angles in SUSY-GUT Theories with explicit R-Parity Breaking*, Nucl. Phys. **B478** (1996) 3--30, arXiv:hep-ph/9511288.

[50] B. W. Lee, C. Quigg, and H. B. Thacker, *Weak Interactions at Very High-Energies: The Role of the Higgs Boson Mass*, Phys. Rev. **D16** (1977) 1519.

[51] H. E. Haber, *Present status and future prospects for a Higgs boson discovery at the Tevatron and LHC*, J. Phys. Conf. Ser. **259** (2010) 012017, arXiv:1011.1038 [hep-ph].

[52] S. P. Martin, *A Supersymmetry Primer*, arXiv:hep-ph/9709356.

[53] S. Weinberg, *The quantum theory of fields. Vol. 3: Supersymmetry*. Cambridge, UK: Univ. Pr. (2000) 419 p.

[54] S. R. Coleman and J. Mandula, *All Possible Symmetries of the S Matrix*, Phys. Rev. **159** (1967) 1251--1256.

[55] The ATLAS Collaboration, *Search for squarks and gluinos using final states with jets and missing transverse momentum with the ATLAS detector in $\sqrt{s} = 7$ TeV proton-proton collisions*, arXiv:1102.5290 [hep-ex].

[56] C. G. Lester, *Model independent sparticle mass measurements at ATLAS*, CERN-THESIS-2004-003, cds:705139.

[57] The ATLAS Collaboration, *Luminosity Determination Using the ATLAS Detector*, ATLAS-CONF-2010-060.

[58] The ATLAS Collaboration, *Characterization of Interaction-Point Beam Parameters Using the pp Event-Vertex Distribution Reconstructed in the ATLAS Detector at the LHC*, ATLAS-CONF-2010-027.

[59] The ATLAS Collaboration, *ATLAS Public Results*, https://twiki.cern.ch/twiki/bin/view/AtlasPublic/WebHome.

[60] The ALICE Collaboration, *Events recorded by the ALICE experiment from the first lead ion collisions, at a centre-of-mass energy of 2.76 TeV per nucleon pair*, cds:1305399.

[61] The ATLAS Collaboration, *ATLAS: Detector and Physics Performance - Technical Design Report, Volume 1*, CERN-LHCC-99-014, cds:391176.

[62] The ATLAS Collaboration, *ATLAS: Detector and Physics Performance - Technical Design Report, Volume 2*, CERN-LHCC-99-015, cds:391177.

[63] The ATLAS Collaboration, *ATLAS Pixel Detector - Technical Design Report*, CERN-LHCC-98-013, cds:381263.

[64] The ATLAS Collaboration, *ATLAS Calorimeter Performance*, CERN-LHCC-96-040, cds:331059.

[65] The ATLAS Collaboration, *ATLAS Liquid Argon Calorimeter - Technical Design Report*, CERN-LHCC-96-041, cds:331061.

[66] The ATLAS Collaboration, *ATLAS Muon Spectrometer - Technical Design Report*, CERN-LHCC-97-022, cds:331068.

[67] The ATLAS Collaboration, *The ATLAS Experiment at the CERN Large Hadron Collider*, JINST **3** (2008) S08003.

[68] The ATLAS Collaboration, *ATLAS Detector Photos*, http://atlas.ch/atlas_photos.html.

[69] The ATLAS Collaboration, *ATLAS Inner Detector - Technical Design Report, Volume 1*, CERN-LHCC-97-16, cds:331063.

[70] The ATLAS Collaboration, *ATLAS Inner Detector - Technical Design Report, Volume 2*, CERN-LHCC-97-17, cds:331064.

[71] The ATLAS Collaboration, *ATLAS Computing - Technical Design Report*, CERN-LHCC-2005-022, cds:837738.

[72] The ATLAS Collaboration, *The ATLAS Simulation Infrastructure*, Eur.Phys.J. **C70** (2010) 823--874, arXiv:1005.4568 [physics.ins-det].

[73] G. Corcella et al., *HERWIG 6.5: an event generator for Hadron Emission Reactions With Interfering Gluons (including supersymmetric processes)*, JHEP **01** (2001) 010, arXiv:hep-ph/0011363.

[74] T. Sjostrand, S. Mrenna, and P. Skands, *PYTHIA 6.4 Physics and Manual*, JHEP **05** (2006) 026, arXiv:hep-ph/0603175.

[75] The GEANT4 Collaboration, *GEANT4: A simulation toolkit*, Nucl. Instrum. Meth. **A506** .

[76] E. Richter-Was, D. Froidevaux and L. Poggioli, *ATLFAST 2.0 a fast simulation package for ATLAS*, ATL-PHYS-98-131, cds:683751.

[77] E. Richter-Was, *AcerDET: A particle level fast simulation and reconstruction package for phenomenological studies on high p_T physics at LHC*, arXiv:hep-ph/0207355.

[78] The ATLAS Collaboration, *Calorimeter Clustering Algorithms: Description and Performance*, cds:1099735.

[79] The ATLAS Collaboration, *ATLAS Monte Carlo tunes for mc09*, ATL-PHYS-PUB-2010-002, cds:1247375.

[80] A. Sherstnev and R. S. Thorne, *Parton Distributions for LO Generators*, Eur. Phys. J. **C55** (2008) 553--575, arXiv:0711.2473 [hep-ph].

[81] The ATLAS Collaboration, *Observation of Inclusive Electrons in the ATLAS Experiment at $\sqrt{s} = 7$ TeV*, ATLAS-CONF-2010-073.

[82] M. Aharrouche et al., *Response Uniformity of the ATLAS liquid argon electromagnetic calorimeter*, Nuclear Instrumentation Methods **A582** (2007) 429--455.

[83] The ALEPH Collaboration, *Precision electroweak measurements on the Z resonance*, Phys. Rept. **427** (2006) 257, arXiv:hep-ex/0509008.

[84] A. D. Martin, W. J. Stirling, R. S. Thorne, and G. Watt, *Parton distributions for the LHC*, Eur. Phys. J. **C63** (2009) 189--285, arXiv:0901.0002 [hep-ph].

[85] C. Anastasiou, L. J. Dixon, K. Melnikov, and F. Petriello, *High precision QCD at hadron colliders: Electroweak gauge boson rapidity distributions at NNLO*, Phys. Rev. **D69** (2004) 094008, arXiv:hep-ph/0312266.

[86] A. D. Martin, R. G. Roberts, W. J. Stirling, and R. S. Thorne, *Uncertainties of predictions from parton distributions - 1: Experimental errors*, Eur. Phys. J. **C28** (2003) 455--473, arXiv:hep-ph/0211080.

[87] J. Pumplin et al., *Uncertainties of predictions from parton distribution functions. 2. The Hessian method*, Phys. Rev. **D65** (2001) 014013, arXiv:hep-ph/0101032.

[88] A. D. Martin, W. J. Stirling, R. S. Thorne, and G. Watt, *Uncertainties on α_S in global PDF analyses and implications for predicted hadronic cross sections*, Eur. Phys. J. **C64** (2009) 653--680, arXiv:0905.3531 [hep-ph].

[89] I. Hinchliffe, F. E. Paige, M. D. Shapiro, J. Soderqvist, and W. Yao, *Precision SUSY measurements at CERN LHC*, Phys. Rev. **D55** (1997) 5520--5540, arXiv:hep-ph/9610544.

[90] B. C. Allanach, C. G. Lester, M. A. Parker, and B. R. Webber, *Measuring sparticle masses in non-universal string inspired models at the LHC*, JHEP **09** (2000) 004, arXiv:hep-ph/0007009.

[91] D. Costanzo and D. R. Tovey, *Supersymmetric particle mass measurement with invariant mass correlations*, JHEP **04** (2009) 084, arXiv:0902.2331 [hep-ph].

[92] The D0 Collaboration, *Search for associated production of charginos and neutralinos in the trilepton final state using 2.3 fb^{-1} of data*, Phys. Lett. **B680** (2009) 34--43.

[93] S. Frixione, P. Nason, and C. Oleari, *Matching NLO QCD computations with Parton Shower simulations: the POWHEG method*, JHEP **11** (2007) 070, arXiv:0709.2092 [hep-ph].

[94] S. Frixione, E. Laenen, P. Motylinski, and B. R. Webber, *Single-top production in MC@NLO*, JHEP **0603** (2006) 092, arXiv:hep-ph/0512250 [hep-ph].

[95] S. Frixione and B. R. Webber, *Matching NLO QCD computations and parton shower simulations*, JHEP **0206** (2002) 029, arXiv:hep-ph/0204244 [hep-ph].

[96] P. M. Nadolsky et al., *Implications of CTEQ global analysis for collider observables*, Phys. Rev. **D78** (2008) 013004, arXiv:0802.0007 [hep-ph].

[97] M. L. Mangano, M. Moretti, F. Piccinini, R. Pittau, and A. D. Polosa, *ALPGEN, a generator for hard multiparton processes in hadronic collisions*, JHEP **07** (2003) 001, arXiv:hep-ph/0206293.

[98] D. Stump et al., *Inclusive jet production, parton distributions, and the search for new physics*, JHEP **10** (2003) 046, arXiv:hep-ph/0303013.

[99] J. M. Butterworth, J. R. Forshaw, and M. H. Seymour, *Multiparton interactions in photoproduction at HERA*, Z. Phys. **C72** (1996) 637--646, arXiv:hep-ph/9601371.

[100] M. Bahr et al., *Herwig++ 2.3 Release Note*, arXiv:0812.0529 [hep-ph].

[101] F. E. Paige, S. D. Protopopescu, H. Baer, and X. Tata, *ISAJET 7.69: A Monte Carlo event generator for pp, anti-p p, and e+e- reactions*, arXiv:hep-ph/0312045 [hep-ph].

[102] W. Beenakker, R. Hopker, and M. Spira, *PROSPINO: A program for the PROduction of Supersymmetric Particles In Next-to-leading Order QCD*, arXiv:hep-ph/9611232.

[103] U. Langenfeld, S. Moch, and P. Uwer, *Measuring the running top-quark mass*, Phys. Rev. **D80** (2009) 054009, arXiv:0906.5273 [hep-ph].

[104] K. Melnikov and F. Petriello, *Electroweak gauge boson production at hadron colliders through O(alpha(s)**2),High precision QCD at hadron colliders*, Phys. Rev. **D74** (2006) 114017, hep-ph/0609070.

[105] R. Gavin, Y. Li, and F. Petriello, *FEWZ 2.0: A code for hadronic Z production at next-to-next-to-leading order*, arXiv:1011.3540.

[106] J. Butterworth, E. Dobson, U. Klein, B. Mellado Garcia, T. Nunnemann, J. Qian, D. Rebuzzi, and R. Tanaka, *Single Boson and Diboson Production Cross Sections in pp Collisions at* $\sqrt{s} = 7$ *TeV*, Tech. Rep. ATL-COM-PHYS-2010-695, CERN, Geneva, Aug, 2010.

[107] M. Cacciari, G. P. Salam, and G. Soyez, *The anti-*k_t *jet clustering algorithm*, JHEP **04** (2008) 063, arXiv:0802.1189 [hep-ph].

[108] The ATLAS Collaboration, E. Abat et al., *Study of energy response and resolution of the ATLAS barrel calorimeter to hadrons of energies from 20 GeV to 350 GeV*, Nucl.Instrum.Meth. **A621** (2010) 134--150.

[109] S. Moch and P. Uwer, *Theoretical status and prospects for top-quark pair production at hadron colliders*, Phys. Rev. **D78** (2008) 034003, arXiv:0804.1476 [hep-ph].

[110] U. Langenfeld, S. Moch, and P. Uwer, *New results for* $t\bar{t}$ *production at hadron colliders*, arXiv:0907.2527 [hep-ph].

[111] The ATLAS Collaboration, G. Aad et al., *Measurement of inclusive jet and dijet cross sections in proton-proton collisions at 7 TeV centre-of-mass energy with the ATLAS detector*, arXiv:1009.5908v2.

[112] The ATLAS Collaboration, G. Aad et al., *Jet energy resolution and selection efficiency relative to track jets from in-situ techniques with the ATLAS Detector Using Proton-Proton Collisions at a Center of Mass Energy $\sqrt{s} = 7$ TeV*, ATLAS-CONF-2010-054, 1281311.

[113] *Muon Momentum Resolution in First Pass Reconstruction of pp Collision Data Recorded by ATLAS in 2010*, cds:1322424.

[114] The ATLAS Collaboration, *Data-Quality Requirements and Event Cleaning for Jets and Missing Transverse Energy Reconstruction with the ATLAS Detector in Proton-Proton Collisions at a Center-of-Mass Energy of $\sqrt{s} = 7$ TeV*, ATLAS-CONF-2010-038.

[115] The ATLAS Collaboration, *Studies of the performance of the ATLAS detector using cosmic-ray muons*, ArXiv e-prints (Nov., 2010) , arXiv:1011.6665 [physics.ins-det].

[116] C. G. Lester and D. J. Summers, *Measuring masses of semiinvisibly decaying particles pair produced at hadron colliders*, Phys. Lett. **B463** (1999) 99--103, arXiv:hep-ph/9906349.

[117] D. R. Tovey, *On measuring the masses of pair-produced semi-invisibly decaying particles at hadron colliders*, JHEP **04** (2008) 034.

[118] G. Polesello and D. R. Tovey, *Supersymmetric particle mass measurement with the boost- corrected contransverse mass*, JHEP **03** (2010) 030, arXiv:0910.0174 [hep-ph].

[119] The ATLAS Collaboration, *Measurement of the top quark pair production cross-section with ATLAS in pp collisions at $\sqrt{s} = 7$ TeV*, 2010. arXiv:1012.1792.

[120] J. O. Irwin, *The Frequency Distribution of the Difference between Two Independent Variates following the same Poisson Distribution*, Journal of the Royal Statistical Society **100** (1937) no. 3, pp. 415--416. http://www.jstor.org/stable/2980526.

[121] The CDF Collaboration, T. Aaltonen et al., *Inclusive Search for Squark and Gluino Production in $p\bar{p}$ Collisions at $\sqrt{s}$ = 1.96-TeV*, Phys. Rev. Lett. **102** (2009) 121801, arXiv:0811.2512 [hep-ex].

[122] The D0 Collaboration, *Search for squarks and gluinos in events with jets and missing transverse energy using 2.1 fb^{-1} of $p\bar{p}$ collision data at $\sqrt{s}$ = 1.96 TeV*, Phys. Lett. **B660** (2008) 449--457.

[123] LEP SUSY Working Group (ALEPH, DELPHI, L3, OPAL), Notes LEPSUSYWG/01-03.1 and 04-01.1, http://lepsusy.web.cern.ch/lepsusy/Welcome.html.

[124] The ATLAS Collaboration, *Search for supersymmetry in pp collisions at $\sqrt{s} = 7$ TeV in final states with missing transverse momentum and b-jets*, arXiv:1103.4344 [hep-ex].

[125] The ATLAS Collaboration, *Search for supersymmetry using final states with one lepton, jets, and missing transverse momentum with the ATLAS detector in $\sqrt{s} = 7$ TeV pp collisions*, arXiv:1102.2357 [hep-ex].

[126] The CMS Collaboration, *Search for Supersymmetry in pp Collisions at 7 TeV in Events with Jets and Missing Transverse Energy*, Phys. Lett. **B698** (2011) 196--218, arXiv:1101.1628 [hep-ex].

[127] The CMS Collaboration, S. Chatrchyan et al., *Search for Physics Beyond the Standard Model in Opposite- Sign Dilepton Events at $\sqrt{s} = 7$ TeV*, arXiv:1103.1348 [hep-ex].

[128] The ATLAS Collaboration, SUSY Working Group, Supplementary material for "Search for an excess of events with an identical flavour lepton pair and significant missing transverse momentum in $\sqrt{s} = 7$ TeV proton-proton collisions with the ATLAS detector", https://atlas.web.cern.ch/Atlas/GROUPS/PHYSICS/PAPERS/susy-2leptonFS_01/.

[129] B. C. Allanach et al., *Measuring supersymmetric particle masses at the LHC in scenarios with baryon-number R-parity violating couplings*, JHEP **03** (2001) 048, arXiv:hep-ph/0102173.

[130] J. M. Butterworth, J. R. Ellis, A. R. Raklev, and G. P. Salam, *Discovering baryon-number violating neutralino decays at the LHC*, arXiv:0906.0728 [hep-ph].

[131] J. M. Butterworth, B. E. Cox, and J. R. Forshaw, *WW scattering at the CERN LHC*, Phys. Rev. **D65** (2002) 096014, arXiv:hep-ph/0201098.

[132] A. Y. Smirnov and F. Vissani, *Upper bound on all products of R-parity violating couplings λ' and λ'' from proton decay*, Phys. Lett. **B380** (1996) 317--323, arXiv:hep-ph/9601387.

[133] G. Bhattacharyya, *R-parity-violating supersymmetric Yukawa couplings: A mini-review*, Nucl. Phys. Proc. Suppl. **52A** (1997) 83--88, arXiv:hep-ph/9608415.

[134] H. K. Dreiner, *An introduction to explicit R-parity violation*, arXiv:hep-ph/9707435.

[135] V. D. Barger, W. Y. Keung, and R. J. N. Phillips, *Possible sneutrino pair signatures with R-parity breaking*, Phys. Lett. **B364** (1995) 27--32, arXiv:hep-ph/9507426.

[136] The ALEPH Collaboration, D. Buskulic et al., *Four-jet final state production in e^+e^- collisions at centre-of-mass energies of 130 GeV and 136 GeV*, Z. Phys. **C71** (1996) 179--198.

[137] A. K. Grant, R. D. Peccei, T. Veletto, and K. Wang, *Speculations on ALEPH's Dijet Enhancement*, Phys. Lett. **B379** (1996) 272--278, arXiv:hep-ph/9601392.

[138] P. H. Chankowski, D. Choudhury, and S. Pokorski, *ALEPH four-jet excess, R(b) and R-parity violation*, Phys. Lett. **B389** (1996) 677--686, arXiv:hep-ph/9606415.

[139] D. K. Ghosh, R. M. Godbole, and S. Raychaudhuri, *Can the ALEPH four jet excess be explained in a supersymmetric model with R-parity violation ?*, Z. Phys. **C75** (1997) 357--365, arXiv:hep-ph/9605460.

[140] J. M. Butterworth, J. P. Couchman, B. E. Cox, and B. M. Waugh, *KtJet: A C++ implementation of the K(T) clustering algorithm*, Comput. Phys. Commun. **153** (2003) 85--96, arXiv:hep-ph/0210022.

[141] B. C. Allanach et al., *The Snowmass points and slopes: Benchmarks for SUSY searches*, Eur. Phys. J. **C25** (2002) 113--123, arXiv:hep-ph/0202233.

[142] R. Barbier et al., *R-parity violating supersymmetry*, Phys. Rept. **420** (2005) 1--202, arXiv:hep-ph/0406039.

[143] B. C. Allanach, A. Dedes, and H. K. Dreiner, *Bounds on R-parity violating couplings at the weak scale and at the GUT scale*, Phys. Rev. **D60** (1999) 075014, arXiv:hep-ph/9906209.

[144] S. Frixione and B. R. Webber, *The MC@NLO 3.2 event generator*, arXiv:hep-ph/0601192.

[145] J. Pumplin et al., *New generation of parton distributions with uncertainties from global QCD analysis*, JHEP **07** (2002) 012, arXiv:hep-ph/0201195.

[146] W. Lampl et al., *Calorimeter clustering algorithms: Description and performance*, ATL-LARG-PUB-2008-002, cds:1099735.

[147] M. Wolter (on behalf of the ATLAS Collaboration), *Tau identification using multivariate techniques in ATLAS*, ATL-PHYS-PROC-2009-016, cds:1152704.

[148] N. Arkani-Hamed, H. Cheng, J. L. Feng, and L. J. Hall, *Probing Lepton Flavor Violation at Future Colliders*, Phys. Rev. Lett. **77** (1996) 1937--1940, arXiv:hep-ph/9603431.

[149] N. Arkani-Hamed, J. L. Feng, L. J. Hall, and H. Cheng, *CP violation from slepton oscillations at the LHC and NLC*, Nucl. Phys. **B505** (1997) 3--39, arXiv:hep-ph/9704205.

[150] K. Agashe and M. Graesser, *Signals of supersymmetric lepton flavor violation at the LHC*, Phys. Rev. **D61** (2000) 075008, arXiv:hep-ph/9904422.

[151] J. Hisano, R. Kitano, and M. M. Nojiri, *Slepton oscillation at Large Hadron Collider*, Phys. Rev. **D65** (2002) 116002, arXiv:hep-ph/0202129.

[152] T. Goto, K. Kawagoe, and M. M. Nojiri, *Study of the slepton non-universality at the CERN Large Hadron Collider*, Phys. Rev. **D70** (2004) 075016, arXiv:hep-ph/0406317.

[153] R. Kitano, *A Clean Slepton Mixing Signal at the LHC*, JHEP **03** (2008) 023, arXiv:0801.3486 [hep-ph].

[154] B. C. Allanach, J. P. Conlon, and C. G. Lester, *Measuring Smuon-Selectron Mass Splitting at the CERN LHC and Patterns of Supersymmetry Breaking*, Phys. Rev. **D77** (2008) 076006, arXiv:0801.3666 [hep-ph].

[155] S. Kaneko, J. Sato, T. Shimomura, O. Vives, and M. Yamanaka, *Measuring Lepton Flavour Violation at LHC with Long-Lived Slepton in the Coannihilation Region*, Phys. Rev. **D78** (2008) 116013, arXiv:0811.0703 [hep-ph].

[156] A. De Simone, J. Fan, V. Sanz, and W. Skiba, *Leptogenic Supersymmetry*, Phys. Rev. **D80** (2009) 035010, arXiv:0903.5305 [hep-ph].

[157] Z. Chacko and E. Ponton, *Yukawa deflected gauge mediation*, Phys. Rev. **D66** (2002) 095004, arXiv:hep-ph/0112190.

[158] R. N. Mohapatra, N. Okada, and H.-B. Yu, *ν-GMSB with Type III Seesaw and Phenomenology*, Phys. Rev. **D78** (2008) 075011, arXiv:0807.4524 [hep-ph].

[159] The MEGA Collaboration, *New Limit for the Family-Number Non-conserving Decay μ^+ to $e^+\gamma$*, Phys. Rev. Lett **83** (1999) 1521--1524, arXiv:hep-ex/9905013.

[160] G. Marchesini et al., *HERWIG: A Monte Carlo event generator for simulating hadron emission reactions with interfering gluons. Version 5.1 - April 1991*, Comput. Phys. Commun. **67** (1992) 465--508.

[161] J. R. Ellis, A. R. Raklev, and O. K. Oye, *Gravitino dark matter scenarios with massive metastable charged sparticles at the LHC*, JHEP **10** (2006) 061, arXiv:hep-ph/0607261.

[162] S. Tarem, S. Bressler, H. Nomoto, and A. Di Mattia, *Trigger and reconstruction for heavy long-lived charged particles with the ATLAS detector*, Eur. Phys. J. **C62** (2009) 281--292.

[163] J. L. Feng, A. Rajaraman, and B. T. Smith, *Minimal supergravity with $m(0)^2 < 0$*, Phys. Rev. **D74** (2006) 015013, arXiv:hep-ph/0512172.

[164] A. Rajaraman and B. T. Smith, *Discovering SUSY with $m(0)^2$ < 0 in the first CERN LHC physics run*, Phys. Rev. **D75** (2007) 115015, arXiv:hep-ph/0612235.

[165] A. Rajaraman and B. T. Smith, *Determining Spins of Metastable Sleptons at the Large Hadron Collider*, Phys. Rev. **D76** (2007) 115004, arXiv:0708.3100 [hep-ph].

[166] W. Verkerke and D. P. Kirkby, *The RooFit toolkit for data modeling*, arXiv:physics/0306116.

[167] The CMS Collaboration, *Search for Physics Beyond the Standard Model in Opposite-Sign Dilepton Events at $\sqrt{s} = 7$ TeV*, arXiv:1103.1348 [hep-ex].

[168] R. Achenbach et al., *The ATLAS level-1 calorimeter trigger*, JINST **3** (2008) P03001.

[169] The ATLAS Collaboration, *L1Calo Public Results*, https://twiki.cern.ch/twiki/bin/view/AtlasPublic/LArCaloPublicResults2009.

[170] J. Adelman et al., *ATLAS offline data quality monitoring*, J. Phys. Conf. Ser. **219** (2010) 042018.

[171] Y. Nomura, M. Papucci, and D. Stolarski, *Flavorful Supersymmetry*, Phys. Rev. **D77** (2008) 075006, arXiv:0712.2074 [hep-ph].

[172] G. Hiller, Y. Hochberg, and Y. Nir, *Flavor Changing Processes in Supersymmetric Models with Hybrid Gauge- and Gravity-Mediation*, JHEP **03** (2009) 115, arXiv:0812.0511 [hep-ph].

[173] C. D. Froggatt and H. B. Nielsen, *Hierarchy of Quark Masses, Cabibbo Angles and CP Violation*, Nucl. Phys. **B147** (1979) 277.

[174] J. L. Feng and T. Moroi, *Tevatron signatures of longlived charged sleptons in gauge mediated supersymmetry breaking models*, Phys. Rev. **D58** (1998) 035001, arXiv:hep-ph/9712499.

[175] J. L. Feng, A. Rajaraman, and F. Takayama, *Superweakly-interacting massive particles*, Phys. Rev. Lett. **91** (2003) 011302, arXiv:hep-ph/0302215.

[176] S. Ambrosanio, G. D. Kribs, and S. P. Martin, *Three-body decays of selectrons and smuons in low-energy supersymmetry breaking models*, Nucl. Phys. **B516** (1998) 55--69, arXiv:hep-ph/9710217.

[177] J. L. Feng, I. Galon, D. Sanford, Y. Shadmi, and F. Yu, *Three-Body Decays of Sleptons with General Flavor Violation and Left-Right Mixing*, Phys. Rev. **D79** (2009) 116009, arXiv:0904.1416 [hep-ph].

[178] A. Buckley, *hepthesis - a LaTeX document class for academic theses*, http://www.ctan.org/tex-archive/help/Catalogue/entries/hepthesis.html.

Bibliography entries of the form `arXiv:<identifier>` can be found on the World Wide Web at `http://arxiv.org/abs/<identifier>`. Those of the form `cds:<number>` can be found on the CERN document server at `http://cdsweb.cern.ch/record/<number>`. All ATLAS Collaboration notes have additional identifiers of the form `ATL-???-xxxx-yy` (or sometimes

also ATLAS-???-xxxx-yy) where ??? details the type of note, xxxx the year and yy the unique reference number for the publication. Only public ATLAS notes, PUB, ATLAS conference proceedings, PROC, and ATLAS Conference Notes, CONF, are publicly available. ATLAS Internal Notes, INT, and ATLAS Communications, COM, can only be accessed on cds by members of the ATLAS Collaboration. Scientific Committee Paper's, with identifiers of the form CERN-LHCC-YY-XXX, where YY is the year and XXX the unique identifier number, are all publicly available on the CERN document server.

List of Figures

List of Tables